VNIVERSITAT DE VALÈNCIA Facultat de Física

Departament de Física de la Terra i Termodinàmica

TESI DOCTORAL

Doctorat en Teledetecció

Influence of land cover in the atmospheric water vapor content and the generation of summer storms in the Turia River Basin

Dirigida per

Dr. José Antonio Valiente Pardo
Dra. Raquel Niclòs Corts
Dr. José Luis Palau Aloy

Presentada per

Pau Benetó Vallés

Burjassot, Maig de 2022

Dr. JOSÉ ANTONIO VALIENTE PARDO, investigador en el Departament de Meteorologia i Dinàmica de Contaminants de la Fundació Centre d'Estudis Ambientals del Mediterrani (CEAM).

Dr. JOSÉ LUIS PALAU ALOY, director de l'Àrea d'Innovació i I+D de l'empresa BIONICIA S.L.,

Dra. RAQUEL NICLÒS CORTS, Professora Titular de Física de la Terra, en el departament de Física de la Terra i Termodinàmica de la Facultat de Física, Universitat de València,

CERTIFIQUEN:

Que la present memòria *"Influence of land cover in the atmospheric water vapor content and the generation of summer storms in the Turia river basin"*, presentada per Pau Benetó Vallés ha sigut realitzada sota la seua direcció constituint la seua Tesi Doctoral per a optar al Grau de Doctor per la Universitat de València dins del Doctorat en Teledetecció.

I perquè així conste, en compliment de la legislació vigent, firmen el present certificat en Burjassot, a 18 de maig de 2022.

Firmat:	Firmat:	Firmat:
Dr. José Antonio Valiente Pardo	Dr. José Luis Palau Aloy	Dra. Raquel Niclòs Corts

A la meua família

Acknowledgments/Agraïments

Those who can imagine anything,
can create the impossible.
(Alan Turing)

Ja hi som.

Aquest doctorat està arribant al seu final després d'haver-me acompanyat durant tant de temps que és difícil recordar tota la gent que hi ha estat afectada d'alguna forma o altra, i tota aquella que hi ha participat d'una manera més o menys activa. Per això vull agrair a totes aquestes persones la seua col·laboració i disponibilitat per a facilitar-me un punt de recolzament que m'ha permés arribar a aquest moment.

En primer lloc m'agradaria donar les gràcies als meus directors per l'ajuda i recolzament proporcionats durant tot aquest temps. Al Dr. José Antonio Valiente Pardo i el Dr. José Luis Palau Aloy per l'oportunitat de formar part del seu equip, que em va permetre endinsar-me encara més en el meravellós món de la meteorologia, i a la Dra. Raquel Niclòs Corts per la seua disponibilitat i rapidesa a l'hora de gestionar qualsevol qüestió. A tos ells agrair-los la seua implicació en aquesta Tesi Doctoral i l'assessorament des de l'experiència i la saviesa que han acumulat durant tot el seu temps dedicat a la recerca.

No me n'oblide dels que començaren com col·legues al CEAM a l'inici d'aquest doctorat i que han acabat esdevenint amics i amigues, i inclús veïns. Elisabeth, you cannot imagine how happy I am to have had the chance to meet you and share this exciting adventure with you. I am very grateful for the wonderful light you brought in the darkest moments of our journey. *Paco Alacreu, d'ara endavant veí, agrair-te els bons consells, la calma i el somriure que sempre has compartit en tot moment malgrat l'estrés i els daltabaixos. Juntament amb Maria i Ainhoa, m'heu adelitat la vida.*

També donar les gràcies al CEAM per haver-me brindat els mitjans i les eines per a dur a terme aquesta Tesi Doctoral, així com a la gent que forma part del CEAM, tant la part administrativa com la investigadora, per la seua disponibilitat per a resoldre qualsevol tipus de qüestió. Recordar també als estudiants de pràctiques i altres persones que temporalment han passat per la institució i que d'alguna manera han contribuït a aquesta Tesi Doctoral. Particularment a Núria, Chulvi, Konstantina, Xristina, Leticia, Bernat i Hassane.

Un agraïment especial als meus amics de tota la vida (Rafa, Antonio i Carlos) per tenir la paciència i entendre el significat de "no puc, he d'acabar la tesi". Igualment als amics que vaig trobar a la facultat de físiques ara fa uns anys (en especial a Núria, Andrés i Javi), ja que aquesta tesi ha deixat moltes celebracions pendents. Tranquils, les recuperarem.

Amb el permís de tots els meus amics i amigues, he de fer un agraïment particularment especial a Andrés, ja que les nostres xarrades sobre meteorologia en les que sempre

demostres la teua passió i coneixements han aportat un toc distintiu a aquesta tesi. Gràcies.

Gli effetti di questa tesi sono arrivati all'altro lato del Mediterraneo. Per questo, vorrei anche ringraziare la mia famiglia salernitana (Antonio, Luisa, Roberta, Fabio e Giulia) per procurarmi un posto di studio a casa vostra, aiutarmi davanti a qualsiasi difficoltà e darmi una vita piena di sole e cibo, tanto cibo. Vi voglio bene.

Un agraïment de tot cor als meus pares (Vicenta i Rafael) i al meu germà Joan, que també s'han vist afectats per aquesta tesi doctoral. Gràcies per la vostra paciència, els ànims i les abraçades que m'han fet més fàcil avançar, no sols durant aquest període, si no durant tota la meua vida. Vos estime.

Amb ulls humits de l'emoció escric aquestes paraules d'agraïment a les meues filles Mar i Laia que espere que algun dia llegisquen. Els vostres somriures i les vostres besades m'han fet oblidar qualsevol problema i m'han endolcit el dia a dia. Gràcies. Vos estime.

Finalmente, ringraziare anche la mia compagna di vita, Giovanna. Tu sei chi ha sofferto le conseguenze di questa tesi di più e, dopo tanti anni, ancora mi sorprendi con la tua forza, intelligenza ed ottimismo che ogni volta mi riportano al giorno in cui i tuoi occhi penetrarono in fondo alla mia anima. Ti amo.

The Precipitation - CMORPH Climate Data Record (CDR) used in this study was acquired from the NOAA National Centers for Environmental Prediction (NCEP). This CDR was developed by Pingping Xie of NOAA-CPC, Robert Joyce, Shaorong Wu Soo-Hyun Yoo, Yelena Yarosh, Fengying Sun, and Roger Lin of Innovim, LLC.

ERA5 data was downloaded from the Copernicus Climate Change Service (C3S) Climate Data Store. The results contain modified Copernicus Climate Change Service information 2020. Neither the European Commission nor ECMWF is responsible for any use that may be made of the Copernicus information or data it contains.

SPAIN02 precipitation gridded dataset at a 5-km horizontal resolution used in this doctoral thesis was provided by AEMET.

The surface observations used in this doctoral thesis were provided by IVIA-SIAR, XVVCCA and CEAM.

Observation from GNSS networks were provided by ARAGEA, ERVA, CatNET and ERGNSS) and processed at the *Intitut Cartogràfic i Geodèsic de Catalunya* (ICGC).

For this study, the Fundación CEAM was partly supported by *Generalitat Valenciana* and research projects "DESESTRES" PROMETEOII/2014/038 (*Consellería de Cultura*), "IMAGINA" PROMETEU/2019/110 (*Consellería de Cultura* GVA) and "VERSUS" CGL2015-67466-R (MINECO/FEDER). Also, thank the research project PID2020-118797RB-I00 funded by MCIN/AEI/10.13039/501100011033.

RESUM **1**

LIST OF ACRONYMS **13**

LIST OF SYMBOLS **17**

CHAPTER 1: INTRODUCTION **21**

1. The Mediterranean basin 23
2. Sea breeze and summer storms 25
   2.1. Sea breeze structure and forcings 26
   2.2. Summer storms 31
   2.3. Modeling 37
3. Structure and goals 39

CHAPTER 2: MATERIALS AND METHODS **43**

1. Area of study 45
2. The Weather Research and Forecasting model 47
   2.1. Static data 48
   2.2. WRF parametrizations 50
   2.3. Land Surface Models 56
3. Observations 62
   3.1. Reanalysis datasets 63
   3.2. Satellite products 63
   3.3. Surface stations 65
   3.4. Models and analysis tools 67
4. Summer storms and sea breeze 68
   4.1. Study period: May-October 2015 68
   4.2. Sea breeze characterization 69
5. Simulation strategy 71
   5.1. Model set up 72
   5.2. Model validation 77
6. SVA energetic exchanges 78
   6.1. Mixing diagram approach 78
   6.2. Trajectories 82

CHAPTER 3: SUMMER STORMS AND MODELING **87**

1. Summer storms episodes in eastern Spain 89
   1.1. May-October 2015 89
   1.2. Case study 91
2. ESS simulations 99
   2.1. Statistical analysis 99
   2.2. Precipitation 101
   2.3. Evapotranspiration 104
3. Comparative analysis 109
   3.1. Statistical analysis 109
   3.2. Precipitation 112

CHAPTER 4: LAND USE INFLUENCE IN SUMMER STORMS **115**

1. Sea breeze classification 117
2. Characterization of SVA energetic exchanges 120
   2.1. Atmospheric conditions in the TRB 120
   2.2. Sea breeze circulation during JJA 121

2.3. Case study: 15th - 23rd of July 2015 130
3. HIGH-RESOLUTION SIMULATION OVER THE TRB 131
3.1. Statistical analysis 131
3.2. Precipitation 133
3.3. Mixing ratio, temperature and winds 135
4. SVA ENERGETIC EXCHANGES 140
4.1. Sea breeze and summer storms 140
4.2. Land-atmosphere interactions: mixing diagrams 143
4.3. Land-atmosphere interactions: trajectories 155

CHAPTER 5: GENERAL DISCUSSION 175

1. MESOSCALE MODELING 177
1.1. The hydrological cycle 177
1.2. Representation of summer storms 179
2. LAND-ATMOSPHERE INTERACTIONS 182
2.1. Sea breeze and summer storms 182
2.2. Surface moisture and heat fluxes 184

CHAPTER 6: CONCLUSIONS 189

APPENDIX 191

1. WRF MODEL PARAMETRIZATIONS 191
1.1. Planetary Boundary Layer schemes 193
1.2. Calculation of H 196
1.3. Noah-MP input vegetation tables 197
1.4. Data flow using ndown.exe 198
2. MIXING DIAGRAMS FROM OBSERVATIONS 199
3. INTERMEDIATE SEA BREEZE FRONT 201
4. MIXING DIAGRAMS FROM STM SIMULATION 203
5. TRAJECTORIES 212

BIBLIOGRAPHY 217

RESUM

INTRODUCCIÓ

La conca mediterrània és una zona fortament afectada pel canvi climàtic amb importants variacions de temperatura de la mar i precipitació. En les últimes dècades s'ha destacat una clara tendència ascendent en la temperatura de la mar (Shaltout and Omstedt, 2014; Pastor et al., 2019), un factor clau en la formació de precipitacions intenses en la costa mediterrània de la península ibèrica, així com un decreixement significatiu de la precipitació especialment marcat a l'estiu (Milano et al., 2013; Valdés-Abellán et al., 2017). La reducció dels recursos hídrics a l'est de la península ibèrica, lligada al decreixement generalitzat de la precipitació, genera problemes d'abastiment a les grans zones urbanes situades al llarg de la costa i als camps de cultiu amb el conseqüent impacte socioeconòmic. La manca d'aigua també genera canvis importants als ecosistemes com ara la reducció de la massa forestal i la desertificació. A més, l'augment de la població condueix a un increment en el consum d'aigua i a una expansió de les zones urbanes. En conseqüència, aquests factors accentuen la pèrdua de boscos i generen un canvi important en la distribució dels usos del sòl que poden tenir un paper important en la formació de precipitació associada a circulacions locals.

Generalment, les circulacions a escala sinòptica són febles durant l'estiu de manera que la major part de la precipitació està associada a circulacions locals. Aquestes condicions atmosfèriques propicien la formació de circulacions de brisa al litoral i prelitoral, a causa de les diferències tèrmiques entre la superfície de la mar i el continent durant el dia, i afavoreixen l'advecció de masses d'aire d'origen marítim cap a zones d'interior. Les característiques de la brisa (estructura, duració, intensitat i extensió) depenen dels diferents forçaments als que se sotmet, com ara la orientació de la costa, la topografia i les condicions sinòptiques, entre d'altres, factors que també influeixen els fenòmens associats a aquest tipus de circulacions. En el cas de la topografia, aquesta pot modificar o dificultar l'avanç de la brisa cap a l'interior, així com facilitar la formació de núvols de tipus orogràfic. Les circulacions sinòptiques principalment poden influenciar la direcció i intensitat dels corrents de retorn de la brisa en capes més altes i, a més, determinar el desenvolupament vertical de les circulacions de brisa.

En la costa mediterrània de la península ibèrica, la brisa es canalitza a través de les valls assolint les capçaleres dels principals rius on es generen línies de convergència, és a dir,

zones on les masses d'aire superficials s'injecten a capes més altes de l'atmosfera i, en ocasions, donen lloc a la formació de sistemes convectius coneguts com tronades d'estiu. Aquests fenòmens meteorològics associats a les circulacions de brisa ocorren principalment entre els mesos d'abril i octubre. A més, la formació d'una baixa tèrmica al centre de la península ibèrica intensifica les brises a la costa, encara que també dificulta la formació de tronades als sistemes muntanyosos propers a la mar a causa de la subsidència associada que es genera sobre la mar Balear. A part, la formació de núvols convectius presenta una dependència en diversos factors meteorològics com la presència d'aire fred en capes superiors de l'atmosfera, l'altitud de les serralades (altura d'injecció de l'aire en superfície) i les propietats de la massa d'aire injectada (contingut de vapor d'aigua i temperatura). En referència a aquest últim factor, les interaccions entre el sòl i l'atmosfera modifiquen les característiques de la massa d'aire advectada des de la mar a mesura que aquesta avança cap a l'interior. De fet, Millán et al. (2005a) exposà que l'increment en temperatura de la massa d'aire d'origen marítim dificulta la formació de tronades d'estiu a causa d'un augment de l'altura a la qual es generen els núvols, *cloud condensation level* (CCL) en anglés, contràriament a l'efecte produït per l'increment en vapor d'aigua atmosfèric associat a la evapotranspiració. Concretament, si la CCL és més elevada que l'altura a la que s'injecta la massa d'aire superficial, determinada pels sistemes muntanyosos, no es produirà la condensació. En cas contrari, la injecció de la massa d'aire humit a capes més altes de l'atmosfera pot donar lloc a precipitacions de diferents intensitats depenent també dels factors comentats prèviament. Amb tot açò, Millán et al. (2005a) recalcà la importància dels usos del sòl en la formació de tronades d'estiu al llarg de la costa mediterrània.

Les tronades d'estiu representen una font d'aigua important en la conca mediterrània, ja que aporten aigua durant els mesos més secs de l'any, amb la qual cosa ajuden a mantenir els cabdals dels rius. Llavors, és alarmant que aquest tipus de sistemes convectius presenten una tendència decreixent en les últimes dècades com indicà Miró et al. (2018). En aquest aspecte, Millán et al. (2005b) remarcà que la tendència negativa de la precipitació associada a aquest tipus d'esdeveniments podria generar la pèrdua de boscos i intensificar la desertificació del mediterrani peninsular. A més, exposà que la reducció de la massa forestal conduiria a una pèrdua addicional de tronades d'estiu i a la conseqüent exacerbació de la desertificació en la zona.

L'extens coneixement assolit en les característiques de la brisa i els fenòmens associats a aquesta (com les tronades d'estiu) s'ha produït gràcies als avanços en les últimes dècades tant en l'increment i millora de les observacions com en l'elevada complexitat dels models meteorològics i climàtics utilitzats en l'actualitat. Aquests models incorporen un ample ventall de parametritzacions dels processos atmosfèrics. Addicionalment, la millora dels sistemes de computació d'alt rendiment permeten l'ús de simulacions de molt alta resolució espacial i temporal que milloren la representació de la dinàmica atmosfèrica lligada a processos locals. Amb tot açò, juntament amb el seu cost relativament baix, la modelització es avui en dia una eina molt utilitzada en les ciències atmosfèriques.

OBJECTIUS

En aquesta tesi es consideren alguns dels arguments i hipòtesis exposades en Millán et al. (2005a) i Millán (2014), amb especial interès en la rellevància de les interaccions entre el sòl i l'atmosfera, així com també en el seu efecte en la formació de les tronades d'estiu. Concretament, en aquesta tesi es pretén:

- Estimar els canvis en vapor d'aigua i temperatura associats a fluxos superficials de les masses d'aire involucrades en la formació de tronades d'estiu en la vall del Túria.
- Quantificar les contribucions dels diferents usos del sòl al vapor d'aigua atmosfèric i calor que caracteritzen l'àrea d'estudi juntament amb altres processos atmosfèrics.

Per a dur a terme els dos principals objectius, altres qüestions necessàries s'han hagut de plantejar en aquesta tesi doctoral, de manera que s'han estudiat les característiques de l'àrea d'estudi, les condicions sinòptiques que afavoreixen la formació de tronades d'estiu i les configuracions disponibles de la principal eina emprada en aquesta tesi: el model meteorològic *Weather Research and Forecasting* (WRF). En particular, s'han realitzat:

- L'avaluació del model meteorològic WRF amb dues parametritzacions dels processos superficials per a un episodi de tronades d'estiu respecte a les principals variables hidrometeorològiques.

- La caracterització de les principals propietats de la brisa marina i altres circulacions locals en la conca del Túria mitjançant l'anàlisi de mesures de temperatura i humitat.
- La comparació de fluxos superficials de vapor d'aigua i calor sensible en zones amb vegetació i sense vegetació en diferents punts de la zona d'estudi.

Aquests anàlisis han proporcionat informació respecte a les incerteses en la modelització dels processos de superfície, així com un millor coneixement de les condicions atmosfèriques a escala local que propicien la generació de tronades d'estiu en situacions de brisa.

La tesi s'estructura en un total de sis capítols. Al primer capítol es presenta un recull del coneixement actual respecte a la brisa marina i les tronades d'estiu amb especial èmfasi a la costa mediterrània de la península ibèrica. Al segon capítol s'introdueixen el model meteorològic WRF i les diferents dades observacionals emprades tant per a la validació del model com per a l'anàlisi de les condicions atmosfèriques i els episodis de tronades d'estiu. Els episodis de tronades d'estiu estudiats en detall i els resultat obtinguts de l'avaluació de les diferents simulacions amb el model WRF es presenten al tercer capítol. Al quart capítol s'exposen els resultats de l'anàlisi dels fluxos superficials durant l'episodi de tronades d'estiu segons els tipus de sòl. Finalment, als capítols cinqué i sisé es presenten una discussió general dels resultats i les conclusions, respectivament.

METODOLOGIA

L'estudi s'ha centrat en la costa est de la península ibèrica, concretament al País Valencià i a la conca del riu Túria. Per al desenvolupament de la present tesi doctoral i la resposta a les diferents qüestions plantejades en la mateixa s'ha emprat el model meteorològic WRF validat amb observacions des de satèl·lit i mesures de les diferents xarxes d'estacions disponibles en la zona d'estudi. Per a un anàlisi més complet, diverses simulacions amb distintes configuracions dels processos en superfície s'han realitzat en el model.

Prèviament als exercicis de simulació s'han dut a terme dos anàlisis per a la selecció del període d'estudi i la caracterització de la brisa a la conca del riu Túria. D'una banda, s'ha seleccionat el període a estudiar mitjançant un anàlisi del número d'episodis de

precipitació que han ocorregut durant anys recents, concretament per a l'estació estival ampliada (ESS, per les seues inicials en anglés), definida com el període comprés entre maig i octubre. Una vegada seleccionat l'any d'estudi (2015), tot seguit, s'han identificat els dies de pluja associats a la formació de tronades d'estiu a partir de mapes sinòptics seguint la metodologia introduïda a Millán et al., (2005b). Específicament, s'han generat mapes amb dades de temperatura i geopotencial a 500hPa, i pressió atmosfèrica a nivell de la mar. A l'anàlisi s'ha considerat la formació de la baixa tèrmica sobre la península ibèrica com a indicador de condicions atmosfèriques en superfície favorables per a la formació de tronades d'estiu. En aquests mapes també s'han analitzat les condicions atmosfèriques en base a la presència d'aire fred o tàlvegs a 500hPa, ja que són indicadors de la inestabilitat atmosfèrica. Addicionalment, imatges del satèl·lit Meteosat s'han visualitzat per a detectar la formació i evolució de nuclis convectius als sistemes muntanyosos de la península ibèrica. Amb aquest procediment s'han detectat set episodis de tronades d'estiu afectant les cadenes muntanyoses dels Sistemes Ibèric i Prebètic durant l'any 2015, especialment la conca del riu Túria.

D'altra banda, mesures de la velocitat i direcció del vent de les torres meteorològiques de la xarxa del CEAM situades en la vall del Túria s'han emprat per a identificar els dies de brisa en el període 2005-2015, d'acord amb la disponibilitat de dades. D'aquesta manera s'ha conduit un estudi extens de les variacions d'humitat i temperatura associades a la brisa en les diferents localitzacions de la vall del Túria: Paterna (PA; litoral), Villar del Arzobispo (VI; prelitoral) i Aras de los Olmos (AR; interior). En concret, la detecció de dies de brisa s'ha dut a terme de manera que:

- S'han generat roses dels vents a les diferents localitzacions sobre mapes topogràfics per a visualitzar l'efecte de la topografia i/o la posició respecte de la costa, si escau, en la direcció del vent.
- Les dades de vent s'han filtrat per a les hores diürnes (05-19 UTC) juntament amb la exclusió de vents menors d'1 $m \cdot s^{-1}$ i majors de 7 $m \cdot s^{-1}$ a l'estació de PA situada al litoral. Com que les torres meteorològiques estan alineades al llarg de la conca del riu Túria, els dies de brisa en VI s'han filtrat en base als dies de brisa identificats en PA i, anàlogament, el dies de brisa en AR respecte dels identificats en VI. Després de l'aplicació d'aquests filtres, s'ha representat la distribució de la direcció del vent en un gràfic de barres i s'ha ajustat a una distribució de Gauss (o dues combinades) per a cadascuna de les estacions. Tot

seguit, s'ha seleccionat l'interval de confidència 95 % per a definir el rang de variació de la brisa a cadascuna de les estacions.

- Finalment, els dies de brisa s'han definit com els dies amb un 50 % de les hores diürnes (7 h) amb una direcció del vent continuada entre els rangs definits en cadascuna de les localitzacions. Posteriorment, s'han extret els percentatges de dies de brisa a cada estació respecte del total de dies amb dades per al període 2005-2015.

Respecte als exercicis de simulació, dues simulacions a alta resolució espacial (~1 km) sobre el País Valencià per al període maig-octubre de 2015 s'han dut a terme amb els models de superfície Noah-MP i Pleim-Xiu. El principal objectiu d'aquestes simulacions ha consistit en analitzar les diferències entre ambdues parametritzacions. Concretament, s'han avaluat la representació de les variables hidrometeorològiques principals (precipitació, evapotranspiració, temperatura, humitat relativa i vent) que afecten el cicle hidrològic de la zona d'estudi. Addicionalment, s'han executat tres simulacions a una resolució espacial de 3 km sobre la península ibèrica d'un dels episodis de tronades d'estiu identificats anteriorment. En aquestes simulacions s'han comparat diferents parametritzacions dels processos de superfície, així com de la capa superficial atmosfèrica per a detectar la configuració produint les millors estimacions. A continuació, la configuració que ha generat els millors resultats respecte a les variables meteorològiques analitzades s'ha emprat en una última simulació a molt alta resolució (680 m) sobre la conca del riu Túria. A partir d'aquesta última simulació s'han avaluat les interaccions sòl-vegetació-atmosfera (SVA) i s'han estimat les contribucions dels fluxos superficials al vapor d'aigua atmosfèric i a la temperatura de l'aire.

Dues aproximacions s'han utilitzat en aquesta tesi per a estudiar la rellevància de les interaccions SVA i les contribucions de la superfície a la recàrrega de vapor d'aigua atmosfèric i l'escalfament de l'aire en situacions prèvies a la formació de tronades d'estiu. D'una banda, els intercanvis en el sistema SVA s'han calculat amb els diagrames de mescla o *mixing diagrams* que representen les variacions de θ en funció de q en l'espai energia per unitat de massa (Santanello et al., 2009). En aquesta aproximació se suposa que l'evolució de la capa límit durant el dia, incloent-hi l'*entrainment* a la part superior de la mateixa, es pot determinar a partir dels fluxos superficials d'humitat i calor, i dels valors de temperatura i humitat prop de la superfície en situacions sense condensació. Aquest mètode facilita l'estimació de les diferents

contribucions a q i θ associades a la superfície, a l'advecció i a l'*entrainment* i permet identificar les variacions temporals de θ respecte a q d'una manera directa, així com incorporar altres variables termodinàmiques a l'anàlisi com la humitat relativa i/o la temperatura potencial equivalent. D'altra banda, les contribucions per part de la superfície a q i θ també s'han analitzat des d'un punt de vista Lagrangià. Concretament, s'han extret trajectòries associades a la formació de tronades d'estiu i a circulacions de brisa i s'han calculat les contribucions des de la superfície i l'efecte de l'*entrainment*. En aquesta aproximació s'han considerat parcel·les d'aire que avancen des de la vall del Túria i des de la mar fins al punt on s'inicia la convecció en cadascun dels esdeveniments estudiats. A més, s'han calculat les contribucions des de la superfície associades als diferent usos del sòl presents al model al llarg de les trajectòries.

RESULTATS

La comparativa entre els dos models de superfície implementats en WRF indica que la major complexitat del Noah-MP comporta una millor representació de les circulacions a nivell superficial i de la precipitació que el Pleim-Xiu. Tanmateix, l'extensa anàlisi estadística realitzada mostra xicotetes diferències entre ambdues parametritzacions respecte a temperatura i humitat. A més, els resultats indiquen que el Pleim-Xiu reprodueix més acuradament la evapotranspiració que el Noah-MP indicant la rellevància de la representació més realista de les profunditats del sòl; el Pleim-Xiu considera una profunditat de fins a 1 m, mentre que el Noah-MP considera 2 m.

En general, les majors diferències entre les dues configuracions analitzades es donen al camp de precipitació. El Noah-MP mostra una major precisió en la reproducció de les tronades d'estiu i una menor sobreestimació de les quantitats acumulades respecte al Pleim-Xiu, el qual presenta desviacions en mitjanes espacials de fins a 4 $mm \cdot dia^{-1}$. A més, la configuració del Noah-MP amb la parametrització de la capa superficial MM5 (MM5-NaohMP) incrementa lleugerament la precisió respecte a l'altra configuració (PX-NoahMP) en l'episodi de tronades d'estiu estudiat. Aquest resultat remarca la importància de l'estimació dels coeficients d'intercanvi sobre la mar, ja que el Noah-MP s'encarrega de calcular els intercanvis entre l'atmosfera i el sòl en la capa superficial sobre el continent, mentre que la parametrització de la capa superficial realitza aquest càlcul sobre aigua. Amb tot açò, la configuració MM5-NoahMP s'ha utilitzat per a realitzar una simulació a molt alta resolució (680 m) sobre la conca del riu Túria.

La caracterització de la brisa marina en la conca del riu Túria remarca la importància d'aquest tipus de circulació durant l'estiu estenent-se típicament fins a 100-120 km terra endins. La brisa té un paper dominant en la zona d'estudi induint canvis bruscos d'humitat i temperatura al prelitoral i litoral. Aquest fet s'observa clarament als diagrames de mescla obtinguts a partir de dades observacionals a PA, VI i AR, els quals mostren variacions associades a la circulació de brisa en forma d'U invertida. Específicament, pel matí, l'efecte dominant del fluxos superficials de calor sensible generen un increment ràpid de θ que també suposa el creixement de la capa límit, en anglés *Planetary Boundary Layer* (PBL), per l'efecte de l'*entrainment*. A migdia, s'observa un increment sobtat de q a θ constant indicatiu de l'advecció d'una massa d'aire humit lligada a la circulació de brisa. Finalment, a mesura que decreix la intensitat de la radiació solar i es redueixen també els fluxos superficials de calor sensible, s'observa un decreixement de θ a q constant, aquest últim associat a l'homogeneïtat de la massa d'aire d'origen marítim.

Les variacions descrites anteriorment estan influenciades per les característiques del sòl que determinen la intensitat dels fluxos superficials. De fet, els anàlisis mostren que les zones vegetades presenten valors de q de fins a 0.5 $g \cdot kg^{-1}$ superiors i valors de θ de fins a 2 ºC menors que les zones sense vegetació al prelitoral. Tanmateix, aquestes diferències no s'observen a les estacions situades al litoral, ja que estan influenciades des de l'eixida del sol per masses d'aire més humit d'origen marítim.

L'anàlisi de l'episodi de tronades d'estiu amb els paràmetres simulats a alta resolució indiquen que, en la majoria dels casos, la convecció s'inicia abans de l'arribada de la massa d'aire més humit remarcada als diagrames de mescla generats a partir d'observacions. Aquesta massa d'aire advectada, definida com front de brisa marina intermedi (ISBF, per les seues inicials en anglés) en aquesta tesi, pot intensificar la precipitació associada a les tronades d'estiu a mesura que avancen cap a la costa.

En base a l'arribada del ISBF, les contribucions dels diferents usos del sòl presents al model remarquen una major aportació durant el primer període de la U invertida, és a dir, abans de l'arribada del ISBF. A més, les contribucions màximes es produeixen al litoral i sobre zones de cultiu lligades principalment a la fracció de vegetació i a un menor desenvolupament de la capa límit. Tanmateix, l'*entrainment* és el factor dominant en les variacions de q i θ tant a la costa com a les zones d'interior. Aquest efecte genera una important reducció del contingut en vapor d'aigua i un increment de

la temperatura de l'aire contrarestant substancialment les variacions associades principalment a l'advecció.

A l'anàlisi de trajectòries, es mostra que l'evapotranspiració contribueix en un 7 % al total del contingut en vapor d'aigua de la massa advectada abans de ser injectada a capes superior de l'atmosfera. A més mostra la major aportació de vapor d'aigua a l'atmosfera per part dels camps de cultius presents al llarg de les trajectòries que representen al voltant d'un 50 % de la contribució total, ja que són l'ús de sòl majoritari en la zona d'estudi. Contràriament, les contribucions a θ associades als fluxos superficials de calor sensible representen un 40 % de l'increment total al llarg del recorregut de la brisa. En general, les zones urbanes generen les majors contribucions a θ, fins a un 50 %, especialment en les trajectòries amb origen a la mar, ja que travessen l'àrea metropolitana de València.

CONCLUSIONS

Les principals conclusions extretes d'aquesta tesi doctoral són les següents:

1. La comparativa dels dos models de superfície Noah-MP i Pleim-Xiu implementats en WRF indica una representació similar de les típiques variables meteorològiques. Tanmateix, el Noah-MP presenta una millor estimació de la precipitació convectiva associada a tronades d'estiu durant el període estudiat. A més, s'ha demostrat que el Noah-MP reprodueix més acuradament l'episodi de tronades d'estiu que el Pleim-Xiu, especialment quan s'implementa amb la parametrització MM5 de la capa superficial.
2. L'anàlisi de les variacions de θ respecte a q mitjançant els diagrames de mescla (espai d'energia per unitat de massa) en les diferents estacions dins de la zona d'estudi indica que la brisa indueix a variacions en forma d'U invertida. Aquestes variacions estan determinades per l'efecte dels fluxos superficials de calor i humitat, l'*entrainment* i l'advecció associada a les circulacions de brisa. Concretament, es poden discernir tres períodes diferents:
    a. Increment ràpid de θ a q constant, aproximadament, lligat al domini dels fluxes superficials de calor sensible i *entrainment*, juntament amb fluxos de calor latent poc marcats.

   b. Increment de q a θ constant, aproximadament, associat a l'arribada d'una massa d'aire humit malgrat els efectes marcats dels fluxos de calor sensible i *entrainment*.

   c. Decreixement de θ a q constant lligats a la minva de la radiació solar i la homogeneïtat de la massa d'aire d'origen marítim advectada per la circulació de brisa, respectivament.

3. Les variacions de q *i* θ s'han estudiat en diferents localitzacions (litoral, prelitoral i interior) i usos del sòl (urbà, sòl nu i cultius), de manera que s'ha identificat una dependència en la distància respecte a la mar i les característiques del sòl. D'una banda, les zones amb vegetació presenten valors lleugerament menors de θ i majors de q respecte a zones sense vegetació al prelitoral. Contràriament, aquestes diferències no s'observen al litoral entre àrees urbanes i zones de cultiu (amb vegetació). D'altra banda, el retràs en l'arribada de l'aire més humit a les zones del prelitoral i interior remarca la importància dels fluxos superficials a escala local, així com l'*entrainment* a pesar de l'advecció. A més, indica que les tronades d'estiu poden iniciar-se abans de l'arribada de la massa d'aire més humit.

4. La dinàmica atmosfèrica modelitzada i les variacions de q i θ indiquen que la majoria de les tronades d'estiu s'inicien abans de l'arribada del ISBF observat als diagrames de mescla com un marcat increment de q. Aquest fet recalca la rellevància de les interaccions a escala local i l'*entrainment* durant les circulacions de brisa.

5. La recàrrega en vapor d'aigua de l'atmosfera, juntament amb els increments en temperatura de l'aire, s'ha estimat utilitzant els paràmetres modelitzats durant un episodi de tronades d'estiu. Aquestes estimacions indiquen que les contribucions a q associades a l'evapotranspiració representen un 7 % del valor de q de la massa d'aire abans de la formació de les tronades d'estiu. A més, la major part de les contribucions al vapor d'aigua atmosfèric des de la superfície són degudes a camps de cultiu i en zones litorals lligades al poc desenvolupament vertical de la capa límit.

6. Les variacions de la temperatura de l'aire associades als fluxos de calor sensible en superfície representen un 40 %, en promig, de l'increment total de θ durant

les circulacions de brisa. Açò remarca la rellevància de l'escalfament de la superfície en l'increment de θ que comporta l'increment de la CCL en les línies de convergència. Anàlogament a q, un major increment de θ ocorre al litoral sobre zones urbanes a causa d'un menor desenvolupament de la capa límit respecte al prelitoral i interior.

7. L'*entrainment* és el factor amb més influència en les variacions de q i θ a la part superior de la capa límit. Per una part, aquest efecte produeix un assecament substancial de la massa d'aire per dilució entre dues i deu vegades més intens que la recàrrega de vapor d'aigua atmosfèric lligada als fluxos en superfície. Per altra part, els increments de θ causats pels fluxos superficials de calor sensible són d'intensitats comparables als produïts per l'*entraiment*. Contràriament a les contribucions a q i θ, l'*entrainment* presenta un gradient des de la costa cap a l'interior corresponent al desenvolupament de la capa límit.

LIST OF ACRONYMS

ABL	*Atmospheric Boundary Layer*
ACM2	*Asymmetric Convective Model, version 2*
AFWA	*Air Force Weather Agency*
ALADIN	*Aire Limitée Adaptation dynamique Développement InterNational*
AR	*Aras de los Olmos*
ARW	*Advanced Research WRF*
BC	*Boundary Conditions*
CAPS	*Center for Analysis and Prediction of Storms*
CCL	*Cloud Condensation Level*
CEAM	*Mediterranean Center for Environmental Studies*
CLC	*Corine Land Cover*
CMORPH	*CPC Morphing Technique*
COSMO	*COnsortium for Small-scale MOdeling*
CPC	*Climate Prediction Center*
DJF	*December-January-February*
ECMWF	*European Centre for Medium-range Weather Forecasts*
ERA5	*5th generation of ECMWF's ReAnalysis*
ESRL	*Earth System Research Laboratory*
ESS	*Extended Summer Season*
FAA	*Federal Aviation Administration*
GCM	*Global Climate Model*
GFS	*Global Forecast System*
GMTED	*Global Multi-resolution Terrain Elevation Data*
GNSS	*Global Navigation Satellite System*
GPCP	*Global Precipitation Climatology Project*
HCJ	*Hydrographic Confederation of the Jucar*

HIRLAM	*High Resolution Limited Area Model*
HPC	*High Performance Computing*
IC	*Initial Conditions*
ICGC	*Intitut Cartogràfic i Geodèsic de Catalunya*
IFS	*Integrated Forecasting System*
IP	*Iberian Peninsula*
IPCC	*Intergovernmental Panel on Climate Change*
IR	*InfraRed*
ISBA	*Interaction-Soil-Biosphere-Atmosphere*
ISBF	*Intermediate Sea Breeze Front*
ISLSCP-I	*International Satellite Land Surface Climatology Project-Initiative*
ITL	*Iberian Thermal Low*
IVIA-SIAR	*Valencian Institute for Agronomic Research - Agroclimatic Information System for Irrigation*
JJA	*June-July-August*
KF-CuP	*Kain-Fristch Cumulative Potential*
KHB	*Kelvin-Helmholtz Billow*
LSM	*Land Surface Model*
MAM	*March-April-May*
MedECC	*Mediterranean Experts on Climate and environmental Change*
MM5	Fifth-Generation Penn State/NCAR Mesoscale Model
MMM	*Mesoscale and Microscale Meteorology*
M-O	*Monin-Obukhov*
MODIS	*Moderate Resolution Imaging Spectroradiometer*
MSG	*Meteosat Second Generation*
MYNN	*Mellor-Yamada-Nakanishi-Niino level 2.5*
NASA	*National Aeronautics and Space Administration*

NCAR	*National Center for Atmospheric Research*
NCEP	*National Centers for Environmental Prediction*
NMM	*Non-hydrostatic Mesoscale Model*
NOAA	*National Oceanic and Atmospheric Administration*
NRL	*Naval Research Laboratory*
NWP	*Numerical Weather Prediction*
PA	*Paterna*
PBL	*Planetary boundary layer*
PDF	*Probability Density Function*
PE	*Potential Evapotranspiration*
PLE	*Potential Latent Heat flux*
PX	*Pleim-Xiu*
RAMS	*Regional Atmospheric Modeling System*
RRTM	*Rapid Radiative Transfer Model*
SBC	*Sea-Breeze Circulation*
SBF	*Sea-Breeze Front*
SBG	*Sea-Breeze Gravity current*
SBH	*Sea-Breeze Head*
SBS	*Sea-Breeze System*
SEVIRI	*Spinning Enhanced Visible and InfraRed Imager*
SL	*Surface Layer*
SON	*September-October-November*
SPAN	*Surface Parameter ANalysis*
SRTM	*Shuttle Radar Topography Mission*
SVA	*Soil-Vegetation-Atmosphere*
TKE	*Turbulent Kinetic Energy*
TPW	*Total Precipitable Water*

TRB	*Turia River Basin*
UHI	*Urban Heat Island*
UPP	*Unified Post Processor*
USGS	*United States Geological Survey*
VAPOR	*Visualization and Analysis Platform for Ocean, Atmosphere, and Solar Researchers*
VI	*Villar del Arzobispo*
VIS	*Visible*
VR	*Valencia Region*
WMB	*Western Mediterranean Basin*
WPS	*WRF Preprocessing System*
WRF	*Weather Research and Forecasting*
XVVCCA	*Xarxa Valenciana de Vigilància i Control de la Contaminació Atmosfèrica*
YSU	*YonSei University*

LIST OF SYMBOLS

$\vec{v}_{adv}$	*Advection vector*
$\vec{v}_{ent}$	*Entrainment vector*
$\vec{v}_{sfc}$	*Surface vector*
C_e^w	*Evaporation conductance*
C_t^w	*Transpiration conductance*
Δq_{PBL}	*Total q increment within the PBL*
Δq_{ent}	*Increment of q associated with entrainment*
Δq_{sfc}	*Increment of q associated with surface moisture flux*
$\Delta\theta_{PBL}$	*Total θ increment within the PBL*
$\Delta\theta_{ent}$	*Increment of θ associated with entrainment*
$\Delta\theta_{sfc}$	*Increment of θ associated with surface heat flux*
C_p	*Specific heat capacity for air*
E	*Evapotrasnpiration*
e_c	*Water vapor pressure of air below canopy*
E_{can}	*Evaporation from canopy*
EF	*Evaporative Fraction*
E_{soil}	*Evaporation from soil*
E_{tr}	*Transpiration*
F_{VEG}	*Vegetation fraction*
F_{wet}	*Canopy fraction covered by liquid water*
G	*Soil heat flux*
g	*Earth's gravity acceleration*
H	*Sensible heat flux*
IOA	*Index Of Agreement*

L	*Latent heat of vaporization*
LAI	*Leaf Area Index*
LE	*Latent heat flux*
MBE	*Mean Bias Error*
MSE	*Moist Static Energy*
N	*Number of samples*
O_i	*Measured value*
p_0	*Standard reference pressure*
$PBLH$	*Planetary Boundary Layer Height*
P_i	*Modeled value*
q	*Mixing ratio*
Q_c	*Cloud water*
Q_g	*Cloud graupel*
Q_i	*Cloud ice*
Q_r	*Cloud rain*
Q_s	*Cloud snow*
q_s	*Saturation mixing ratio*
r_{aw}	*Aerodynamic resistance for water vapor*
$r_{aw,g}$	*Aerodynamic resistance for water vapor below the canopy*
r_{bw}	*Quasi-laminar boundary layer for water vapor*
r_c	*Canopy resistance*
R_d	*Gas constant*
RH	*Relative humidity*
RH_g	*Air relative humidity in the surface soil pore space*
Ri_b	*Richardson number*
Ri_{cr}	*Critical Richardson number*
$RMSE$	*Root Mean Squared Error*

$RMSE_V$	*Vector Wind Difference RMSE*
R_n	*Net radiation*
r_{soil}	*Soil surface resistance*
SAI	*Stem Area Index*
SR_q	*Surface to entrainment ratio for q*
SR_θ	*Surface to entrainment ratio for θ*
T	*Absolute air temperature*
T_{bot}	*Bottom temperature*
$T_{g,b}$	*Ground temperature over bare soil*
$T_{g,v}$	*Ground temperature over vegetated soil*
T_{sfc}	*Surface temperature*
T_v	*Vegetation canopy surface temperature*
u	*Wind vector component in the x-axis*
v	*Wind vector component in the y-axis*
w	*Vertical (z-axis) wind vector component*
z	*Height above ground*
β	*Availability factor of water from soil*
γ	*psychometric constant*
Δt	*Time increment*
ΔT_{sfc}	*Surface temperature increment*
θ	*Potential temperature*
θ_e	*Equivalent potential temperature*
ρ	*Air density*
ρ_{PBL}	*Air density within the PBL*

CHAPTER 1

INTRODUCTION

This chapter introduces the background in which this thesis is based. First, the Mediterranean basin is described. Then, an extensive description of sea breeze regarding its structure and forcings, and its connection with the development of summer storms is presented, together with the advances in the modeling of these processes. Finally, the structure and goals of this thesis are introduced.

1. The Mediterranean basin

The Mediterranean Sea is a closed and warm sea surrounded by complex topography. It is a huge reservoir of energy, in form of moisture and heat, that plays an important role in driving the weather in southern and central Europe (Astraldi and Gasparini, 1992; Lebeaupin et al., 2006; Millán, 2014; Poulos, 2020). Its main area of influence is defined as the Mediterranean basin (Figure 1.1), which is subject to changes directly associated with global warming such as the sea surface temperature increase (Shaltout and Omstedt, 2014; Pastor et al., 2018; 2019). In fact, the Mediterranean basin is defined as a high-sensitive area to climate variations, i.e., a climate change hotspot, for droughts and intense precipitation (Giorgi, 2006; Giorgi and Lionello, 2008; Diffenbaugh and Giorgi, 2012; Tuel and Eltahir, 2020). In this context, many studies have pointed out the general decrease in precipitation over the Mediterranean, especially in summer and along eastern Spain (De Luis et al., 2010; Milano et al., 2013; Fernández-Montes and Rodrigo., 2015; Valdés-Abellán et al., 2017; Miró et al., 2018), together with an increase in the number and intensity of droughts during the last decades (Hoerling et al., 2012; Cook et al., 2016; Hertig and Tramblay, 2017; Miró et al., 2018). These variations indicate a reduction in water availability with the corresponding socio-economic impact, such as water restrictions for human consumption and agricultural activities, and the significant changes in the ecosystems, e.g., loss of forest areas and desertification (IPCC, 2019). In addition, the growing population further amplifies the water demand and the expansion of urban areas, the latter affecting land use characteristics that can play an important role in the generation of precipitation associated with local circulations.

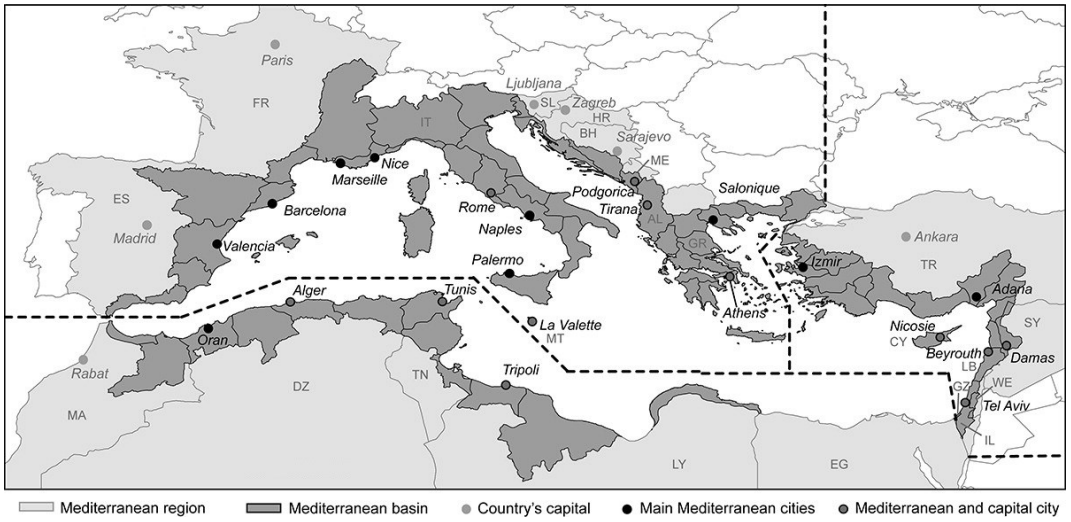

Figure 1.1 - Mediterranean basin with main river basins and country boundaries (ES: Spain, FR: France, IT: Italy, SL: Slovenia, HR: Croatia, BH: Bosnia and Herzegovina, ME: Montenegro, AL: Albania, GR: Greece, TR: Turkey, MT: Malta, CY: Cyprus, SY: Syria, LB: Lebanon, IL: Israel, EG: Egypt, WE: West Bank, GZ: Gaza Strip, LY: Libya, TN: Tunisia, DZ: Algeria, MA: Morocco. Extracted from Milano et al. (2013).

In the Mediterranean basin, mechanisms from synoptic to local scales enhance the transport of moisture and heat that trigger different extreme meteorological phenomena, with substantial consequences over highly populated areas (Delrieu et al., 2005; Rebora et al., 2013; Mariani and Parisi, 2014; Lorenzo-Lacruz et al., 2019; Rosselló-Geli and Grimalt-Gelabert, 2021), as well as provide precipitation crucial to maintain water resources in the region, especially in eastern Spain (Millán et al., 2005a; Miró et al., 2018). At local scales, sea breeze is a characteristic circulation that originates along coastal and pre-littoral areas of the Mediterranean basin. This local circulation influences atmospheric conditions and can trigger or enhance meteorological phenomena such as orographically-aided convective systems, especially during summer (Millán et al., 2005a). In addition, this region is semi-arid which enhances thermal gradients between land and sea, crucial in the formation and development of thermally driven circulations such as the sea breeze (Miller et al., 2003). However, the characteristics of the land use can modify the thermodynamical properties of the air masses advected within the sea breeze which can lead to a reinforcement or weakening of the associated meteorological phenomena. Besides, Millán et al. (2005b) hypothesized that these land-atmosphere interactions at local scale in the Mediterranean basin generate perturbations that can propagate to regional and global scales throughout sea breeze circulations.

Based on this, land use influence can be determinant in the water availability within the Mediterranean basin due to the associated surface heat and moisture fluxes and their impact on precipitation. This remarks the importance of a good administration of land use along the Mediterranean, especially in terms of the accelerated climate change during the last decades in this region (MedECC, 2020).

2. Sea breeze and summer storms

Sea breeze is the most common thermally driven circulation along coastal and pre-littoral areas of the Mediterranean basin, especially under weak synoptic conditions, although this atmospheric circulation can be observed throughout the world from polar regions to the equator (Miller et al., 2003). It is formed due to air temperature differences between land (warmer) and sea surface (cooler) during daytime which create a pressure gradient force from sea to land so that moist marine air is displaced inland. It has been widely demonstrated that sea breeze can have a crucial effect on reducing temperature and increasing humidity so that fog and thunderstorms can be generated (Simpson, 1994; Silva dias and Machado, 1997; Fovell and Dailey, 2001; Fovell, 2005; Azorín-Molina et al., 2014), as well as it can have a strong impact on improving or reducing air quality at the surface (Simpson, 1994; Caicedo et al., 2019). Several studies have shown that sea breeze can interact with other atmospheric phenomena related to synoptic circulations such as cold fronts (Brümmer et al., 1995; Rhodin, 1995; Miller et al., 2003; Allende-Arandía et al., 2020), generating an enhancement or reduction of the associated precipitation and/or its intensity, as well as other local thermally driven phenomena (e.g., upslope winds and local convection) strongly dependent on the characteristics of the region such as topography and land cover (Millán et al, 2005a; b). For instance, many studies have analyzed the interaction of the sea breeze with the Urban Heat Island (UHI) and have shown that it can modify main features of the sea breeze such as its duration, intensity and vertical development (Yoshikado, 1992; Ohashi and Kida 2002; Freitas et al., 2007; Hai et al., 2018; He et al, 2020). Other studies focused on the impact of topography in the forcing of near surface air flows associated with the sea breeze leading to the formation, development and triggering of orographically-aided convective systems, commonly known in eastern Spain as summer storms, and its link to land use features (Millán et al, 2005a; b; Millán et al., 2014).

2.1. Sea breeze structure and forcings

According to the description in Miller et al. (2003) and shown schematically in Figure 1.2, in the sea breeze system (SBS), the sea breeze circulation (SBC) is a mesoscale cell that rotates vertically with an onshore flow near the surface and a returning (offshore) flow aloft at about 900 hPa. Near the surface a cool and moist marine air flow toward land is established, known as the sea breeze gravity current (SBG), with the sea breeze front (SBF) the landward edge of the SBG, usually associated with abrupt changes in wind, temperature and humidity. As the marine air collides against continental air an updraft generates and creates a raised head above and slightly behind the SBF called the sea breeze head (SBH). Besides, the intensification of the SBC can lead to the formation of waves (known as Kelvin-Helmholtz billows, KHBs) along the upper limit of the SBG due to low static stability which tend to reduce the inland progression of the sea breeze (Sha et al., 1991; Buckley and Kurzeja, 1997; Fovell and Dailey, 2001; Miller et al., 2003; Plant and Keith, 2007).

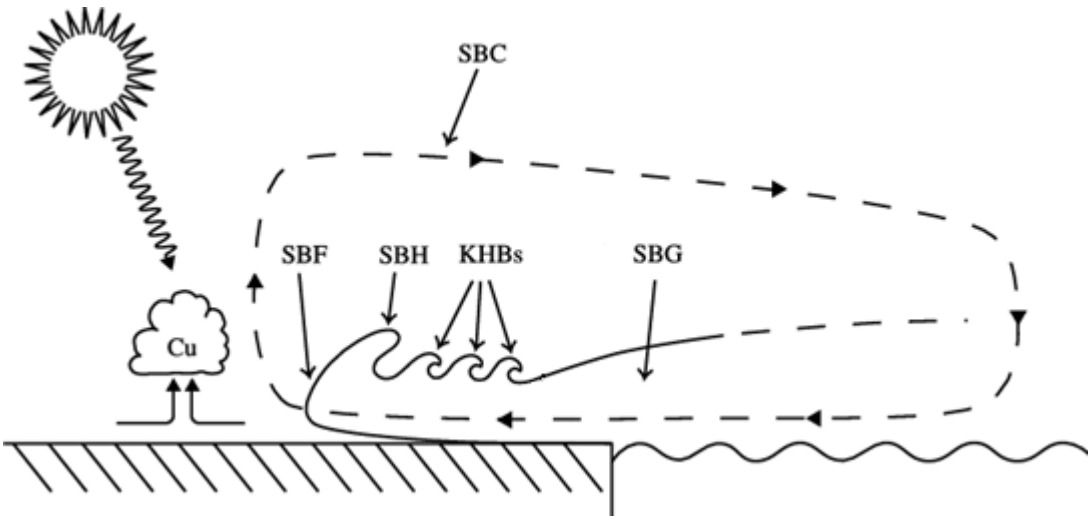

Figure 1.2 - Schematic representation of the sea breeze system (SBS) with the main components: sea breeze circulation (SBC), sea breeze gravity current (SBG), sea breeze front (SBF), sea breeze head (SBH) and Kelvin-Helmholtz billows (KHBs). Adapted from Miller et al. (2003).

2.1.1. Life cycle

The SBS can be divided into five stages regarding its dynamics: immature, early mature, late mature, early degenerate, and late degenerate (Clarke, 1984; Buckley and Kurzeja, 1997; Miller et al., 2003). Mature stages denote the evolution of sea breeze during

daytime with insolation greater than zero, including after sunset, and degenerate stages describe sea breeze evolution at nighttime with no insolation.

The sea breeze immature stage describes the SBC generation and enhancement with the increasing insolation during daytime. During this stage, land areas start to rapidly heat after sunrise in contrast with the slower heating of the sea surface so that thermal differences arise, and a pressure gradient force originates from sea to land. This leads to the generation of an onshore wind near the surface advecting moist marine air over land, i.e., the SBG forms. The SBC expands rapidly so that the returning (seaward) flow generates at upper levels, at about 900 hPa according to Miller et al. (2003), defining the mesoscale circulation. Besides, the near surface air flow toward inland yields the formation of the SBF due to the interaction with relatively warm and dry continental air, as well as the convergence of these two air masses leads to the formation of the SBH where air mixing occurs. In some cases, KHBs generate behind the SBF producing an increased turbulence, an additional air mixing, at the upper boundary of the gravity flow (Jiang, 2021), which can generate important changes in the thermodynamical properties (e.g., temperature and humidity) of the moist marine air mass as it moves toward inland areas. This effect is known as entrainment, and, in meteorology, it describes the environmental air mixing into an organized air flow so that the environmental air becomes part of the flow, as defined by the American Meteorological Society (AMS; https://glossary.ametsoc.org/wiki/Entrainment, last access: 02-09-2021).

The early mature stage describes the evolution of the SBC in the afternoon when insolation begins to reduce. This produces the decay of the SBH and the KHBs, and the corresponding air mixing at the top boundary of the SBG (entrainment) and acceleration of the sea breeze progression (Sha et al., 1991; Buckley and Kurzeja, 1997). During this stage, moist marine air further displaces toward inland areas along the valleys and over plateaus due to the low top friction, and especially when insolation reduces toward zero at the late mature stage. During the late mature stage, temperature difference between land and sea that drives the SBC vanishes and the SBF separates from the main flow of moist marine air. However, the leading edge may remain acute and a shift of the SBC toward land may also occur (Clarke, 1984). Besides, the increase in the radiative cooling diminishes vertical mixing and reduces the SBH which may continue to move further inland (Clarke, 1984), although this is not commonly observed in eastern Spain. The SBH, as an independent entity, can travel hundreds of kilometers

providing moisture to inland areas after sunset during the early degenerate stage. During this stage, the SBH may interact with a temperature inversion layer, or other features at low levels, leading to the formation of a cutoff vortex or undular bore (Clarke, 1984; Simpson 1994), whilst during the late degenerate stage the inland penetration of the marine air mass is limited.

The stages of the sea breeze described above are strongly dependent on the prevailing synoptic conditions and topography that may, for instance, limit or enhance the development of the SBC or the penetration of the remnant of the sea breeze after sunset.

2.1.2. Synoptic forcing

Large-scale circulations have a crucial impact on regional-to-local scale circulations which can be enhanced or weakened. In the Mediterranean basin, sea breeze dominates local circulations during summer although it is strictly subject to prevailing westerly winds in the Northern Hemisphere associated with synoptic circulations that can restrict or shape the development of the SBC. For instance, the returning flow aloft in the SBC is strongly influenced by synoptic winds that may lead to a non-closed system (Adams et al., 1997; Miller et al., 2003). Besides, it must be noticed that the influence of synoptic winds on the SBC is strictly linked to the orientation of the coastline since it determines sea breeze flows.

Regarding the influence of synoptic circulations at upper atmospheric levels on the SBC, Adams et al., 1997 described four categories for the Northern Hemisphere: pure, corkscrew, backdoor and synoptic. Here, the synoptic category is disregarded since it considers a synoptic onshore flow at the surface commonly defined as *levante* in eastern Spain. Thus, focusing on the first three definitions, a pure sea breeze occurs under weak synoptic circulations with a geostrophic force pointing seaward at a right angle with respect to the coastline that allows the generation of a closed system. In the corkscrew sea breeze, the synoptic wind blows from the southwest in the Mediterranean coast of the Iberian Peninsula, which implies a higher pressure over sea and lower pressure over land (Lutgens and Tarbuck, 1995). A southerly wind component and low pressure over land generate a region of low-level divergence close to the coast, when surface friction differences between land areas and sea are considered, so that upper air sinks into the divergence area and aids sea breeze initiation (Miller et al, 2003). In this case the circulation is counterclockwise and presents a helical shape in form of a corkscrew

(Adams et al., 1997). The contrary synoptic circulation occurs in the backdoor sea breeze with the large-scale wind presenting northerly component leading to higher pressure over land and lower pressure over sea (Lutgens and Tarbuck, 1995), and the corresponding low-level convergence near the coastline when surface friction is considered. This fact prevents upper air from sinking and constrains the initiation of sea breeze generating a helical clockwise circulation southward, opposite to the corkscrew sea breeze case. According to Adams et al., 1997, the backdoors sea breeze is weaker than the corkscrew.

Synoptic conditions, in addition to modifying the SBC, also can restrict its expansion toward inland so that sea breeze may remain confined to littoral areas, moving a short distance over land, or may not form under strong near-surface synoptic winds with an offshore component. This situation is relatively frequent in eastern Spain during summer, where *ponent* (westerly synoptic wind) opposes sea breeze flow and limits its progress toward inland areas as it develops during daytime.

2.1.3. Complex topography

The Mediterranean basin is characterized by a very complex topography with considerably high mountain ranges near the coast and valleys that substantially influence the SBS. For instance, complex topography may lead to the generation of several sea breeze systems along the coast. This is usually associated with valleys separated by orographic barriers, approximately perpendicular to the coastline, that produce a channeling of the sea breeze low-level flow as it develops during daytime. Besides, marine moist air displaces following topography features toward inland merging or interacting with other local circulations and converging at the mountain ranges. For example, convergence zones can originate due to the interaction of two opposite sea breeze flows at the mountain ranges. In addition, the inland penetration of the sea breeze is strictly subject to topography characteristics such as the height of mountain ranges, their proximity to the coastline and the orientation of slopes with respect to the surface air flow so that high mountains with a slope facing the sea can confine the SBS. Oppositely, upslope winds, that generate due to surface heterogeneous heating along seaward facing slopes, can merge with the sea breeze flow leading to an earlier occurrence and amplification of the SBC. This have been shown in several studies conducted along eastern Spain (Millán et al., 2000; Miao et al., 2003; Millán et al., 2005a; b; Pérez-Landa et al., 2007; Azorín-Molina et al., 2011).

Under weak synoptic conditions, topography shapes main features of the sea breeze determining convergence zones at the main mountain ranges where the SBG interacts with other regional and local circulations (Millán et al., 2014). This is crucial in the generation of meteorological phenomena associated with the SBC, such as the formation, development and triggering of orographically-aided summer storms (Millán et al., 2005a; b).

2.1.4. Meteorological phenomena

In general, the generation of meteorological phenomena is associated with the interaction between continental and marine air masses at the SBF with cold front characteristics. At the leading edge of the sea breeze, air is forced upwards, and condensation may occur leading to the formation of clouds. The generation and development of convective clouds is directly connected to the strength of the SBF denoted by differences in the thermodynamic properties of continental and marine air masses (Miller et al., 2003). Besides, other phenomena triggered by sea breeze such as undular bores, propagating disturbances that generate changes in height of surface stable layers, may lead to the generation of clouds (Goler, 2009). However, prefrontal phenomena occurring prior to the SBF arrival may develop over inland areas linked to the sea breeze forerunner (Geisler and Bretherton, 1969), a cluster of waves initiated with the generation of the land-sea thermal gradient and preceding the SBF. These waves may generate an advection of local (continental) air toward inland in the same direction as the sea breeze flow (Miller et al., 2003), usually observed as short temporal fluctuations in temperature, humidity, and wind (Alpert and Rabinovich-Hadar, 2003), that can lead to the development of convective clouds.

In the Mediterranean basin complex topography plays an important role in shaping sea breeze flows near the surface, as introduced in the previous section, so that it influences the generation of meteorological phenomena associated with the SBC. For instance, in eastern Spain, orographically-aided summer storms originate at the mountain ranges where surface flows converge. Specifically, under dominating sea breeze conditions, marine moist air is channeled along the valleys reaching the convergence zones where it is forced upwards so that convective precipitation is triggered. It has been shown that this type of events is a key source of water during summer in eastern Spain and they are strictly connected to the SBC and other thermally driven circulations (Millán et al., 2005a; b; Miró et al., 2018).

2.2. Summer storms

2.2.1. Precipitation types

Millán et al., 2005b conducted a classification of precipitation events at a daily base with respect to the different mechanisms producing precipitation in the Valencia region in eastern Spain, so that three main types were identified: (i) Atlantic fronts, (ii) orographically-aided summer storms and (iii) backdoor cold fronts. To categorize daily precipitation according to these three types, Millán et al. (2005a; b) analyzed synoptic maps at 00, 06, 12 and 18 UTC of surface pressure, as well as other meteorological variables (e.g., geopotential, air temperature and winds) at 500 hPa and 300 hPa. According to this methodology, the main characteristics of these three types are, as described in Millán et al. (2005b):

- Atlantic fronts produce precipitation over inland areas, usually in the west-facing slopes of the mountain systems, and they are more frequent from the beginning of autumn to late spring. Precipitation assigned to this type is produced by the passage of mid-latitude frontal lines over the Iberian Peninsula and/or dominating Atlantic (westerly) advection with the presence of a trough at 500 hPa.

- Orographically-aided summer storms occur in the afternoon during the period from April to September and produce main precipitation on mountain ranges near the coast. These events are associated with dominating combined breeze (upslope winds and sea breeze) circulations. The presence of the Iberian Thermal Low (ITL) is indicative of an atmospheric situation favorable for the formation of this type of events. In addition, the presence of cold air at upper atmospheric levels (e.g., at 500 hPa) is important in the formation, development and triggering of these convective systems.

- Backdoor cold fronts occur mainly during autumn and winter and describe an advection of relatively cold air over a warm Mediterranean Sea. Under this situation, intense precipitation can affect coastal areas and sea-facing slopes near the coast that can last up to four days. Precipitation is assigned to this type when a high-pressure system displaces and establishes over central Europe. These synoptic conditions can coincide with the displacement of a cold pool of air at upper atmospheric levels toward the Iberian Peninsula and the

development of a cutoff low at the southwest of the Iberian Peninsula yielding longer and more generalized precipitation events.

In this thesis, special emphasis is put on the study of orographically-aided summer storms so that this type of events is described in detail in the following subsections.

2.2.2. Atmospheric conditions and development of summer storms

In late spring and summer, the Iberian Peninsula is generally under stable synoptic conditions, relatively isolated from the passage of mid-latitude low-pressure systems from the Atlantic Ocean and their associated fronts. Relatively high pressure establishes in the western Mediterranean with the development of an anticyclonic circulation over the Balearic Sea so that local to regional circulations dominate over the eastern coast of the Iberian Peninsula. This atmospheric situation favors the formation of the ITL at the center of the peninsula during the day as local thermally driven circulations merge and organize into a larger scale circulation (Millán et al., 2000). This circulation produces a dynamic compensation over the Mediterranean Sea leading to an intensification of the anticyclonic subsidence over the Balearic Sea, as well as modifying the depth of the sea breeze layer at the coast (Millán et al., 1997; 2000; Alonso et al., 2000). Under anticyclonic conditions during summer, the ITL achieves a quasi-permanent property and represents the most common atmospheric situation at the surface (Palau et al., 2005). This atmospheric situation intensifies sea breeze in the Western Mediterranean Basin (hereafter referred to as WMB) although it tends to inhibit the development of summer storms due to compensatory subsidence over the Balearic Sea. Under these conditions, the presence of cold air aloft can be key in the formation and development of this type of convective systems.

In the WMB, sea breeze forms along the coast and advances toward inland areas merging with upslope circulations during the early mature stage, in the morning and early afternoon (Millán et al., 1998; 2005a; b). Additionally, upslope winds yield an intensification of the SBC as well (Mahrer and Pielke 1977; Miao 2003; Azorín-Molina et al., 2011). Along the Mediterranean coast of the Iberian Peninsula, sea breeze circulation develops earlier and presents a greater intensity due to the early morning surface heating over the slopes facing to east and south (Millán et al, 2005b). In this situation, convergence lines establish over mountain ranges at about 100 km from the coastline where updrafts inject near-surface moist marine air to upper atmospheric levels connecting surface flows to return flows aloft (Millán et al, 2005a; b). Some

studies pointed out that the SBF remains locked at the ridges of the mountains that surround the Mediterranean basin (Millán et al, 2000; 2002; 2005a). Millán et al. (1997) suggested that a regional recirculation system generates in the WMB due to the self-organization of the sea breeze gravity flow at the surface, their return flow aloft and the associated compensatory subsidence, as observed in other Mediterranean regions (Kallos et al., 1998). These atmospheric conditions favor the generation of convective clouds at the convergence lines; however, convection can be inhibited or vertically confined due to the compensatory subsidence occurring over some inland areas where surface flows converge as well (Millán et al, 2005b).

In terms of the recirculation in the WMB, the properties of the moist marine air (i.e., temperature and moisture content) determine the cloud condensation level (CCL) at the convergence lines so that two scenarios were contemplated in Millán (2014). In the first case, a convective system forms (i.e., the CCL is achieved) and develops vertically reaching the tropopause so that recirculation does not occur leading to an open circulation, i.e., water vapor and pollutants are advected outside the WMB (Figure 1.3a). Contrarily, a closed circulation (recirculation) is observed when the CCL is not reached at the convergence line and no storm develops so that moist marine air is injected and incorporates to the returning seaward flows aloft (Figure 1.3b). According to Millán (2014), this closed circulation, under compensatory subsidence, yields a strongly confined gravity flow near the surface, and the formation of atmospheric layers up to 4000 m where water vapor and pollutants accumulate over the WMB.

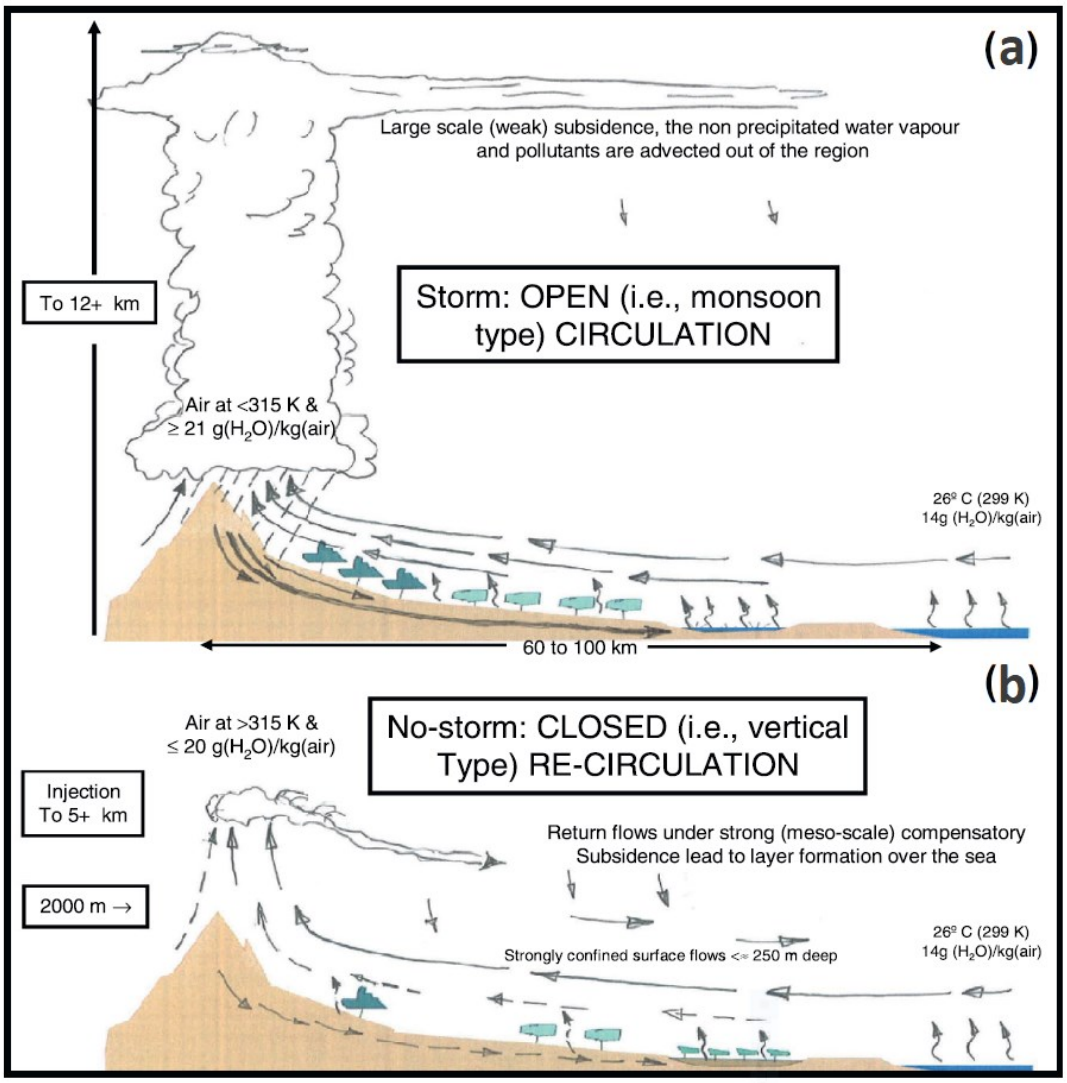

Figure 1.3 - Circulations in coastal areas of the WMB (a) open and (b) closed (recirculation). Extracted from Millán (2014).

The convective systems that generate under the atmospheric conditions described above are referred to as orographically-aided summer storms, as introduced in subsection 2.2.1. These convective systems develop during the early mature stage of the sea breeze (see subsection 2.1.1), usually on the east-facing slopes of the mountains, in the case condensation is not inhibited due to entrainment effect (e.g., mixing with continental dry air at the SBH) and the updraft exceeds anticyclonic subsidence. The vertical development of summer storms is also subject to the presence of cold air at upper atmospheric levels that can advance their formation, lead to generalized convective precipitation, or favor their development for several consecutive days (Millán et al, 2005b). Besides, cold air aloft can be a key factor in the development of summer storms over mountain ranges where, for instance, sea breeze entrance occurs in the evening,

since upslope winds can yield the injection of near-surface moist air to upper levels of the atmosphere. This thermally driven circulations at local scale also produce convergence lines leading to the formation of summer storms over inland areas outside the SBC during daytime.

2.2.3. Influence of land use

In a situation with clear sky and dominant sea breeze along the coast, moist marine air displaces from the sea toward inland areas throughout the valleys that characterize the Mediterranean basin. Besides, on one hand, land surface is subject to a strong heating, regarding the intense incoming solar radiation, that increases the temperature of the marine air mass as it displaces over the continent. On the other hand, vegetation, wetlands, and water bodies along the path provide additional moisture throughout transpiration and evaporation. Thus, surface heat and moisture fluxes influence the properties of the air mass injected to upper levels of the atmosphere at the convergence zones limiting or favoring the formation of summer storms, as schematically shown in Figure 1.3.

Along the convergence lines, topography approximately determines the height that a moist marine air moving within the sea breeze will reach, whereas the properties (i.e., temperature and humidity) of the air mass determine the CCL, as introduced previously (see subsection 2.2.2). This indicates that land-atmosphere interactions can play an important role in the formation of summer storms by modifying the properties of the air advected over land. In the WMB, semi-arid areas with dry soil conditions (low evaporation) increase the temperature of the surface marine air mass which increases the CCL and limits the formation of summer storms at the convergence lines. Contrarily, vegetation (e.g., forest areas and croplands) provides moisture to the surface air mass which decreases the CCL and may favor the generation of summer storms over the mountains. In this context, Millán et al. (2005a) hypothesized that main changes in summer precipitation over the Valencia region were connected to land use changes contributing to diminish the frequency of summer storms. Specifically, this study exposed that surface drying associated with land use changes, such as urbanization of the coast, contributes to heat moist marine air traveling inland and decrease evapotranspiration leading to higher CCL at the convergence lines over the mountains (situation shown in Figure 1.3b). Additionally, Millán et al. (2005a) pointed out that the loss of summer storms (reduction in water availability) yields:

- a loss of vegetation, which further reduces evapotranspiration and increases surface heating, enhancing desertification.
- a warmer Mediterranean Sea at the end of summer and beginning of autumn that could produce an increase in the number of precipitation events along the coast, associated with backdoor cold fronts (see subsection 2.2.1), and their intensity.
- an enhanced soil erosion over vegetated slopes due to flash floods leading to a further intensification of desertification.

Apart from these effects, it was suggested that perturbations to the hydrological cycle initiated at local-to-regional scale due to land use changes in the WMB may propagate to other Mediterranean and nearby regions (Millán et al., 2005a; b), as well as to the global climate system (Millán, 2014).

2.2.4. Relevance in eastern Spain

Summer storms originate over the mountain ranges due to local circulations providing precipitation at the headwaters of the main river basins, especially during summer with typically weak synoptic conditions. This fact remarks the importance of summer storms in maintaining river flows during the driest season of the year. At an annual basis, Millán et al. (2005a) estimated that the precipitation associated with this type of events represents about 11 % of the total annual precipitation over the Valencia region in eastern Spain. However, at certain mountain ranges located near the coastline in eastern Spain summer storms contribution to the total annual precipitation can represent up to 25 % (Miró et al, 2018). Besides, these contributions are even greater during summer with relatively stable conditions at synoptic scale and dominating sea breeze circulations. This typical summer conditions show a tendency to expand to early autumn in the Valencia region (Miró et al., 2015), which further increases the importance of the precipitation provided by summer storms in the region.

In eastern Spain, several studies pointed out the significant decrease in precipitation during summer associated with the reduction in the frequency of summer storms in the last decades (Millán et al., 2005a; b; Miró et al., 2018). This drying trend indicates that a decrease in the number of summer storms providing precipitation over the main headwaters of the river basins leads to an important decrease in the water availability during summer. Besides, in the context of climate change, projected scenarios in the

WMB point out a general decrease in mean precipitation (Lopez-Moreno et al., 2009; Tramblay and Somot, 2018, Lionello and Scarascia, 2018; Miró et al., 2021), particularly during summer (Coppola et al., 2021; Miró et al., 2021), that will further reduce water availability and enhance desertification in the region.

In the Valencia region, the highly populated areas near the coast (e.g., the city of València) and the large crop fields of great socioeconomic importance for the region are strongly dependent on water resources. Hence, the decrease in the frequency of summer storms, the main source of water during summer, can enhance desertification (e.g., loss of forests) in the region and authorities may be forced to apply water restrictions, already implemented in southern regions of Spain, affecting directly crop field irrigation activities and human consumption. In addition, as pointed out in Millán et al. (2005a), the loss of vegetated areas would suppose positive feedback toward a decrease in summer storms occurrence and the corresponding further reinforcement of desertification in the region.

2.3. Modeling

The Royal Swedish Air Force Weather Service was the first institution to produce real-time numerical weather predictions in 1954 using a regional barotropic model (Bergthorsson et al., 1955). In the 1960s meteorological models began to gain complexity and apply the Bjerkness/Richardson primitive equations replacing barotropic and baroclinic models (Edwards, 2001). During the late 1960s and early 1970s meteorological models implemented solar radiation, moisture, and rain feedback on convection effects, as well as latent heat due to the increase in computational power (Lynch, 2008). Besides, the new advances emerging rapidly in computer sciences allowed a further increase in computational power availability and the corresponding increase in model's accuracy (Harper et al., 2007; Bauer et al., 2015), also related to efficiency developments that improved global model's dynamical cores since the 1970s (Williamson, 2007). This yielded the introduction of the first regional (or limited-area) and global forecast models during 1971 and 1974, respectively, in the United States (Shuman, 1989). In 1975, the European Centre for Medium-Range Weather Forecasts (ECMWF) was established to provide accurate global weather forecasts and the first operational forecast was conducted in 1979 (Lynch, 2008). This fact facilitated the development of regional models in Europe such as the High Resolution Limited Area Model (HIRLAM; http://hirlam.org/index.php/hirlam-programme-53, last access:

03-10-2021) established in 1985, the *Aire Limitée Adaptation dynamique Développement InterNational* (ALADIN) used in France since 1995 (Côté et al., 1998), and the Consortium for Small-scale Modeling (COSMO; https://www.cosmo-model.org/, last access: 03-10-2021) developed in Germany since 1998. In the United States, several mesoscale models were developed for short-range and high-resolution applications such as the Fifth-Generation Penn State/National Center for Atmospheric Research (NCAR) Mesoscale Model (MM5; Anthes and Warner, 1978) during the late 1970s, the Regional Atmospheric Modeling System (RAMS; https://rams.atmos.colostate.edu/rams-description.html, last access: 03-10-2021) in the late 1980s, and the Weather Research and Forecasting (WRF; Sckamarock et al., 2008) model introduced in 1998 .

Initially, most of these meteorological models were introduced in the context of weather forecasting; however, their usage and development for atmospheric research purposes have demonstrated their versatility. In fact, these models are currently used for different applications such as climate projections and the modeling of extreme meteorological phenomena and pollutant dynamics from global to local scales. Besides, the complexity of meteorological models has further increased in the past four decades due to the continuous implementation of new parametrized physical processes, key in model's predictive skill, in conjunction with increasing spatiotemporal resolutions linked to improvements in high performance computing (HPC) systems (Dudhia, 2014; Bauer et al., 2015). On one hand, greater computing power allows to include a greater number of prognostic variables (integration of physical equations) in meteorological models enhancing their predictive skill. Furthermore, it allows the use of high spatial resolutions providing an accurate description of topographic features and land properties in the models that improve the representation of near-surface flows driven by local processes, e.g., sea breeze penetration along narrow valleys near the coast. However, computational power still represents a limiting factor in the present regarding the great complexity of atmospheric processes, together with the great energetic cost involved in the use of HPC systems (Bauer et al., 2015). On the other hand, a more accurate representation of initial conditions (IC) and lateral boundary conditions (BC) in mesoscale models provided by Global Climate Models (GCMs) such as the Global Forecast System (GFS), or reanalysis products such as the 5th generation of ECMWF's Reanalysis (ERA5), enhances their performance in reproducing atmospheric dynamics.

For example, the increasing horizontal resolution of the global atmospheric reanalysis, from 125 (ERA-40) to 25 km (ERA5), produced at the ECMWF shows the significant improvements achieved in the last two decades. In addition, the increase in the number of observations considered in this reanalysis, especially from satellites, have further improved the representation of atmospheric conditions.

The increasing availability of computational power and the knowledge gained in the past decades have provided a higher accuracy in atmospheric modeling at regional and local scales. For instance, many studies have shown the ability of meteorological models to accurately reproduce sea breeze circulations for different terrain characteristics and atmospheric conditions (Soler et al., 2011; Steele et al., 2015; Drobinski et al., 2018; Lim and Lee, 2021), as well as to capture diverse extreme weather phenomena at different scales (Flesch and Reuter, 2012; Zollo et al., 2015; Singh et al., 2021). Based on this, mesoscale models can provide a fine spatiotemporal representation of atmospheric dynamics in 3-dimensional grids, which can be expensive to measure, such that they can be regarded as a crucial approach to complete the missing information from in situ measurements and satellite observations. Atmospheric modeling provides information about the atmospheric dynamics and processes, and the opportunity to contrast main estimated variables to observations. Currently, atmospheric modeling is the most extended tool to analyze meteorological phenomena at relative low cost from Eulerian and Langrangian perspectives.

3. Structure and goals

The purpose of this thesis is to bring an insight into the comprehension of the role that land use plays in the formation of summer storms in eastern Spain following some of the arguments exposed in Millán et al. (2005a) and Millán (2014). Concretely, this thesis intends to

1) Estimate the recharge in water vapor and temperature variations associated with surface moisture and heat fluxes of the near-surface air involved in the generation of summer storms along the Turia valley in eastern Spain.

2) Quantify the contributions to the atmospheric water vapor content and heat from the different land use categories that characterize the study area together with other relevant atmospheric processes.

The work conducted in this thesis mainly evaluated the relevance of water vapor contributions from vegetation to the near-surface air flows feeding a limited number of summer storms during a selected year. To accomplish this goal, additional issues needed to be addressed regarding the characteristics of the study area, the atmospheric conditions favoring the formation of summer storms and the available configurations of the main tool selected to conduct this study (the WRF mesoscale model). Specifically, several analyses were conducted in this thesis in order to

- Evaluate the performance of two parametrizations of surface processes implemented in the model for a period covering several summer storm episodes regarding main hydrometeorological variables.
- Characterize the main features of sea breeze and other local circulations for a long period over the Turia valley in terms of temperature and humidity changes using in situ measurements.
- Compare heat and moisture fluxes at the surface over vegetated and non-vegetated locations within the study area using in situ measurements.

These analyses served to validate the performance of several model parametrizations in charge of surface processes and dynamics for the periods of interest. Besides, they provided a better understanding of the local atmospheric conditions favoring the occurrence of summer storms and the dominant role that sea breeze plays in the evolution of air temperature and humidity near the surface.

Principally, this thesis was part of the project: *Improving surveillance and regional forecasting of atmospheric risks. Evaluation of the role of changes in land use in the accumulation of re-charging of water vapor and pollution (VERSUS; REF: CGL2015-67466-R)*, which was funded by the *Ministerio de Economía y Competitividad* and the *Generalitat Valenciana*.

This thesis consists of a total of 6 chapters. An introduction to the state of the art regarding the background on sea breeze and summer storms, including the main factors driving and influencing the generation of this type of convective events, has been presented in this chapter (**Chapter 1**).

Chapter 2 presents the study area, methodologies and tools used to answer the questions posed in this thesis, as well as the observation datasets used to conduct previous analyses and to validate simulated variables.

Chapter 3 describes the atmospheric conditions of the summer storm events to be analyzed in detail throughout high-resolution simulations, and the performance of the different model configurations implemented with respect to several reference products.

Chapter 4 estimates the influence of surface heat and moisture fluxes during a summer storm episode, consisting of several events, over the study area regarding dominant land use categories with the two approaches selected.

Chapter 5 is a general discussion of the results obtained in this thesis with respect to the previous research introduced previously in Chapter 1.

Finally, **Chapter 6** exposes the most relevant conclusions of this thesis and further work.

CHAPTER 2

MATERIALS AND METHODS

This chapter describes the materials and methodologies used in this research. First, a brief introduction to the study area is shown. Then, an extensive description of the Weather Research and Forecasting (WRF) mesoscale model with especial focus on land surface parametrizations and observational datasets are presented. Next, the methodologies implemented for the identification and selection of sea breeze days and summer storm episodes are introduced, as well as a description of the simulation strategy followed in this work. Finally, the two approaches for the quantification of energetic exchanges within the SVA system during sea breeze and prior to summer storm formation are exposed.

1. Area of study

This investigation focuses on the extended Turia River Basin (TRB) located in the eastern part of the Iberian Peninsula, and especially in its lower part (Figure 2.1). The TRB is characterized by a complex topography and extends about 200 km from the coast toward northeast of the Valencian coast, covering an area of about 6850 km^2. The initial 40-50 km (from the coast) the river basin is relatively flat with terrain heights lower than 500 m asl although it is confined between the Calderona mountain range at the north (denoting the limit between the TRB and the Palancia river basin) and other lower mountains at the south with heights of about 600 m. The Calderona mountain range extends from coastal areas to inland areas with heights from 367 m (peak of El Picaio at about 10 km from the coastline) up to the 1015 m of Montemayor peak. After this initial section of the TRB, the Turia valley narrows considerably delimited southward by the Negrete or Utiel Mountains (between 1000 and 1400 m asl) and Javalambre Mountains northward with peaks exceeding 2000 m asl. In the uppermost part of the TRB, extending mainly northward, the valley is delimited by the Albarracín (about 1800 m) and Gúdar Mountains (about 2000 m) to the east, respectively, also limiting with Mijares river basin on the east. The latter mountain ranges in the TRB described conform the southern part of the Iberian System which defines the southern limit of the Ebro valley in northeastern Spain.

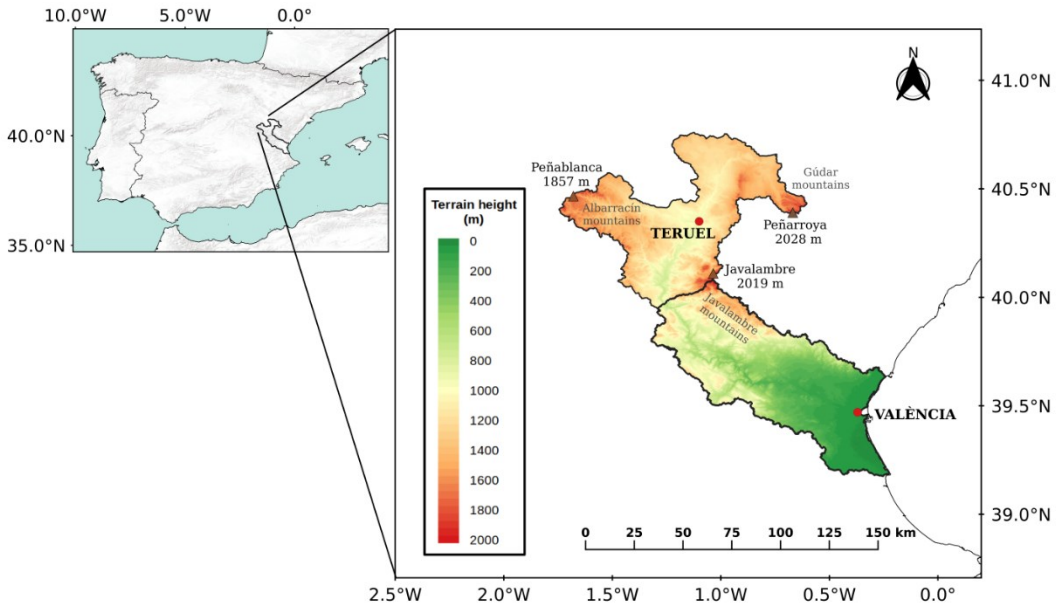

Figure 2.1 – Location of the TRB in the Iberian Peninsula (left) and TRB topography map with highlighted study area (solid black thick line) along with main cities and mountain ranges (right).

The Turia river is the second most important river in the Valencia region regarding streamflow, after the Júcar river, with headwaters of both rivers located in the Iberian System. This fact highlights the importance of precipitation over this area to maintain water flows of the main rivers sustaining water resources in the Valencia region. In fact, annual precipitation shows a coast-to-inland increase in the TRB with accumulated values ranging from 300 to 500 mm at the coast and up to 1000 mm at the upper part (Miró et al., 2018). Besides, generally hot and dry summers, that characterize the region, further remark the relevance of precipitation over the headwater of the Turia river during the driest period of the year. During this period, atmospheric dynamics are generally dominated by thermally driven winds (e.g., sea breeze), although synoptic westerly winds (*ponents*) can limit or overcome local and sea breeze circulations along the TRB. Sea breeze, as well as local winds, are key in the generation of orographically-aided summer storms at the convergence zones, which are identified as the main source of water during summer over the mountain ranges in the Valencia region (Millán et al., 2005b; section 2 in Chapter 1). It must be highlighted, that sea breeze flows along the Mijares and Palancia river basins also influence the formation, development and triggering of summer storms in the upper part of the TRB (Javalambre and Gúdar mountains). In addition, land use may represent an important factor in local circulations leading to convection. Moisture and heat surface fluxes can yield changes in the features of air advected (temperature and humidity) toward inland influencing the formation of this type of convective systems (see section 2.3 in Chapter 1). In this context, land-atmosphere interactions under these meteorological conditions may play a crucial role regarding their additional heat (e.g., urban areas) and water vapor contributions (e.g., croplands and forests) to the low troposphere that need to be quantified. To this end, the lowest part of the TRB, covering the initial 100 km from the coast approximately, was established to study the sea breeze characteristics and SVA fluxes (Figure 2.1). This study area covers an extension of 4190 km^2 and the metropolitan area of València (of about 630 km^2) is the main urban area distributed along the coast. Excluding wetland and water bodies, about 50 % of the study area is covered by natural land surfaces and 21 % by conifer forests (Larsen, 2021). According to these characteristics and the fact that this area is usually influenced by the sea breeze development before insolation begins to decay, main land-atmosphere interactions affecting summer storms formation is expected along the study area. Besides,

meteorological towers and sites with transpiration measurements are distributed within the area providing data of good quality.

2. The Weather Research and Forecasting model

All the information used in this section for the Weather Research and Forecasting (WRF) model description have been extracted from Skamarock et al., (2008).

The WRF is a non-hydrostatic mesoscale Numerical Weather Prediction (NWP) model globally used for atmospheric research and weather forecasting. The WRF model was developed as a collaboration among several agencies: the National Center for Atmospheric Research's (NCAR) Mesoscale and Microscale Meteorology (MMM) Division, the National Oceanic and Atmospheric Administration's (NOAA) National Centers for Environmental Prediction (NCEP) and Earth System Research Laboratory (ESRL), the Department of Defense's Air Force Weather Agency (AFWA) and Naval Research Laboratory (NRL), the Center for Analysis and Prediction of Storms (CAPS) at the University of Oklahoma, and the Federal Aviation Administration (FAA), with the participation of university scientists. It can be implemented with two solvers: the NMM (Non-hydrostatic Mesoscale Model) and the ARW (Advanced Research WRF); the WRF-NMM is mainly used for producing forecast, whereas the WRF-ARW is used for both forecasting and research purposes with more complex dynamics and physics. In particular, this study is performed with the version 3.8.1 of the WRF-ARW model (hereafter referred to as WRF). A more detailed description of the model can be found in Appendix A.

The WRF model presents several physics categories regarding radiation, cumulus parametrization, microphysics, Atmospheric Boundary Layer (ABL) and surface processes (Figure 2.2), with different parametrization options within each category. An overview of the different parametrization is presented in the following section along with the WRF configuration implemented for each physics category in this study. Land surface models (LSM) are presented in a different section due to their importance in the outcomes of this research.

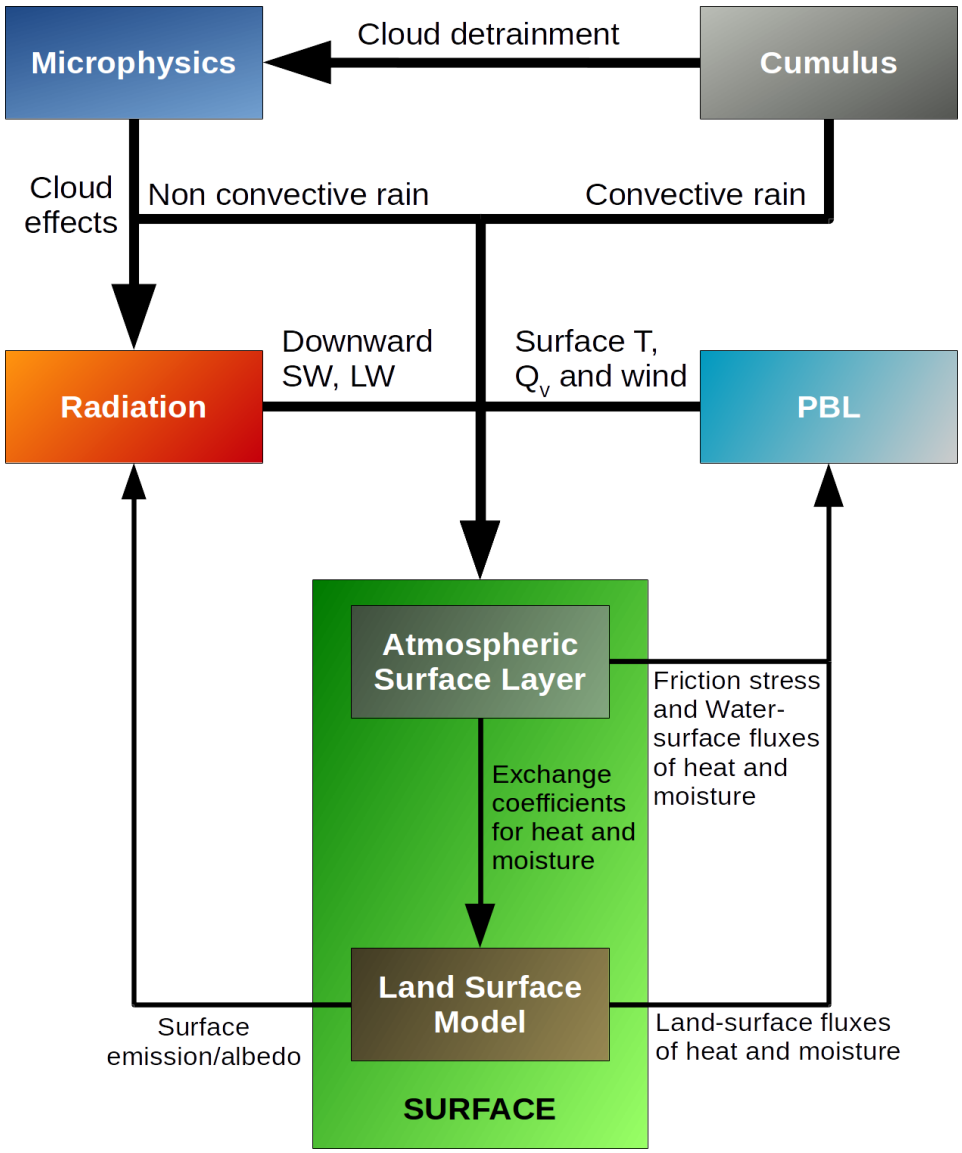

Figure 2.2 - Schematic representation of the direct interactions among the different schemes in WRF. Adapted from WRF tutorial.

2.1. Static data

The WRF Preprocessing System (WPS) uses invariant variables (i.e., geographical data) to describe the study area with a wide number of datasets that can be implemented in order to execute a simulation. However, the objectives of this study implied to execute the WRF model at very high horizontal resolutions, as well as to represent more realistically land cover over the study area. To this end, new datasets in raster format were converted to binary for the area of interest following the instructions available in the WRF user's guide and were implemented in the model. The two datasets implemented are the Shuttle Radar Topography Mission (SRTM; Farr et al., 2007) and

the Corine Land cover (CLC2012), the newest version available at the moment of implementation. The SRTM was a joint effort of the National Aeronautics and Space Administration (NASA) and the German and Italian Space Agencies started in 2000. It provides global high-resolution topography data (about 30 m) enhancing the representation of mountain ranges and valleys, which are important in the generation of local winds, in contrast with the 1-km resolution Global Multi-resolution Terrain Elevation Data (GMTED) available in WRF. The CLC2012 was produced within the frame of the Copernicus Land Monitoring Service providing consistent information about land cover in Europe. This dataset improved the representation of land use categories regarding resolution (100 m) and distribution of the different categories of land use in the Turia valley with respect to the other land cover datasets available over Europe, e.g., those retrieved from the EOS Moderate Resolution Imaging Spectroradiometer (MODIS; https://modis.gsfc.nasa.gov/data/dataprod/mod12.php) and the United States Geological Survey (USGS; https://www.usgs.gov/centers/eros/science/national-land-cover-database) land cover datasets available in WRF. The implementation of CLC2012 was carried out following the reclassification exposed in Pineda et al. (2004) in order to adapt the land use categories available in CLC2012 to the ones used in USGS. This reclassification reduced the number of land cover types from 44 to 11 (see Pineda et al., 2004); however, it provided a more accurate representation of the land use distribution over the area (Figure 2.3).

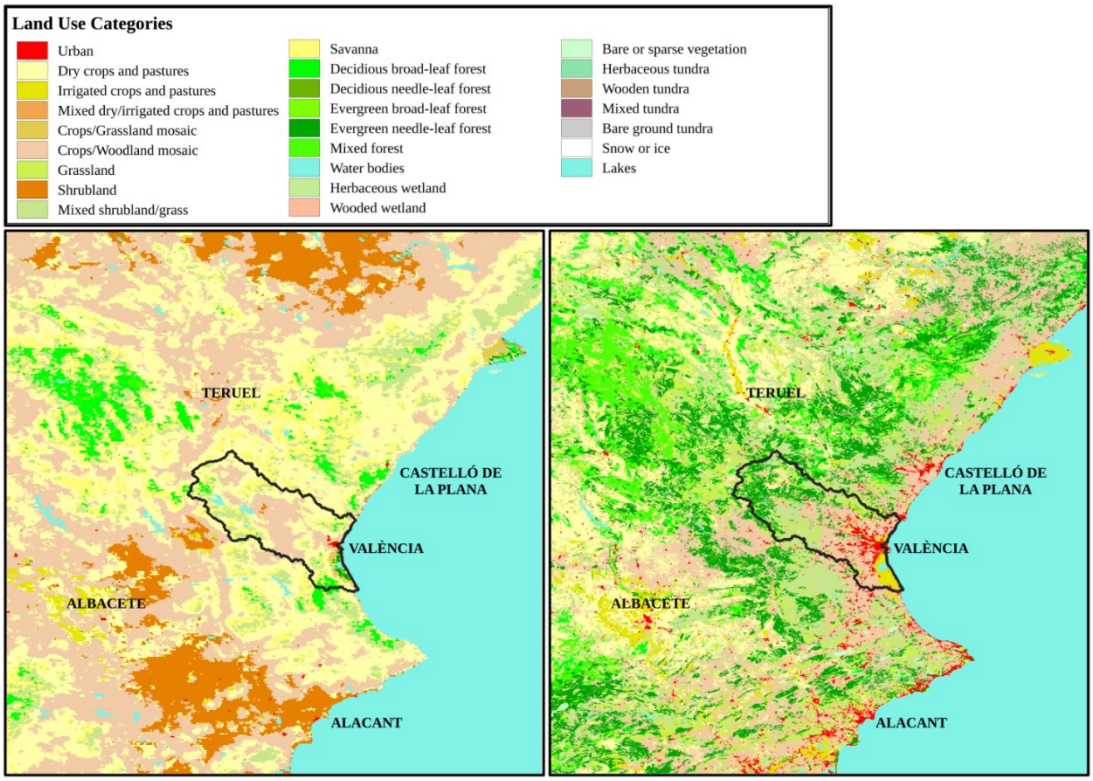

(a) (b)

Figure 2.3 – Land cover datasets implemented in WRF: (a) USGS and (b) reclassified CLC2012, along with the study area (solid black line).

2.2. WRF parametrizations

The configuration of each parametrization available in the WRF model is presented in this subsection along with a brief introduction to the calculations conducted by the corresponding module. A more detailed description of the modules, together with the selected configuration, can be consulted in Appendix A.

2.2.1. Radiation

Radiation schemes compute shortwave and longwave radiative fluxes that provide atmospheric heating throughout predicted parameters such as temperature, humidity, cloud coverage, as well as monthly-averaged climatology for aerosols and the main trace gases (Figure 2.4). In the WRF model, several well-tested radiation schemes are available for the calculation of radiative fluxes. These schemes differ in complexity, such as the number of microphysical interactions and the methodology to account for cloud fraction, as well as the input ozone profiles, which yield different model outputs.

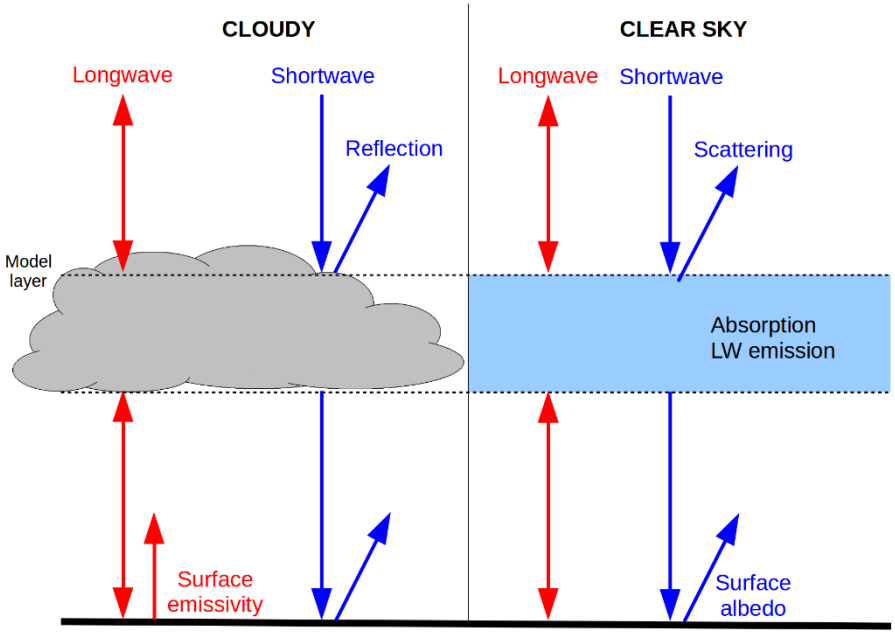

Figure 2.4 - Schematic representation of radiation processes considered in a radiation scheme for both cloudy and clear conditions. Adapted from WRF tutorial.

In this study, the Rapid Radiative Transfer Model (RRTM) for General Circulation Models (GCM), RRTMG, is selected to represent the radiative processes in the WRF model. This scheme is selected after a detailed analysis among all the available possibilities according to the schemes description and performance found in the bibliography (Montornès et al., 2015a; b), as well as a preliminary comparison with the New Goddard radiation parameterization (Chou and Suarez, 1999). The RRTMG presents a high number of spectral bands (16 short-wave and 14 long-wave bands), considers the interaction among four microphysical species (cloud water, rain drops, cloud ice and snow) to compute radiation scattering, it uses constant values for CO_2, N_2O and CH_4, as well as climatological ozone and aerosol data (latitudinal, height and temporal variation), and the statistical technique known as Monte Carlo Independent Column Approximation (McICA) is implemented to represent subgrid-scale cloud variability including cloud overlap (Mlawer et al. 1997; Iacono et al., 2008). Moreover, this scheme is currently operative in the ECMWF Integrated Forecasting System (IFS) as exposed in Hogan and Bozzo (2016). Hence, the RRTMG scheme is considered to be the most convenient radiation parameterization for the purposes of this study.

2.2.2. Cumulus

Cumulus schemes represent the effect of convective and/or shallow clouds at subgrid scale. They are intended to describe vertical fluxes generated by non-resolved updrafts and downdrafts, as well as the compensating subsidence outside the cloud (Figure 2.5). They provide vertical heating and moistening profiles on individual columns, surface precipitation due to convection and, most of them, moisture tendencies for cloud and precipitation fields. Also, several schemes compute momentum tendencies in the column caused by convective transport of momentum. Cumulus schemes are used for coarse resolutions (greater than 10 km) when convective eddies cannot be resolved by the model, although in some cases they may help triggering convection in grid resolutions of 3-10 km. In the 3-10 km grid scale range, known as the gray zone for cumulus, convection may start to be resolved and only some parametrizations are designed to be implemented within this range; hence it is recommended to avoid this range when defining domains. Additionally, in the two-way nesting simulations, issues may appear on the parent (coarse) domains when physics are different across nest boundaries; thus, several options must be considered to avoid such issue: (i) to use the same parametrizations in the coarse and fine domains, (ii) to define a large-enough nested domain to maintain effects away from inside of the coarse domain, or (iii) to use the one-way nesting.

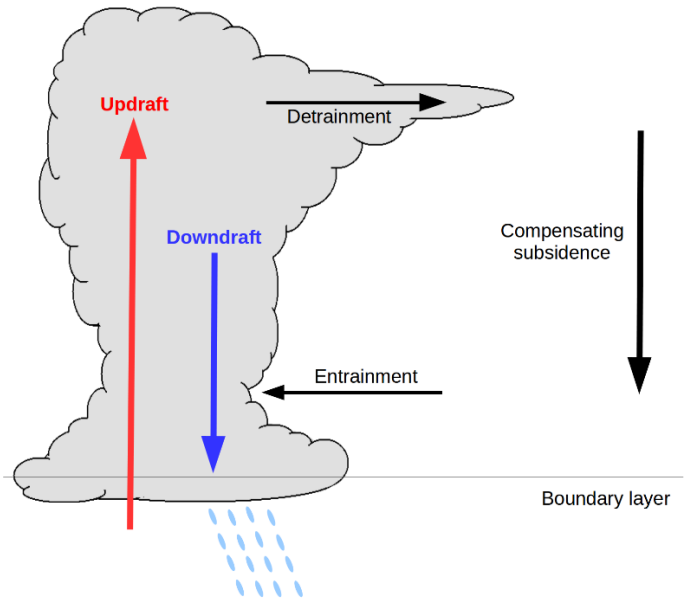

Figure 2.5 - Schematic representation of cumulus processes considered in a cumulus scheme. Adapted from WRF tutorial.

The Kain-Fristch Cumulative Potential (hereafter referred to as KF-CuP) was the cumulus scheme used in the WRF configuration to resolve clouds in the domains with the coarsest resolutions. This scheme was selected as it computes moisture tendencies for four hydrometeors: cloud water, rain, cloud ice and snow, as well as it shows improvements compared to the Kain-Fristch (KF) regarding predicted boundary layer and shallow cumuli (Berg et al., 2013). Other schemes such as the Multi-scale KF (Zheng et al., 2016), which also enhances KF simulated cloudiness, and the New SAS (Simplified Schubert-Arakawa; Han and Pan, 2011) were discarded due to limitations related to possible configurations, e.g., Multi-scale KF must be used with the Yonsei University (YSU) PBL scheme only, hence comparison between different PBL parametrizations could not be carried out.

2.2.3. Microphysics

Microphysics schemes explicitly resolve water vapor, cloud and precipitation processes. Specifically, an adjustment process is performed at the end of the time step in order to ensure an accurate final saturation balance for the updated moisture and temperature; hence, tendencies are not provided. These schemes present significant differences regarding the hydrometeors, the microphysical interactions, as well as the consideration of ice and/or mixed phases processes, the former resulting from interaction with ice and water particles. Also, microphysics schemes differ in the number of prognostic variables; for instance, one-moment bulk schemes (prognostic number concentration) and two-moment bulk schemes (prognostic mass moment and number concentration) are available in WRF.

The one-moment bulk Goddard scheme was the microphysics parameterization used in this study. It considers ice and mixed phases, as well as the interaction among six hydrometeors: water vapor (Q_v), cloud water (Q_c), rain (Q_r), cloud ice (Q_i), snow (Q_s) and graupel or hail (Q_g) as shown in Figure 2.6. The interaction between ice and water particles is crucial for the generation of graupel and/or hail, typically formed during intense summer storms. Other two-moment bulk schemes also consider the mixed-phase (e.g., Morrison and Milbrandt-Yau), however, several authors have proved that one- and two-moment bulk schemes show a very similar behavior under different conditions (Cossu and Hocke, 2014; Wheatley et al., 2014; Weverberg et al., 2014).

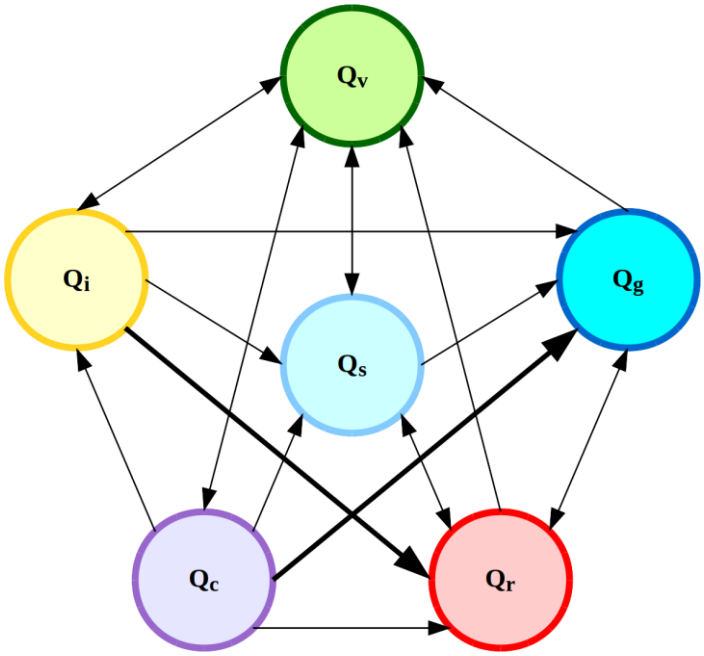

Figure 2.6 - Schematic representation of the microphysics processes considered in a 6-class microphysics scheme (e.g., Goddard). Adapted from WRF tutorial.

2.2.4. Planetary Boundary Layer

Planetary boundary layer (PBL) schemes compute flux profiles within both the well-mixed boundary layer and the stable layer providing temperature, moisture and horizontal momentum tendencies in the atmospheric column, hence, handling vertical diffusion processes.

The use of schemes based on horizontal deformation or constant eddy viscosity values are recommended since horizontal and vertical mixing are considered independently. Besides, these one-dimensional schemes assume a well-defined scale separation between subgrid and resolved eddies. This assumption must be taken into account when fine grid resolutions (about 200 m) are set; in this situation, the PBL scheme should be replaced by a Turbulent Kinetic Energy (TKE) scheme that resolves eddies within the boundary layer. However, as it occurs in cumulus schemes, the accuracy of PBL assumptions, e.g., non-resolved eddies, is reduced within the gray zone (between 200 m and 1 km). In general, PBL schemes are divided into two classes depending on the interactions within the atmospheric column: local and non-local schemes (Figure 2.7). On one hand, local schemes solve for TKE in each column (i.e., buoyancy, shear production, dissipation and vertical mixing) and the main difference among this class of PBL schemes arises in diagnostic mixing length-scale calculations. On the other hand,

non-local schemes use stability profiles or the so-called bulk Richardson number method to calculate PBL height (PBLH), in which PBLH is defined as the altitude where the bulk Richardson number Ri_b achieves a critical value Ri_{cr}. The physics behind the parametrization of processes within the boundary layer, especially the non-local closure, are presented in the following paragraphs. A more detailed description of both local and non-local approaches can be found in Stull (1988).

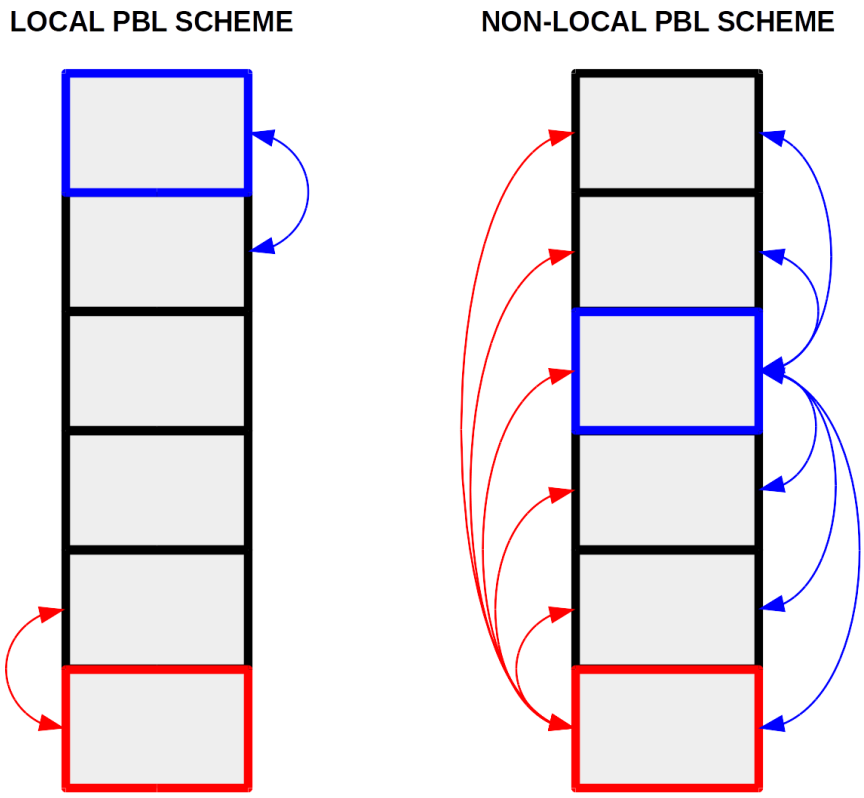

Figure 2.7 - Schematic representation of the atmospheric variables interactions among the layers, highlighted in red and blue, in local (left) and non-local (right) PBL schemes.

Many studies have discussed WRF model performance in representing PBL processes under different conditions and concluded that, generally, non-local schemes describe fluxes more accurately compared to local schemes (Hu et al., 2010; Xie et al., 2012; García-Díez et al., 2013). An extensive description of the various WRF PBL parameterizations and their performance can be found in Cohen et al., (2015). Banks et al., (2016) exposed that the non-local YSU and Asymmetric Convective Model, version 2 (ACM2), and the local BouLac PBL schemes properly captured the evolution of near-surface variables, while the local scheme Mellor-Yamada-Nakanishi-Niino level 2.5 (MYNN) represented slightly better the PBL evolution, as shown in Milovac et al.,

(2016) as well. Therefore, regarding the bibliography consulted, the YSU and ACM2 PBL scheme present very good performances in general; however, the ACM2 PBL scheme was selected to be implemented in WRF regarding the characteristics of the LSMs chosen (see section 2.3 in this chapter). A more detailed description of PBL schemes can be found in Appendix A.1.

2.2.5. Surface Layer

The surface layer (SL) schemes determine exchange coefficients at the surface and friction stress, fed posteriorly to the PBL scheme, as well as 2-meter temperature, 2-meter relative humidity and 10-meter winds. In addition, SL scheme calculations are used as upper boundary conditions in the LSM. Thus, the implementation of the SL parameterization in WRF is strictly connected to both the PBL scheme and the LSM. Only two SL schemes were considered in this study: the Revised MM5 Monin-Obukhov (M-O) SL (Jiménez et al., 2012) and the Pleim-Xiu (PX) SL (Pleim, 2006). It is recommended to use the PX SL scheme together with the ACM2 PBL scheme, whereas the Revised MM5 M-O SL scheme can be implemented along with the majority of PBL parametrizations available in WRF. Even though the latter SL parameterization cannot be used with the YSU PBL, the so-called Pleim-Xiu configuration (ACM2 PBL + PX SL + PX LSM) has been widely tested within the WRF community and it has been proved to enhance the representation of the atmospheric processes in comparison with other configurations (Gilliam and Pleim, 2010).

2.3. Land Surface Models

LSMs use precipitation (from cumulus and microphysics schemes), radiative forcing (from radiation scheme), input parameters computed by the SL schemes and other input parameters describing land surface properties and land state to calculate heat and moisture over land and sea-ice. These fluxes are used as lower boundary conditions for the PBL scheme (or diffusion schemes) to compute vertical transport. In general, LSMs use the surface energy balance among net radiation (R_n), sensible (H) and latent (LE) heat fluxes at the surface, and soil heat flux (G), i.e.

$$R_n = H + LE + G \tag{2.1}$$

to compute soil temperature variations with R_n provided by the radiation scheme and H and LE usually computed by the LSM using SL scheme inputs (e.g., exchange

coefficients and winds). The complexity of LSMs can vary considerably depending on the number of predicted variables and soil layers, as well as the methods implemented to calculate surface fluxes. Moreover, some LSMs consider vegetation, root and canopy effects, and predict snow cover. In LSMs, tendencies are not computed and horizontal interaction between neighboring points is not considered, i.e., they are defined as one-dimensional column models. In this study two models were implemented in WRF: the Pleim-Xiu LSM (Pleim 2006) and the Noah-MP LSM (Niu et al., 2011). A further description of these LSMs is presented in the following subsections and main differences between these models are shown in Table 2.1.

Table 2.1 - Parametrizations of the Noah-MP LSM and the Pleim-Xiu LSM in WRF.

Option	Noah-MP LSM	Pleim-Xiu LSM
Evapotranspiration	Energy balance equation	Humidity differences over resistance
Land use categories	Only dominant category per pixel	Weighted categories per pixel
Vegetation parameters for land use categories	From input table *VEGPARM.TBL*	Hardcoded
Additional parameters	From input table *MPTABLE.TBL*	Hardcoded
Soil layer structure	(1) 0.00 - 0.10 m (2) 0.10 - 0.40 m (3) 0.40 - 1.00 m (4) 1.00 - 2.00 m	(1) 0.00 - 0.01 m (2) 0.01 - 1.00 m
Soil type structure	Same for all layers	Can vary for each layer
Dynamic vegetation	OFF *LAI and* F_{VEG}^{max} *from table*	Not available *LAI and* F_{VEG} *from table*
Aerodynamic resistance	Monin-Obukhov	Monin-Obukhov
Stomatal resistance	Ball-berry scheme	Updated Jarvis, 1976 (*Xiu, 2001*)
Soil moisture factor for stomatal resistance	Using soil moisture β factor (Noah)	Using soil moisture β factor (*Xiu, 2001*)
Runoff and groundwater	TOPMODEL with groundwater *Niu et al. (2007)*	Runoff from soil moisture excess *Pleim and Xiu (1995)*
Radiative transfer	Modified two-stream approach	Radiation at the surface (radiation scheme input)
Surface evaporation resistance	*Sakaguchi and Zeng, 2009*	*Lee and Pielke, 1992*
Exchange coefficients	*Computed over land* *SL scheme over water*	*SL scheme*

2.3.1. Pleim-Xiu LSM

A schematic description of the different processes considered in the LSM are shown in Figure 2.8. This model is based on the Interaction-Soil-Biosphere-Atmosphere (ISBA; Noilhan and Planton, 1989) LSM with a set of significant improvements regarding stomatal and canopy parametrizations (Xiu and Pleim, 2001). The PX LSM integrates soil temperature and moisture in two layers of 0-1 cm and 1-100 cm, as well as liquid canopy water by resolving five partial differential equations introduced in Pleim and Xiu, (1995). In the first layer, soil temperature variations are calculated using G (defined as the heat storage rate; Noilham and Planton, 1989) determined from

Equation 2.1, whereas the second soil layer is implemented as a heat reservoir that slowly varies in time and influences the above layer as a restoring force. Evapotranspiration (E) is defined as mixing ratio differences over a resistance related to soil and canopy properties and it is calculated as the sum of three components: transpiration (E_{tr}), evaporation from soil (E_{soil}), and evaporation from wet canopies (E_{can}), given as

$$E_{tr} = \frac{F_{VEG}(1 - F_{wet})}{r_{aw} + r_{bw} + r_c}\left[q_s(T_{sfc}) - q\right] \tag{2.2}$$

$$E_{can} = \frac{\rho F_{VEG} F_{wet}}{r_{aw} + r_{bw}}\left[q_s(T_{sfc}) - q\right] \tag{2.3}$$

$$E_{soil} = \frac{(1 - F_{VEG})\beta}{r_{aw} + r_{bw}}\left[q_s(T_{sfc}) - q\right] \tag{2.4}$$

where q is the mixing ratio, q_s the saturated mixing ratio, T_{sfc} the surface temperature, ρ the air density, β is the availability factor of water from wet soil, F_{VEG} the vegetation fraction, F_{wet} the fraction of canopy covered by liquid water, r_{aw} the aerodynamic resistance for water vapor, r_{bw} the quasi-laminar boundary layer resistance for water vapor and r_c the canopy resistance. The term LE in Equation 2.1 is computed by multiplying E by the latent heat of vaporization (L) and H is calculated from potential temperature differences and aerodynamic resistance (see Appendix A.2); in addition, 2-meter temperature and mixing ratio are computed in this LSM and posteriorly fed to the SL scheme. Besides, Pleim-Xiu computes soil characteristics for both top and bottom layers using a fractional soil type, as well as it considers several land use categories per grid point so that surface fluxes are computed as a weighted average over the different categories present in a pixel. A more detailed description of the Pleim-Xiu LSM can be consulted in Pleim and Xiu, (1995, 2003) and Xiu and Pleim, (2001).

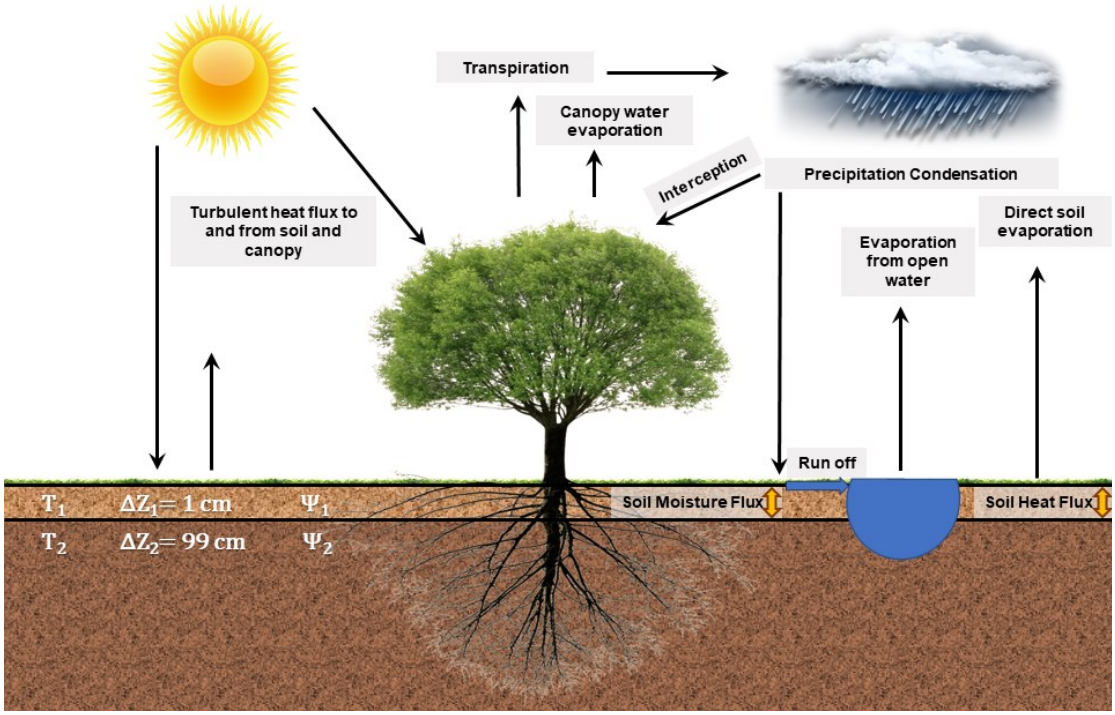

Figure 2.8 - Schematic representation of PX LSM processes.

2.3.2. Noah-MP LSM

The following description of the Noah-MP LSM is based on Niu et al. (2011) and its evaluation can be consulted in Yang et al. (2011).

A schematic representation of processes considered in the Noah-MP LSM are shown in Figure 2.9. The Noah-MP is the result of an extended version of the Noah LSM that offers a wide range of physical parametrizations such as leaf dynamics, radiation transfer through canopy, stomatal resistance, groundwater and runoff. The Noah-MP LSM computes surface heat fluxes as a function of T_{sfc} and consists of four soil layers of 10, 30, 60 and 100 cm with an unconfined aquifer at the bottom. Soil moisture and soil temperature within the four active layers are calculated using the Richard's equation and the thermal diffusivity equation, respectively, and in the aquifer, the temporal variation of the water stored follows the Darcy's law (Niu et al., 2007). For soil temperature lower boundary condition, a bottom temperature (T_{bot}) at 8 m is introduced from an input file containing annual mean data of 2-meter air temperature (at 1-degree) based on the International Satellite Land Surface Climatology Project-Initiative (ISLSCP-I) dataset.

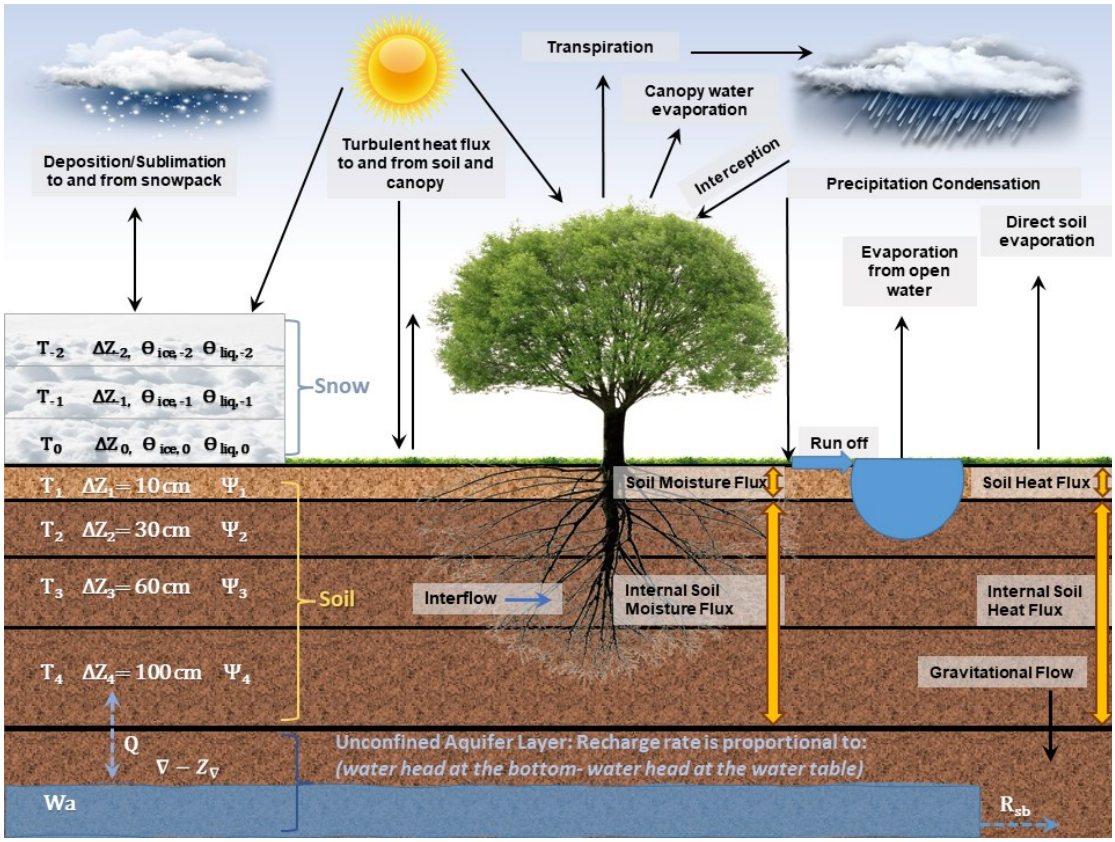

Figure 2.9 - Schematic representation of Noah-MP LSM processes. Adapted from Niu et al. (2011).

In this LSM, the energy balance equation (Equation 2.1) over each grid cell is resolved using an iterative method that updates skin temperature and the corresponding surface fluxes every iteration step. Once the energy balance is achieved (from T_{sfc} increment, $|\Delta T_{sfc}| \leq 0.01$ K), or a certain number of iterations is reached (5 iterations), the iteration process stops. Furthermore, the Noah-MP LSM uses an advanced method to compute the energy balance over the continent: the so-called *semi-tile* approach. This method considers shortwave radiation over an entire grid cell accounting for canopy gaps so that fractions of sunlit and shaded leaves are computed along with their absorbed solar radiation; whilst, longwave radiation, H and G are calculated separately over bare and vegetated soil. Moreover, surface fluxes are computed over canopy and between soil and canopy for vegetated tiles; thus, over a vegetated grid cell, SVA exchanges are computed as a weighted sum of canopy, underneath canopy and bare ground fluxes. As for PX LSM, the total evapotranspiration is the sum of three components (E_{tr}, E_{can} and E_{soil}) although these are computed from the LE term of the energy balance equation (Equation 2.1) such that over a grid cell:

$$LE_{tr} = \frac{\rho C_p F_{VEG}}{\gamma} C_t^w [e_s(T_v) - e_c] \quad (2.5)$$

$$LE_{can} = \frac{\rho C_p F_{VEG}}{\gamma} C_e^w [e_s(T_v) - e_c] \quad (2.6)$$

$$LE_{soil} = \frac{\rho C_p}{\gamma} \left\{ \frac{(1 - F_{VEG})[e_s(T_{g,b}) RH_g - e]}{r_{aw} + r_{soil}} + \frac{F_{VEG}[e_s(T_{g,v}) RH_g - e_c]}{r_{aw,g} + r_{soil}} \right\} \quad (2.7)$$

where C_p is the dry-air specific heat capacity, γ the psychometric constant, e_s the saturated water vapor pressure, e the water vapor pressure of air, e_c the water vapor pressure of air below canopy, RH_g the air relative humidity in the surface soil pore space, T_v the vegetation canopy surface temperature, $T_{g,b}$ the ground temperature over bare soil and $T_{g,v}$ the ground temperature over vegetated soil, $r_{aw,g}$ the aerodynamic resistance for water vapor below the canopy, r_{soil} soil surface resistance, and C_e^w and C_t^w the evaporation and transpiration conductance (inverse of resistance), respectively, both a function of effective *LAI* (Leaf Area Index) and *SAI* (Stem Area Index). The corresponding E_{tr}, E_{can} and E_{soil} are obtained dividing Equations 2.5 – 2.7 by L. In a similar manner, Noah-MP calculates H over bare and vegetated soil, as well as over canopy (above and underneath canopy), using ground and surface temperature differences (see Appendix A.2).

The parametrizations for the Noah-MP are selected in the *namelist.input* file of the WRF model whereas other parameters dependent on land use category are define in two main tables regarding vegetation (VEGPARM.TBL) and other parameters (MPTABLE.TBL) that facilitate additional modifications if needed (Table 2.1). The main parameters defined for the land use categories in the VEGPARM.TBL and MPTABLE.TBL can be consulted in Table A.1 (Appendix A.3).

3. Observations

Observations provide the most realistic representation of the atmospheric state so that these are commonly used as reference to evaluate models' performance. Hence, this thesis used observations from a wide set of sources to both analyze atmospheric conditions and validate estimates obtained with the WRF model since this was the main tool employed in this study.

3.1. Reanalysis datasets

3.1.1. ERA5

ERA5 represents the fifth generation of the ECMWF reanalysis products which improves several crucial aspects of its predecessor ERA-Interim. ERA5 reanalysis provides hourly data for the period from 1979 to the present (with a delay of 2-3 months) using a 4D-Var data assimilation in the IFS version CY41R2 of the ECMWF. Additionally, a preliminary version of this product is also available from 1950 to 1978 (ERA5 reanalysis back extension). The spectral resolution of the ERA5 is T639 (about 31 km over Earth's surface) and it consists of 137 hybrid (sigma/pressure) vertical levels with the top level at 0.01 hPa; however, ERA5 atmospheric data is also available at 37 interpolated pressure levels. Furthermore, an extensive number of surface parameters (e.g., precipitation, 2-meter temperature and surface pressure) and other single level parameters (e.g., vertically integrated water vapor) are available, as well as soil parameters (e.g., soil moisture and soil temperature) obtained from the coupling of the IFS to a soil model. A more detailed description of the ERA5 product can be consulted in Hersbach et al. (2020).

ERA5 reanalysis provides useful information about the state of the atmosphere and soil conditions that is used to perform synoptic analysis, as well as to initialize WRF simulations in this study. Concretely, temperature and geopotential at 500 hPa, and mean sea level pressure are used to evaluate atmospheric conditions for the periods of interest, whilst a wide set of meteorological variables are used to initialize atmospheric conditions and drive coarsest domains in WRF simulations.

3.2. Satellite products

3.2.1. Meteosat Second Generation

Images from the visible (VIS) and Infrared (IR) spectral channels of the geostationary Meteosat Second Generation (MSG) are available every 15 minutes over Europe. Meteosat images are provided by the 12-channel Spinning Enhanced Visible and Infrared Imager (SEVIRI) imaging radiometer providing continuous images of the earth-atmosphere system. These high-resolution images facilitate a closer view of the meteorological conditions for a given period, as well as allow the tracking of features such as the formation and evolution of localized storms during the study period. A more detailed description is presented in Schmetz et al. (2002).

Specifically, satellite images from the VIS were downloaded from the website http://www2.sat24.com/history.aspx?culture=en (last access: 22-11-2019).

3.2.2. CMORPH

The Climate Prediction Center (CPC) produces global precipitation estimates (from 60ºS to 60ºN) using the so-called CPC Morphing Technique (CMORPH) at a spatial horizontal resolution of about 8 km at the Equator, and a temporal resolution of 30 minutes for the period from 1998 to present (with a delay of 3-4 months). This product obtains precipitation estimates using passive microwave observations from low orbiter satellites (e.g., the NOAA meteorological satellites) posteriorly propagated with motion vectors derived from different IR data (e.g., Meteosat IR). Besides, the data obtained is subject to bias corrections with respect to CPC daily precipitation measurements over land and adjusted against the merged analysis of pentad (5 days) precipitation from the Global Precipitation Climatology Project (GPCP) over ocean. A detailed description of the product can be found in Ferraro (1997), Ferraro et al. (2000), Joyce et al. (2004) and Xie et al. (2017).

CMORPH high-resolution precipitation data can be used to evaluate the accuracy of the WRF model in reproducing precipitation. Specifically, WRF estimated precipitation from the different simulations is compared to CMORPH data at different spatiotemporal scales to analyze the performance of the model.

3.2.3. MODIS

The Moderate Resolution Imaging Sepectroradiometer (MODIS), both on board EOS-TERRA and EOS-Aqua platforms, provides an extensive amount of atmospheric and surface data at moderate spatial resolution and at global scale. In this thesis, the 8-day evapotranspiration at 500-m spatial resolution from the MOD16A2 v006 product (hereafter referred to as MOD16A2), available from 2000 to present, was used to evaluate the model's performance. This product is generated with an algorithm based on the Penman-Monteith equation and provides values of E, LE, potential evapotranspiration PE and potential latent heat flux PLE together with quality flags (Mu et al., 2013). Other information regarding MOD16A2 product improvements, issues, quality and file specifications can be found in https://lpdaac.usgs.gov/products/mod16a2v006/ (last access: 21-10-2021).

Evapotranspiration estimates from MODIS can be used as a reference to evaluate WRF model in terms of surface moisture fluxes at high horizontal resolution. Concretely, *E* spatiotemporal averages calculated from WRF long-term simulations output are compared to MODIS estimates over the area of study.

3.3. Surface stations

3.3.1. CEAM, IVIA-SIAR and XVVCCA networks

The analyses and model validations were conducted using several meteorological stations with sufficient measurements from three different networks: (i) the Mediterranean Center for Environmental Studies (CEAM), (ii) the Valencian Institute for Agronomic Research - Agroclimatic Information System for Irrigation (IVIA) and (iii) the *Xarxa Valenciana de Vigilància i Control de la Contaminació Atmosfèrica* (XVVCCA). A short description of the characteristics of the main stations used in this study are shown in Table 2.2.

Table 2.2 – Characteristics of meteorological stations located within the study area, where *D* is the distance to the coastline and *Hgt* the altitude above sea level.

Station	ID	Source	D (km)	Hgt (m)	Land use description
Burjassot	BU	XVVCCA	8	36	*Urban*
Montcada	MO	IVIA-SIAR	10	61	*Fruit tree plantations*
Paterna	PA	CEAM	13	124	*Urban*
Bétera	BE	IVIA-SIAR	15	97	*Fruit tree plantations*
Villar del Arzobispo	VI	CEAM	47	370	*Non-cultivated arable land*
Xulilla	XU	IVIA-SIAR	47	375	*Fruit tree plantations*
Aras de los Olmos	AR	CEAM	82	1277	*Semi-natural shrubland*

The IVIA-SIAR agrometeorological network consists of 55 surface stations in the Valencia region implemented to capture atmospheric parameters over different crop fields, so that crop water necessities are controlled, and a more efficient water usage can be performed. Further information can be consulted in http://riegos.ivia.es/meteorologia (last access: 21-10-2021).

The XVVCCA is an automatic network that consists of more than 50 surface stations (25 meteorological towers) with the scope of controlling atmospheric pollution within

the Valencia region. Most of the stations measure the typical meteorological variables such as temperature, relative humidity, atmospheric pressure, solar radiation, precipitation and, wind speed and direction, apart from pollutants concentrations, in real time. These measurements are regularly subjected to validation in the *Centre de Control de la Qualitat de l'Aire*, as well as at CEAM. Further details can be consulted in https://agroambient.gva.es/va/web/calidad-ambiental (last access: 22-10-2021).

3.3.2. GNSS network

Active Geodetic networks use Global Navigation Satellite System (GNSS) receivers to provide an accurate positioning using signals received from satellite constellations such as GPS, GLONASS, Galileo and Beidou. This infrastructure was mainly used for navigation, time transfer and relative positioning until Bevis et al., (1992) presented a method to determine the atmospheric total precipitable water (TPW) content throughout the analysis of small signal deviations produced by atmospheric water vapor. Values of TPW can be determined with an accuracy of 1-2 mm (Haan et al., 2006).

In this thesis, data from four different GNSS networks available in eastern Spain (ARAGEA, ERVA, CatNET and ERGNSS) and processed at the *Intitut Cartogràfic i Geodèsic de Catalunya* (ICGC) were used to derive the TPW using the approach presented in Bevis et al., (1994). The obtained data was used to evaluate the performance of the different WRF simulations in reproducing the total water vapor available in the corresponding atmospheric columns and crucial in the generation of precipitation.

3.3.3. SPAIN02 product

The Spain02 version 1 is a series of daily gridded precipitation datasets at different horizontal resolutions (50, 20 and 5 km) developed for peninsular Spain and the Balearic Islands using more than 2000 quality-controlled meteorological stations from the Spanish National Meteorological Agency (AEMET). It is based on the Surface Parameter Analysis (SPAN; Rodríguez et al., 2003; Navascués et al., 2003; Quintana et al., 2016) system used in the HIRLAM weather prediction model, operative at AEMET until 2017, with slight modifications such as the parameter controlling properties of the Optimal Interpolation method. The highest horizontal resolution (5 km) dataset available is selected to perform this study in order to visualize a more detailed distribution of precipitation. Further information regarding the 5-km Spain02 dataset can be consulted in Peral et al., (2017).

The gridded daily precipitation provided in the Spain02 dataset at high spatial resolution allows to perform a preliminary analysis of precipitation spatiotemporal distribution in Spain, and especially in eastern Spain, with no gaps. Besides, this facilitates the comparison with simulated precipitation in the WRF model at a daily base.

3.4. Models and analysis tools

3.4.1. Hydrobal

The HYDROBAL model is a useful tool developed to estimate water balances in forest areas with different vegetation types (Bellot and Chirino, 2013; Mouthair, 2016). It calculates daily water fluxes from the following input variables: minimum and maximum temperatures, potential evapotranspiration, solar radiation, and vegetation and soil characteristics. This model has been applied and validated over different areas providing successful results (Touhami et al., 2013; 2014; 2015; Manrique-Alba et al., 2017; Moutahir et al., 2016; 2019), as well as it has been used to study soil-water fluxes over strategically instrumented sites in the study area of this thesis.

Concretely, two sites or field plots (green triangles in Figure 2.11 in section 5 of this chapter) were established within the study area where vegetation and soil characteristics were described, as well as sap-flow and soil moisture measurements were carried out in parallel to the work presented in this thesis. These observations, together with the description of soil and vegetation features, were used to estimate transpiration (main contribution to evapotranspiration in forests) throughout the sap-flow technique and evapotranspiration *E* with the HYDROBAL model. Specifically, HYDROBAL was set according to the vegetation and soil characteristics, and soil moisture measurements at each site so that *E* was estimated and compared to the values obtained from the sap-flow approach showing a good agreement at a daily base over coastal and inland sites. The good performance of the HYDROBAL model encouraged the use of this model as a reference of moisture fluxes at these locations to evaluate simulated values in WRF during 2015. An extensive description of the two methodologies and the corresponding results over the field plots instrumented in the lower part of the TRB can be consulted in Larsen (2021).

3.4.2. VAPOR

The Visualization and Analysis Platform for Ocean, Atmosphere, and Solar Researchers (VAPOR; Li et al., 2019) is a user-friendly tool for meteorological and climatological

data analysis developed by the NCAR as an open-source tool. It is an interactive 3D platform that facilitates the visualization, analysis and presentation of data and results, especially from WRF simulations, although files in other data formats, such as MOM, POP, ROMS, GRIB and NetCDF, can be directly imported as well. In the present study, this program was used to analyze the advection of several parameters in the study area due to SBC, as well as to calculate time-varying (unsteady) trajectories. The calculation of unsteady trajectories is conducted with the Rutten-Kutta fourth-order method assuming massless particles previously defined in space and time by the user. This option was used in this thesis to determine backward trajectories from connective clouds and the displacement of air parcels associated with sea breeze and other locally-driven circulations.

4. Summer storms and sea breeze

Summer storms are convective events linked to sea breeze dominating conditions (Millán et al. ,2005b; see section 2.2 in Chapter 1). Thus, it is crucial to identify sea breeze occurrence and determine its characteristics in order to facilitate the analysis of the formation, development and triggering of summer storms. In this context, the following subsections introduce the methodology followed for the selection of the study periods, the identification of summer storms and the characterization of the sea breeze.

4.1. Study period: May-October 2015

A study period was selected regarding the occurrence of summer storms, commonly from May to October, according to Millán et al. (2005b). Then, all precipitation data was analyzed within the Hydrographic Confederation of the Jucar (HCJ) in eastern Spain to select the year of interest. In particular, the steps below were followed:

i. Initially, the study period May-October 2015 was selected regarding the high number of precipitation days identified during the extended summer season (ESS) according to daily precipitation and the number of precipitation days within the ESS from the Spain02 dataset in the period (1988-2017). In order to select precipitation days within the HCJ three filters were applied to Spain02 precipitation so that, first, pixels with daily precipitation lower than 1 $mm \cdot day^{-1}$ were discarded (i.e., treated as zero); then, the days with less than 5 contiguous pixels with precipitation in the HCJ were disregarded; and finally, the days with total accumulated precipitation (i.e., sum of all pixels in the HCJ) lower than 10 $mm \cdot day^{-1}$ were not considered. Once the precipitation days were identified,

several years of interest were further analyzed for the ESS using monthly climatological reports from AEMET to select the study year, considering other meteorological observations availability in the study area as well. The results of this analysis are explained in section 4 of Chapter 3.

ii. Regarding the characteristics of summer storms (Millán et al. (2005b), synoptic maps generated with ERA5 mean sea level pressure and geopotential height and temperature at 500hPa were used to analyze atmospheric instability at upper levels and to detect the formation of the ITL. These maps facilitated the filtering out of precipitation events associated with the passage of Atlantic fronts or Mediterranean advection.

iii. Additionally, hourly MSG-SEVIRI images were visualized to detect the areas in eastern Spain where convective clouds developed, as well as their characteristics (e.g., clouds extension and displacement).

A set of episodes were identified using this approach and further analyzed with high-resolution simulations focused on eastern Spain, specifically in the TRB.

4.2. Sea breeze characterization

In the Mediterranean region, winds present different characteristics over inland and littoral locations strictly influenced by distance to the coastline, altitude and topography; thus, surface stations are usually divided into three types (littoral, pre-littoral and inland) to conduct atmospheric studies using a combination of these three features. In this study, the classification of surface stations was also implemented using the three types introduced following previous classifications conducted over meteorological stations in the Valencia region (Millán et al., 2005a; b; Pérez-Landa et al., 2007). Specifically, stations situated in *Aras de los Olmos* (AR), *Villar del Arzobispo* (VI) and *Paterna* (PA) from the CEAM network were described as inland, pre-littoral and littoral, respectively, regarding their location within the Turia valley (Figure 2.1; as shown in Table 2.2). Afterwards, days with the occurrence of sea breeze during the period 2005-2015 over AR, VI and PA were selected according to the following steps:

i. Wind roses were generated setting 1-degree and 1-ms^{-1} bins for wind direction and wind speed, respectively, such that the effect of topography in the wind direction and/or the location of the coastline could be distinguished.

ii. Data was filtered for daytime (05-19 UTC) and a bar chart of frequency of wind direction occurrence was generated in order to visually identify the wind direction bins that represented the sea breeze flow. For the coastal station PA, a wind speed threshold of 1-7 ms^{-1} was defined to exclude onshore flows due to dominating synoptic conditions. The upper limit of 7 ms^{-1} was selected since winds associated with intense sea breeze circulation are about 5-7 ms^{-1} in the Mediterranean region, whereas the lower limit of 1 ms^{-1} was set to filter out light early-morning thermally driven winds due to surface heating, especially during summer. The upper limit for wind speeds was not applied over pre-littoral and inland stations (VI and AR, respectively) since the sea breeze flow can be intensified by upslope winds and exceed this wind speed threshold (Millán et al., 2005a; b; Pérez-Landa et al., 2007). Instead, data over VI was filtered according to the sea breeze days detected in PA from the analysis. Analogously, the sea breeze days obtained from the analysis in VI were used to select sea breeze days in AR. This procedure could be conducted since the three meteorological stations from the CEAM network line up in the direction of sea breeze flows within the study area so that sea breeze days identified in AR must be also detected in VI and PA, and sea breeze days observed in VI must be detected in PA as well.

iii. The analysis was conducted such that the bins representing the combined breeze were adjusted to one (or two combined) Gauss distribution and the 95 % confidence level was selected to define the range of wind direction variation corresponding to the sea breeze. Specifically, the Gauss adjustment was conducted using the MATLAB function *fit* for one Gausian distribution and for a combination of two Gaussian distributions selecting the options *gauss* and *gauss2*, respectively, (a more detailed description of the function can be consulted in https://es.mathworks.com/help/curvefit/gaussian.html?lang=en, last access: 23-08-2021). Afterwards, the adjustment with the greatest coefficient of determination (R-squared) was selected to set wind direction variations. As commented previously, this methodology was first applied to wind observations at PA, and the detected sea breeze days were used as an initial filter to select days with sea breeze occurrence at VI. Then, the approach was applied to wind observations at VI and the obtained sea breeze days were used

to select sea breeze days at AR. Finally, the same approach was applied to wind observations at AR.

iv. Once obtained the wind direction thresholds for the sea breeze, days with at least 50 % of the time (7 h) with winds continuously blowing within the set wind direction and speed ranges were considered breeze days, and the percentage of breeze days with respect to the total number of days with available data was calculated for the whole period (2005-2015), as well as for winter (DJF), spring (MAM), summer (JJA) and autumn (SON).

This methodology facilitated the identification of sea breeze occurrence and provided crucial information about its features over each type of station.

5. Simulation strategy

Several simulations were performed with the WRF model in order to fulfill the objectives of this thesis. First, the ESS was simulated with two LSMs (PX and Noah-MP) to identify main differences between these two surface parametrizations regarding the modeling of the hydrological cycle. Additionally, a comparison among three different parametrizations of land-atmosphere interactions was conducted for a specific summer storm episode (case study) to evaluate their accuracy in reproducing the characteristics of the different summer storms occurred in this episode (e.g., precipitation and winds). Finally, the episode was simulated at high resolution in order to evaluate SVA interactions and the surface fluxes contribution to atmospheric water vapor content and air temperature. A scheme of the simulation strategy is presented in Figure 2.10 along with the corresponding simulations IDs. The model set up, including the characteristics of each simulation, and the validation procedure are described in the following subsections.

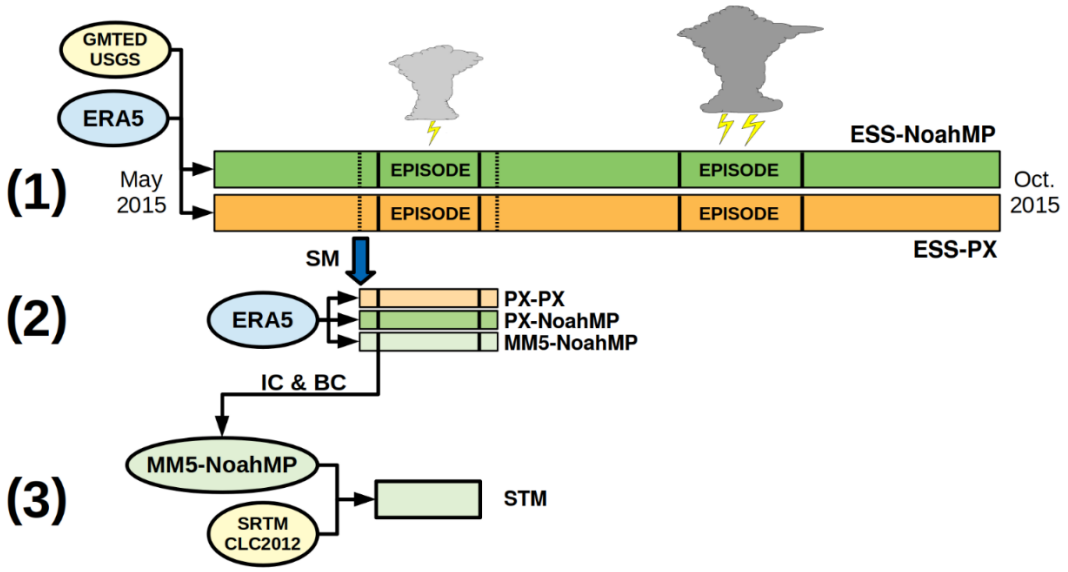

Figure 2.10 - Simulation strategy summarizing the three sets of simulations: (1) ESS, (2) summer storm episode comparison, and (3) high-resolution summer storm episode (STM) simulations.

5.1. Model set up

The general parametrizations unchanged in all simulations were the RRTMG (radiation), the KF-CuP (cumulus), the Goddard (microphysics) and the ACM2 (PBL). In the following paragraphs the simulations executed are described according to the simulation strategy (Figure 2.10).

5.1.1. Extended Summer Season (ESS)

The main goal of ESS simulations was to estimate atmospheric parameters at high spatiotemporal resolution so that a performance evaluation of the two LSMs in the representation of hydrological cycle components such as evapotranspiration and precipitation (e.g., summer storms previously identified with observations) could be conducted. Specifically, these simulations were used to identify main differences associated with the parametrization of surface processes for relatively long periods (6 months), as well as the corresponding influence over convective precipitation linked to summer storms along the Mediterranean coast. Additionally, these simulations provided valuable information about WRF model deficiencies at local scale over eastern Spain and the correction for next runs if feasible. To this end, two simulations of the ESS (May-October 2015) covering the WMB, the Iberian Peninsula (IP) and the Valencia region (VR) at horizontal resolutions of 10.3, 3.4 and 1.1 km, respectively, were set for the two LSMs selected (PX and Noah-MP). The extensions of the domains

WMB, IP and VR were selected in order to accurately simulate synoptic conditions (e.g., Atlantic and Mediterranean advections over eastern Spain), the characteristic ITL and the generation of summer storms associated with the sea breeze circulation, respectively. In both simulations the KF-CuP cumulus scheme was only activated for the outermost domain WMB and the PX SL scheme was used to reduce parametrization differences between simulations. However, it must be noticed that SL schemes implemented with the Noah-MP only compute exchange coefficients over water, whereas the Noah-MP performs this calculation over land (Table 2.1). This fact emphasized the need of an additional analysis regarding the SL parametrization implemented together with the Noah-MP LSM to identify (and reduce if possible) inconsistencies related to the calculation of exchange coefficients over water bodies (see next subsection). ERA5 data was used to set initial conditions, as well as to update boundary conditions of the coarsest domain every 6 h. In addition, a model spin-up of 20 days was considered to avoid initially unreliable results associated with the initial conditions. Topography and land cover were represented according to GMTED and USGS datasets, respectively, with maximum resolutions of 1 km. Simulation domains are shown in Figure 2.11, along with the observations within domain VR used in the model validation, and main information is summarized in Table 2.3.

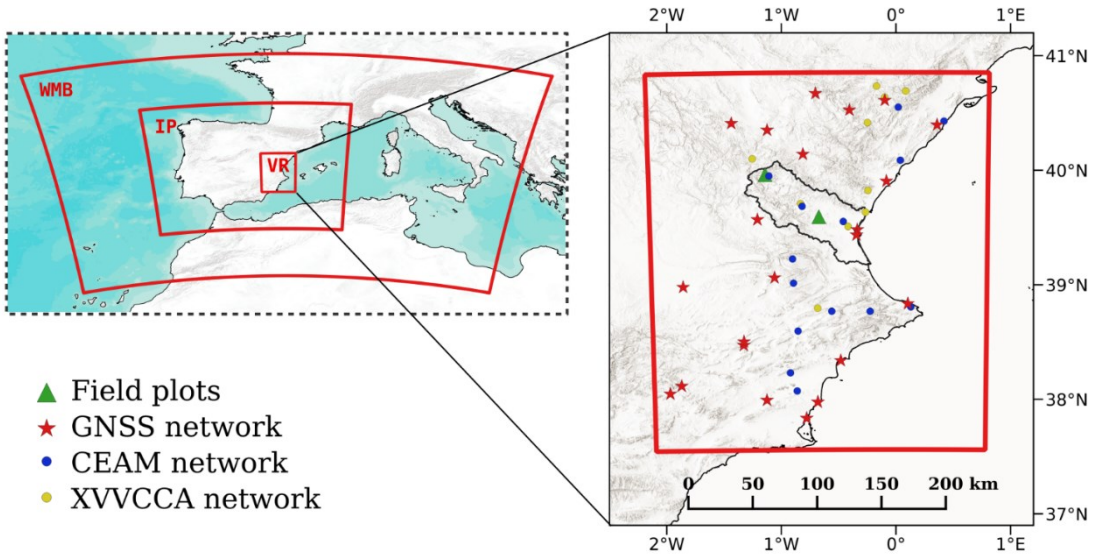

Figure 2.11 - Domains for ESS-PX and ESS-NoahMP simulations with all observations used for the innermost domain (VR) validation of the model.

Table 2.3 - Main characteristics for ESS-PX and ESS-NoahMP simulations.

Domain	1	2	3
Domain ID	WMB	IP	VR
Simulated period	01/05 - 01/11/2015	01/05 - 01/11/2015	01/05 - 01/11/2015
Grid points	331x206	417x348	222x321
Time step	45 s	15 s	5 s
Horizontal resolution	10.3 km	3.4 km	1.1 km
Vertical levels	45	45	45
IC and BC	ERA5	Domain 1	Domain 2
Land cover	USGS (4 km)	USGS (1 km)	USGS (1 km)
Topography	GMTED (4 km)	GMTED (1 km)	GMTED (1 km)
Radiation	RRTMG	RRTMG	RRTMG
Cumulus	KF-CuP	Resolved	Resolved
Microphysics	Goddard	Goddard	Goddard
PBL	ACM2	ACM2	ACM2
SL	PX	PX	PX

ESS simulations were compared to in situ measurements (Figure 2.11), including the Spain02 dataset, as well as to satellite estimates of *E* (MOD16A2) and precipitation (CMORPH) in order to evaluate the modeling of main hydrometeorological variables for the study period (see Sections 3.2 and 3.3 in this chapter). Besides, the HYDROBAL model was used to estimate *E* at the field plots regarding its good performance in reproducing *E* (see section 3.4 in this chapter). Estimates of *E* were computed using simulated precipitation, *PE* and soil moisture during May-October 2015 from the corresponding ESS simulation. Concretely, HYDROBAL generated *E* estimates at the sites (shown in Figure 2.11) according to the input values from ESS-PX and ESS-NoahMP (runs were identified as HYDROBAL-PX and HYDROBAL-NoahMP, respectively), and then these were used as reference to evaluate simulated *E* from the corresponding ESS simulation.

5.1.2. Summer storms episode

ESS simulations were executed with two LSM covering a 6-month period to evaluate the model in reproducing the hydrological cycle. However, it has been widely demonstrated that the performance of meteorological models decreases with simulated time (e.g., Balmaseda and Anderson, 2009), i.e., meteorological phenomena are more accurately reproduced in simulations initialized close to the meteorological event. Hence, a comparison of a specific summer storms episode was conducted to further evaluate differences between PX LSM and Noah-MP LSM in reproducing the formation, development and triggering of summer storms. Besides, ESS simulations

were executed with two different LSM but the same SL scheme so that the LSM was the only different parametrization between the simulations. However, the simulation of surface processes is also subject to the selected SL scheme which can reduce or enhance the performance of a given LSM, i.e., it is recommended to use the PX SL scheme together with the PX LSM, whereas other SL schemes can be implemented with the Noah-MP LSM. This indicates that the implementation of a different SL parametrization (such as the Revised MM5) with the Noah-MP LSM may improve Noah-MP performance over the study area. Specifically, differences in the representation of meteorological variables would be related to water-atmosphere interactions (i.e., lakes and sea) regarding that SL schemes only compute exchange coefficients over water bodies when used with the Noah-MP LSM (see Table 2.1). Thus, this additional parametrization (referred to as MM5-NoahMP) in the WRF model was executed to consider differences associated with the SL scheme selection.

To this end, three simulations of a summer storm episode from the 13th to 24th of July 2015 (consisting of 4 main summer storm events occurred the 16th, 18th, 21st and 22nd) were executed with three different combinations regarding SL scheme and LSM. The period to simulate was selected regarding the high number of summer storms occurring in a week which allowed the analysis of several summer storms with a single simulation reducing the computational cost. Simulations covered WMB and IP domains (Figure 2.11) at horizontal resolutions of 10.3 and 3.4 km (same as ESS), respectively. Besides, the WRF model configuration was set up as in ESS simulations with differences regarding the simulated period (13th to 24th July 2015) and the initialization of soil conditions, i.e., ERA5 was used to initialized atmospheric conditions but soil conditions were extracted from the corresponding ESS simulations. Specifically, ESS-PX soil conditions were used to initialize PX-PX simulation, whereas PX-NoahMP and MM5-NoahMP were initialized with ESS-NoahMP soil conditions for consistency (Table 2.4). The main objective of these simulations was to evaluate their accuracy in reproducing a particular episode over the Turia valley and select the most suitable configuration for a high-resolution simulation of the same episode. Regarding this objective, validation efforts with all available observations focused over the selected domain for the posterior high-resolution simulation (see Figure 2.12). Besides, apart from surface observations, CMORPH precipitation data was used to evaluate the representation of precipitation in the TRB domain.

Table 2.4 - Options changed with respect to ESS simulations.

Simulation ID	PX-PX	PX-NoahMP	MM5-NoahMP
SL	PX	PX	Revised MM5
LSM	PX	Noah-MP	Noah-MP
Initial soil conditions	ESS-PX	ESS-NoahMP	ESS-NoahMP

After an evaluation of the three simulations, the same episode of summer storms was simulated at a high-resolution. All meteorological and hydrological parameters used to initialize and drive this simulation were extracted from the finest domain (IP) of the corresponding previous simulation and several static parameters (i.e., land cover and topography) were modified in order to improve results (see Section 2.1). The extraction of initial conditions was performed using the Unified Post Processor (UPP) tool available in WRF, whilst boundary conditions were generated with the program *ndown.exe* (see Appendix B.3). A new simulation domain is defined to focus in the summer storms that develop over the mountain ranges of the TRB (Figure 2.12), and the number of model levels is increased. The main information about simulation set up is summarized in Table 2.5.

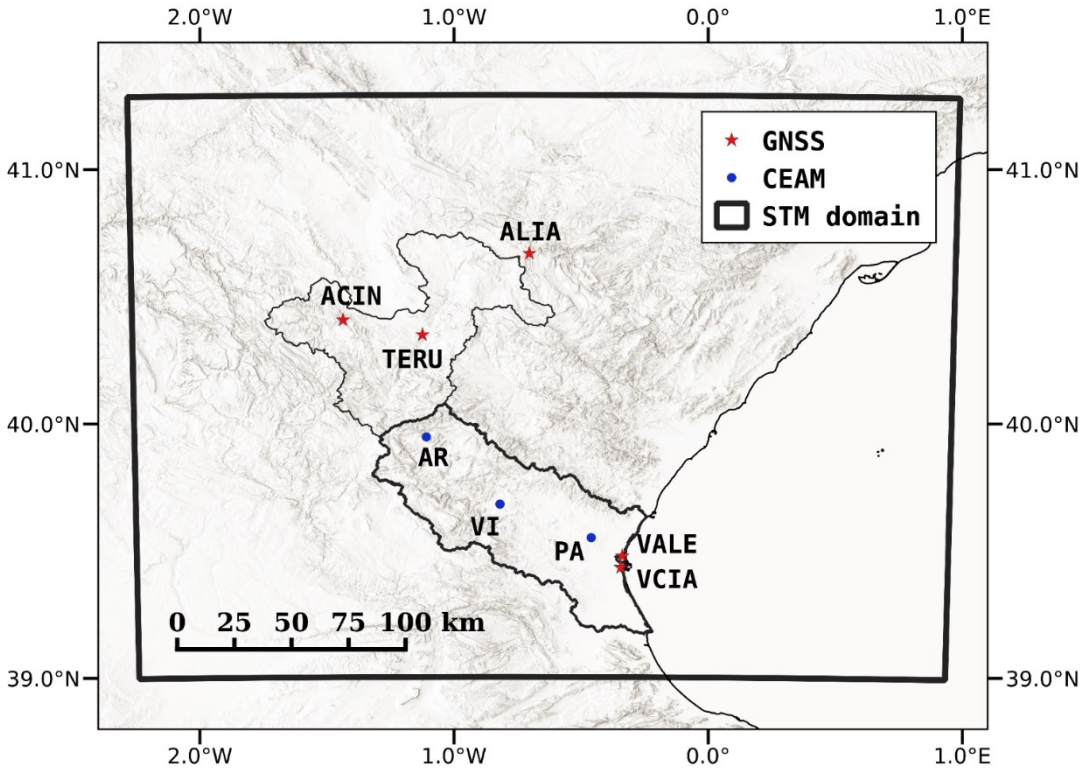

Figure 2.12 - Domain for STM simulation along with observations used in the validation.

Table 2.5 - High-resolution simulation set up.

Simulated period	15/07 - 23/07/2015
Simulation ID	STM
Grid points	200x200
Time step	3 s
Horizontal resolution	680 m
Vertical levels	54
SL	Revised MM5
LSM	Noah-MP
IC and BC	MM5-NoahMP
Land cover	CLC 2012 (100 m)
Topography	SRTM (30 m)

5.2. Model validation

All simulations performed with the WRF mesoscale model were subject to validation throughout direct comparison of spatial distribution and time series of typical meteorological and hydrological variables (i.e., precipitation, temperature, humidity, winds and evapotranspiration) from the different sources introduced in section 3 of this chapter. The model validation was performed using all observations available within the finest simulation domain after a quality control regarding data availability and continuity. In the high-resolution simulation (STM), the validation focused over the TRB using the observations shown in Figure 2.12. In addition, statistical analyses were conducted; specifically, the commonly used mean bias error (MBE; Equation 2.8) root mean square error (RMSE; Equation 2.9) and index of agreement (IOA; Equation 2.10) were calculated (Willmott et al., 1985):

$$MBE = \frac{1}{N}\sum_{i=1}^{N}(P_i - O_i) \tag{2.8}$$

$$RMSE = \left[\frac{1}{N}\sum_{i=1}^{N}(P_i - O_i)^2\right]^{\frac{1}{2}} \tag{2.9}$$

$$IOA = 1 - \frac{\sum_{i=1}^{N}(P_i - O_i)^2}{\sum_{i=1}^{N}(|P_i - \bar{O}| + |O_i - \bar{O}|)} \tag{2.10}$$

where N is the number of samples, P_i represents the modeled value and O_i the measured value at a given time i, and the overbars denote the average for the corresponding period. Additionally, the so-called RMSE of the horizontal vector wind difference ($RMSE_V$) was calculated as:

$$RMSE_V = \left[\frac{1}{N}\sum_{i=1}^{N}\left(u_{p,i} - u_{o,i}\right)^2 + \left(v_{p,i} - v_{o,i}\right)^2\right]^{\frac{1}{2}} \quad (2.11)$$

where u and v are the wind vector components in x and y axes, respectively, and the subscripts p and o denoting modeled and observed values.

6. SVA energetic exchanges

Two methodologies were used to study land-atmosphere moisture and heat exchanges under sea breeze circulations and their influence on the formation, development and triggering of summer storms. On one hand, the energetic exchanges in the SVA system were analyzed with measurements and simulated parameters using the so-called mixing diagrams (Betts, 1984; Betts, 1992; Santanello et al., 2009). On the other hand, humidity and temperature changes in air masses displaced within the sea breeze were analyzed using time-varying trajectories extracted from the finest WRF simulation with VAPOR. The two approaches are described in the following subsections.

6.1. Mixing diagram approach

The mixing diagram approach was introduced by Betts (1992) and broadly used for intercomparing PBL schemes and LSMs in Santanello et al., (2009, 2011, 2013), as well as for the analysis of SVA feedbacks under different atmospheric conditions (Erlingis and Barros, 2014; Milovac et al., 2016; Santanello et al., 2019; Sun et al., 2020a; b), in a diurnal timescale. This method states that the diurnal boundary layer evolution, including PBL top entrainment rates, can be determined from surface heat and moisture fluxes and near-surface values of temperature and humidity in a perfectly mixed PBL. In this approach, no condensation occurs so that moisture fluxes contribute to increase the water vapor content of the atmosphere whereas heat fluxes tend to generate variations in air temperature. Thus, $C_p\theta$ (in the y axis, with θ the potential temperature) denotes temperature variations of the SVA system linked to sensible heat, whilst the specific latent heat content Lq is represented in the x axis. The variations in these two terms in the SVA system describe variations in the so-called moist static energy (*MSE*; Wallace and Hobbs, 2006) given as:

$$MSE = C_pT + gz + Lq \quad (2.12)$$

where the term *gz* represents the geopotential (*g* is the Earth's gravity acceleration and *z* the height above ground) and *T* the absolute air temperature. The *MSE* is a good indicator of the potential for near-surface heat and moisture to influence cloud formation and precipitation (Santanello et al., 2011), hence, mixing diagrams facilitate the interpretation and quantification of the land-atmosphere processes and feedbacks involved in the generation of summer storms throughout the representation of q and θ variations in energy space per unit mass, i.e., $C_p\theta$ versus Lq. In addition, mean heat and moisture fluxes can be disaggregated into three components representing surface, advection and entrainment as vectors for a given increment of time Δt.

The quantified contribution from the surface to the total mean flux within the PBL is represented by the surface vector $\vec{v}_{sfc}$ with the x and y components given by:

$$L\Delta q_{sfc} = \frac{\overline{LE}\Delta t}{\rho_{PBL}\overline{PBLH}} \tag{2.13}$$

$$C_p\Delta\theta_{sfc} = \frac{\overline{H}\Delta t}{\rho_{PBL}\overline{PBLH}} \tag{2.14}$$

where ρ_{PBL} is the PBL air density and the overbars indicate averaged values over Δt.

The advection at a location is not often negligible, hence an expression to quantify the advected part must be included to close the budget equation (Santanello et al., 2005). The x and y components of the advection vector $\vec{v}_{adv}$ are given by:

$$L\Delta q_{adv} = L\Delta t\left\{\left\langle \bar{u}\frac{\partial\bar{q}}{\partial x}\right\rangle + \left\langle \bar{v}\frac{\partial\bar{q}}{\partial y}\right\rangle\right\} \tag{2.15}$$

$$C_p\Delta\theta_{adv} = C_p\Delta t\left\{\left\langle \bar{u}\frac{\partial\bar{\theta}}{\partial x}\right\rangle + \left\langle \bar{v}\frac{\partial\bar{\theta}}{\partial y}\right\rangle\right\} \tag{2.16}$$

where the brackets represent averaged values within the PBL. The residual vector that connects $\vec{v}_{adv}$ with the final values Lq and $C_p\theta$ at final time t_{end} is called the entrainment vector $\vec{v}_{ent}$, in which the x and y components represent moisture and heat fluxes at the interface layer.

The thermodynamic properties of the SVA system can be analyzed by overlaying variables such as the equivalent potential temperature θ_e (as derived in De Ridder, 1997), which determines the potential for moist convection (analogous to *MSE*), and the relative humidity *RH* in mixing diagrams for a diurnal average of surface pressure $\bar{p}$

(Betts and Ball, 1995; Betts et al., 1996; Santanello et al., 2009; Santanello et al., 2011). These variables can be determined as:

$$RH = \frac{q}{q_s} \tag{2.17}$$

$$\theta_e = \left(T + \frac{L}{C_p} q\right)\left(\frac{p_0}{\bar{p}}\right)^{\frac{R_d}{C_p}} \tag{2.18}$$

where the q_s is temperature dependent, p_0 is the standard reference pressure and R_d is the gas constant for air. Regarding the definition of θ_e in Equation 2.18, this variable indicates the energy partitioning between humidity and temperature so that a q-θ evolution along isolines of θ_e (constant value) denotes a tendency to equilibrium between Lq and $C_p\theta$. For example, an increasing $C_p\theta$ (heating) along a θ_e isoline indicate that the corresponding Lq decrease (drying) balances the energy partitioning with a null change in the *MSE* of the SVA system denoted by θ_e. Furthermore, considering that $\vec{v}_{sfc}$, $\vec{v}_{adv}$ and $\vec{v}_{ent}$ are the three quantified contributions to Lq and $C_p\theta$ leading to energy variations in the SVA system, a constant θ_e with changing q and θ indicates a balance among surface, advection and entrainment contributions to *MSE*. Similarly, *RH* definition in Equation 2.17 states a partitioning between q and θ denoting the saturation degree of air.

Additionally, the Evaporative Fraction (*EF*) can be calculated as:

$$EF = \frac{LE}{LE + H} \tag{2.19}$$

so that the relevance of moisture fluxes in the SVA system can be quantified. Specifically, this definition has been extensively used in the analysis of energy partition over land surfaces (De Ridder et al., 1997; Dirmeyer et al., 2000; Gentine et al., 2006; Seneviratne et al., 2010; Santanello et al., 2011; 2015; 2018) and ranges between 0 and 1 denoting dry and freely evaporating surfaces, respectively. In this study, the *EF* is used to quantify differences among land use categories and locations with the output of the STM simulation.

In summary, mixing diagrams are useful to diagnose land-atmosphere level of coupling during daytime as total heat and moisture fluxes can be determined within the PBL, as well as the surface, advection and entrainment mean contributions to the total mean flux using the previously defined vectors. Specifically, the positive/negative values of

the x (Lq) and y ($C_p\theta$) components in $\vec{v}_{ent}$ denote a moist/dry and hot/cold air influx at the top of the PBL (from the free atmosphere or previous residual layers). Further information regarding mixing diagrams and vector calculation can be consulted in Santanello et al. (2009, 2011, 2013).

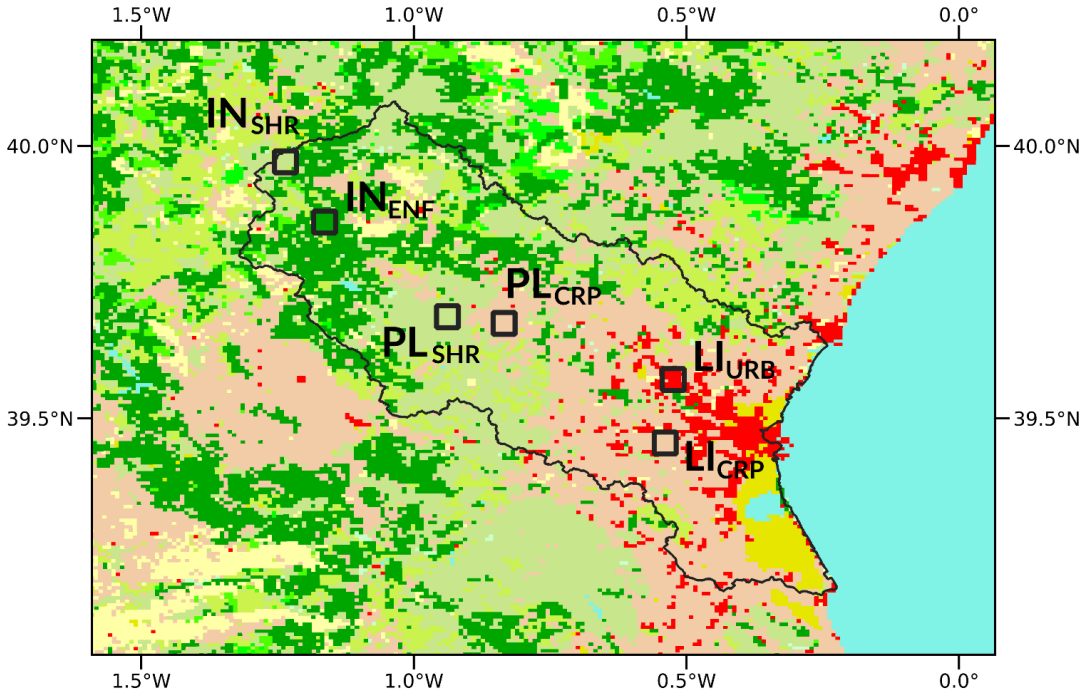

Figure 2.13 - Selected littoral (LI), pre-littoral (PL) and inland (IN) locations for the representation of mixing diagrams within the study area over the land-use category map defined in STM. The subscripts indicate the WRF land use dominant category of the model grid-point: urban (URB), crops/woodland mosaic (CRP), mixed shrubland/grassland (SHR) and evergreen needle-leaf forest (ENF). See Figure 2.3 for complete legend of land use categories.

In this work, mixing diagrams were generated using both observations and simulated variables. However, the corresponding vectors were only calculated with the model output since observed surface fluxes were not available at the study area. Mixing diagrams were generated with WRF data over selected model grid points regarding distance to sea, terrain height and land use categories in order to highlight the links between land-atmosphere energetic exchanges and land cover (Figure 2.13). Regarding land use, it was selected the middle grid point of a homogeneous area of at least 25 grid points (about 3 km^2) with the same dominating land use category according to the model. Besides, two periods for the calculation of vectors are selected: (1) before and

(2) after the arrival of an Intermediate Sea-Breeze Front (ISBF; see Section 4 in Chapter 4) to the given point. In the case that sea breeze winds were influenced by other meteorological phenomena (e.g., circulations due to the development of a storm), vectors were calculated before wind changes occur. Concretely, the selection of periods for vector calculation was conducted according to the homogeneous evolution of Lq and $C_p\theta$ so that two main periods of several hours could be identified and analyzed in detail.

6.2. Trajectories

In this methodology, an air parcel of height delimited by the PBLH is considered to represent the air mass that is displaced by the formation of the sea breeze. This air parcel moves forward modifying its features (e.g., temperature and humidity) according to the input from surface fluxes (moist and heat) and the entrainment effect as it interacts with the surrounding air. Hence, this approach provides the possibility to quantify surface contributions to moving air masses linked to the generation of convective clouds.

To this end, the VAPOR tool is used to extract time-varying backward and forward trajectories from (1) the convective clouds generated over the TRB according to WRF hourly output files and (2) at the ISBF when the displacement toward inland occurs, representing the air parcels that displace within the ISBF not always associated to the formation of storms. Specifically, the trajectories were calculated for the first trajectory (1) as:

- First, a box with a volume of at least 1x1x0.1 km was selected in a cloud and seeds (points) were evenly distributed within it with separations of 100 m horizontally and 10 m in the vertical).
- Then, unsteady (time-varying integration of flows) backward trajectories were computed from each seed using horizontal (u,v) and vertical wind vectors (w). Forward trajectories were also calculated to visualize air parcels displacement after the convective cloud generation.
- Finally, the centroid of the trajectories was selected and the corresponding series of points with a constant time increment Δt_k =18s and a varying distance Δl was extracted.

For the case of air parcels moving along with the ISBF (2), trajectories were obtained regarding whether late afternoon convective clouds formed due to the ISBF or not. In

the case convective clouds generated, the same procedure as for (1) was followed, otherwise:

- First, a box was situated 5 km behind the ISBF extending from the surface up to the PBLH, 1 km toward the coastline and 1 km parallel to the frontal line (i.e., the dimensions of the box were 1x1xPBLH in km).
- Analogously to the first trajectory, seeds were evenly distributed within the volume with separations of 100 m horizontally and 10 m vertically.
- Then, flows were integrated forward and backward (to ensure air parcels origin from the sea) in time from each seed using horizontal and vertical wind vectors (u, v and w).
- Finally, the centroid trajectory was selected as in the first case and the corresponding series of points extracted to an ASCII file.

Before the analysis, initial trajectory points were selected at 06 UTC for (1) and at the time the air parcel reached the coastline in the morning for (2) in order to filter out sea contributions. Considering the PBLH as the height of the air parcel, the final points to analyze were set at the time PBL *breaks*, i.e., a sudden PBLH decrease and/or convective cloud formation occurred. Afterwards, variables from the WRF hourly output were linearly interpolated to the trajectory points so that for a given trajectory point k, nearest to model grid point (i,j), and time t, between WRF output times t_0 and t_1, variable $q_{k,t}$ was computed, for instance, as:

$$q_{k,t} = (1 - \Delta t_{WRF}) q_{i,j,t_0} + \Delta t_{WRF} q_{i,j,t_1} \quad (2.20)$$

where $\Delta t = t - t_0$. Equation 2.20 was also applied to other meteorological and hydrological variables (e.g., E, H, $PBLH$ and θ, among others), as well as it was used to estimate values in the vertical of the trajectory (i.e., at each model level) to generate cross-section like plots and to calculate q and θ averages within the PBL.

Specifically, this methodology was used to quantify water vapor and heat contributions to the PBL, as well as the entrainment effect, similarly to the mixing diagram approach, but considering an air parcel of height $PBLH$ moving along the TRB. In other words, a well-mixed air parcel, characterized by q and θ averages within the PBL, was considered so that surface heat and moisture contributions, as well as the interaction with the surrounding air, changed the overall properties of the air parcel during Δt_k.

Hence, the contributions to q and θ from the surface to the air parcel over each trajectory point k were computed as:

$$\Delta q_{sfc,k} = 1000 \frac{E_k \Delta t_k}{\rho_{PBL,k} \overline{PBLH_k}} \tag{2.21}$$

$$\Delta \theta_{sfc,k} = \frac{H_k \Delta t_k}{c_p \rho_{PBL,k} \overline{PBLH_k}} \tag{2.22}$$

where the factor 1000 in Equation 2.21 is used to convert the units to $g \cdot kg^{-1}$ to simplify the interpretation of the results. The entrainment was calculated as:

$$\Delta q_{ent,k} = \Delta q_{PBL,k} - \Delta q_{sfc,k} \tag{2.23}$$

$$\Delta \theta_{ent,k} = \Delta \theta_{PBL,k} - \Delta \theta_{sfc,k} \tag{2.24}$$

where the subscript *sfc* indicates variations due to surface fluxes, *ent* the changes produce by the entrainment effect, calculated as the difference between the total increments (Δq_{PBL} and $\Delta \theta_{PBL}$) and the increment caused by surface fluxes, and the subscript *PBL* indicating the average in the PBL. In Equation 2.24 differences were calculated in terms of energy per unit mass (i.e., $C_p \Delta \theta$) although C_p cancels out so that it is not shown for simplicity. In this approach, it is important to notice that the entrainment effect (mixing with the surrounding air) was not only produced at the top of the air parcel but also at the front and at the lateral sides as it displaces forward. The importance of the total contribution of surface fluxes with respect to entrainment (i.e., surface to entrainment ratio) for q (SR_q) and θ (SR_θ) can be quantified as:

$$SR_q = \frac{\sum_{k=1}^{N_k} \Delta q_{sfc,k}}{\sum_{k=1}^{N_k} \Delta q_{ent,k}} \tag{2.25}$$

$$SR_\theta = \frac{\sum_{k=1}^{N_k} \Delta \theta_{sfc,k}}{\sum_{k=1}^{N_k} \Delta \theta_{ent,k}} \tag{2.26}$$

where N_k is the total number of trajectory points. Additionally, q and θ total contributions for each land use category with respect to trajectory length can be calculated as:

$$\overline{\Delta q_{sfc,c}} = \frac{\sum_{c=1}^{N_c} \Delta q_{sfc,c}}{\Delta L_c} \tag{2.27}$$

$$\overline{\Delta \theta_{sfc,c}} = \frac{\sum_{c=1}^{N_c} \Delta \theta_{sfc,c}}{\Delta L_c} \tag{2.28}$$

where c denotes the land use category, N_c the number of trajectory points over c, and ΔL_c the total distance traveled by the air parcel over c, i.e.:

$$\Delta L_c = \sum_{c=1}^{N_c} \Delta l_c \tag{2.29}$$

CHAPTER 3

SUMMER STORMS AND MODELING

In this chapter, the performance of the two LSMs implemented in the WRF model is analyzed using high-resolution simulations over eastern Spain. First, the period under study is introduced, along with the summer storms identified, with special focus on the atmospheric conditions during the four convective precipitation events detected in the period 15th - 23rd July 2015. Then, the two LSMs are compared regarding the representation of typical meteorological variables at the surface (wind, temperature and relative humidity), evapotranspiration and precipitation using the two simulations of the extended summer season (ESS) covering the period May-October 2015. Finally, the output of three additional 3-km horizontal resolution simulations of the study case implemented with different LSMs and SL schemes is analyzed in order to further compare the performance of the two selected LSMs.

1. Summer storms episodes in eastern Spain

1.1. May-October 2015

Summer storms are mainly observed during the period May-October, defined here as the extended summer season (ESS) since these are linked to sea breeze (Millán et al., 2015a; b), as well as other thermally driven circulations (e.g., upslope winds) over inland regions. Hence, the study year is selected regarding high number of precipitation days and accumulated precipitation observed during the ESS, and especially in summer (JJA).

The number of days with precipitation and accumulated precipitation over Hydrographic Confederation of the Jucar (CHJ) during ESS (see methodology in section 4 of Chapter 2) of the period 1988-2017 (30-year reference climatological period) are exposed in Figure 3.1. This figure shows similar precipitation days during ESS along the last three decades, despite the decreasing trend, and several maxima can be identified, especially for JJA. Focusing on the most recent years regarding the greatest number of observations and climatic reports available, three maxima are detected in the last decade (in 2010, 2013 and 2015) when only precipitation days for JJA are considered (Figure 3.1a). These peak values are also detected in accumulated precipitation during JJA (Figure 3.1b) so that 2010, 2013 and 2015 were contemplated as potentially interesting periods for this study. Then, based on monthly climatological reports from AEMET a more accurate analysis of precipitation during summer for the selected years was conducted. According to these reports and focusing on the CHJ, June and August were considered as wet and very wet months in 2010, respectively (AEMET, 2010a; c), whereas July was dry regarding climatological averages for the period 1981-2010 (AEMET, 2010b). Similarly, in 2013, July and August were wet and very wet, respectively (AEMET, 2013b; c), whilst June was a dry month (AEMET, 2013a). In contrast, June and July 2015 were very wet months (AEMET, 2015a; b) and August was wet (AEMET, 2015c). This suggests that more and/or heavier summer storms occurred during 2015 with a considerable number of them concentrated in July (AEMET, 2015b), which additionally reduces the modeling efforts planned in this work. In fact, following the methodology based on Millán et al. (2005b) and presented in Section 4 of Chapter 2, a total of 43 days with summer storm events are detected in 2015 over the CHJ, most of them (32) observed from June to August. The

characteristics of several of these episodes regarding synoptic conditions are presented in the following section for a more detailed analysis of the subperiod 15th to 23rd of July.

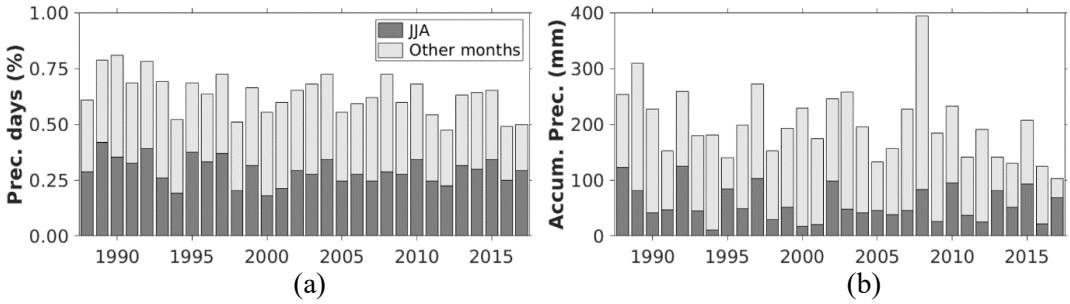

Figure 3.1 – For the period 1988-2017: (a) Relative precipitation days and (b) mean accumulated precipitation in the CHJ for the extended summer season (ESS) according to Spain02 dataset. Precipitation and precipitation days for summer (JJA) and the other months (May, September and October) are colored in dark and light gray, respectively.

Despite the identification of summer storms has been conducted within a specific area in eastern Spain (Figure 3.1), other regions of the Iberian Peninsula are also influenced by this type of events under these synoptic conditions. In fact, Spain02 total accumulated precipitation during the ESS in 2015 and accumulated precipitation due to the 43 days with summer storms occurrence highlight the importance of this precipitation type over eastern Spain (Figure 3.2). However, it must be noticed that a precipitation filter has been apply to the Spain02 data within the area selected to identify summer storms so that the development of summer storms generating precipitation outside the CHJ are not considered. This implies that the distribution of precipitation associated with summer storms over Spain (Figure 3.2, bottom) does not represent all events although it accurately remarks the main areas affected by summer storms regarding the synoptics yielding these events. Concretely, Figure 3.2 indicates that precipitation due to summer storms mainly occurs over mountain ranges where convergence of surface flows is observed (Millán, 2014). Moreover, summer storms provide considerable amounts of precipitation over the Pyrenees, the Iberian System and the Sub-Betic System (Figure 3.2, bottom); for example, the mountains nearest to the Mediterranean sea in the Iberian System within the CHJ (delimiting the upper part of the TRB, see Figure 2.1 in Chapter 2) show maximum accumulated precipitation amounts of about 300 mm due to summer storms which represent more than a 50 % of the total accumulated precipitation (about 500 mm) during ESS 2015 (Figure 3.2). This fact remarks the key role that summer storms play in the water supply over the

headwaters of the Mediterranean basin in eastern Spain, and especially over the TRB, in accordance with previous studies (Millán et al, 2005a; b; Miró e al, 2018).

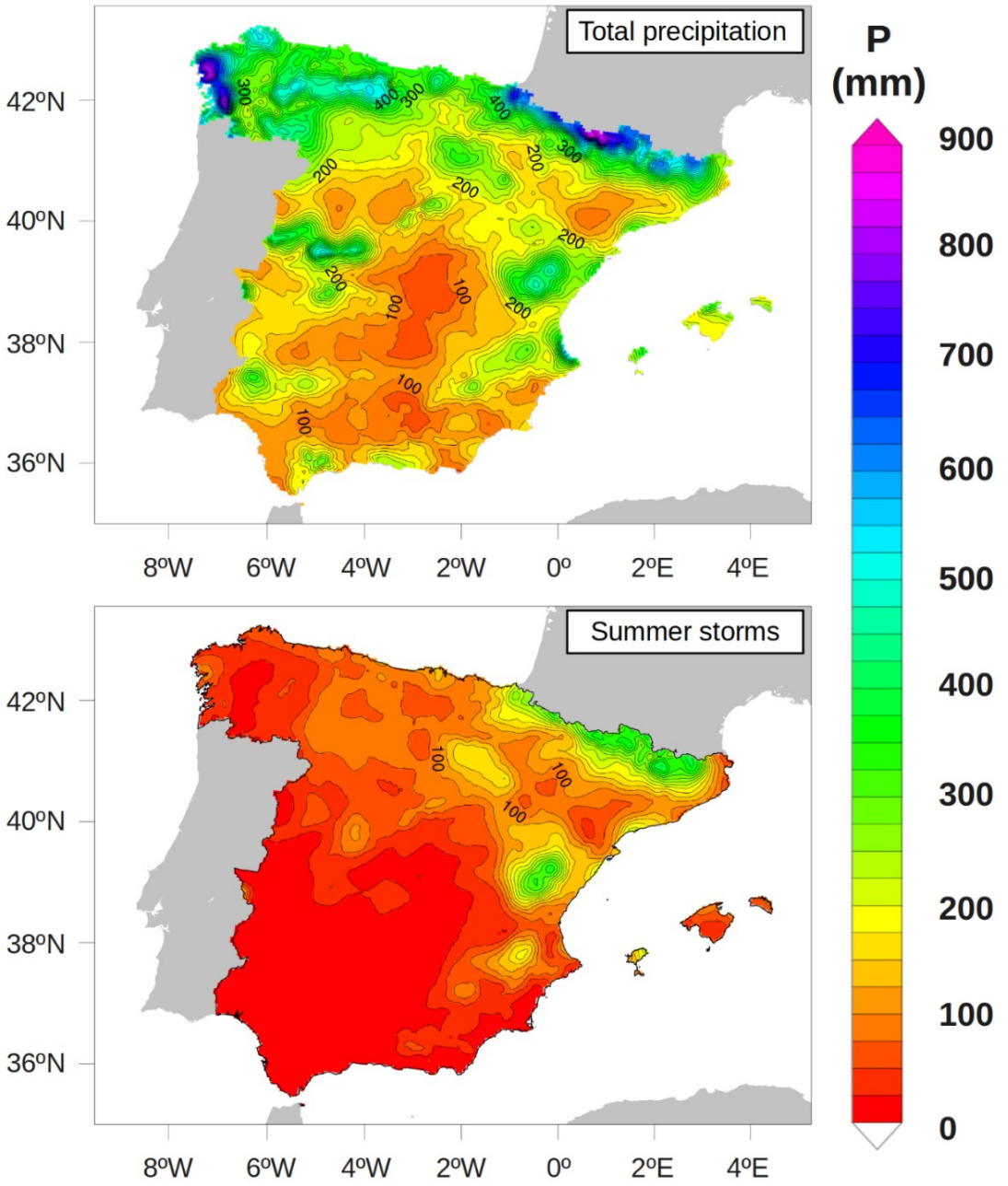

Figure 3.2 – Total (top) and summer storms (bottom) accumulated precipitation during the period May-October 2015 over Spain according to Spain02 dataset.

1.2. Case study

Several summer storm episodes over the TRB were selected to be further investigated regarding the precipitation amounts that these provide in general. In the following paragraphs, the events occurring between the 15th and 23rd of July are described regarding synoptic circulations, with special focus on the Iberian Peninsula, to remark

the peculiarities of each convective precipitation event. Two main features regarding large-scale circulations are considered to conduct the description of these events: the formation of the Iberian Thermal Low (ITL) and the presence of cold air at 500hPa, in accordance with Millán et al. (2005b). Particularly, most days within the period from the 15th to the 23rd of July 2015 were characterized by the presence of cold air in upper levels of the atmosphere leading to recurrent summer storms producing precipitation over inland and pre-littoral areas in the Valencia region. In addition, the presence of cold air aloft yielded generalized convective precipitation for some days that reached the coast as well.

1.2.1. Event 1: 16th of July

A ridge at upper levels extended over the Western Mediterranean at the beginning of the second week of July 2015 (Figure 3.3a). These synoptic conditions favor a situation of stability over the IP, i.e., strong insolation and the corresponding temperature increase at the surface, which also yielded the formation of the ITL (Figure 3.3a).The same atmospheric conditions prevailed the following day, leading to the formation of the thermal low over the IP, although the ridge was slightly displaced by a weak trough moving from the Atlantic Ocean toward the Mediterranean, with an associated low-pressure system at the surface over the west coast of the United Kingdom (Figure 3.3b). During both the 15th and the 16th, weak synoptic conditions favor the formation of local thermally driven winds such as upslope winds and sea breeze that forced surface air to be injected to upper atmospheric levels at the convergence zones. These surface conditions together with the large-scale circulations, that favored the advection of cold air at 500hPa over the IP, led to the development of summer storms over the mountain ranges, mainly over the Iberian and the Sub-Betic Systems (Figure 3.4). However, the earlier formation of summer storms the 16th (at about 13 UTC) than the 15th (at about 17 UTC) shown in Figure 3.4 is probably linked to the colder air mass (-12 ºC at 500hPa) that extended over the IP during the second day in comparison to the 15th (Figure 3.3), among other flow differences at surface levels. Besides, temperature differences at 500hPa between the two days are also the main factor influencing the greater development of the convective systems during the 16th, yielding more abundant and generalized precipitation along the Spanish Mediterranean coast. During both days, summer storms moved toward the coast, as well as showed a displacement toward the

northeast as these developed in the vertical (Figure 3.4), in accordance with the dominating southeastern synoptic flow at 500hPa (Figure 3.3).

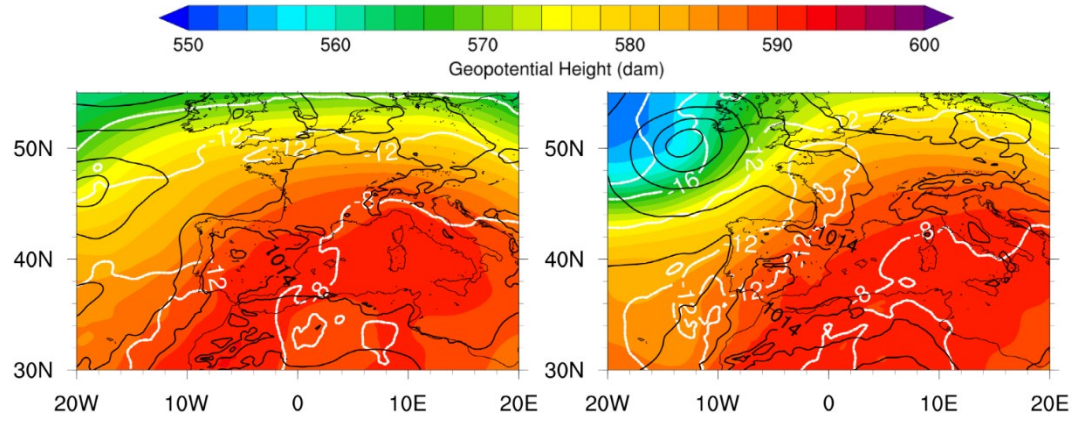

Figure 3.3 – Synoptic conditions, i.e., geopotential height (colormap) and temperature at 500hPa (white lines), and mean sea level pressure (black lines) for the (a) 15th of July at 15 UTC and (b) 16th of July 2015 at 12 UTC obtained from ERA5 product. Low- and high-pressure systems are indicated as L and H, respectively.

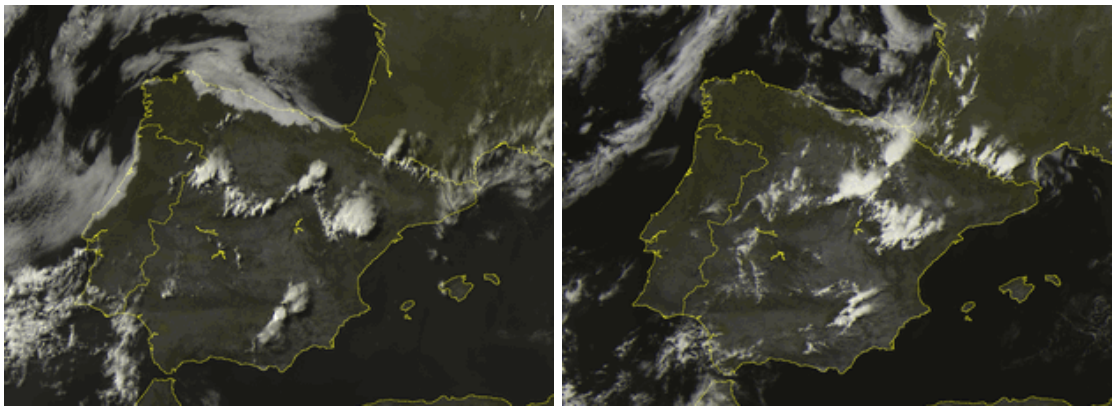

Figure 3.4 - Meteosat cloud over images for the (a) 15th of July a 17 UTC and (b) 16th of July at 12 UTC. © Sat24.com/Eumetsat/Met Office

1.2.2. Event 2: 18th of July

The ridge at upper levels situated over the IP at the beginning of the second week of July displaced toward the Eastern Mediterranean as the trough weakened and slowly crossed the northern part of the IP from west to east (Figure 3.5). Concretely, the trough was situated over southwestern areas of the IP the 17th and reached eastern Spain the 18th in the afternoon, so that more unstable conditions at upper atmospheric levels were

found over the IP than the previous days (Figure 3.5). At the surface, the Azores High was located at southern Atlantic Ocean and relatively high pressures extended over the Western Mediterranean indicating stable atmospheric conditions (Figure 3.5). Besides, a weak thermal low generated due to the lower insolation over southern IP during the 17th (Figure 3.6a), although the trough at the southwest enhanced the deepening of the ITL at surface levels (Figure 3.5a). In contrast, the insolation over the IP during 18th was greater than the 17th since no clouds covered land areas enhancing the generation of the ITL (Figure 3.6b), further intensified by low relative instability at upper levels (Figure 3.5b). The absence of clouds in eastern Spain during both days favored the formation of dominating upslope winds and sea breeze circulations over the Mediterranean basins implying the injection of surface layers to upper atmospheric levels (Figure 3.6a). Under these synoptic conditions, the convergence of surface flows at the mountain ranges driven by upslope winds and sea breeze favored the formation of convective clouds over the Iberian System (Figure 3.5). Additionally, the relative unstable conditions at middle tropospheric levels enhanced the development of convective storms, especially the 18th of July when the cold air aloft displaced toward the Mediterranean coast (Figure 3.6b). The 17th main precipitation occurred outside the TRB boundaries with low accumulated amounts in northern areas of the TRB, whereas the 18th convective clouds generated over most mountain ranges of the Valencia region with generalized precipitation (Figure 3.6b). Convective systems moved from inland areas toward the coast at surface levels, whereas the upper-level synoptic flows forced a displacement toward northeast at 500hPa.

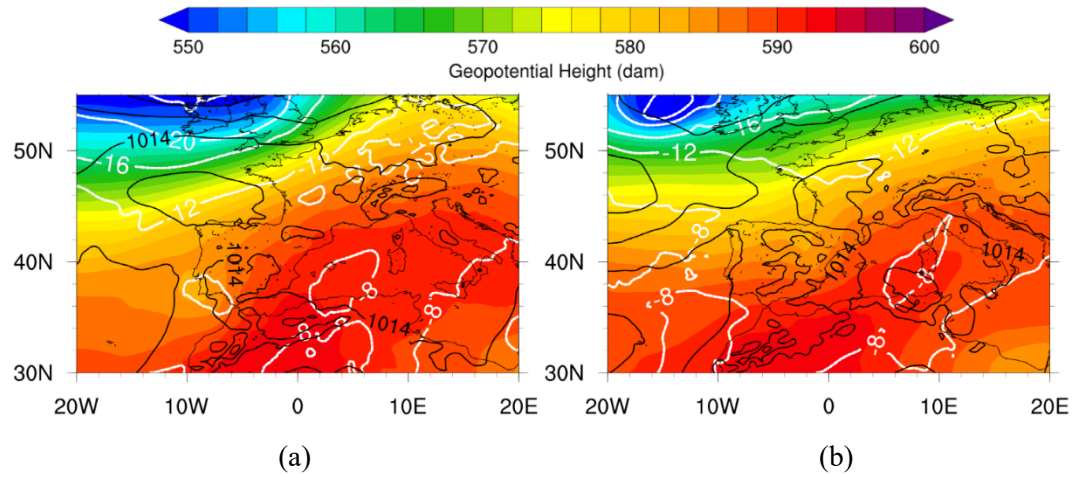

Figure 3.5 - Same as Figure 3.3 but for the (a) 17th of July at 16 UTC and (b) 18th of July at 17 UTC.

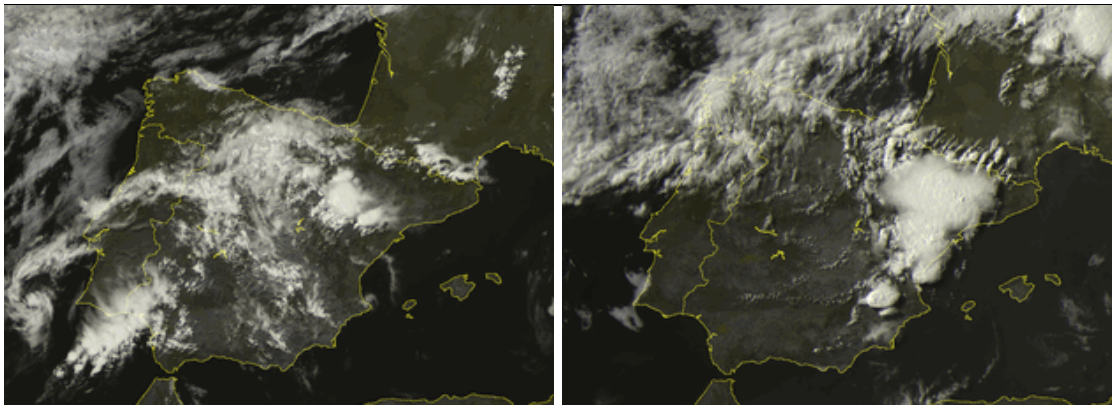

(a) (b)

Figure 3.6 - Meteosat cloud cover images for the (a) 17th of July a 14 UTC and (b) 18th of July at 17 UTC. © Sat24.com/Eumetsat/Met Office

1.2.3. Event 3: 21st of July

In the middle and upper levels of the atmosphere, the trough displaced further east the 19th, it narrowed the 20th and then detached from the general flow the 21st so that a pool of cold air aloft remained over the eastern coast of Italy (Figure 3.7). These synoptic dynamics favored the formation of a ridge over the IP in the period between the 19th and 21st although cold air at 500hPa remained over eastern Spain (Figure 3.7). At the surface, relative high pressures extended from the Atlantic Ocean to Central Europe indicating stable atmospheric conditions which favored the formation of the ITL during this period (Figure 3.7), as well as the formation of sea breeze along the Mediterranean coast, especially the 20th and 21st.

Concretely, morning clouds were observed during the 19th reducing insolation over the Spanish Mediterranean coast and leading to the later (at about 17 UTC) formation of a less intense sea breeze than previous days (Figure 3.8a), although the thermal low formed over the IP (Figure 3.7a). Sea breeze circulations advected moist marine air toward inland areas throughout the valleys that were injected to upper atmospheric levels at the convergence zones and yield the formation of localized summer storms (Figure 3.8a). Convective clouds showed the usual displacement from inland to the coast at the surface, whilst it moved toward the east at 500hPa regarding synoptic flows (Figure 3.7a). The 20th, the absence of clouds facilitated the earlier formation of the ITL and thermally driven winds (upslope winds and sea breeze), as well as the pool of cold air aloft further extended over the IP (Figure 3.7b). This situation led to localized convective initiation over the Iberian and Sub-Betic Systems at about 14 UTC (Figure

3.8b). However, convective systems were short-lived and showed no displacement toward coastal areas (Figure 3.8b) linked to the weak or absent upper-level synoptic flows (Figure 3.7b). In contrast, the ridge weakened the 21st which produced slightly greater unstable atmospheric conditions over the IP with northeasterly winds at 500hPa (Figure 3.7c). As for the previous days, clear sky conditions dominated (Figure 3.8c) so that the ITL formed along with local thermally driven winds enhancing the convergence of surface flows at the mountain ranges (Figure 3.7c). These atmospheric dynamics led to the formation of summer storms over the Iberian System and the Pyrenees in easter Spain (Figure 3.8c). Besides, storms development was intensified by the presence of cold air aloft which produced generalized precipitation over the upper part of the TRB (Figure 3.7c).

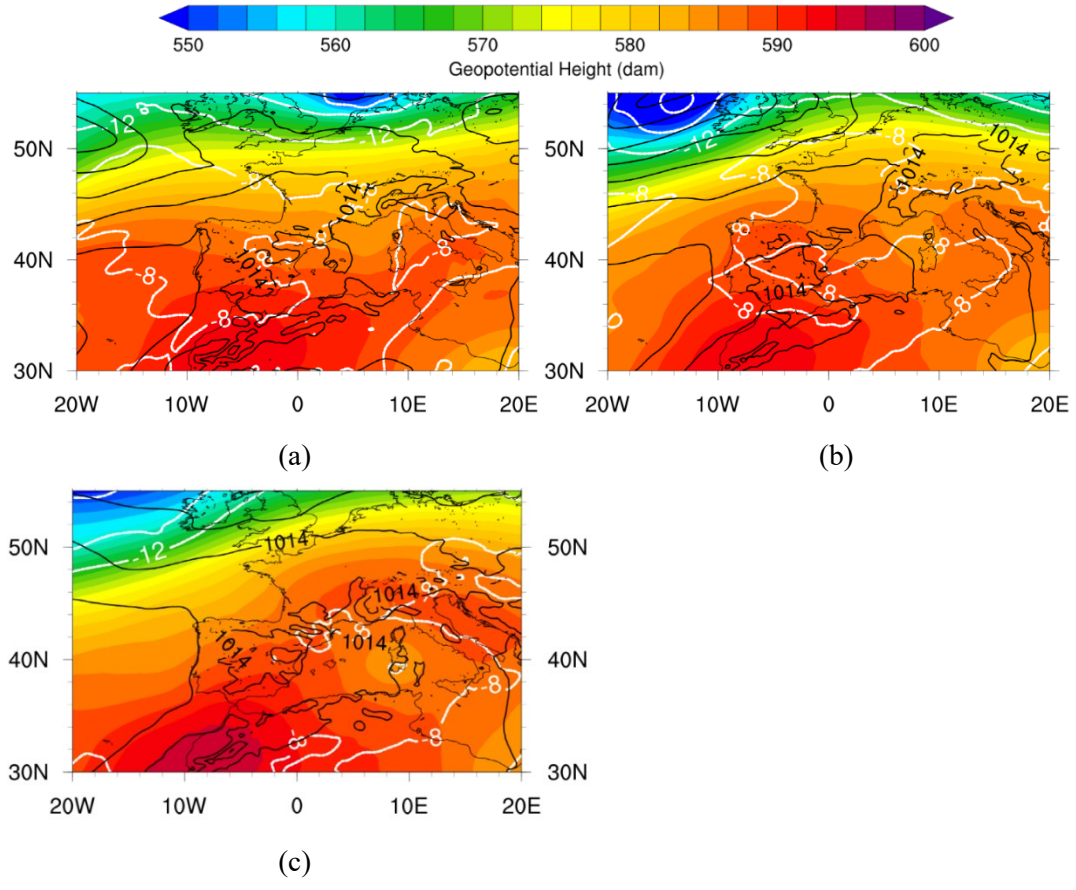

Figure 3.7 – Same as Figure 3.3 but for the (a) 19th of July at 17 UTC, (b) 20th of July at 13 UTC and (c) 21st of July at 13 UTC.

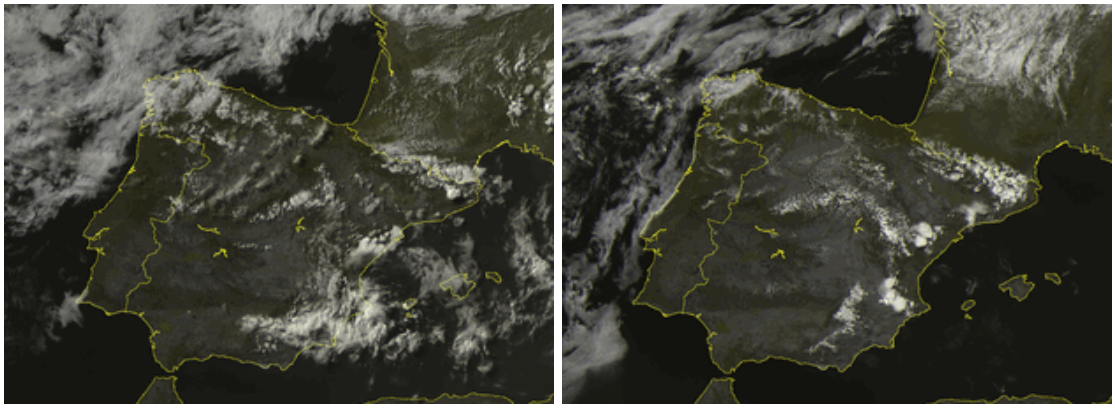

(a) (b)

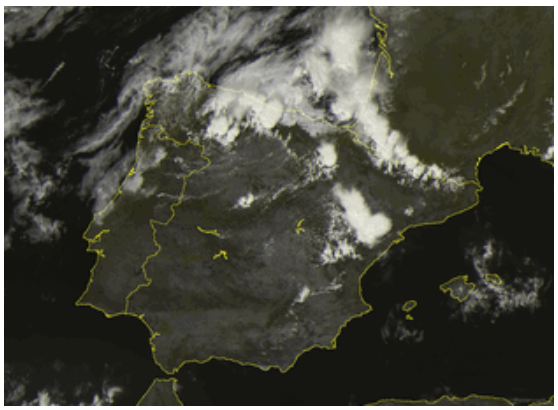

(c)

Figure 3.8 - Meteosat cloud cover images for the (a) 19th of July at 17 UTC, (b) 20th of July at 14 UTC and (c) 21st of July at 13 UTC. © Sat24.com/Eumetsat/Met Office

1.2.4. Event 4: 22nd of July

In general, the same atmospheric conditions during the period between the 19th and 21st of July 2015 were observed the following two days (the 22nd and 23rd) with high pressures covering a large area from the Atlantic Ocean to Central Europe favoring the formation of the thermal low over the IP (Figure 3.9), as well as upslope winds sea breeze. However, the ridge further weakened the 22nd so that cooler air in the upper atmosphere (less than -8 ºC at 500hPa) covered the IP generating relatively unstable conditions (Figure 3.9). This fact, along with the convergence of surface flows at mountain ranges led to the formation, development and triggering of summer storms localized over the Iberian and Sub-Betic Systems in eastern Spain (Figure 3.10a). These convective systems presented a wide circular anvil, indicating the weak upper-level synoptic flows, and displaced toward coastal areas along the valleys producing generalized precipitation, especially in the Valencia region (Figure 3.10a). The following day, instability at upper atmospheric levels decreased, although cold air was

still present at 500hPa, and clear-sky conditions yielded the formation of the ITL and local thermally driven circulations at the surface (Figure 3.9b). Hence, analogously to the 22nd, the injection of surface air to upper atmospheric levels at the convergence zones led to the generation of summer storms over the Iberian and Sub-Betic Systems (Figure 3.10b). In this case, summer storms were short-lived and localized with respect to those originated the 22nd regarding the more stable atmospheric conditions (Figure 3.9b). However, it must be noticed that initial wet atmospheric conditions and enhanced moisture fluxes at the surface may have had further influenced the generation of summer storms during the 23rd, considering the generalized precipitation occurred the previous day over the Valencia region.

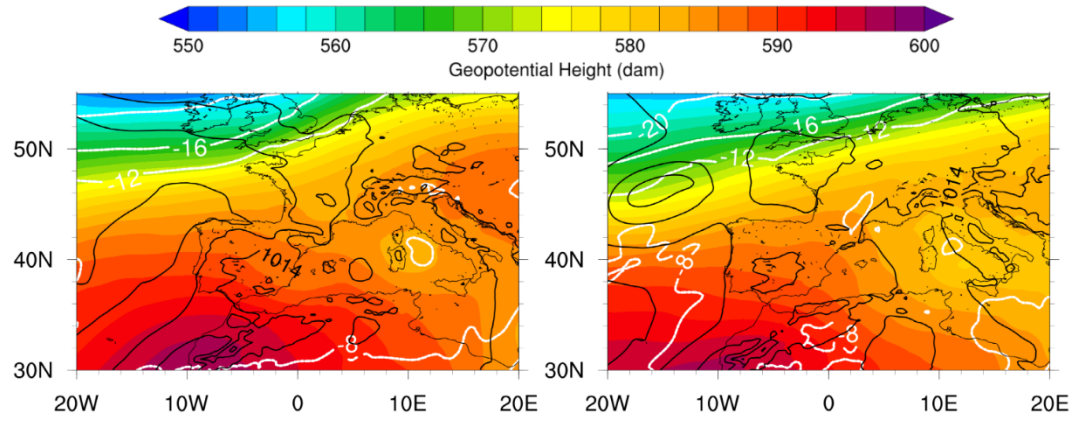

Figure 3.9 - Same as Figure 3.2 but for the (a) 22nd of July at 15 UTC and (b) 23rd of July at 12 UTC.

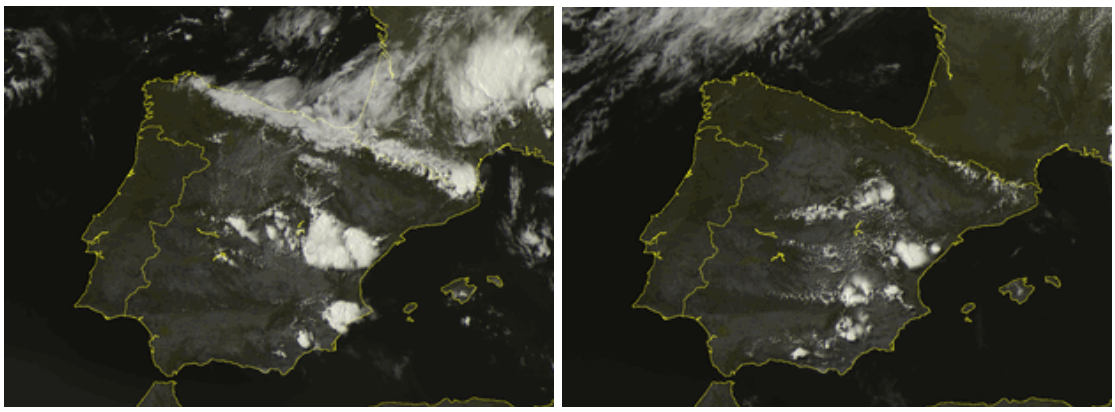

Figure 3.10 - Meteosat cloud cover images for the (a) 22nd of July a 15 UTC and (b) 23rd of July at 15 UTC. © Sat24.com/Eumetsat/Met Office

2. ESS simulations

The WRF model was used to reproduce the atmospheric conditions over the Valencia region during the period May-October 2015 exposed in the previous section with two different parametrizations of surface processes defined as ESS-PX and ESS-NoahMP (see section 5 in chapter 2). The quality of these two high-resolution (1 km) simulations was evaluated in this section regarding hydrometeorological variables that play a key role in the generation of summer storms along the Mediterranean coast. The two ESS simulations were initially evaluated against observations from different sources such in situ measurements (CEAM, XVVCCA and GNSS networks), satellite observations (MODIS and CMORPH) and model estimates (HYDROBAL) over the Valencia region (see Chapter 2).

2.1. Statistical analysis

Initially, the performance of the two WRF simulations was assessed throughout the calculation of statistical scores and uncertainties following the methodology introduced in section 5 of Chapter 2. In general, the IOA scores obtained for the study period indicate that variations of temperature and relative humidity at 2 m above ground were accurately represented in both simulations (IOA scores greater than 0.75) although RMSE and MBE values denote slightly greater inconsistencies for the ESS-NoahMP regarding temperature (Table 3.1). In addition, MBE denotes a low warm bias for ESS-PX in contrast with the cold bias obtained for ESS-NoahMP (temperature difference of 1 ºC between simulations), whereas relative humidity was slightly underestimated in both runs (negative MBE) as shown in Table 3.1. Besides, the RMSE of 19 % indicates that humidity values presented greater discrepancies with respect to observations in the two simulations (Table 3.1). Overall, these statistical scores indicate that the difference in the surface fluxes parametrization between the LSMs leaded to an overall air overheating in ESS-PX, whilst the contrary effect occurred in ESS-NoahMP, despite the generally well-reproduced atmospheric conditions (temperature and humidity) near the surface. Oppositely, the statistical scores for the wind vector are considerably lower than those obtained for the other two variables denoting a less accurate modeling of air flow variations at 10 m above ground (Table 3.1). Nevertheless, wind vector IOA values are about 0.60 with similar discrepancies regarding observations since both simulations generated more intense winds (MBEs of about 1 ms^{-1}) and present RMSE and $RMSE_V$ of about 2 ms^{-1} and 3 ms^{-1}, respectively, on average (Table 3.1). Overall, these values

indicate that wind speeds were slightly overestimated, i.e., stronger atmospheric dynamics at the surface than observed.

Table 3.1 - Statistical scores (IOA, RMSE, $RMSE_V$ and MBE) for ESS-NoahMP and ESS-PX using all data available from meteorological stations during all period (*All*) and days with summer storms (*Stm*).

		Wind (ms^{-1})				Temp. (ºC)			RH (%)		
	SIM	IOA	RMSE	MBE	$RMSE_V$	IOA	RMSE	MBE	IOA	RMSE	MBE
All	ESS-NoahMP	0.59	2.4	0.9	3.2	0.92	3.2	-0.7	**0.77**	19	**-1**
	ESS-PX	**0.60**	**2.3**	**0.8**	**3.1**	0.92	**3.0**	**0.5**	0.76	19	-2
Stm	ESS-NoahMP	0.55	2.3	1.0	3.2	0.90	3.2	-0.6	**0.74**	**19**	**-1**
	ESS-PX	**0.57**	**2.2**	1.0	**3.1**	0.90	**3.0**	**0.4**	0.73	20	-4

An accurate parametrization of surface fluxes is crucial to reproduce summer storms since these are usually linked to weak synoptic conditions. Hence, the same statistics were calculated for the identified days with summer storm occurrence during the simulated period. These statistical scores indicate that both simulations presented slightly greater difficulties in reproducing temperature, humidity and wind variations according to the obtained IOA values (Table 3.1). However, temperature variations were still accurately represented with IOA values of 0.90, as well as humidity showing IOA scores greater than 0.70 (Table 3.1). Wind variations were less accurately reproduced in the model regarding the IOA scores below 0.60 in this case, although errors (RMSE, $RMSE_V$ and MBE) show a very low increase, this occurs for temperature and humidity as well (Table 3.1). Wind statistics obtained for days with summer storms show that both simulations overestimated wind intensities about 1 ms^{-1}, which denotes more intense sea breeze flows along the coast of the Valencia region regarding the sea breeze dominating conditions. This fact may lead to the corresponding overdrawn injection of moist air to upper levels of the atmosphere at the convergence zones influencing summer storm triggering and precipitation intensity. However, other factors such as the dry biases obtained for both configurations indicate an overall underestimation of humidity that may reduce condensation at convergence zones (less water vapor advected toward inland areas). Besides, errors of in situ measurements (e.g., 3-5 %, 0.5 ºC and 0.5 ms^{-1} for humidity, temperature and wind speed, respectively) must

be also considered so that model estimates could be even greater or lower than observed values.

2.2. Precipitation

Summer storms were mainly detected during summer months (June-August) for the ESS in 2015, as indicated in Section 1 of this chapter, so that CMORPH satellite product (considering precipitation over land and sea) and Spain02 dataset (considering only precipitation over land) were used to conduct an initial evaluation of the monthly mean distribution of precipitation in the WRF model within the VR domain (see Figure 2.11 in Chapter 2). At a first glance, ESS-NoahMP significantly underestimates total monthly precipitation during July and September in comparison to CMORPH and Spain02 (Figure 3.11a; b), more than a 50 % over land. In contrast, ESS-PX shows a more accurate representation of monthly mean precipitation over the VR domain in general, except for October when it abruptly overestimates mean precipitation. In addition, discrepancies between ESS-NoahMP and CMORPH remain when only days with summer storm occurrence were considered (Figure 3.11c), whereas monthly precipitation associated with summer storms is more accurately captured during September in the comparison with Spain02 (Figure 3.11d). In contrast, model inconsistencies during August increase for summer storms precipitation, whereas they decrease during October due to the low precipitation contribution of summer storms during this month (Figure 3.11c; d). Besides, it can be noticed that summer storms contribution represents an important part of the total accumulated precipitation during July (almost 100 %) despite the very low precipitation amounts, which remarks the slightly more accurate representation of monthly precipitation in the ESS-PX compared to the ESS-NoahMP over the VR domain.

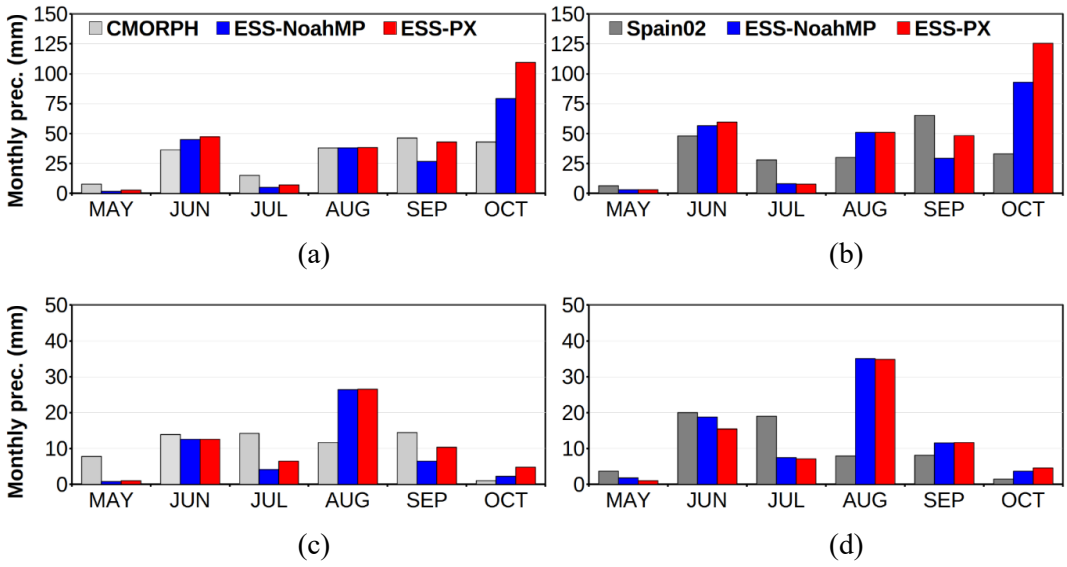

Figure 3.11 - Spatially averaged monthly precipitation over domain VR (see Figure 2.11 in Chapter 2) from ESS-NoahMP (in blue), ESS-PX (in red), and (a,c) CMORPH (in light gray) and (b,d) Spain02 (in dark gray) during the period 21st of May to 31st of October considering (a,b) all days and (c,d) days with summer storms.

Apart from temporal distribution of precipitation associated with summer storm events, the Spain02 dataset (the product with higher spatial resolution) denotes a specific area within the VR domain where summer storm precipitation dominates in comparison to other areas (Figure 3.12a). According to this product, an area where summer storms provide important amounts of precipitation can be defined so that the model performance can be evaluated in detail. This is conducted by setting a threshold of 5 $mm \cdot day^{-1}$ for the days with summer storm occurrence so that the area denoted by the black line in Figure 3.12a is obtained. In general, the calculation of the probability density function (PDF) within this area indicates that both simulations tend to overestimate precipitation intensity (Figure 3.12b). Concretely, the number of summer storms reproduced in the model with intensities less than 30 $mm \cdot day^{-1}$ is lower than those in Spain02, whilst the contrary occurs for the number of summer storms with intensities greater than this value (Figure 3.12b). Besides, ESS-NoahMP produced slightly heavier summer storm events than Spain02 and ESS-PX, reaching intensities up to 80 $mm \cdot day^{-1}$ (Figure 3.12b).

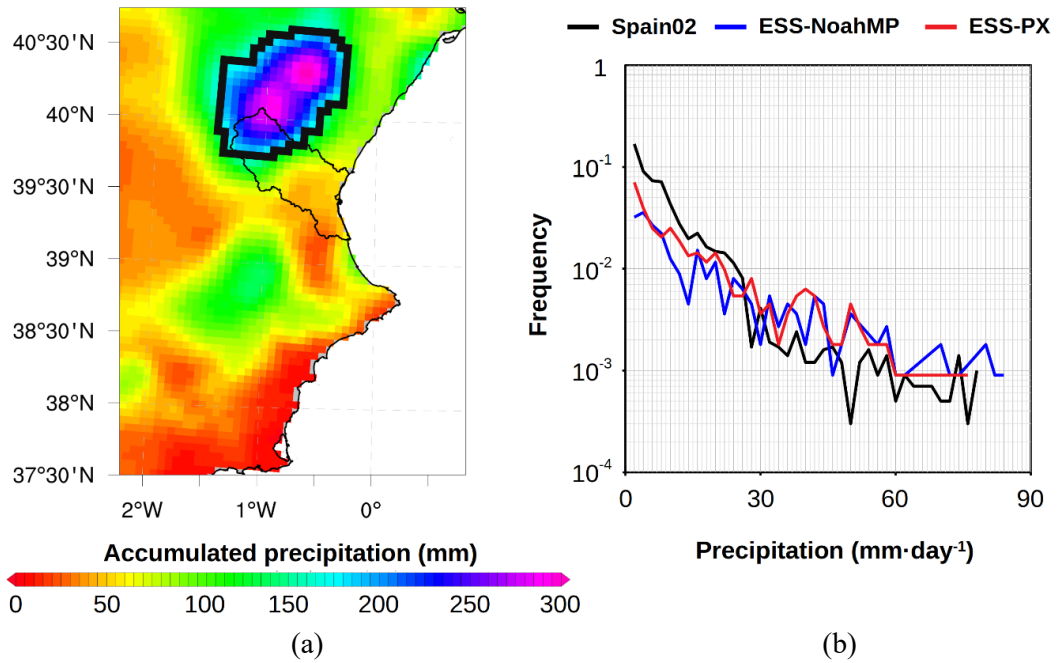

Figure 3.12 - (a) Spain02 total accumulated precipitation over land for the days with summer storm events within the period 21st of May to 31st of October 2015 in the Valencia region. The Spain02 grid points with the heaviest summer storms (mean intensity greater than 5 mm·day^{-1}) are indicated by the black line. (b) The corresponding probability density functions (PDFs) for Spain02 (in black) ESS-NoahMP (in blue) and ESS-PX (in red) within the area highlighted in (a).

Despite the slight differences between the two simulations highlighted previously, maximum accumulated values associated with summer storms within the period May-October 2015 within the highlighted area in Figure 3.12a are significantly overestimated regarding Spain02 accumulated precipitation. Specifically, accumulated precipitation reaches up to 551 mm in ESS-PX and 472 mm in ESS-NoahMP compared to the 324 mm observed in Spain02. Despite the influence of rain gauge measurements interpolation on the reduction of the observed precipitation maxima (Quintana-Seguí et al., 2017), as well as spatial resolution differences, ESS-PX local precipitation maxima indicate an important inconsistency regarding the simulation of summer storm events. In addition, both WRF simulations denote considerable accumulated precipitation amounts over large areas in the northern part of the domain which are not depicted in Spain02 further increasing precipitation excess, i.e., leading to precipitation accumulated averages over the VR domain of 148 mm and 176 mm for ESS-NoahMP and ESS-PX (reprojected to Spain02 5-km grid), respectively, in contrast with the 89 mm obtained for Spain02.

These significant differences in precipitation between the two simulations remark the important role that the parametrization of surface processes play in the generation of summer storms in the Valencia region, as well as the need to further investigate the surface impact on the formation of these convective systems.

2.3. Evapotranspiration

The comparison of ESS-NoahMP and ESS-PX simulations regarding moisture fluxes at the surface with MOD16A2 estimates over the study area, covering the period between the 26th of May and the 25th of October, provide valuable information about WRF representation of *E*. On one hand, spatial averages of *E* within the study area indicate that both simulations reproduced correctly mean moisture fluxes, with values of 1.4 mm·day^{-1} for ESS-NoahMP and 1.2 mm·day^{-1} for ESS-PX, in comparison to the 1.2 mm·day^{-1} obtained from MODIS. However, important differences can be noticed with respect to the spatial distribution of *E*. According to Figure 3.13, MOD16A2 indicates that greatest water vapor contribution to the atmosphere occurred near the coast, especially in the Albufera of Valencia reaching values of *E* up to 4.4 mm/day. Oppositely, both simulations generated greatest moisture fluxes over northern inland areas with maximum *E* values of 1.8 and 2.8 mm·day^{-1} for ESS-NoahMP and ESS-PX, respectively, in contrast with the range 1.5-2.0 mm observed in MOD16A2 (Figure 3.13). This fact is mainly related to the land use distribution within the study area based on USGS land cover dataset (see Figure 2.3 in Chapter 2), e.g., the Albufera of Valencia was considered as forest or croplands, whilst it mainly consists of rice fields which provide important amounts of water vapor to the atmosphere (Figure 3.13). Another significant difference between modeled surface moisture fluxes and MOD16A2 estimates is observed over the city of Valencia and its metropolitan area, which was not accurately represented in the WRF model, i.e., the model represented a smaller urban area. This induced inconsistencies in the representation of *E* values near the coast, i.e., moisture fluxes at the surface were overestimated in both simulations over the city of Valencia (Figure 3.13). In addition, an important difference between the two simulations arose from the fact that PX LSM considered a non-zero water vapor contribution from urban areas in contrast to the zero-contribution hardcoded in the Noah-MP LSM for this land use category, leading to differences regarding minimum moisture fluxes (0.6 mm·day^{-1} for ESS-PX). Besides, the ESS-PX simulation showed important moisture fluxes in the northernmost part of the study area around the

Javalambre mountains (see Figure 2.1 in Chapter 2), where this simulation also showed greater accumulated precipitation associated with summer storms compared to ESS-NoahMP, as commented in the previous subsection.

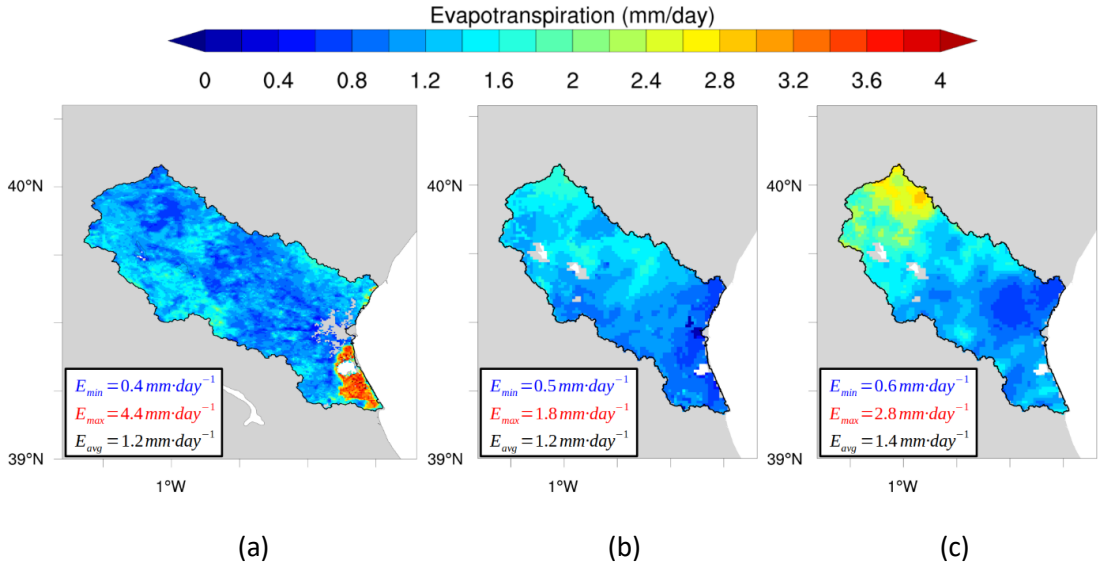

Figure 3.13 - Daily temporal average of the period 26/05/2015 - 25/10/2015 obtained for (a) MOD16A2, (b) ESS-NoahMP and (c) ESS-PX.

On the other hand, the analysis of the temporal evolution of *E* (8-day composite) over the study area showed similar variations for both simulations, in the range 0.7-2.3 mm·day^{-1}, although these are generally greater than MOD16A2 estimates, from 1.0 to 1.6 mm·day^{-1} (Figure 3.14). Besides, on average, both simulations present a RMSE of 0.5 mm·day^{-1}, as well as MBE values are close to zero (-0.1 and 0.2 mm·day^{-1} for ESS-NoahMP and ESS-PX, respectively). However, *E* temporal variations regarding 8-day averages were more abrupt for ESS-PX in comparison with the ESS-NoahMP regarding standard deviations (Figure 3.14). Greatest discrepancies were found during the period from the 19th of June to the 5th of July with biases between 0.7 and 1.0 mm·day^{-1} between the two simulations and MOD16A2, as well as the 14th of August with an overestimated peak value of 2.3 mm·day^{-1} in ESS-PX. Also, the last month of the study period (October) ESS-PX overestimated *E* (up to 0.6 mm·day^{-1}), whereas ESS-NoahMP estimates were below observed values (between -0.5 and -0.6 mm·day^{-1}) according to Figure 3.14.

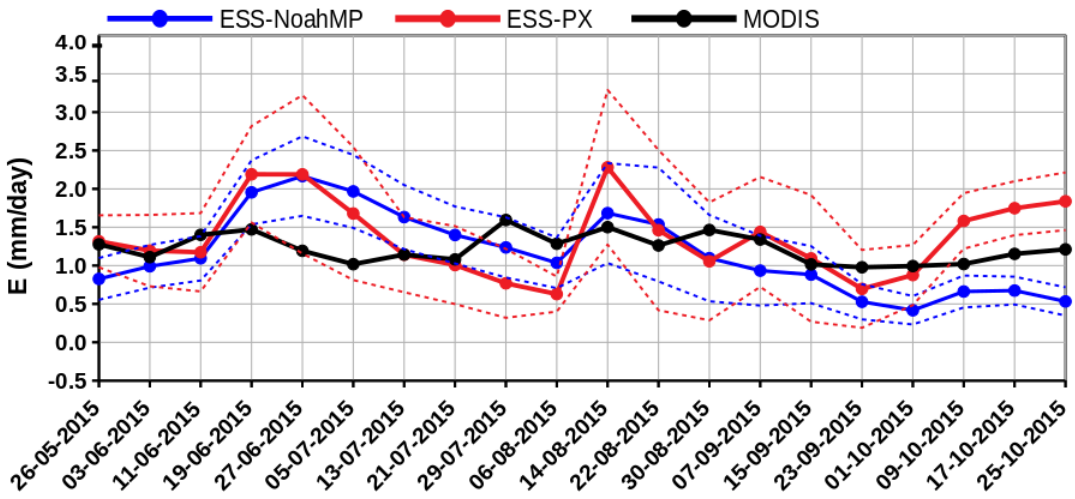

Figure 3.14 - Temporal evolution of *E* spatial averages over the study area for MODIS (black line), ESS-NoahMP (blue line) and ESS-PX (red line). The temporal standard deviation with respect to the 8-day averages are denoted by the blue and red dashed line for ESS-NoahMP and ESS-PX, respectively.

These results indicate that the WRF model with the two considered LSMs presented a tendency to punctually overestimate *E* regarding spatial averages within the study area. These inconsistencies are in agreement with the generally overestimated precipitation obtained in the previous analysis (see Section 2.2 of this chapter). Thus, regarding the dependence of surface moisture fluxes on soil moisture (with precipitation the main source of water) in the study area, *E* inconsistencies between MOD16A2 and both simulations were mainly related to precipitation temporal and spatial discrepancies.

Analogously, the temporal evolution of modeled *E* from the two simulations was compared to HYDROBAL estimates over the specific field plots implemented along the study area using the corresponding modeled parameters from WRF as input for the HYDROBAL model (see section 5 of Chapter 2) so that precipitation inconsistencies were not considered in the comparison. In this context, statistical scores indicate that ESS-PX represented more accurately *E* variations (greater IOA scores) over VM_{FP} than ESS-NoahMP, whereas the opposite was obtained at the inland site $AR_{FP,}$ although ESS-PX also captured *E* variations accurately at this site (Table 3.2). However, RMSE and MBE scores show greater inconsistencies at AR_{FP} with values ranging from 0.9-1.2 mm·day^{-1} and 0.6-0.9 mm·day^{-1} (overestimate), respectively, whereas MBE values are slightly lower over VM_{PF}, 0.4-0.5 mm·day^{-1} (Table 3.2). Overall, both simulations captured *E* variations accurately with a slight difference over the site located near the coast where the ESS-PX showed a better performance.

Table 3.2 - Statistical scores (IOA, RMSE and MBE) for *E* (in mm·day^{-1}) at the two locations (AR_{FP}, and VM_{FP}) for ESS-NoahMP and ESS-PX using HYDROBAL-NoahMP and HYDROBAL-PX as the corresponding references, respectively.

	AR_{FP}			**VM_{FP}**		
SIM	**IOA**	**RMSE**	**MBE**	**IOA**	**RMSE**	**MBE**
ESS-NoahMP	**0.78**	**0.9**	**0.6**	0.63	**0.8**	0.5
ESS-PX	0.76	1.2	0.9	**0.76**	**0.8**	**0.4**

Despite the generally well-represented *E* evolution over the instrumented sites, time series of *E* over VM_{PF} and AR_{PF} show that the ESS-NoahMP overestimated moisture fluxes at the surface the first half of the study period (from the 25th of May to 9th of August), although peak values were well-captured (Figure 3.14). Besides, the last half of the period ESS-NoahMP simulated values were similar to HYDROBAL-NoahMP estimates at VM_{PF}, although *E* was underestimated the last two weeks of October at both sites (Figure 3.15). Similarly, ESS-PX overestimated moisture fluxes with a strong sensibility to precipitation although it generally captured accurately the occurrence of peak values and the following decrease in *E* compared to HYDROBAL-PX estimates (Figure 3.16). The strong *E* variations due to precipitation leaded to punctual overestimated moisture fluxes up to 4 mm·day^{-1}, even the days with light precipitation such as the 31st of July at VM_{PF} (Figure 3.16). These results are probably related to PX LSM superficial soil layer of 1 cm, as well as its more realistic soil depth (1 m) in contrast to Noah-MP (more complex LSM) soil depths of 2 m (see Table 2.1 in Chapter 2), regarding the sites considered.

Overall, both LSMs present a tendency to overestimate surface moisture fluxes, especially over inland areas, although ESS-NoahMP simulated more accurately *E* variations and maxima over the inland site where simulated precipitation events were more intense as well. Instead, ESS-PX tends to overestimate peak moisture fluxes due to precipitation with a better representation of *E* evolution at VM_{FP} than ESS-NoahMP.

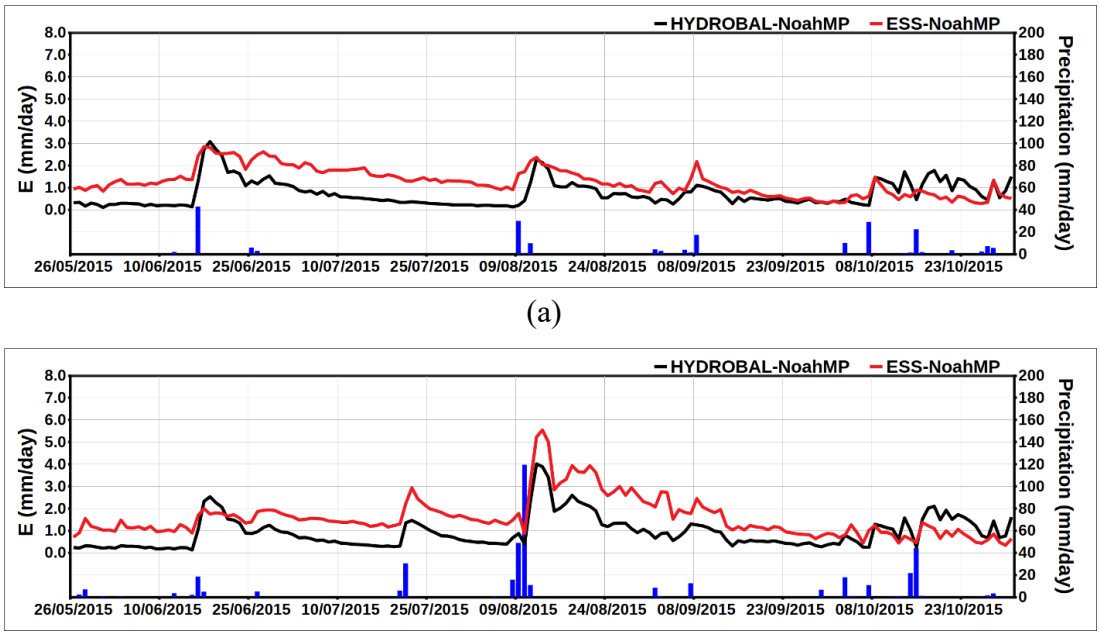

(a)

(b)

Figure 3.15 - Temporal evolution of *E* obtained from HYDROBAL-NoahMP (black line) and ESS-NoahMP (red line), together with simulated precipitation in ESS-NoahMP (bar chart), at (a) VM_{PF} and (b) AR_{FP}.

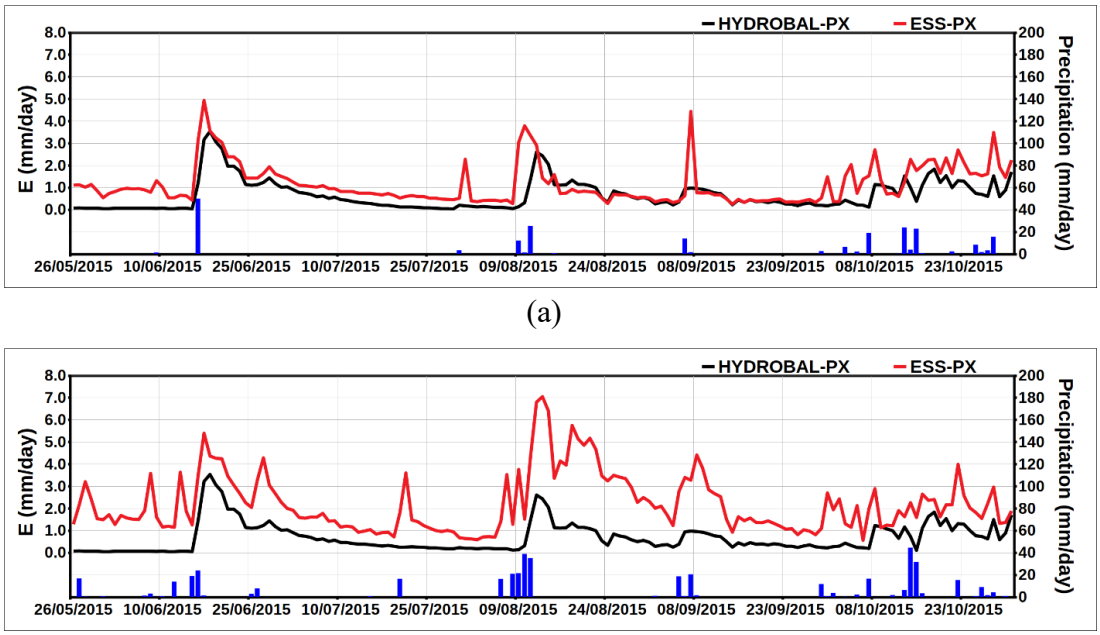

(a)

(b)

Figure 3.16 - Same as Figure 3.15 but for HYDROBAL-PX and ESS-PX.

3. Comparative analysis

Following the general analysis of ESS simulations, the three simulations of the case study covering the period from the 15th to 23rd of July 2015 (see Section 1 of this chapter) at a horizontal resolution of 3 km was conducted with special focus over the TRB domain (see Figure 2.12 in Chapter 2). Similarly to the previous section, the outputs from the simulations (PX-PX, PX-NoahMP and MM5-NoahMP) were compared to observations, focusing on in-situ measurements and precipitation from CMORPH. In this analysis, Spain02 product is not used since it is mainly intended to conduct climatological studies (Peral et al., 2017). This comparison facilitated the performance assessment of the WRF model with the different implemented parametrizations, as well as the selection of the most accurate representation of the summer storms episode for a next high-resolution simulation (see Section 3 in Chapter 4). It must be noticed that the SL scheme implemented together with the Noah-MP LSM in WRF only performs the calculation of exchange coefficients over water body categories (see Table 2.1 in Chapter 2) so that main differences between MM5-NoahMP and PX-NoahMP were generated due to SL schemes energetic exchanges between sea (and lakes) and the atmosphere. The comparison between these two configurations allows to analyze the accuracy of the SL parametrization in coupling with the Noah-MP LSM over water bodies and its influence in the model performance.

3.1. Statistical analysis

Overall, the statistical analysis with all observations available from CEAM, IVIA-SIAR and XVVCCA networks described in Section 3.3 of Chapter 2 and within the domain for the STM simulation (see Figure 2.12 in Chapter 2) at a horizontal resolution of 3 km indicate generally low differences among the three simulations according to statistical scores shown in Table 3.3. The three simulations present good IOA scores for temperature and relative humidity at 2 m above ground (greater than 0.90 and 0.80, respectively), with slightly greater values obtained in the PX-PX (Table 3.3). This is also observed when data is evaluated separately for daytime (05-19 UTC) and nighttime (19-05 UTC), as well as for the analysis regarding the location of meteorological stations (littoral, pre-littoral or inland), especially for 2-m temperature with IOA values up to 0.96 over pre-littoral areas (Table 3.3). However, main inconsistencies in reproducing relative humidity and temperature variations at 2 m above ground were obtained during nighttime showing the lowest values, especially for the simulations

using the Noah-MP LSM. In fact, this parametrization of surface processes presents IOA values below 0.80 for 2-m temperature and 0.70 for 2-m relative humidity (Table 3.3). Despite these differences in the representation of 2-m temperature variations, all simulations present similar values of RMSE and MBE ranging between 1.7 and 3.0 ºC, and between -1.0 and 1.0 ºC, respectively (Table 3.3). Maximum RMSE values (ranging from 2.5 to 3.0 ºC) are obtained over inland stations, and greatest MBEs of about 1 ºC (warm bias) are obtained over pre-littoral stations at nighttime, in contrast with MBEs of -1 ºC (cold bias) occurring over inland stations during daytime, only for Noah-MP simulations (Table 3.3). Analogously, relative humidity variations show the same behavior with RMSE values in the 10-16 % range and a generally dry bias (mainly negative MBE values) ranging from -8 % to 2 % as indicated in Table 3.3. In general, temperature and relative humidity were more accurately reproduced over the TRB when the PX-PX configuration was implemented in the WRF model, whilst the other two parametrizations with the Noah-MP LSM showed the same inconsistencies with respect to observations.

Oppositely, wind variations were better reproduced in the MM5-NoahMP simulation in general, except for littoral stations in which the configuration PX-NoahMP shows slightly greater IOA scores and lower errors than the other two parametrizations (Table 3.3). However, IOA values are generally lower than those obtained for 2-m temperature and relative humidity (below 0.70), except for littoral and pre-littoral stations during daytime (05-19 UTC), in the latter group of stations exceeding IOAs of 0.80 (Table 3.3). In contrast, nighttime IOA values are about 0.50 which indicates the lower accuracy of all simulations in capturing wind features between 19 and 05 UTC (Table 3.3). Although the low differences among the scores obtained for wind in the three simulations, these indicate that wind features were more accurately reproduced when the Noah-MP LSM was implemented in WRF, especially when it was used along with the MM5 SL (this is not observed for 2-m temperature and relative humidity).

Table 3.3 - Statistical scores Index Of Agreement (IOA), Root Mean Squared Error (RMSE), Mean Bias Error (MBE) and Root-Mean-Squared Vector Wind Difference Error ($RMSE_V$) computed using N number of values within the study area. Calculations were carried out using all data available but also regarding stations' location (inland, pre-littoral or littoral) and Day (from 05 UTC to 19 UTC) or Night (from 19 UTC to 05 UTC of the following day). The best statistical scores among simulations (PX-PX, PX-NoahMP and MM5-NoahMP) are highlighted in bold numbers.

			Wind (ms^{-1})					Temp. (ºC)				RH (%)			
			IOA	**RMSE**	**MBE**	**$RMSE_V$**	**N**	**IOA**	**RMSE**	**MBE**	**N**	**IOA**	**RMSE**	**MBE**	**N**
MM5-NoahMP	All	All	**0.67**	**1.9**	**1.1**	**2.5**	3653	0.90	**2.6**	**-0.1**	4219	0.83	**14**	-3	4461
		Day	0.69	**1.8**	**1.1**	**2.4**	2014	0.84	**2.9**	-0.9	2326	0.82	**13**	**-3**	2482
		Night	**0.56**	**2.2**	1.2	**2.6**	1639	0.78	2.5	-0.3	1893	0.68	16	**-1**	1979
	Inland	All	**0.61**	**2.0**	**1.0**	2.7	2538	0.88	2.8	-0.9	3108	0.81	15	**-1**	3358
		Day	**0.65**	**1.9**	**1.1**	**2.6**	1473	0.81	3.0	-1.0	1713	**0.81**	**13**	**-3**	1869
		Night	**0.53**	**2.2**	0.9	2.8	1065	0.76	2.7	-0.7	1395	0.69	16	1	1489
	Pre-littoral	All	0.81	**1.3**	**0.7**	**1.9**	533	0.95	2.1	**0.2**	561	0.84	15	-5	561
		Day	**0.85**	**1.1**	**0.5**	**1.7**	303	0.94	2.1	-0.5	307	0.78	14	-2	307
		Night	0.58	**1.5**	**1.0**	2.1	254	0.85	**2.1**	**1.0**	230	0.70	16	-7	254
	Littoral	All	0.73	1.5	1.1	2.1	1035	0.92	1.8	-0.2	1415	0.82	11	2	1395
		Day	0.74	**1.5**	1.1	2.1	595	0.83	**1.9**	-0.2	780	0.76	11	1	780
		Night	0.50	1.5	1.0	2.0	440	0.79	1.7	-0.3	635	0.66	12	5	614
PX-NoahMP	All	All	0.66	2.0	**1.1**	**2.5**	3653	0.90	2.7	-0.6	4219	0.83	15	-3	4461
		Day	0.69	**1.8**	**1.1**	**2.4**	2014	0.84	**2.9**	-0.9	2326	0.82	**13**	**-3**	2482
		Night	0.55	**2.2**	**1.1**	**2.6**	1639	0.78	2.6	-0.3	1893	0.67	16	-2	1979
	Inland	All	**0.61**	2.1	2.2	**2.6**	2538	0.88	2.8	-0.9	3108	0.81	15	-2	3358
		Day	**0.65**	2.0	2.2	**2.6**	1473	0.81	3.0	-1.0	1713	**0.81**	**13**	**-3**	1869
		Night	0.52	**2.2**	**0.7**	**2.7**	1065	0.76	2.7	-0.7	1395	0.69	16	1	1489
	Pre-littoral	All	0.81	1.4	0.8	2.0	533	**0.96**	2.1	**0.2**	561	0.84	15	-5	561
		Day	0.83	1.2	0.6	1.9	303	0.94	2.1	-0.5	307	0.79	13	-2	307
		Night	0.60	**1.5**	1.1	2.1	230	**0.86**	**2.1**	**1.0**	254	0.70	16	-8	254
	Littoral	All	**0.77**	**1.4**	**0.9**	**1.9**	1035	0.92	1.8	-0.3	1415	0.83	11	2	1394
		Day	**0.76**	**1.5**	**1.0**	**2.0**	595	0.83	1.9	-0.2	780	0.76	**10**	1	780
		Night	0.53	**1.3**	**0.6**	**1.7**	440	0.78	1.7	-0.4	635	0.69	12	5	614
PX-PX	All	All	0.65	2.1	1.2	2.6	3653	**0.91**	2.7	-0.3	4219	**0.84**	**14**	-3	4461
		Day	0.69	2.0	1.2	2.6	2014	**0.85**	3.0	**-0.4**	2326	0.82	14	-4	2482
		Night	0.52	2.3	**1.1**	2.7	1639	**0.82**	**2.4**	**-0.1**	1893	**0.73**	**15**	-2	1979
	Inland	All	0.60	2.2	1.1	2.8	2538	**0.89**	2.8	**-0.4**	3108	**0.82**	15	-3	3358
		Day	0.64	2.1	1.2	2.8	1473	**0.82**	3.0	**-0.5**	1713	0.80	14	-5	1869
		Night	0.48	2.4	0.9	2.9	1065	**0.79**	**2.5**	**-0.4**	1395	**0.74**	**15**	-1	1489
	Pre-littoral	All	0.81	1.4	0.9	2.0	533	**0.96**	2.1	0.4	561	**0.87**	**14**	**-3**	561
		Day	0.83	1.3	0.7	1.9	303	**0.95**	**1.9**	**-0.2**	307	**0.85**	**12**	**-1**	307
		Night	**0.63**	1.6	1.1	2.1	230	0.85	2.2	1.1	254	**0.72**	16	**-6**	254
	Littoral	All	0.73	1.6	1.1	2.1	1035	0.92	1.8	**0.1**	1415	**0.85**	**10**	**1**	1394
		Day	0.72	1.8	1.3	2.2	595	**0.84**	2.0	0.2	780	**0.79**	**10**	-1	780
		Night	**0.55**	1.4	0.8	1.9	440	**0.81**	1.7	**-0.1**	635	**0.72**	**10**	**4**	614

Table 3.4 - Statistical scores for TPW (in cm) with highest scores highlighted in bold.

SIM	*All*			*Day*			*Night*		
	IOA	**RMSE**	**MBE**	**IOA**	**RMSE**	**MBE**	**IOA**	**RMSE**	**MBE**
MM5-NoahMP	**0.78**	**0.6**	**0.1**	**0.78**	**0.6**	**0.1**	**0.77**	**0.7**	0.2
PX-NoahMP	0.77	**0.6**	**0.1**	**0.78**	**0.6**	**0.1**	**0.77**	**0.7**	**0.1**
PX-PX	0.75	**0.6**	0.2	0.76	**0.6**	**0.1**	0.75	**0.7**	0.2

In a similar manner to temperature and relative humidity variations exposed previously, the differences between the SL schemes implemented with the Noah-MP LSM show no differences in the statistical analysis for the TPW with all observations available from the GNSS network (Table 3.4). However, differences are noticed in the IOA values for the PX-PX simulation showing a slightly less accurate representation of TPW average variations with respect to the other two simulations, despite the generally high IOA values greater than 0.75 (Table 3.4). These values contrast with the generally better representation of relative humidity at 2 m above ground for PX-PX obtained in the analysis with meteorological stations suggesting slightly greater humidity inconsistencies at upper atmospheric levels for the PX LSM configuration than for those using the Noah-MP LSM. Besides, it must be noticed that the integrated water vapor is independent of temperature whereas the relative humidity presents a dependence on temperature which may lead to a better representation of this variable regarding the very good modeled 2-m temperature in the PX-PX parametrization (Table 3.3), and the corresponding less accurate representation of water vapor amounts in the atmosphere than the Noah-MP LSM simulations.

The differences between the two simulations implemented with the Noah-MP LSM are very low, e.g., IOA of 0.77 and 0.78 for PX-NoahMP and MM5-NaohMP. However, the amount of water vapor in the atmospheric column is crucial in the generation of precipitation so that slight differences in TPW representation can be determinant in the occurrence and/or intensity of a summer storm.

3.2. Precipitation

Daily precipitation is evaluated for the period from the 15th to the 23rd of July 2015 over the STM domain (see Figure 2.12 in Chapter 2), as conducted in the previous statistical analyses, using CMORPH satellite product as reference precipitation. At a first glance, the summer storm event with low mean daily precipitation within the STM domain occurred the 15th is not represented in any of the three simulations (Figure 3.17).

Similarly, convective precipitation in the TRB occurring the 20th is only reproduced in the MM5-NoahMP simulation with an overestimation of mean precipitation, whilst the other parametrizations using the PX SL produce no precipitation over the domain (Figure 3.17). The following day, the 21st of July, CMORPH indicates mean precipitation values exceeding 2 mm·day^{-1}, whereas WRF simulations show low mean precipitation (less than 0.3 mm·day^{-1}), especially simulations implemented with the PX SL scheme (Figure 3.17).

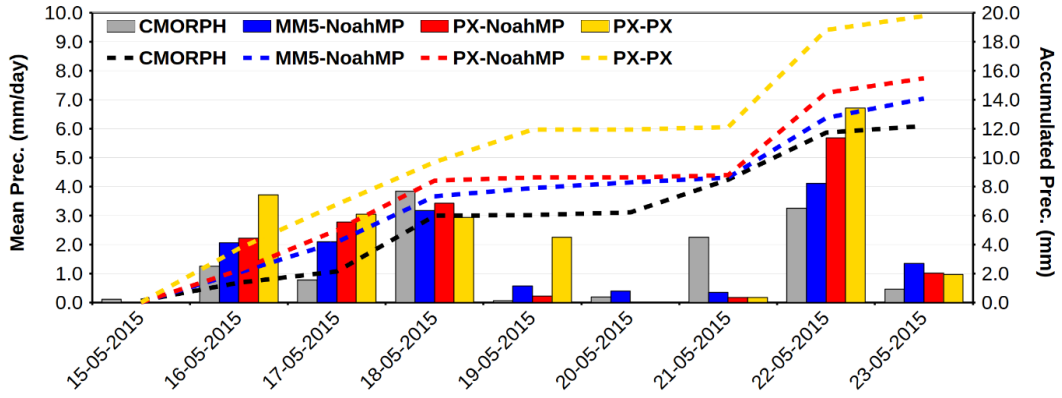

Figure 3.17 - CMORPH (gray), MM5-NoahMP (blue), PX-NoahMP (red) and PX-PX (yellow) daily precipitation spatially averaged over the STM domain (Figure 2.12), along with the corresponding cumulative sum (dashed lines).

Oppositely, the rest of days WRF simulations reproduce mean precipitation at a daily scale although significant differences among simulations, as well as model inconsistencies, are detected. First, overall mean precipitation is considerably overestimated (up to 4 mm·day^{-1} the 22nd) for the PX-PX simulation whereas the ones implemented with the Noah-MP LSM present closer values to CMORPH, especially MM5-NoahMP (Figure 3.17). The other days, MM5-NoahMP shows the most accurate representation of simulated precipitation with respect to the other two simulations using the PX SL scheme, although it tends to overestimate mean precipitation within the STM domain up to 1 mm·day^{-1} the 17th of July (Figure 3.17). In fact, mean precipitation is overestimated in WRF simulations except for the 18th, as well as the previously commented situation on the 21st. The well-simulated mean precipitation on the 18th of July may be linked to a relatively stronger synoptic circulations than the other studied events (see Section 1.2 of this chapter), i.e., the WRF model reproduces accurately synoptic conditions so that precipitation events influenced by large-scale circulations

tend to be well-captured. The ability of the WRF model in reproducing large-scale circulations in the Mediterranean region is also associated with the accuracy of the ERA5 product, used in the initialization and boundary update of the outermost domain (see Section 5.1 in Chapter 2), in reproducing the state of the atmosphere at large scales (Gevorgyan, 2018; Dunzenli et al., 2021; Molina et al., 2021).

Regarding the total accumulated mean precipitation in the STM domain, the MM5-NoahMP parametrization captured precipitation amounts accurately compared to CMORPH, despite mean precipitation inconsistencies at a daily scale. In fact, MM5-NoahMP presents a slight overestimate of about 2 mm, in contrast to overestimated accumulations of about 4 mm and 8 mm obtained for PX-NoahMP and PX-PX simulations, respectively (Figure 3.17). These results indicate that the influence of the SL scheme is crucial in the representation of precipitation associated with summer storms, even when it only computes exchange coefficients over sea and lakes. In combination with the Noah-MP LSM, the MM5 SL scheme shows a better performance compared to the PX SL regarding the considered summer storm events.

CHAPTER 4

LAND USE INFLUENCE IN SUMMER STORMS

In this chapter, the energetic exchanges between land and atmosphere are investigated under situations of dominating sea breeze circulation using both observations and WRF high-resolution simulations. First, the sea breeze is characterized during JJA for a period of 10 years using observations in the study area and mixing diagrams are analyzed to identify main SBC features and differences among land use categories. Then, q and θ variations are investigated for the case study (15th - 23rd July 2015) using a high-resolution simulation, as well as surface moisture and heat contributions to the atmosphere are quantified with the mixing diagram approach. Finally, an additional calculation of contributions to q and θ from the surface is conducted along the time-varying trajectories extracted with the VAPOR program. This last analysis is also performed regarding land use categories along the trajectories.

1. Sea breeze classification

An initial identification of days with sea breeze formation was performed following the methodology presented in Chapter 2 section 4. The features of the sea breeze were studied over the meteorological towers PA (littoral), VI (pre-littoral) and AR (inland) from the CEAM network located at about 15, 50 and 100 km from the coastline (Chapter 2 section 3.3, Table 2.2).

First, wind roses were generated using all the available wind measurements within the period 2005-2015 over each station to perform an initial analysis of winds. As shown in Figure 4.1, PA and VI are more influenced by orography than AR regarding their location in the Turia valley. Generally, sea breeze presents a wider range of variation regarding wind direction at the coastline and then it is channeled through the Turia valley as indicated in the wind roses over PA and VI (Figure 4.1a). This situation is also given under dominating easterly winds, as well as light downslope winds at nighttime, which are channeled through the valley toward the sea (Figure 4.1a). Instead, inland areas such as AR, at about 1200 m asl and where wind confluence occurs, a wider range of wind directions is obtained denoting two situations: the first with dominating sea breeze circulations along the Turia valley (southwesterly winds) and the second with dominating *ponents* (easterly to southerly winds) as indicated in Figure 4.1b. According to this, two main dominant winds/modes can be distinguished over all stations: easterly and westerly winds, especially over PA and VI. Specifically, easterly winds frequency shows very clear peaks over both PA and VI locations blowing from the sea. In PA, wind direction variations are within the range 45-135º, and wind speeds reach up to 6 ms^{-1}, whilst in VI, winds range between 90 and 180º with peak velocities up to 7 ms^{-1} (Figure 4.1a). The occurrence of easterly winds in AR, mainly associated with sea breeze circulations, is not as high as over PA and VI; however, a peak frequency is observed between 90º and 225º with wind speeds exceeding 9 ms^{-1}, approximately (Figure 4.1b).

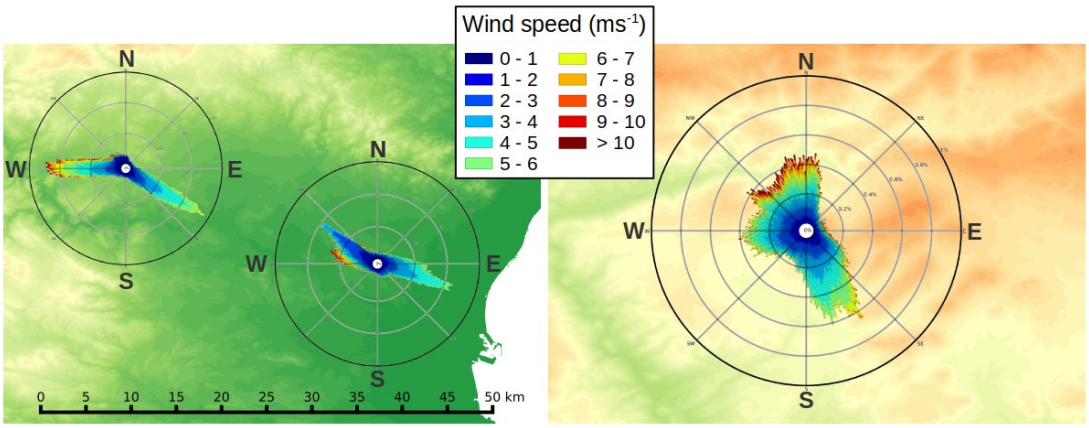

(a) (b)

Figure 4.1 – Wind roses over (a) PA and VI, and (b) AR with the corresponding topography. Wind speed and direction bins to compute wind roses have been set from 0-10 ms^{-1} with 1 m/s width and from 0-360º with 1º width, respectively.

Following the methodology introduced in Section 4 of Chapter 2, wind data was selected for daytime (from 05 to 19 UTC) and all stations. Also, only wind speeds between 1 ms^{-1} and 7 ms^{-1} during daytime were considered at PA, whilst no upper threshold was set over VI and AR. Then, an adjustment to two combined Gaussian distributions was applied to the wind direction frequency over PA and the limits of the 95 % confidence interval were considered to give wind directions ranging 11-173º. Afterwards, days with sea breeze formation, defined as 7-hour continuously blowing wind (at least) between the set threshold directions and velocities, were detected (Figure 4.2a). The same procedure was used to identify sea breeze days over VI and AR although only the days identified in PA were considered regarding sea-land moist air advection along Turia valley, and the location of the stations which are aligned in the direction of sea breeze flows (Figure 4.1a). The wind ranges obtained are 55-173º for VI and 95-221º for AR with the limits of the 95 % confidence interval of the two combined Gauss adjustments of wind direction frequency (Figure 4.2).

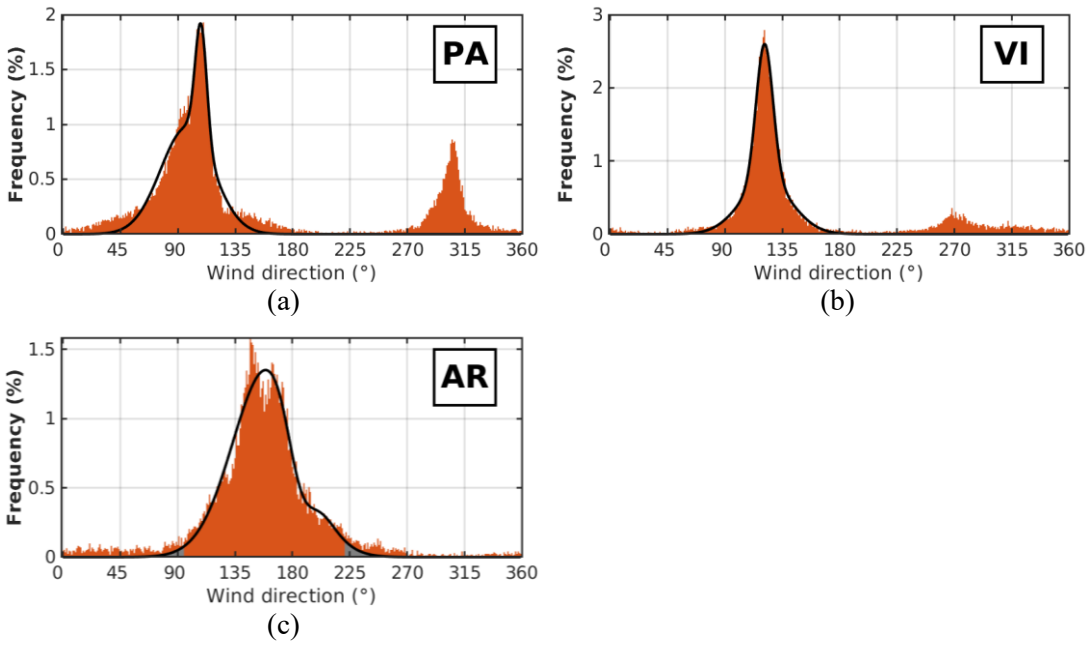

Figure 4.2 – Wind direction frequency adjusted to Gauss distributions with calculated 95% confidence level (excluded areas in gray) for (a) PA, (b) VI and (c) AR for the period 2005-2015 between 05 and 19 UTC. Wind speed values lower than 1 ms^{-1} have been removed for all stations, whereas an additional upper threshold of 7 ms^{-1} has been applied in (a).

In Table 4.1 the percentage of sea breeze days is shown over AR, VI and PA for the whole period 2005-2015, as well as for each season. These results remark the importance of the local circulations during summer in the TRB since the sea breeze circulation reaches inland areas (AR) more than 40 % of days in contrast with the very low percentages (3 %) obtained over pre-littoral and inland locations during winter. The sea-land moist air advection due to the sea breeze during MAM is also considerable regarding that marine air masses reach mountain ranges of the TRB almost 25 % of days. Overall, the TRB can be described as an area moderately affected by local sea-land circulations (more than 20 % of sea breeze days per year) that strongly influence land-atmosphere energetic exchanges during daytime.

Table 4.1 – Percentage of days with sea breeze circulation in the TRB over PA, VI and AR. for winter (DJF), spring (MAM), summer (JJA), autumn (SON) and the period 2005-2015.

Station	DJF (%)	MAM (%)	JJA (%)	SON (%)	ANNUAL (%)
PA	11	59	83	39	52
VI	3	34	60	22	31
AR	3	24	42	17	22

2. Characterization of SVA energetic exchanges

The energy exchanges in the SVA system are analyzed in order to quantify the heat and moisture contributions at local scale during sea breeze occurrence that might be crucial in the triggering of summer storms over the mountain ranges of the TRB. In this section, the mixing diagram method (Section 5 of Chapter 2) with long-term observations are used to describe variations of near-surface variables (e.g., q and θ), focusing on sea breeze days.

2.1. Atmospheric conditions in the TRB

Firstly, mixing diagrams are used to highlight energy exchange differences in the SVA system between days with and without sea breeze occurrence at certain locations of interest within the TRB. To this end, an example of two consecutive days in August 2015, the 12th, with dominant sea breeze circulation, and the 13th, with dominant *ponent* (synoptic westerly wind), over VI is shown in Figure 4.3. On one hand, under dominant *ponents* that overcome sea breeze circulation, dry air is advected from inland areas producing an abrupt decrease of humidity and increasing θ over VI, further enhanced by the entrainment effect at the top of PBL as it develops (Figure 4.3). In this particular day, the q decrease and θ increase occurs at an approximately constant rate until the features of the corresponding to advected air are matched, or an inversion layer at upper levels is reached that limits the PBL development is reached. On the other hand, under weak synoptic conditions, heat and moisture fluxes increase q and θ, respectively, whereas entrainment at the PBL top tends to reduce q and further increase θ in the morning. At noon, the development of the sea breeze leads to moist air advection from the sea over VI generating a considerable increment of q and limiting the increase of θ. Later, as insolation declines, temperature decreases (linked to surface heat fluxes decrease) at an approximately constant q that describes the advected marine air mass (Figure 4.3). Santanello et al., (2009; 2011) observed a similar behavior in mixing diagrams related to wet soils and the corresponding increase in q due to strong surface moist fluxes and weak advection. In the TRB, under dry soil conditions, surface moist fluxes are low so that the increment of q is mainly connected to the advection of moist air from coastal areas. In the example presented in Figure 4.3, the equal maximum values of $C_p\theta$ achieved in both days (~310 K), considering θ as the main marker of PBL growth, suggests a similar PBL height despite the different characteristics of the

advected air; that is, the evolution of the PBL may be limited by an inversion zone at upper levels that remains unchanged between the 12th and the 13th of August 2015.

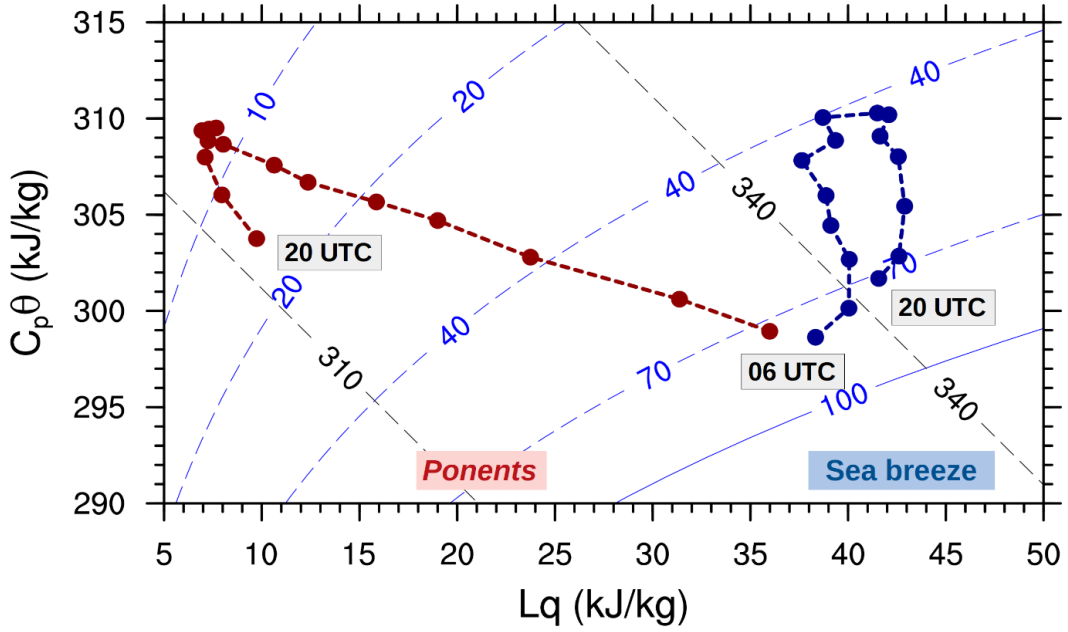

Figure 4.3 - Mixing diagrams of a situation with dominant sea breeze circulation (dashed-blue line), the 12th of August 2015, and a situation with dominant *ponents* (dashed-red line), the 13th of August 2015, over VI under soil dry conditions.

2.2. Sea breeze circulation during JJA

Before the analysis of the summer storm events using the mixing diagram method, it is important to identify the different energetic stages of the SVA system over littoral, pre-littoral and inland areas, and how this system is influenced by the sea breeze formation, especially during summer. To this end, in-situ measurements from meteorological towers, CEAM (AR, VI and PA) and XVVCCA (BU), and from IVIA surface stations (XU, BE and MO) within the area of study are used to analyze SVA exchanges at each location, as well as q and θ differences among locations, and sea breeze influence on H ($C_p\theta$) and LE (Lq). The analysis is conducted using averaged values of all observations available (about 10 years) to provide an overall view of diurnal cycle variations for summer (JJA), similarly to Santanello et al. (2015) and Sun et al., (2020a; b). This is carried out after a previous selection of the sea breeze days conducted in the previous section and the wind direction ranges from JJA results. Concretely, averages of q and θ are computed for days with dominant sea breeze circulation and mixing diagrams are generated for the period JJA in order to provide a general view of land-atmosphere

interactions. Besides, mixing diagrams are generated over different types of land use: (i) fruit trees and berry plantations (MO, BE and XU), (ii) urban/industrial areas (BU and PA), (iii) non-cultivated arable land (VI) and (iv) semi-natural shrublands (AR) to visualize differences in the SVA system.

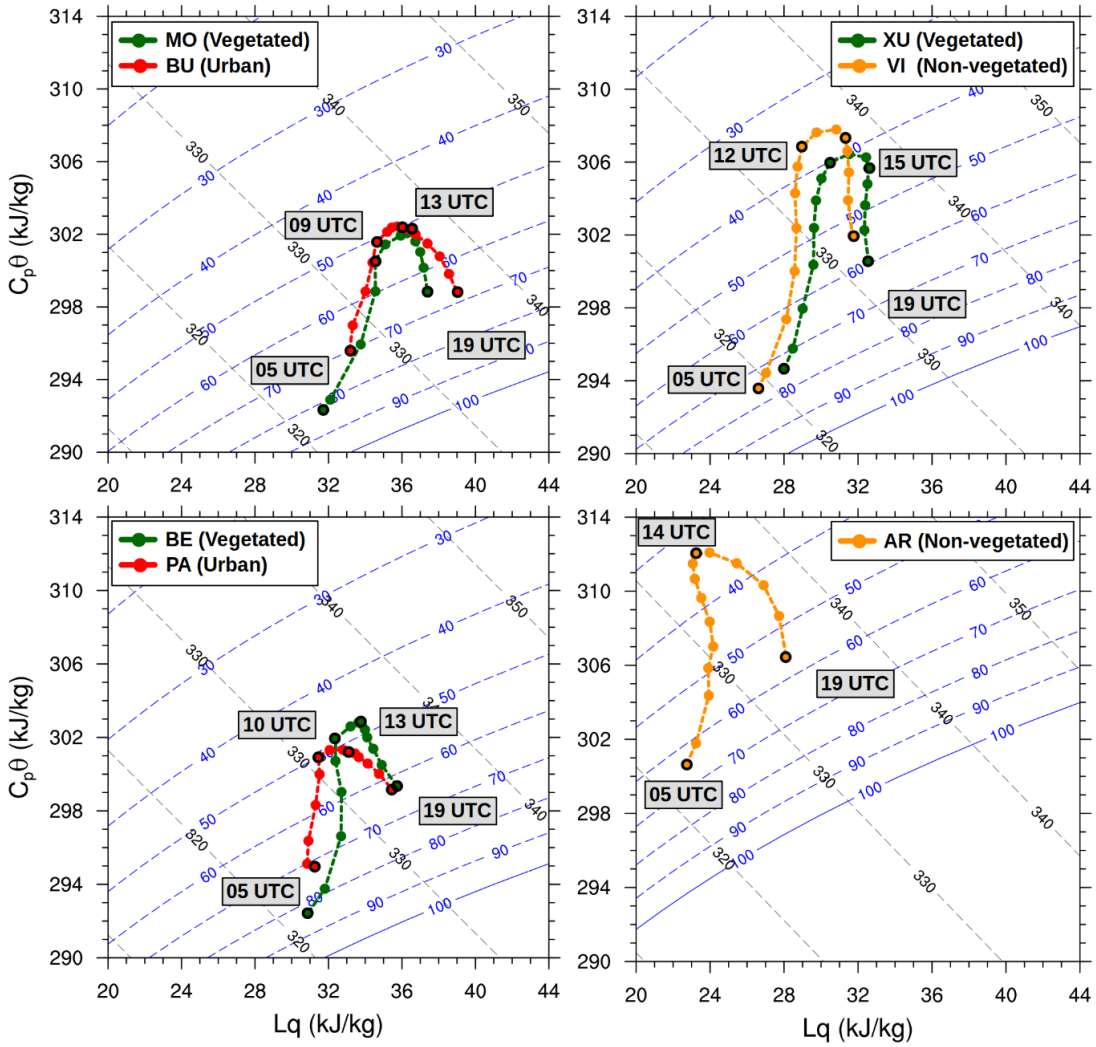

Figure 4.4 - Mixing diagrams at (a) MO and BU, (b) BE and PA, (c) XU and VI, and (d) AR using 10-year hourly averaged values (2005-2015) during summer (JJA) for days with combined-breeze formation. In each plot corresponding time in UTC is shown. Line colors represent urban (red), vegetated (green) and non-vegetated (orange) areas.

Generally, in Figure 4.4, q and θ show a diurnal variation (from 05 to 19 UTC) in the shape of an inverted U over all locations (littoral, pre-littoral and inland) during JJA with amplitude differences mainly associated with cool and moist air advection from the sea toward inland. According to Figure 4.4, on average, the air cooling and moistening due to the generation of the sea breeze occurs earlier at MO, BU, BE and

PA (09 UTC) than over XU, VI (12 UTC) and AR (14 UTC), as well as q variations are subject to evapotranspiration, from soil and vegetation, and variations produced by upslope advection of moist air, that might have accumulated in the valley, toward XU, VI and AR prior to the sea breeze front (SBF) arrival. The inverted U shape obtained for averaged values shows that this is a typical variation of q and θ for sea breeze days. Besides, the inverted U shape is also observed in the mixing diagrams performed for sea breeze days during DJF, MAM and SON so that q-θ variations can be described for these seasons in an analogous manner to JJA, with substantial differences regarding amplitude and maximum values (see Appendix B.1). Therefore, the inverted U shape can be defined as a distinctive feature of the q-θ variation over areas dominated by sea breeze circulations.

As commented previously, q-θ variations during sea breeze circulations are similar to the ones observed for weak advection and wet soil conditions, whereas the evolution of θ and q showed a significant drying and heating of the air mass according to Santanello et al. (2009; 2011) (see Appendix B.2). In the TRB, marine air advection dominates under weak synoptic conditions during JJA reaching inland areas in the afternoon so that the air mass heating and drying is exceeded by the moistening and cooling effect of the SBF. However, it is important to notice that the air located over the Turia valley is advected before the entrance of the SBF; hence, the characteristics of this air mass also produce an effect in the q-θ variations observed in pre-littoral and inland stations. In these terms, Santanello et al. (2009; 2011) remarks LE fluxes as the main limiting factor of the PBL growth. Considering soil dry conditions and low surface moist fluxes in the TRB, the increase of q limiting the PBL growth, before the SBF entrance, is mainly produced due to advection. This is further sustained by the wind plots presented in Figure 4.5. Overall, all stations present a change in wind direction and speed at about 09 UTC that coincides with the changes observed in the mixing diagrams for littoral stations and the corresponding formation of the sea breeze (Figure 4.4a, b). However, the increment in q at an approximately constant θ is not observed over pre-littoral and inland stations until 12 and 15 UTC, respectively (Figure 4.4c, d). This fact is probably linked to the mixing of the PBL with dry air from the residual layer as it develops since the early morning and limiting the moistening due to advection. In the afternoon, an inversion layer is reached restricting the PBL growth so that an effective air moistening due to advection occurs.

A more detailed analysis is conducted in the following paragraphs for each pair of grouped stations regarding land use and location, as well as for the daytime periods of interest (highlighted in black circles in Figure 4.4). Additionally, increments in q and θ for the periods, as well as mean differences between stations, are shown in Table 4.2.

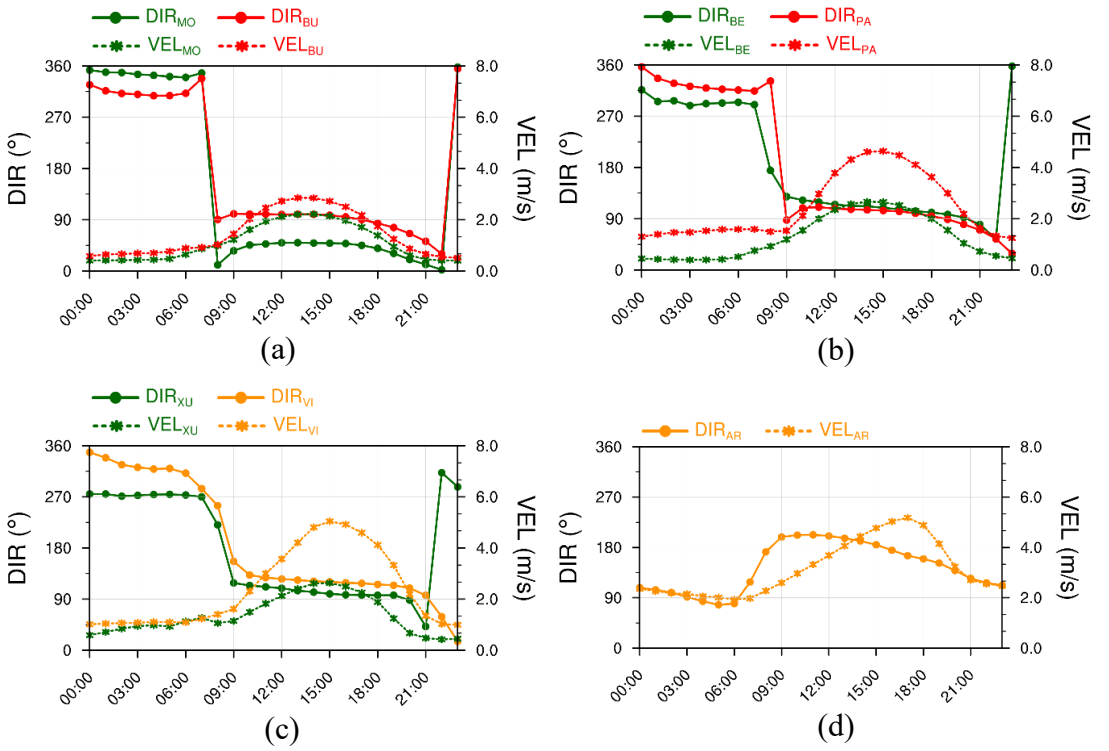

Figure 4.5 - Wind speed and direction averaged for JJA over (a) MO (green) and BU (red), (b) BE (green) and PA (red), (c) XU (green) and VI (orange), and (d) AR corresponding to the mixing diagrams shown in Figure 4.4.

(a) MO and BU

According to the mixing diagrams shown in Figure 4.4a and increments computed in Table 4.2a, q variations in the SVA system present a similar amplitude at both locations whereas θ variations are greater over MO than in BU. Specifically, the amplitude of the Lq variation is equal over MO and BU (about 6 kJ·kg^{-1}), whereas MO shows an amplitude for $C_p\theta$ 3 kJ·kg^{-1} greater than BU due to morning temperature differences associated with heat island effect. Besides, three main time periods can be identified during daytime regarding changes in q-θ variation shown in Figure 4.3a:

- From 05 to 09 UTC, temperature increases rapidly ($\Delta\theta$=8.6 K and $\Delta\theta$=4.9 K at MO and BU, respectively) whereas humidity increment is lower in comparison (Δq=1.3 g·kg^{-1} and Δq=0.6 g·kg^{-1} at MO and BU, respectively) according to

Table 4.2a, reducing RH to a value of about 50 % at both locations (Figure 4.4a). Δq and $\Delta\theta$ differences (about 0.7 g·kg^{-1} and 2.7 K) are originated by the distinct land use characteristics of each location regarding the negligible advection (wind speeds of 0.5-1.0 m/s, Figure 4.5a). Specifically, over vegetated areas such as MO, plants provide additional water vapor to the atmosphere throughout transpiration (*LE* is released instead of *H*) whereas, over urban areas such as BU, the amplitude of the diurnal potential temperature decreases by the heat island effect (surface energy release is mainly as *H*). According to Table 4.2a, the negative values of Δq and $\Delta\theta$ for MO - BU indicate that MO presents a non-significant lower humidity but a considerably lower temperature than BU between 05 and 09 UTC, although main q and θ differences occur in the early morning at 05 UTC. This indicates a cooler and drier air over MO than over BU at 05 UTC despite the greater RH at MO (80 %) than at BU (70 %) as shown in Figure 4.4a.

- From 09 to 13 UTC, wind direction veers to east (northeast) in BU (MO) so that moist and cool air is advected producing an increase of q and limiting the θ increment, which had been increasing since 05 UTC due to surface heating and entrainment. Besides, MO - BU values of Δq=0.3 g·kg^{-1} and $\Delta\theta$=-0.2 K indicate a greater q over MO than over BU and negligible θ differences (Table 4.2a). Thus, the air over MO becomes slightly moister than over BU during this period probably produced by evapotranspiration and entrainment differences, whereas θ maximum value is the same over both stations at 13 UTC (Figure 4.4a).
- From 13 to 19 UTC, q increase is maximum over BU (Δq=1.2 g·kg^{-1}) and slightly higher than the increment observed in MO (Δq=0.4 g·kg^{-1}), whilst θ decreases similarly over MO according to Table 4.2a. However, a tendency towards equilibrium among surface fluxes, advection and entrainment, depicted by a nearly constant θ_e of 337 K in the mixing diagram (Figure 4.4a), is observed only over BU as long as onshore wind perdures (Figure 4.5a). This equilibrium may be caused by the heat island effect that originates over urban areas since surface heat fluxes are significant during longer periods than over other land use categories.

Table 4.2 - q and θ increments for a) MO and BU, b) BE and PA, c) XU and VI, and d) AR within the corresponding periods of interest for each case. Averaged increment differences between each pair of stations within the corresponding period are indicated as a) MO - BU, b) BE - PA and c) XU - VI. Bold numbers indicate maximum Δq and Δθ for each station and positive and negative differences are highlighted in red and blue, respectively. It must be noticed that q and θ values have been divided by the corresponding constant: L and C_p for q and θ, respectively.

a)	**05 - 09 UTC**		**09 - 13 UTC**		**13 - 19 UTC**	
	Δq (g·kg^{-1})	Δθ (K)	Δq (g·kg^{-1})	Δθ (K)	Δq (g·kg^{-1})	Δθ (K)
MO	**1.3**	**8.6**	0.7	1.3	0.4	-4.2
BU	0.6	**4.9**	0.6	0.9	**1.2**	-3.6
MO - BU	**-0.1**	**-1.6**	**0.3**	**-0.2**	**-0.1**	**-0.2**
b)	**05 - 10 UTC**		**10 - 13 UTC**		**13 - 19 UTC**	
	Δq (g·kg^{-1})	Δθ (K)	Δq (g·kg^{-1})	Δθ (K)	Δq (g·kg^{-1})	Δθ (K)
BE	0.6	**9.4**	0.5	0.4	**0.8**	-3.5
PA	0.1	**6.0**	0.6	0.9	**1.0**	-2.1
BE - PA	**0.9**	**-0.2**	**0.9**	**1.3**	**0.2**	**1.0**
c)	**05 - 12 UTC**		**12 - 15 UTC**		**15 - 19 UTC**	
	Δq (g·kg^{-1})	Δθ (K)	Δq (g·kg^{-1})	Δθ (K)	Δq (g·kg^{-1})	Δθ (K)
XU	**1.0**	**11.3**	0.8	-0.3	0.0	-4.1
VI	**1.0**	**13.3**	0.9	0.5	0.2	-4.4
XU - VI	**0.5**	**0.2**	**0.6**	**-1.3**	**0.4**	**-1.7**
d)	**05 - 14 UTC**		**14 - 19 UTC**			
	Δq (g·kg^{-1})	Δθ (K)	Δq (g·kg^{-1})	Δθ (K)		
AR	0.2	**11.4**	**2.0**	-4.5		

(b) BE and PA

Following the mixing diagrams shown in Figure 4.4b and the increments in Table 4.2b, q and θ variations in the SVA system are very similar to the previously analyzed stations MO and BU despite differences in the amplitude ranges and times. It must be noticed that amplitude differences in the diurnal cycle of q and θ between BE and PA, especially θ maxima, may be influenced by the altitude of the stations: BE is situated at 2 m above vegetated ground whereas PA is mounted at the top of a building at about 20 m above ground. As for the previous analysis, three time periods can be identified regarding q-θ evolution as exposed in the following paragraphs:

- From 05 to 10 UTC, surface heat and moisture fluxes produce a considerable temperature increase ($\Delta\theta$=9.4 K and $\Delta\theta$=6.0 K at BE and PA, respectively), as well as a slight q increase at PA but considerable at BE (0.6 g·kg^{-1}), reducing RH down to a value of 50 % over both locations (Figure 4.4b). As in MO and BU comparison, the low wind speeds of 0.5-1.5 m/s (Figure 4.5b) indicate that increment differences between BE and PA are related to the distinct land use categories that affect directly LE and H partitioning: over BE (vegetated area), transpiration provides additional moisture to air; over PA, an industrial area with buildings, the heat island effect contributes to reduce the amplitude of θ diurnal cycle. The distinct increment of q and θ at BE and PA also generate humidity differences (low for θ) between the stations of 0.9 g·kg^{-1} (Table 4.2b), so that a slightly greater air moistening occurs over BE than over PA.

- From 10 to 13 UTC, generation and intensification of westerly winds from the sea, sea breeze (Figure 4.5b), tend to reduce θ increment and increase q similarly at both locations. Moreover, the q-θ evolution presents a tendency towards constant RH of 50 % from 09 to 11 UTC at PA, then θ remains nearly constant (θ ~ 300 K) from 11 to 13 UTC, and a RH of 47 % from 10 to 13 UTC at BE (Figure 4.4b). The values of BE - PA indicate that air continues to be moister over BE than over PA, but also warmer (Table 4.2b).

- From 13 to 19 UTC, the onshore air flow from SE (Figure 4.5b) continues to generate an increase of q (daily maxima of 0.8 g·kg^{-1} and 1.0 g·kg^{-1} over BE and PA, respectively) and θ starts to decrease due to the diminishing surface heat flux, more abruptly over BE than over PA as shown in Table 4.2b. In PA, the q-θ variation follows a constant θ_e of about 334 K indicating an energetic equilibrium in the SVA system among surface fluxes, advection and entrainment. Besides, BE - PA values indicate a tendency toward similar q and θ over both stations.

(c) XU and VI

The comparison of these two stations is performed as in the previous analyses, following the mixing diagrams and values provided in Figure 4.4c and in Table 4.2c. In this particular case, XU and VI mixing diagrams present significant differences in comparison with the previously analyzed littoral stations regarding diurnal cycle amplitudes of both θ and q. According to XU - VI in Table 4.2c, a nearly constant Δq

of about 0.5 g·kg^{-1} and a Δθ ranging between -2 K and 1 K, approximately, is observed in the diurnal cycle of q-θ variation, which indicates a constantly moister air over XU than over VI. A more detailed study of the q-θ evolution is conducted by dividing mixing diagrams into three time periods as presented in the following paragraphs:

- From 05 to 12 UTC, θ increases abruptly (more than 13 K over VI) along with q (up to 1 g·kg^{-1}), principally due to heat and moisture fluxes from the surface regarding the low wind speeds until 09 UTC, and the advection of air masses situated over the TRB after 09 UTC (Figure 4.5c). During this period, *RH* reduces from 75 % to 35 %, approximately (Figure 4.4c). As in the analyses conducted above, land use characteristics are the main factor influencing Δθ and Δq over each location so that over vegetated areas, such as XU, the greater partitioning between *LE* and *H* produce a lower Δθ than over bare soil areas, such as VI. However, the same Δq observed over VI and XU suggests that an additional air moistening occurs due to moist air advection or entrainment. In particular, from 05 to 09 UTC, low wind speed at both locations (about 1 m/s) denotes a slight air advection so that main variations of q may be caused by a moist residual mixing layer with stronger mixing over VI. Overall, regarding averaged q and θ differences between XU and VI exposed in Table 4.2c, slightly moister and cooler air is found over XU than over VI during 05-12 UTC.

- From 12 to 15 UTC, the sea breeze continues to intensify with time, with maximum wind speeds at 15 UTC (Figure 4.5c), and moist and cool air from coastal areas reaches XU and VI producing a significant change in θ, as well as an increase of q, slightly greater over XU (Table 4.2c). These increments lead to slightly increase the differences (XU - VI) so that a maximum difference in q of 0.6 g·kg^{-1} is achieved, indicating a slightly moister and cooler air over XU than over VI.

- From 15 to 19 UTC, after the wind speed maximum at 15 UTC, the moist and cool air advection stabilizes over both locations despite the tendency to decrease (Figure 4.5c). According to Table 4.2c, q is nearly constant and θ decreases rapidly due to the decreasing heat fluxes at the surface. Besides, XU - VI values indicate that q contrast between XU and VI remains equal, whilst temperature differences increase slightly during this period as the air over VI cools down faster due to the absence of plants.

(d) AR

As in the previous analyses, time periods are set following q-θ variations observed in the mixing diagram in order to conduct the detailed analysis introduced in the paragraphs below:

- From 05 to 14 UTC, surface heat fluxes produce a strong increment of θ whereas q approximately constant. However, a slight increase of q occurs due to both surface moisture fluxes and moist air advection from the valley between 05 and 09 UTC, winds from southeast and south (upslope winds), whilst a very low decrease in q, linked to entrainment at the PBL top, is observed after 09 UTC (Figure 4.4d). This occurs despite the considerable advection with southerly winds of 3-4 m/s related to the initial state of the sea breeze (Figure 4.5d) due to strong surface heat fluxes and entrainment. In fact, early morning variation (05-09 UTC) is similar in VI; however, after 09 UTC the air drying in AR suggests a stronger entrainment at the PBL top considering a higher development of the PBL and the corresponding mixing with upper-level atmospheric layers. During this period, the q-θ variations produce a decrease of *RH* from 65 % at 05 UTC to about 35 % at 14 UTC (similar *RH* minimum in VI at 12 UTC).

- From 14 to 19 UTC, the sea breeze intensifies with a maximum average wind speed of about 5 m/s at 17 UTC and posteriorly starts to diminish. Moist and cool air from coastal areas is advected over AR generating increments of q (Δq=2.0 g·kg^{-1}) and θ ($\Delta\theta$=-4.5 K), the latter further intensified by the weakening of surface heat fluxes.

In summary, the q-θ variation for a 10-year average under sea breeze dominant conditions during summer shows that the inverted U shape amplitude observed in the mixing diagrams, from 05 to 19 UTC, is mainly dominated by the cooling and moistening effectivity of the sea breeze. However, in the comparison conducted over VI and XU (at about 40 km from the coastline), cultivated land appears to slightly modify (about 0.5 g·kg^{-1} and 1 K) the U shape with respect to non-cultivated land due to differences in the surface heat and moisture fluxes. Instead, humidity differences between urban and cultivated land use are not observed over areas close to the sea that present generally high values of q, although the heat island effect produces significant temperature contrasts of about 2-3 K (and *RH* of 70-80 %) between urban and vegetated

areas. Besides, the results over AR, located at 1277 m above sea level, indicate a stronger drying of the air mass associated with a greater development of the PBL.

2.3. Case study: 15th - 23rd of July 2015

In this subsection, a comparison between q and θ variations for the period covering from the 15th to the 23rd of July 2015 is conducted. In the context of the results shown in the previous section, a comparison is conducted for q and θ between BE and PA, as well as between XU and VI (the comparison between MO and BU is not shown due to lack of data during the study period). Specifically, time series of q and θ are intercompared during the period 15th to 23rd July 2015.

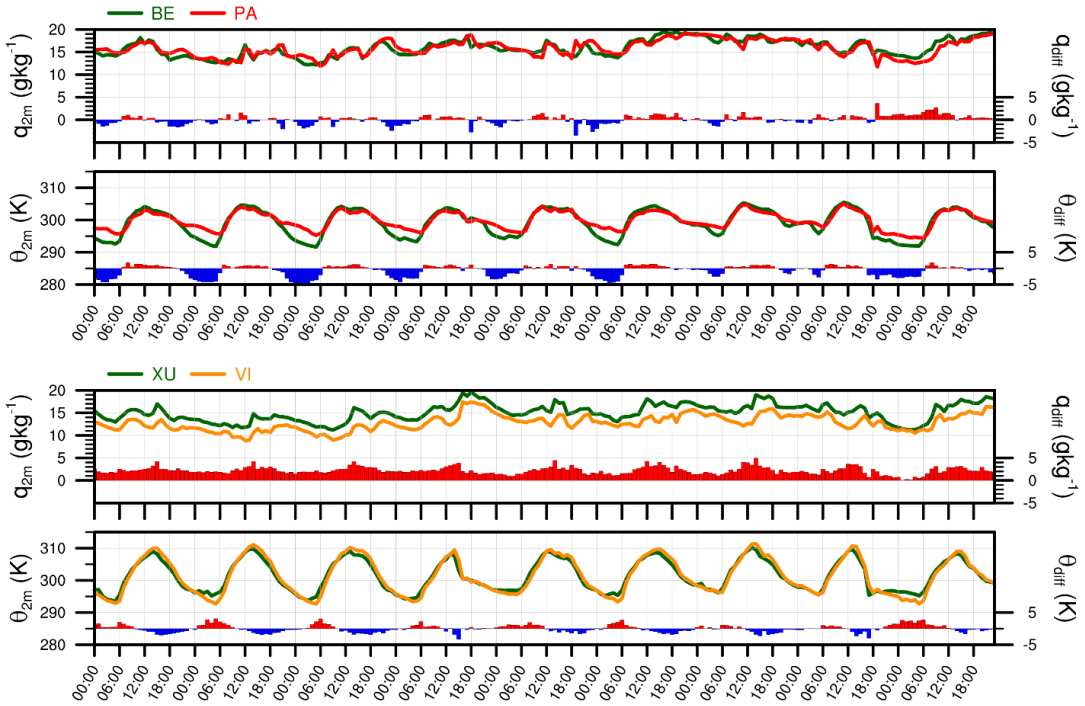

Figure 4.6 - Temporal evolution of q and θ at 2 m above ground over BE and PA (top), and XU and VI (bottom) for the period 15th to 23rd July 2015, along with the corresponding difference between each pair of stations q_{diff} *and* θ_{diff}.

In Figure 4.6, the evolution of q and θ show the diurnal cycle temperature already commented in the previous section. Besides, hourly differences between stations agree with the variations observed for the 10-year averaged values denoting the effect of the heat island at night, lower temperature values over crop fields (BE) than in urban areas (PA), and the greater cooling effect at nighttime over bare soil (VI) than over vegetated areas (XU). Diurnal variations of q are not clearly distinguished at BE and PA since

these are located near the coastline and generally under the influence of marine air masses; however, peak values of q are observed between 12 and 18 UTC in relation with sea breeze formation at XU and VI. In contrast, hourly differences in q denote the slightly greater values at BE in comparison with PA from midday until early morning, as well as the generally moister air found over XU than over VI (~3 $g \cdot kg^{-1}$ on average), with differences up to 5 $g \cdot kg^{-1}$ between 12 and 18 UTC, in correspondence with the maximum sea breeze intensity observed in the previous analysis (Figure 4.5c).

3. High-resolution simulation over the TRB

The analysis performed using meteorological observations within the TRB provides information on SVA energetic exchanges over certain representative locations. However, the use of meteorological models facilitates a wider analysis of the variations in the SVA system since it provides an extensive number of atmospheric fields at a high spatial resolution over surface and an important number of atmospheric layers. Furthermore, it adds the possibility to study the advection of air masses and the corresponding formation, development and triggering of summer storms. In this section, the model validation of the STM performed over the TRB for the different summer storm events occurring between the 15th and the 23rd of July 2015 is exposed.

3.1. Statistical analysis

Observations from PA and VI, as well as the GNSS stations located at the coastal area and at the uppermost part of the TRB (see Figure 2.12 in Chapter 2), are used to conduct this statistical analysis. In general, the statistical scores obtained for winds indicate that the model captures accurately the temporal evolution of the sea breeze in the study area during daytime (05-19 UTC), whereas nighttime winds (19-05 UTC) are less accurately represented (Table 4.3). Besides, the model shows a better representation of temporal wind variations over the littoral and pre-littoral than over inland areas, as well as the lowest RMSE, MBE and $RMSE_V$ values are obtained at VI with slight differences in comparison to PA (Table 4.3). In contrast, AR presents the greatest errors (RMSE, MBE and $RMSE_v$) indicating stronger biases with respect to observations (e.g., RMSE values slightly greater than 2 ms^{-1}). In addition, the model presents warm and dry biases regarding humidity and temperature values, more accurately represented over VI in accordance with wind statistical scores (Table 4.3). Specifically, during daytime, warm and dry biases are more marked over PA, with MBE values up to 2 ºC and -2.1 gkg^{-1}, than over VI with MBEs of 0.1 ºC and -0.7 gkg^{-1} for temperature and humidity,

respectively (Table 4.3). These humidity and temperature inconsistencies may be connected to several factors with respect to the model representation of atmospheric dynamics at local scale that may yield an overdrying due to entrainment effect (the main factor contributing to PBL drying). Additionally, overestimated nighttime winds (e.g., down-valley winds) advecting dry air from inland areas toward the coast may further enhance the overdrying at coastal areas.

Table 4.3 - Statistical scores over PA, VI and AR with highest scores highlighted in bold.

	Station	Wind (ms^{-1})				Temp. (ºC)			q ($g \cdot kg^{-1}$)		
		IOA	**RMSE**	**MBE**	**RMSE$_V$**	**IOA**	**RMSE**	**MBE**	**IOA**	**RMSE**	**MBE**
Night	PA	**0.56**	1.5	0.7	2.1	0.62	2.2	1.5	0.48	3.3	-2.3
	VI	0.53	**1.2**	**0.5**	**1.6**	**0.83**	**2.1**	**0.7**	**0.72**	**1.9**	**-0.7**
	AR	0.47	2.2	1.5	2.5	--	--	--	--	--	--
Day	PA	0.80	1.5	1.1	1.7	0.84	2.4	2.0	0.55	2.8	-2.1
	VI	**0.89**	**1.1**	**0.5**	**1.3**	**0.95**	**2.0**	**0.1**	**0.70**	**1.8**	**-0.7**
	AR	0.72	1.9	1.4	2.9	--	--	--	--	--	--
All	PA	0.77	1.5	0.9	1.9	0.84	2.3	1.8	0.52	3.0	-2.3
	VI	**0.87**	**1.1**	**0.5**	**1.4**	**0.96**	**2.0**	**0.4**	**0.71**	**1.8**	**-0.8**
	AR	0.66	2.1	1.5	2.7	--	--	--	--	--	--

Overall, statistical scores suggest that the WRF model captures wind variations along the study area associated with dominating sea breeze flows during daytime (05-19 UTC). However, inconsistencies regarding the modeling of humidity and temperature over coastal areas need to be considered and further analyzed.

Regarding humidity, simulated values in WRF can be further analyzed using observations of the integrated water vapor column over coastal and inland locations provided by the GNSS network. This comparison shows that the model representation of the temporal evolution over inland areas (uppermost part of the TRB) is considerably less accurate than over the littoral (Table 4.4). However, the RMSE and MBE scores indicate similar inconsistencies over all stations although ACIN and ALIA present a slightly dry bias denoted by the negative MBE values (Table 4.4). Besides, the scores obtained indicate that TPW values and temporal variations are more accurately captured during daytime (05 to 19 UTC) than at night, except for ACIN (Table 4.4). In other words, the model captures better water vapor circulations during situations with dominating thermally driven winds (e.g., upslope winds and sea breeze) occurring at daytime in accordance with the statistical scores obtained previously.

Table 4.4 - Statistical scores for TPW (in cm) with highest scores highlighted in bold.

Location	Station	*All*			*Day*			*Night*		
		IOA	**RMSE**	**MBE**	**IOA**	**RMSE**	**MBE**	**IOA**	**RMSE**	**MBE**
LI	VALE	0.73	**0.4**	0.3	0.75	**0.4**	0.3	**0.70**	0.5	0.4
	VCIA	**0.75**	**0.4**	0.2	**0.78**	**0.4**	0.2	**0.70**	0.5	0.3
IN	TERU	0.59	**0.4**	**0.1**	0.61	0.5	**0.0**	0.55	**0.4**	**0.1**
	ACIN	0.50	0.5	-0.3	0.49	0.6	-0.3	0.57	**0.4**	-0.2
	ALIA	0.69	**0.4**	-0.2	0.74	**0.4**	-0.1	0.60	**0.4**	-0.2

3.2. Precipitation

Total simulated precipitation within the domain of the STM simulation is compared to CMORPH satellite data at an hourly base in order to visualize the model accuracy in capturing the four precipitation events.

From a general point of view, all precipitation events are reproduced in the model except for the 21st of July with no precipitation simulated in contrast to CMORPH, remarking the inability of the WRF model to reproduce this event (Figure 4.7), as obtained in the 3-km horizontal simulation performed previously (see Chapter 3). Besides, the localized precipitation occurred the 15th of July is reproduced in this high-resolution simulation contrasting with the inability to capture this event in the corresponding previous simulation (MM5-NoahMP) at a 3-km horizontal resolution (see Chapter 3). The ability of the model to reproduce the localized event during the 15th is probably related to the high horizontal resolution of STM simulation (680 m), that is, the local circulations key in the generation of this event are more accurately represented at high resolutions. However, the occurrence of summer storms appears to be shifted in time with respect to CMORPH, i.e., the formation and triggering of summer storms occurs later in the model than in CMORPH, although the duration of the precipitation events is well-captured (Figure 4.7). Hourly precipitation maxima in the model domain also differs between CMORPH and STM precipitation in most events except for the 18th of July case with very similar precipitation peaks despite the temporal shift (Figure 4.7). In this case, the well-captured precipitation peaks may be linked to the stronger synoptic conditions during this day compared to the other summer storm events.

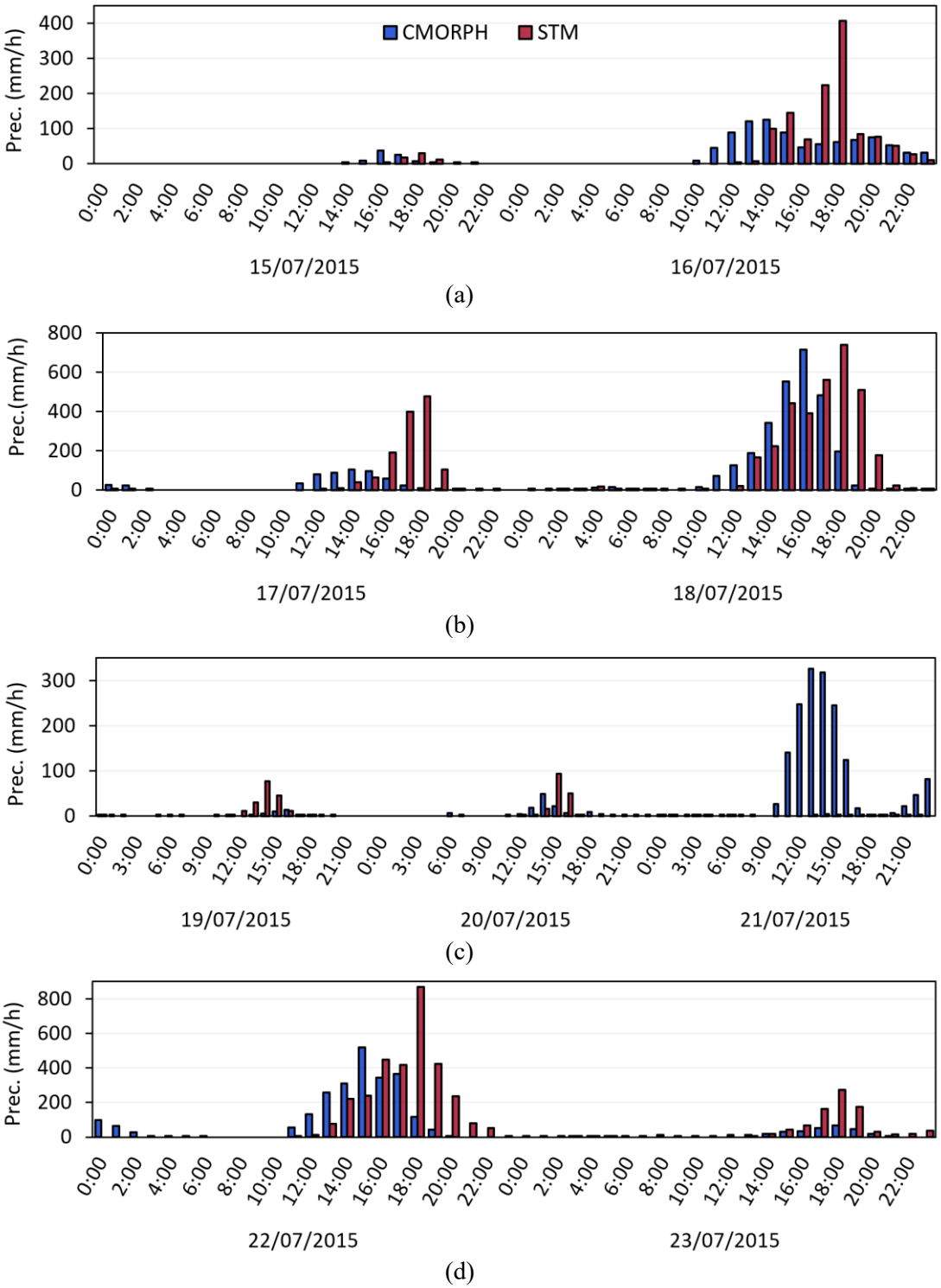

Figure 4.7 - CMORPH (blue) and STM (red) totalized hourly precipitation over the simulation domain (Figure 2.12) for (a) Event 1, (b) Event 2, (c) Event3 and (d) Event 4.

3.3. Mixing ratio, temperature and winds

Despite the generally accurate representation of the state of the atmosphere for the period 15th to 23rd of July, precipitation shows differences regarding each summer storm events. Hence, the evaluation of temporal variation in humidity, temperature and wind is further studied for each summer storm event using time series plots so that the representation of sea breeze features can be further investigated.

3.3.1. Event 1: 15th - 16th July 2015

In PA, the positive bias in temperature is detected before noon (at 10 UTC) during both days whereas nighttime and early morning temperatures are well-captured in this period, specifically, in the subperiods 06-10 UTC and 20-10 UTC (Figure 4.8a). Similarly, q inconsistencies (dry biases) are lower from 06 to 10 UTC and from 18 to 21 UTC the first day, and in the period 08-11 UTC the second one, with a non-reproduced peak from 11 to 14 UTC and a considerable increasing bias after 14 UTC (Figure 4.8a). Oppositely, in VI, the time variations and values of temperature and humidity are well-captured by the STM simulation, although important differences arise (cooler and moister biases in the model) after 11 UTC in q and 14 UTC in temperature (Figure 4.8b). This may explain the time shift observed in precipitation during this event; in fact, model inconsistencies reduce considerably after 20 UTC matching the precipitation reduction (Figures 4.7a and 4.8b). Despite the accurate values simulated over VI, low biases in temperature are observed in periods 08-20 UTC (cool bias) and 01-08 UTC (warm bias) that lead to an overheating of the PBL during daytime the 15th of July (Figure 4.8c).

In PA, model inconsistencies obtained for humidity and temperature are linked to overestimated onshore (from 11 to 23 UTC) and offshore (from 23 to 08 UTC) wind intensities that produce an overdrying at the coast the 15th of July, as well as during the 16th from 10 to 17 UTC (Figures 4.8c, d). Another important effect that may contribute to intense drying and heating at the coast is the overestimated entrainment at the top of the PBL due to surface overheating in the model. In VI, wind intensities are more accurately reproduced with main overestimates of westerly (nighttime and early morning) winds obtained from 20 to 06 UTC (Figures 4.8c, d), that generate an overdrying of the surface air and reduces the local radiative cooling.

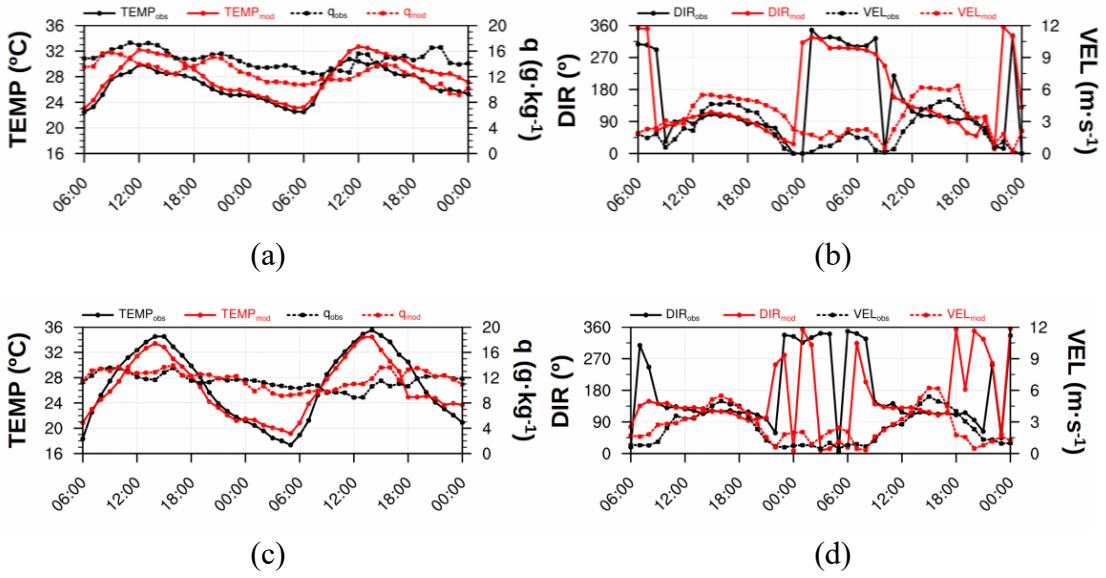

Figure 4.8 -Time series for the period 15th-16th July 2015 of (a, c) 2-meter temperature (*T*; solid lines) and mixing ratio (*q*; dashed lines), and (b, d) 10-meter wind direction (*DIR*; solid lines) and speed (*VEL*; dashed lines) from observations (black lines) and STM (red lines) at (a, b) PA and (c, d) VI.

3.3.2. Event 2: 17th - 18th July 2015

Contrarily to the first simulated event, there is a warm bias over PA during the two days of the second event with maximum differences, also identified for *q*, during daytime (approximately from 10 to 17 UTC) that agree with the generation of localized low clouds over littoral areas not reproduced in the model, as well as with overestimated sea breeze flows (Figures 4.9a, b). This fact produces an overestimation of temperature increase due to surface heat fluxes, a higher development of the PBL and the corresponding overestimate of entrainment at this location that leads to significant *q* inconsistencies (with biases of -5 $g \cdot kg^{-1}$). Besides, nighttime and early morning differences (20-08 UTC) in temperature and humidity are associated with overestimated offshore winds that advect dry air from inland areas and reduce the effect of surface radiative cooling (Figures 4.9a; b). Oppositely, temperature and humidity variations at VI are accurately captured, especially during daytime, although *q* presents considerable dry biases the 18th (about -3 $g \cdot kg^{-1}$) after 07 UTC and temperature is overestimated from 16 to 19 UTC (Figures 4.9b, c), both related to convective precipitation discrepancies (Figures 4.7b). In addition, temperature biases are identified at night and early morning (00-06 UTC) for both simulated days that correspond to overestimated down-valley winds that generate an excess drying of coastal areas (Figures 4.9b, c).

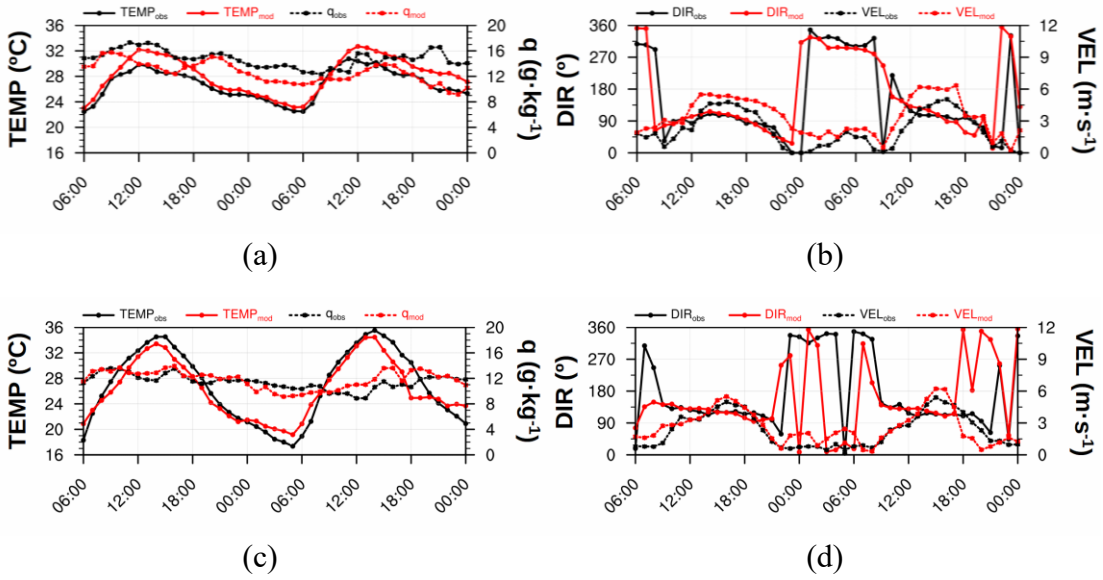

Figure 4.9 - Same as Figure 4.8 but for period 17th-18th July 2015.

3.3.3. Event 3: 19th - 21st July 2015

Humidity differences remarked previously at PA from the previous day (18th) further increase (about -6 g·kg^{-1} at 00 UTC) and extend until 06 UTC of the 19th, reducing the bias (about 2 g·kg^{-1}) until 11 UTC matching the formation and intensification of sea breeze (Figures 4.10a; b). However, modeled q remains nearly constant at about 13-14 g·kg^{-1} during the period 12-17 UTC, after an increase of 3 g·kg^{-1} between 10 and 12 UTC, whilst observed values indicate a sudden increase of q from 14 to 18 g·kg^{-1} at 12 UTC and a slow decrease to about 15 g·kg^{-1} at 17 UTC (Figure 4.10a), matching nearly stable onshore wind speeds, slightly overestimated in the model (Figure 4.10b). The following days (the 20th and 21st) humidity is underestimated in general with biases that reach about 8 g·kg^{-1} during the period 00-03 UTC the 21st, although in the afternoon of the 21st q is more accurately captured in the model (Figure 4.10a). Temperature variations also show a generalized warm bias during the 19th due to the warming (and drying) effect of down-valley winds at night and early morning, and the formation of low-level clouds after 08 UTC that are not reproduced in the model (Figure 4.10a). This non-representation of clouds in the morning also occurs the following two days (the 20th and 21st) despite the well-captured wind variations, whereas nighttime and early morning temperature biases are considerably lower during the last two days compared to the 19th (Figure 4.10a; b).

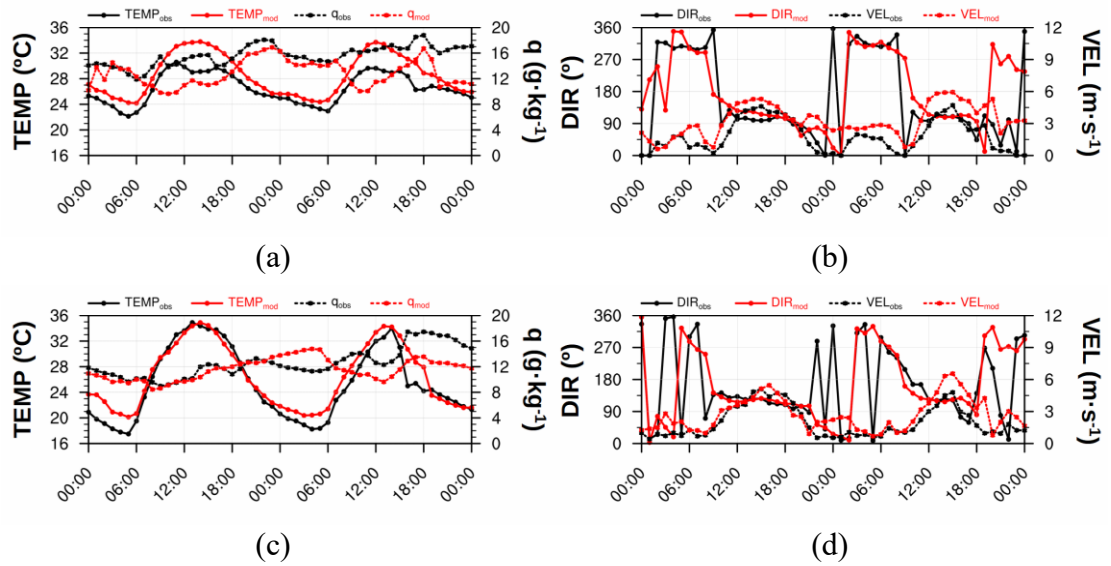

Figure 4.10 - Same as Figure 4.8 but for period 19th-21st July 2015.

At VI, as for the previous events, the accuracy of the model in capturing humidity and temperature is greater than over PA (Figure 4.10c), along with the well-reproduced sea breeze circulations and nighttime winds (Figure 4.10d). In fact, temperature is very well represented, except for the overestimated values during the period 00-06 UTC the 20th, and humidity inconsistencies (dry biases) are within the range between -4 g·kg^{-1} and 0 g·kg^{-1} (Figure 4.10c), although these differences are considerably greater than in the previous events. As for PA, *q* variations linked to sea breeze formation are not properly captured in the afternoon despite the well-represent wind variations (Figure 4.10d); however, the accuracy in representing *q* increases the 21st (Figure 4.10c).

Overall, discrepancies the 19th and 20th regarding coastal low clouds, as well as humidity and temperature considerable inconsistencies, the STM simulation can reproduce the localized summer storms in contrast with the non-captured heavy precipitation the 21st (Figure 4.7c), despite the better represented atmospheric fields over the analyzed locations.

3.3.4. Event 4: 22nd - 23rd July 2015

Values of *q* are well-represented at PA for last two days of the STM simulation despite punctual differences between 18 and 06 UTC (Figure 4.11a) associated with the time shift in summer storms generation and the extend of precipitation highlighted previously (Figure 4.7d). This fact affects more abruptly temperature showing a strong deviation from 11 to 08 UTC with maximum inconsistencies of about -6 ºC during the

night of the 22nd (Figure 4.11a), in contrast with the well-captured wind variations (Figure 4.11b). Concretely, temperature starts to decrease after 11 UTC, with an abrupt decay at 18 UTC (also observed in *q* at 19 UTC) connected to the arrival of a storm to PA, which is not accurately reproduced in the model (Figure 4.11a). The STM simulation generates no precipitation over PA, although winds linked to storms reach the location producing fluctuations in *q* but no variations in temperature since no cooling effect due to precipitation occurs (Figures 4.11a, b). Modeled temperature decreases after 23 UTC although considerable biases between -6 and -4ºC persist until the next morning (09 UTC) with the posterior accurate representation during the 23rd (Figure 4.11a). The increase in *q* is also captured in the model (up to 19 and 17 $g \cdot kg^{-1}$ observed and simulated values at 00 UTC, respectively), remarking the very wet conditions after the generalized precipitation event (Figure 4.11a), as well as the considerable observed nighttime winds and the sea breeze formation that led to the localized summer storms during the 23rd (Figure 4.11b).

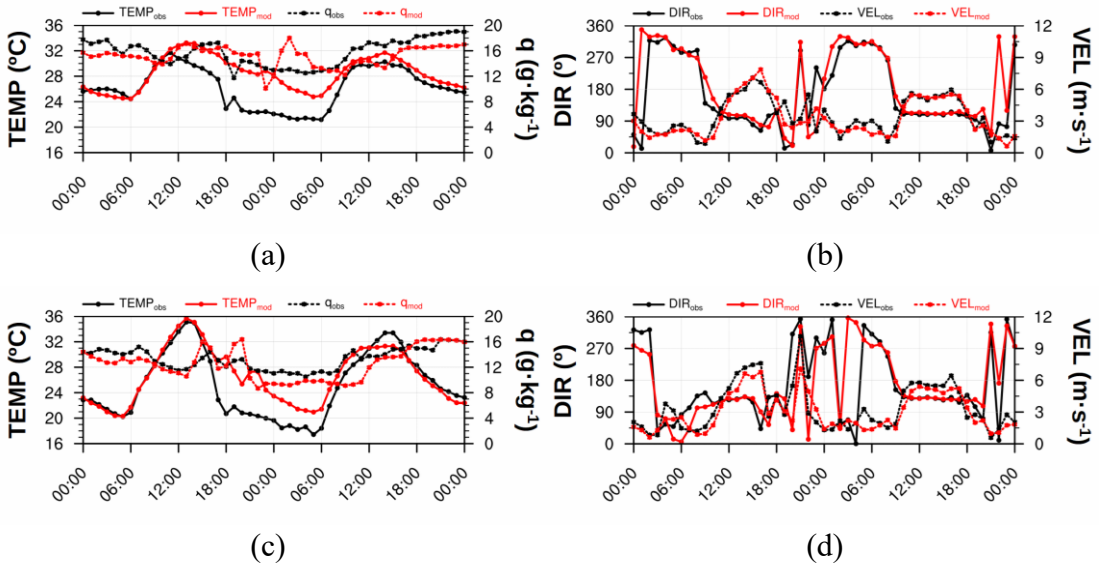

Figure 4.11 - Same as Figure 4.8 but for period 22nd-23rd July 2015.

Precipitation occurrence over VI is not reproduced in the model, however, temperature, humidity and wind variations are well-represented until 17 UTC before the temperature decrease associated with precipitation (Figures 4.11c, d). Analogously to PA, the influence of storm winds, well-represented in the model (Figure 4.11d), that produce light fluctuations in *q* and temperature are noticed between 19 and 22 UTC although

temperature biases ranging from -7 to -3 ºC last until 06 UTC (Figure 4.11c). After 06 UTC, the STM simulation reproduces more accurately temperature variations, except for the peak at 14 UTC, whilst q is underestimated until 13 UTC due to a delayed increase observed at 08 UTC and detected at 11 UTC in the model (Figure 4.11c), matching underestimated sea breeze intensity (Figure 4.11d).

4. SVA energetic exchanges

4.1. Sea breeze and summer storms

Summer storms originate due to the combination of sea breeze and upslope winds in the TRB driven by thermal differences. The analysis of the SVA energetic exchanges using surface measurements exposed in section 2 of this chapter suggests that convective cloud formation is subject to the advection of air masses located within the TRB in the morning and prior to the arrival of a moist and cool air mass from the sea. On average, wind observations over the inland station (AR) indicate that the formation of sea breeze initiates after 09 UTC, whilst q and θ variations denote that the air moistening and cooling starts at 14 UTC (see section 2). According to the well-reproduced features of the sea breeze in the model during daytime (05-19 UTC), a further analysis of the sea breeze stages and the generation of summer storms in the simulation domain is conducted here. Overall, simulated values indicate that almost all convective precipitation events within the period 15th to 23rd of July 2015 initiate before the arrival of an Intermediate Sea-Breeze Front (hereafter referred to as ISBF), except for the light convective precipitation during the 19th and the 23rd (Figure C.1 in Appendix C). This fact remarks the importance of the air masses situated over the TRB in the morning, as well as the land-atmosphere interactions in the formation, development and triggering of summer storms. In the following paragraphs, the summer storm event of the 16th regarding the STM simulation output is analyzed in detailed as an example.

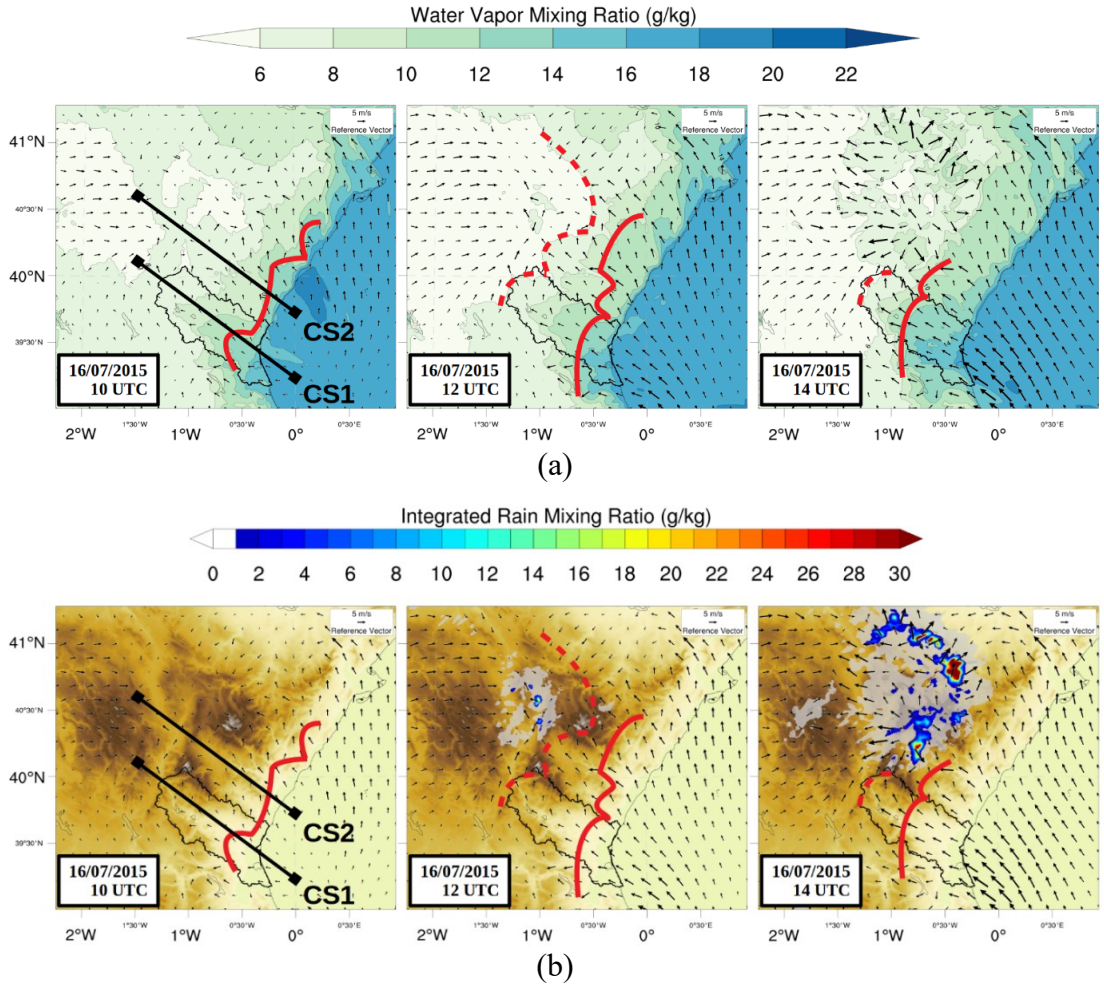

Figure 4.12 - Horizontal wind vectors (black arrows) with (a) 2-m mixing ratio, (b) topography, cloud cover (in gray) and integrated rain (q_{rain}) from STM for the 16th of July 2015 at 10, 12 and 14 UTC (from left to right). The SBF and the ISBF are denoted by the dashed and solid red lines, respectively. Black solid lines in the leftmost images indicate the two cross sections (marked as CS1 and CS2) shown in Figure 4.13.

According to simulated values, the 16th of July the SBF at the leading edge of the sea breeze reaches the upper part of the study area at about 12 UTC, as highlighted by the red dashed lines in Figure 4.12, so that the whole study area is under the influence of dominating sea breeze conditions. Besides, the sea breeze circulation seems to be confined to the extent of the study area from 12 to 14 UTC (static SBF) due to synoptic winds (*ponents*) blowing from the southwest (Figure 4.12). However, *ponents* interaction with the sea breeze generates a light convergence during this period since no sea breeze head is identified along the two considered cross sections (Figure 4.13); instead, the air advected along the study area seems to be forced along the upper part of the TRB, toward the northeast, merging with southwestern synoptic winds (Figure 4.12). Contrarily, the ISBF displaces inland and surpasses the pre-littoral of the study

area at 14 UTC generating a strong moistening near the surface (Figure 4.12a), and up to about 1500 m asl (Figure 4.13a) which analogously occurs in CS2 (Figure 4.13b). In this case, convection initiation occurs at about 12 UTC over the upper part of the TRB, i.e., outside the area affected by the sea breeze circulation within the Turia valley (Figure 4.12b), and it is not influenced by the formation of the SBF (Figure 4.13). This suggests that the formation of convective clouds in the upper part of the TRB is subject to the advection of early morning moist air in the Turia valley to upper levels of the atmosphere with the formation of upslope winds. In fact, an air mass moister and cooler than its surroundings located within the Turia valley is distinguished at 10 UTC in Figures 4.12 and 4.13. Moreover, this is further supported regarding the low water vapor content of the upper atmospheric levels during the period between 10 and 14 UTC (Figure 4.13).

After the formation, development and triggering of the summer storms, these convective systems displace toward coastal areas, perpendicular to upper-level wind direction from the southwest, absorbing moist air masses within the sea breeze that intensify precipitation (Figures 4.12b). Besides, the convergence of the ISBF at the gust front of the storm further enhances precipitation, as well as the formation of new convective cells in the upper part of the study area (see Figure C.2 in Appendix C).

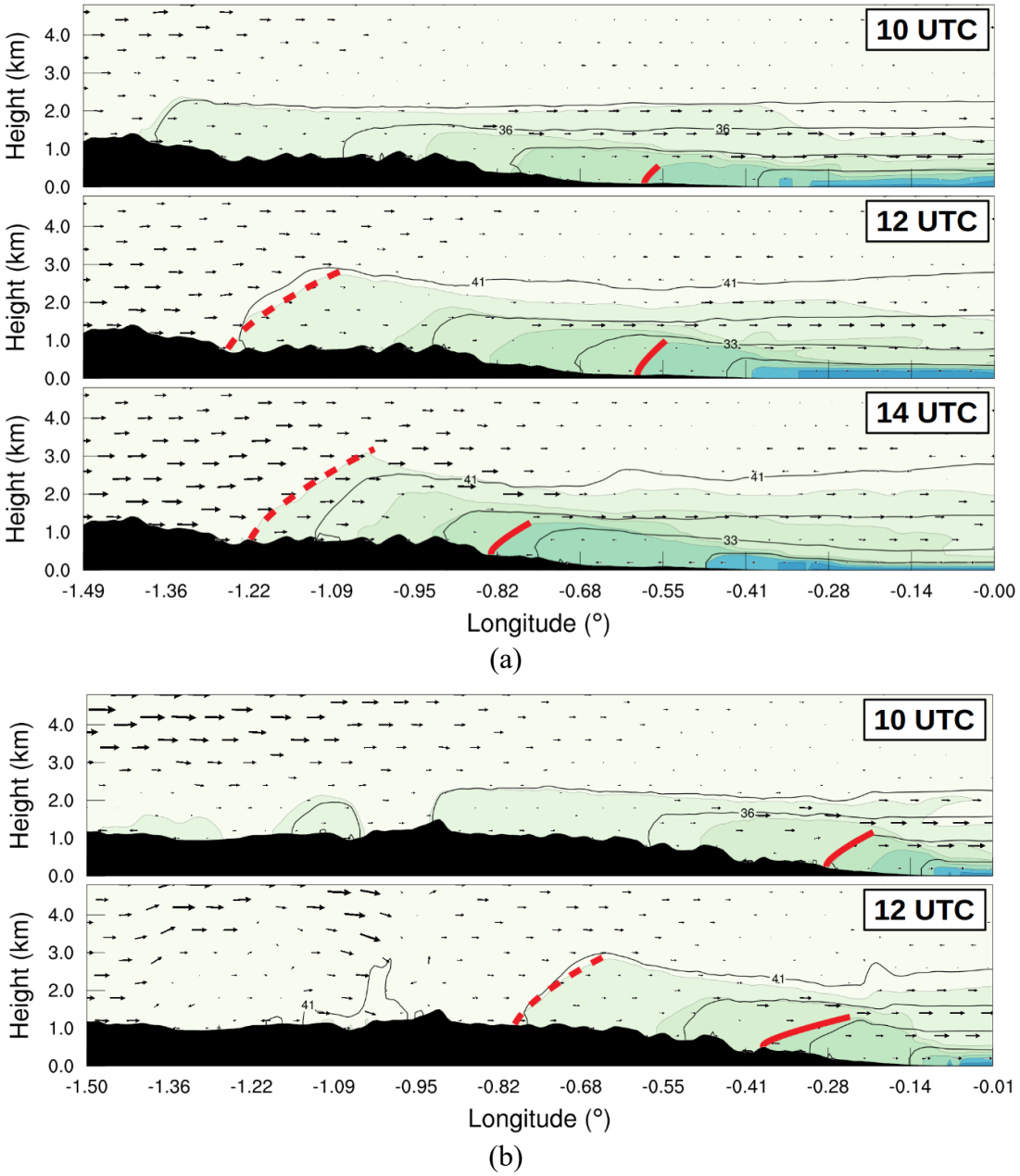

Figure 4.13 - Vertical distribution (0-5km) of wind, mixing ratio and potential temperature (contour lines) along cross sections (a) CS1 at 10, 12 and 14 UTC, and (b) CS2 at 10 and 12 UTC as shown in Figure 4.12.

4.2. Land-atmosphere interactions: mixing diagrams

The moistening and heating of the air advected upslope from the Turia valley before the generation of clouds can be examined using the model output. Concretely, the STM high-resolution simulation is used to quantify the SVA energetic exchanges at littoral, pre-littoral and inland locations within the study area with different dominating land use categories (see Figure 2.13 in Chapter 2). Mixing diagrams are generated for all six

points and nine days (a total of 54 plots) although here only the case for the 16th of July is presented whereas the rest of plots can be consulted in Appendix D.

The mixing diagram for the urban littoral point (LI_{URB}) along with the corresponding surface, advection and entrainment vectors (denoted by subscripts *sfc*, *adv* and *ent*, respectively) is shown in Figure 4.14a in order to provide a more detailed explanation of the information presented in Figure 4.15. In this case, the q-θ variation denotes an increase of θ at nearly constant q from 05 to 12 UTC, and a sudden change after 12 UTC toward increasing q at constant θ denoting the arrival of the ISBF. Thus, vectors are calculated before ISBF (05-12 UTC) and after ISBF (12-17 UTC). In this case, the final time is set at 17 UTC since winds considerable intensify due to the generation of storms after this time (see Figure C.2 in Appendix C). The definition of urban land use category in the Noah-MP LSM implies no moisture flux so that in both periods (before and after ISBF) the surface only produces a heating of the PBL (i.e., increase of θ at constant q), as well as an increment of PBLH (Figure 4.16). The advection vector indicates that the advected air is moister and cooler than the air mass situated over LI_{URB} during both periods denoted by the decreasing θ and increasing q. However, the air moistening is much more effective after the entrance of the ISBF at 12 UTC than in the morning period (05-12 UTC). This fact can be associated with the strong vertical development of the PBL incorporating air from the upper residual layer (entrainment) and limiting the advection cooling and drying effects in the period 05-12 UTC. At noon, the whole residual layer has been mixed in the PBL so that an inversion layer is reached restricting PBL growth (and entrainment) and allowing an effective air moistening related to advection (Figure 4.14a). In addition, the entrainment effect produces a further increase in θ as upper-level atmospheric layers incorporate to the mixing layer, especially before noon (Figure 4.14a). The vectors represented in Figure 4.14a are also obtained for the rest of mixing diagrams with differences associated with the characteristics of each location (e.g., land use category and distance to the sea), as well as large-scale circulations. It must be considered that in Figure 4.14a the initial period (before ISBF) can be further divided into two subperiods: (i) from 05 to 09 UTC, very low advection from inland areas, and (ii) from 09 to 12 UTC, sea breeze early stage as the wind veers to easterlies and intensifies, (Figure 4.14b). Similarly, the second period (after ISBF) can be divided into two subperiods regarding variations of q and θ (Figure 4.14a): (i) increasing q at constant θ from 12 to 14 UTC related to the ISBF entrance,

and (ii) decreasing q and θ at approximately constant RH from 14 to 17 UTC that may be connected to a decreasing PBLH (decreasing surface heat flux) and a strong stabilized advection from the east (Figure 4.14b). This occurs as insolation begins to decline lowering entrainment effects at the top, the residual layer starts to generate as surface layers detach from upper levels (Stull, 1988), so that sea breeze can progress further inland and accelerate (early mature stage of the sea breeze) as described in Miller et al. (2003). However, since the main goal in this section is to quantify surface contributions that can influence the formation of summer storms (mainly before ISBF) and their development or intensification (after ISBF), only these two main periods are considered for vector calculation (Figures 4.14a and 4.15). The main features described here are distinguished for all mixing diagrams generated over each point with differences related to ISBF entrance, i.e., distance to the sea, (Figures C.1 - C.9).

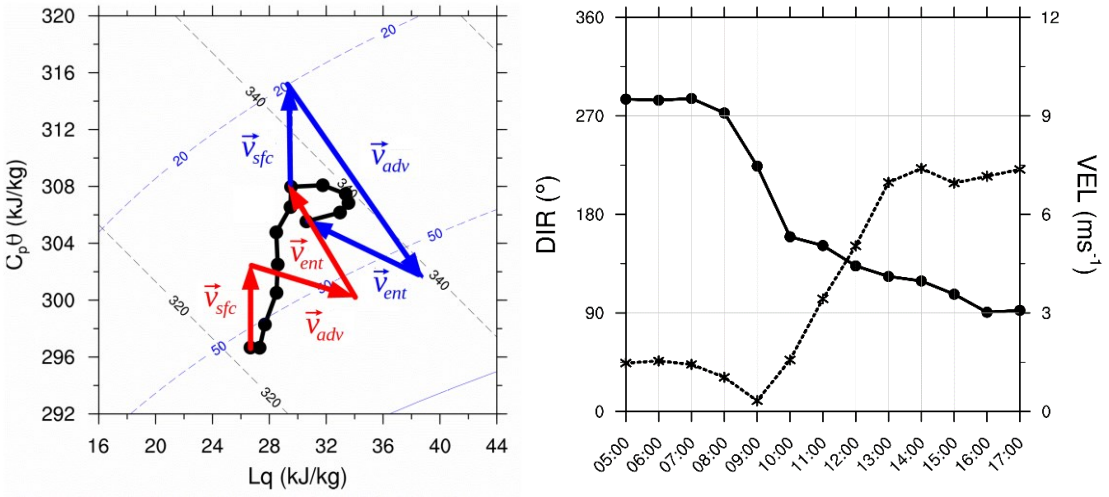

Figure 4.14 - (a) Mixing diagram with calculated surface (*sfc*), advection (*adv*) and entrainment (*ent*) vectors for two periods: before SBF (red) and after SBF (blue) from STM output, for the 16th of July 2015 over littoral urban grid point (LI_{URB}), and (b) the corresponding wind speed (dashed line) and direction (solid line). Dashed blue and black lines in (a) represent isolines of RH (Equation 2.17) and θ_e (Equation 2.18), respectively.

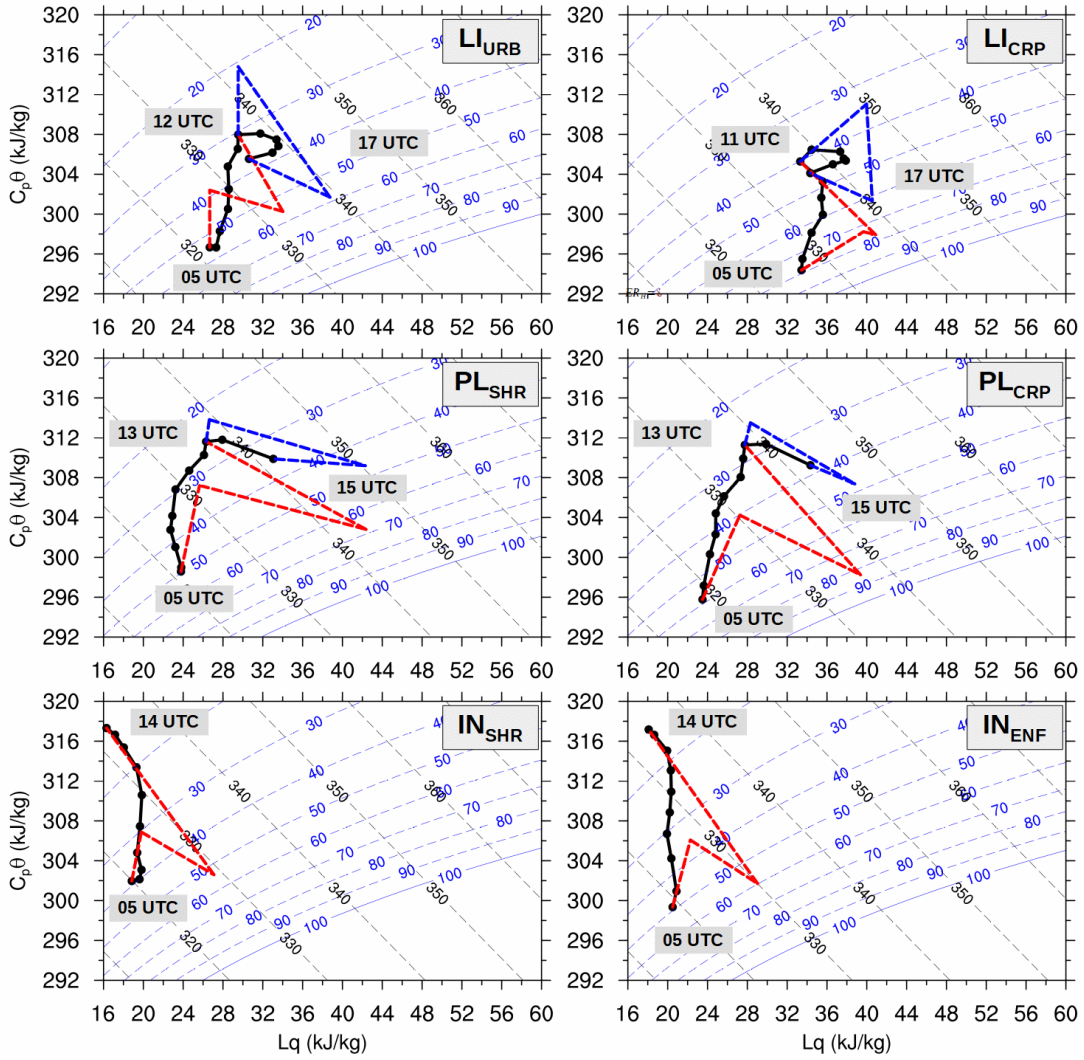

Figure 4.15 - As in Figure 4.12, mixing diagrams with calculated vectors for the 16th of July 2015 over littoral (LI), pre-littoral (PL) and inland (IN) locations and the different land use categories URB, CRP, SHR and ENF (namely urban and built-up land, cropland/woodland mosaic, mixed shrubland/grassland and evergreen needleleaf forest) using the STM output.

Analyzing the different contributions to the SVA system related to surface, advection and entrainment over the selected points facilitates the quantification of surface influence regarding land use and distance to sea. In fact, previously it was highlighted that at LI_{URB} there is no moisture flux from the surface (advection is the only source of moisture) which contrasts with the important moisture flux and very low advection obtained over LI_{CRP}, especially before the ISBF (Figure 4.15). However, LI_{URB} and LI_{CRP} show very similar evolution of q and θ, and a strong entrainment (Figure 4.15), as well as an equal development of the PBL with maximum heights of about 1km (11-12 UTC) despite the considerable differences in H, and especially in LE (Figure 4.16). This indicates that onshore circulations prevail over local surface fluxes reducing

differences between urban and cropland areas (low urban heat island effect) that may be linked to the poorly represented urban buildings in the model which can be improved with the implementation of a urban canopy model. In this simulation, main differences between these two locations are the generally drier conditions at LI_{URB} than over LI_{CRP}, as well as the considerably greater θ values over LI_{URB} than over LI_{CRP} in the morning linked to the urban heat island effect (Figure 4.15), despite the similar PBLH (Figure 4.16).

The croplands located over pre-littoral areas (PL_{CRP}) show lower water vapor contributions than LI_{CRP} linked to strong *LE* and *H* differences yielding higher θ and lower q (Figure 4.16). This contrast is mainly related to vegetation fraction (F_{VEG}) differences between the two locations, F_{VEG} of 0.52 and 0.36 at LI_{CRP} and PL_{CRP}, which strongly influence surface fluxes (see Equations 2.5-2.7 in Chapter 2 and Equations A.13-A.15 in Appendix A). Additionally, the later entrance of the ISBF allows a further development of the PBL, up to 1.5 km (Figure 4.16), due to *H* and the entrainment effect at the top of the PBL exceeding the important advection over PL_{CRP} (Figure 4.15). Overall, θ increases substantially and q increase slightly before the arrival of the ISBF, whilst, after the entrance of the ISBF, θ slightly decrease and q increases considerably at PL_{CRP} (Figure 4.15). The q-θ variations over PL_{SHR} are similar to PL_{CRP} although the former shows drier conditions, in both cases the humidity at 13 UTC is equal to the moisture provided by surface fluxes (Figure 4.15). Vectors indicate lower surface moisture fluxes, as well as a stronger advection and entrainment influence on q, at PL_{SHR} than over PL_{CRP}, whereas the contrary behavior is obtained for surface heat fluxes (Figure 4.15). The low heat and moisture contributions to the atmosphere after 13 UTC is mainly related to the short time considered (only two hours, from 13 to 15 UTC), as well as the decrease in insolation in the afternoon. Similarly to urban areas, the greater surface heat fluxes over mixed shrubland/grassland (SHR) land use category enhance the deepening of the PBL producing an additional reduction of q and an increment of θ by the entrainment effect (Figure 4.16).

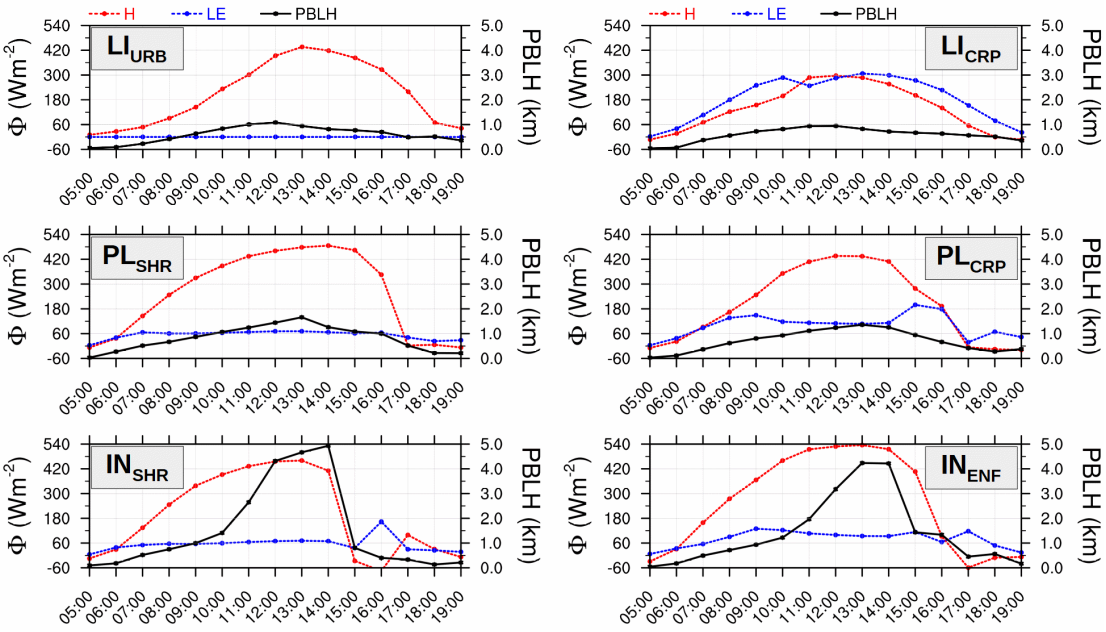

Figure 4.16 - Surface fluxes (Φ) for heat (*H*) and moisture (*LE*) and Planetary boundary layer height (*PBLH*) for the 16th of July 2015 over LI_{CRP}, PL_{CRP} and IN_{ENF} corresponding to mixing diagrams in Figure 4.13.

The two inland points considered show a very similar evolution of q and θ with a rapid increase in θ at nearly constant q until 11 and 12 UTC at IN_{SHR} and IN_{ENF}, respectively (Figure 4.15). After these times, q starts to decrease as θ continues to increase following an isoline of θ_e (about 332-333 K) that indicates an equilibrium among surface, advection and entrainment contributions regarding Equation 2.10 (Figure 4.15). In fact, between 12 and 14 UTC over IN_{SHR}, and from 13 to 14 UTC in IN_{ENF}, the PBL growth slows down (stops over IN_{ENF}) despite the great surface heat fluxes indicating that a limiting layer is achieved in the vertical (i.e., an inversion layer) that reduces entrainment (Figure 4.16). Advection is the main source of water vapor (with an additional input from the surface), as well as generates a cooling of the PBL in contrast to the PBL heating produced by the surface (Figure 4.15). At IN_{SHR} and IN_{ENF}, entrainment and surface heat fluxes produce a strong development of the PBL with the consequent drying at the top of the PBL (Figure 4.15). Besides, the sea breeze extends from the coastline to these locations, approximately (Figure 4.12), whereas the ISBF does not reach these points due to the formation of intense summer storms that significantly modify mesoscale circulations in the TRB.

In general, the evolution of q and θ follows the behavior exposed for the 16th of July 2015 with dominating advection fluxes increasing q, especially after the entrance of the

ISBF, and strong entrainment at the PBL top. Exceptionally, the 19th and 23rd advection fluxes of q are negative (i.e., PBL drying), mainly over inland locations, due to the stronger *ponents* that delay or limit the entrance of the SBF. On average, the dominating moistening effect of advection is shown at all the locations analyzed, except for LI_{CRP} where moisture fluxes exceed advection contributions during the period prior to the arrival of the ISBF (Table 4.5). These values indicate that areas close to the coast are generally under the influence of moist air masses with high *RH* in the early morning (e.g., about 60-80 % at 05 UTC the 16th of July, Figure 4.15) so that advection provides very little increments in q before the entrance of moister marine air. Besides, urban areas in the littoral (LI_{URB}) present lower *RH* (and q) values at 05 UTC than LI_{CRP} linked to the urban heat island effect (Figure 4.15), in agreement with average measurements shown in section 2. In LI_{CRP} a strong evapotranspiration dominates the humidity input to the SVA system with peak contributions close to 3 $g \cdot kg^{-1}$ during the day although entrainment produces a very abrupt drying exceeding surface moisture contribution (Table 4.5). Sensible heat fluxes and the entrainment effect at the PBL top show low differences between LI_{URB} and LI_{CRP} before ISBF, although the average PBL heating due to H at LI_{URB} is 1.4K greater than over LI_{CRP} after ISBF (Table 4.5). Besides, a substantial cooling effect is observed over both locations with the ISBF arrival (Table 4.5). Pre-littoral and inland locations present very similar values of surface and entrainment contributions to θ; in contrast, average q contributions to the PBL from advection (moistening) and entrainment (drying) are more abrupt over pre-littoral (6 $g \cdot kg^{-1}$ and -7 $g \cdot kg^{-1}$ for advection and entrainment, respectively) than over inland locations, remarking the important interactions between the PBL and the upper tropospheric levels under these atmospheric conditions (Table 4.6). Additionally, the q contributions from the surface (up to 1.3 $g \cdot kg^{-1}$ before ISBF at PL_{CRP}) almost cover the negative difference between advection and entrainment due to the mixing with the residual layer at the PBL top, although it must be emphasized that advection is the main factor contributing to the PBL moistening under these conditions (Table 4.5).

Overall, focusing on the averages from the surface over the studied areas presented in Tables 4.5-4.7, it can be noticed that CRP (cropland/woodland mosaic) category is the main source of water vapor to the PBL in the study area with a considerable reduction of contributions from littoral to pre-littoral mainly linked to vegetation fraction differences. Oppositely, mixed shrubland/grassland (SHR) and evergreen needleleaf forest (ENF) inland areas show very little differences in terms of water vapor

contributions; specifically, IN_{ENF} provides between 0.1 and 0.2 $g \cdot kg^{-1}$ more than IN_{SHR} with values up to 0.7 $g \cdot kg^{-1}$. Also, a lower entrainment effect of about -4 $g \cdot kg^{-1}$ is obtained over IN_{ENF} than over IN_{SHR} (around -5 $g \cdot kg^{-1}$). It must be notice that lower moisture contributions from the surface and greater entrainment effect obtained over IN_{SHR} are also linked to the greater distance to the coastline of this location (see Figure 2.13 in Chapter 2). These results indicate that, along with the values obtained over littoral and pre-littoral locations, water vapor contributions due to *LE* decrease from coastal to inland areas associated with the corresponding higher development of the PBL. Moreover, surface contributions to q are significantly exceeded by the entrainment drying effect at the PBL top, also linked to the PBL growth.

Table 4.5 - Daily increments of q and θ for periods (1) before ISBF and (2) after ISBF due to surface (*sfc*), advection (*adv*) and entrainment (*ent*) fluxes over littoral locations in STM. Maximum and minimum q and θ contributions for the period are highlighted in red and blue, respectively. The dashed line '--' indicates that no data is available at the given period and/or location (e.g., no moisture fluxes over urban). The corresponding averaged increments (AVG) for periods (1) and (2) are shown at the bottom with highest absolute values remarked in bold.

DATE	Period	Urban (LI_{URB})						Cropland/Woodland mosaic (LI_{CRP})					
		Δq_{sfc} (g/kg)	Δq_{adv} (g/kg)	Δq_{ent} (g/kg)	$\Delta\theta_{sfc}$ (K)	$\Delta\theta_{adv}$ (K)	$\Delta\theta_{ent}$ (K)	Δq_{sfc} (g/kg)	Δq_{adv} (g/kg)	Δq_{ent} (g/kg)	$\Delta\theta_{sfc}$ (K)	$\Delta\theta_{adv}$ (K)	$\Delta\theta_{ent}$ (K)
15/07	**(1)**	--	1.9	-1.3	5.7	-2.4	8.5	2.5	1.1	-2.6	4.6	0.1	6.5
	(2)	--	1.5	-2.1	4.7	-11.8	4.7	2.0	-0.9	-2.0	4.0	-7.8	**1.9**
16/07	**(1)**	--	2.9	-1.8	5.7	-2.1	7.7	2.5	0.5	-3.0	3.9	-0.3	7.3
	(2)	--	3.7	-3.2	6.8	-13.1	3.8	**2.7**	0.2	-2.5	**5.8**	-9.7	2.8
17/07	**(1)**	--	0.7	-4.7	3.7	-1.4	6.9	2.2	0.9	-5.2	4.8	-0.3	8.2
	(2)	--	5.4	-3.4	6.2	-11.8	5.2	**1.3**	2.2	-2.3	5.0	-9.5	2.2
18/07	**(1)**	--	0.2	-4.3	3.4	**-0.1**	6.2	1.9	-1.0	-5.5	5.6	-2.4	8.4
	(2)	--	9.5	-5.3	6.2	-14.9	6.7	1.0	1.6	0.1	3.5	-8.9	**1.9**
19/07	**(1)**	--	3.0	-2.2	3.6	-3.9	**10.0**	2.2	2.3	-3.5	3.6	-2.5	**10.5**
	(2)	--	5.3	-3.2	6.6	-14.4	4.8	1.6	2.7	-3.1	4.9	**-12.0**	4.2
20/07	**(1)**	--	**-2.8**	5.3	3.4	-1.2	4.3	1.9	-2.3	-4.2	3.6	**1.7**	4.1
	(2)	--	**9.6**	**-8.2**	**8.3**	**-16.7**	8.8	2.2	**4.9**	**-8.5**	5.4	-10.8	4.3
21/07	**(1)**	--	4.2	-4.1	5.2	-2.1	7.1	2.1	2.2	-5.2	5.0	-1.5	7.6
	(2)	--	5.7	-3.2	6.3	-11.4	**3.5**	1.6	3.2	-2.7	5.0	-10.5	3.9
22/07	**(1)**	--	0.4	-2.3	4.6	-1.9	6.1	2.3	0.0	-3.1	4.5	0.2	4.8
	(2)	--	7.7	-5.3	4.7	-10.1	5.9	**1.3**	3.9	-4.0	4.4	-7.2	3.3
23/07	**(1)**	--	-1.2	**-0.8**	**2.3**	-1.0	3.6	1.4	**-5.2**	**0.4**	**2.2**	0.7	5.1
	(2)	--	9.1	-5.0	6.2	-12.3	8.3	1.8	5.9	-4.1	5.2	-9.6	4.0
AVG	**(1)**	--	1.0	**-1.8**	4.2	-1.8	**6.7**	2.1	-0.2	**-2.6**	4.2	-0.5	**6.9**
	(2)	--	**6.8**	-4.8	6.2	**-12.9**	5.7	1.7	2.6	**-3.2**	4.8	**-9.6**	3.2

Table 4.6 - Same as in Table 4.5 but for pre-littoral locations.

DATE	Period	Shrubland (PL_{SHR})						Cropland/Woodland Mosaic (PL_{CRP})					
		Δq_{sfc} (g/kg)	Δq_{adv} (g/kg)	Δq_{ent} (g/kg)	$\Delta\theta_{sfc}$ (K)	$\Delta\theta_{adv}$ (K)	$\Delta\theta_{ent}$ (K)	Δq_{sfc} (g/kg)	Δq_{adv} (g/kg)	Δq_{ent} (g/kg)	$\Delta\theta_{sfc}$ (K)	$\Delta\theta_{adv}$ (K)	$\Delta\theta_{ent}$ (K)
15/07	**(1)**	0.8	9.6	-8.6	**10.5**	**-11.9**	12.8	**2.1**	9.7	-10.2	**9.5**	-9.0	13.6
	(2)	0.2	2.8	-3.3	3.1	-6.3	-0.1	0.5	**-0.6**	**-0.4**	2.7	-6.9	**0.6**
16/07	**(1)**	0.7	6.7	-6.4	8.6	-4.4	8.8	1.5	4.8	-4.6	8.5	-6.0	13.0
	(2)	**0.1**	6.2	-3.7	2.2	-4.6	0.7	0.2	4.2	-1.8	2.2	-6.1	1.9
17/07	**(1)**	0.6	4.6	-4.1	7.1	-0.2	5.9	1.3	1.3	-2.5	6.4	-3.7	11.7
	(2)	0.1	4.7	-3.5	2.1	-4.8	-0.1	0.4	2.9	-1.6	2.8	-8.0	2.5
18/07	**(1)**	0.5	4.5	-8.0	5.4	**0.9**	6.6	1.1	0.1	-5.9	5.6	-2.9	11.9
	(2)	0.1	6.2	-3.5	1.7	-4.6	-0.3	0.3	3.6	-0.6	1.9	-7.7	2.1
19/07	**(1)**	0.7	-1.6	-0.2	2.5	-8.7	-0.7	0.8	5.9	-7.8	3.0	-6.6	17.7
	(2)	0.2	5.2	-2.9	1.2	-1.2	-0.7	**0.1**	3.5	-1.6	**1.1**	-4.5	2.5
20/07	**(1)**	**1.0**	4.4	-5.0	7.2	-7.0	8.3	1.8	5.8	-6.9	6.8	-5.2	10.4
	(2)	0.4	8.6	-6.0	4.2	-8.1	1.8	0.6	6.6	-4.2	4.1	**-10.3**	3.4
21/07	**(1)**	0.9	10.9	**-11.8**	7.9	-6.5	11.4	1.6	7.2	-8.5	8.0	-6.7	13.4
	(2)	0.3	**11.7**	-10.9	3.4	-9.4	3.6	0.5	4.3	-4.3	3.6	-8.6	2.3
22/07	**(1)**	0.5	8.6	-11.2	4.3	-3.8	**13.8**	1.0	9.3	**-12.7**	5.6	-9.3	**19.6**
	(2)	0.1	8.6	-4.0	**0.9**	-3.1	0.1	**0.1**	**10.7**	-5.5	**1.1**	-7.4	3.8
23/07	**(1)**	0.5	**-2.1**	**0.7**	2.7	7.6	**-3.1**	0.9	1.2	-2.2	3.0	**0.7**	5.6
	(2)	0.3	10.2	-5.5	4.3	-7.0	3.5	0.5	7.5	-3.6	4.0	-9.4	6.8
AVG	**(1)**	0.7	6.0	**-7.0**	6.2	-1.8	**7.1**	1.3	5.5	**-7.3**	6.3	-5.4	**13.0**
	(2)	0.2	**7.2**	-4.9	2.6	**-5.4**	0.9	0.4	**4.7**	-2.6	2.6	**-7.7**	2.9

Table 4.7 - Same as in Table 4.5 but for inland locations.

DATE	Period	Shrubland (IN_{SHR})						Evergreen needle-leaf forest (IN_{ENF})					
		Δq_{sfc} (g/kg)	Δq_{adv} (g/kg)	Δq_{ent} (g/kg)	$\Delta\theta_{sfc}$ (K)	$\Delta\theta_{adv}$ (K)	$\Delta\theta_{ent}$ (K)	Δq_{sfc} (g/kg)	Δq_{adv} (g/kg)	Δq_{ent} (g/kg)	$\Delta\theta_{sfc}$ (K)	$\Delta\theta_{adv}$ (K)	$\Delta\theta_{ent}$ (K)
15/07	**(1)**	0.5	**8.0**	**-10.3**	**7.4**	**-10.2**	**16.5**	**1.0**	**9.7**	**-11.3**	**9.8**	**-14.0**	**19.2**
	(2)	0.1	7.4	-2.2	1.4	-7.4	0.0	0.2	6.9	-3.6	2.0	-9.3	0.4
16/07	**(1)**	0.4	2.9	-4.3	4.9	-4.3	14.7	0.7	2.7	-4.4	6.7	-4.4	15.5
	(2)	--	--	--	--	--	--	--	--	--	--	--	--
17/07	**(1)**	0.4	3.7	-3.8	6.0	-6.3	14.2	0.8	1.6	-1.8	7.1	-3.3	11.8
	(2)	0.1	2.0	-1.0	0.8	-2.5	0.4	**0.1**	2.3	-0.5	1.0	-2.9	**-0.9**
18/07	**(1)**	0.3	3.8	-6.5	5.1	-2.7	12.5	0.6	0.5	-4.1	5.3	-0.4	11.3
	(2)	**0.0**	0.3	**1.4**	**0.4**	-0.1	**-2.1**	**0.1**	2.9	-0.4	0.9	-2.1	**-0.9**
19/07	**(1)**	**0.7**	-1.8	-2.3	3.5	-2.9	13.0	0.6	**-2.7**	-0.3	3.2	2.5	9.1
	(2)	--	--	--	--	--	--	**0.1**	-0.8	**1.3**	**0.2**	-0.8	0.1
20/07	**(1)**	0.6	5.1	-7.7	4.9	-5.5	12.7	0.7	5.7	-7.4	6.3	-10.4	16.8
	(2)	0.2	4.8	-0.9	1.2	-5.4	-0.8	0.2	6.1	-3.0	1.6	-8.1	0.4
21/07	**(1)**	0.6	1.7	-5.1	4.8	-1.2	10.8	0.7	2.5	-5.8	6.2	-4.4	14.0
	(2)	0.1	3.0	1.1	0.6	-1.7	-1.9	0.2	6.6	-2.3	2.0	-7.5	-0.2
22/07	**(1)**	0.4	0.4	-4.1	4.0	0.4	7.6	0.5	-4.2	0.5	4.5	1.1	8.3
	(2)	--	--	--	--	--	--	--	--	--	--	--	--
23/07	**(1)**	**0.7**	**-2.9**	0.2	4.8	**8.3**	0.1	0.8	**-2.7**	0.3	4.9	**7.0**	2.2
	(2)	--	--	--	--	--	--	--	--	--	--	--	--
AVG	**(1)**	0.5	2.3	**-4.9**	5.0	-2.7	**11.3**	0.7	2.5	**-3.7**	6.0	-2.9	**12.0**
	(2)	0.1	**3.5**	-0.3	0.9	**-3.4**	-0.9	0.2	**4.0**	-1.4	1.3	**-5.1**	-0.2

In order to further analyze surface differences among the land use categories in the model, the EF is calculated according to Equation 2.19 (section 6.1 in Chapter 2). The EF (the ratio of LE_{sfc} with respect to the total surface fluxes) values show the importance of CRP in littoral areas with dominant *LE* (more than 50 % in general) and the considerable decrease over pre-littoral areas with *LE* representing 30-40 % of the total surface fluxes (Figure 4.17), in accordance with F_{VEG} values of 0.52 and 0.36 at LI_{CRP} and PL_{CRP}, respectively. This contrast is also obtained between PL_{SHR} and IN_{SHR} although differences are much lower (about 1-2 %), also linked to low differences in the F_{VEG} values (Figure 4.17). Besides, EF values over IN_{ENF} denote similar contributions to PL_{SHR} in general, although these are stronger the days with dryer soils (the day after localized convective precipitation or no precipitation) and lower the days with wet soil conditions (the day after extended convective precipitation) in the TRB (Figure 4.17). Days with wet soil conditions are remarked in the bold squares (the 19th and 23rd) in Figure 4.17 and present the greatest EF values in general. The greater EF values over IN_{ENF} during dry soil conditions are apparently connected to the fact that forests (evergreen needleleaf forests in this case) pump into the atmosphere the water available from deeper soil layers (all four soil layers in the model) than mixed shrublands/grasslands (only considering the three layers closer to the surface). The information regarding the extension of root for each type of land use category commented here can be consulted in Table A.1 of Appendix A.

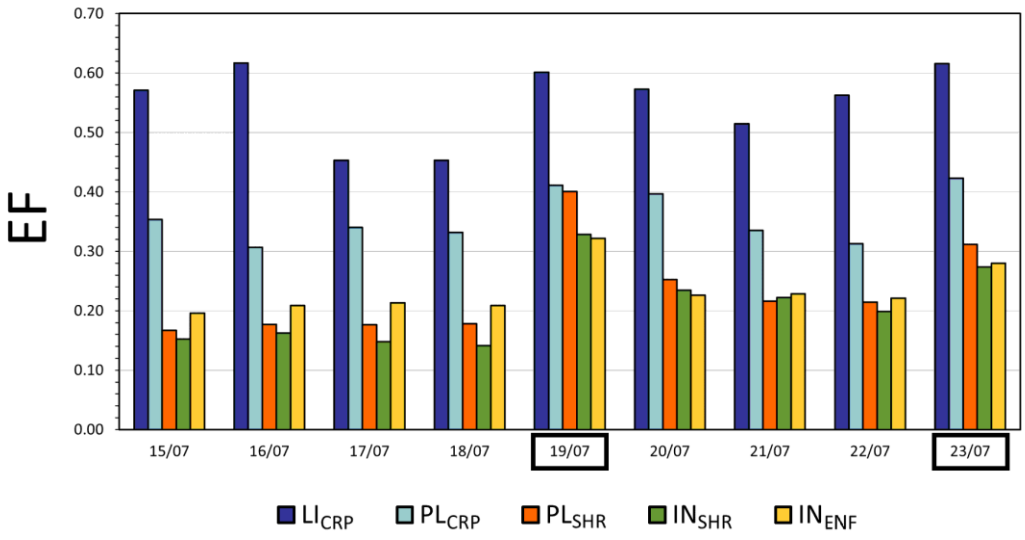

Figure 4.17 - Evaporative fraction (*EF*, Equation 2.19) over locations LI_{CRP}, PL_{CRP}, PL_{SHR}, IN_{SHR} and IN_{FOR}. The dates inside a frame indicate generalized wet soil conditions in the study area due to widespread convective precipitation occurred the previous day.

4.3. Land-atmosphere interactions: trajectories

The quantification of surface contributions to the atmosphere, specifically to the PBL, can be carried out in a similar manner as in subsection 4.2 but from a different point of view following the methodology introduced in the subsection 6.2 of Chapter 2. Analogously to section 4.2, the analysis of trajectories corresponding to the 16th of July is explained in detailed in this subsection although this procedure is conducted for all days in the study period (15th - 23rd). All trajectories can be visualized in Appendix E.

The calculation of trajectories related to the formation and development of summer storms with the VAPOR tool shows different origins within the TRB of the air parcels, which seems to be linked to local nighttime wind direction and speed. The 16th of July 2015, convection initialization occurs over the uppermost part of the TRB with air advected from lower parts of the TRB according to the backward unsteady trajectory calculated (Figure 4.18a). Specifically, the air parcel displaces upwards along the Turia valley from 06 to 10 UTC due to the formation of thermally driven winds; at about 10 UTC, it displaces slightly up and down, marking the strong air mixing within the PBL, and between 11 and 12 UTC the air parcel moves significantly upwards generating clouds and precipitation intensities exceeding 5 mm·h^{-1} in the period 12-13 UTC (Figure 4.18a). In the afternoon, these convective systems further develop, and new ones originate in the interior areas of the domain, especially in the upper TRB, with an intensification of convective precipitation over middle parts of the TRB as indicated by precipitation rates exceeding 30 mm·h^{-1} according to the model (Figure 4.18b). In this case, a storm generates outside the limits of the study area and then intensifies as it displaces over the Turia valley (Figure 4.18b). The air mass providing moisture and mainly responsible for the intensification of the convective system is advected from the sea along the sea breeze flow (i.e., the ISBF), as shown in Figure 4.18b. It must be noticed that the convergence zones over southern areas of the domain are influenced by the storm winds from the previous generation of convective systems that slightly modify sea breeze paths and its intensity (see Figure C.2 in Appendix C).

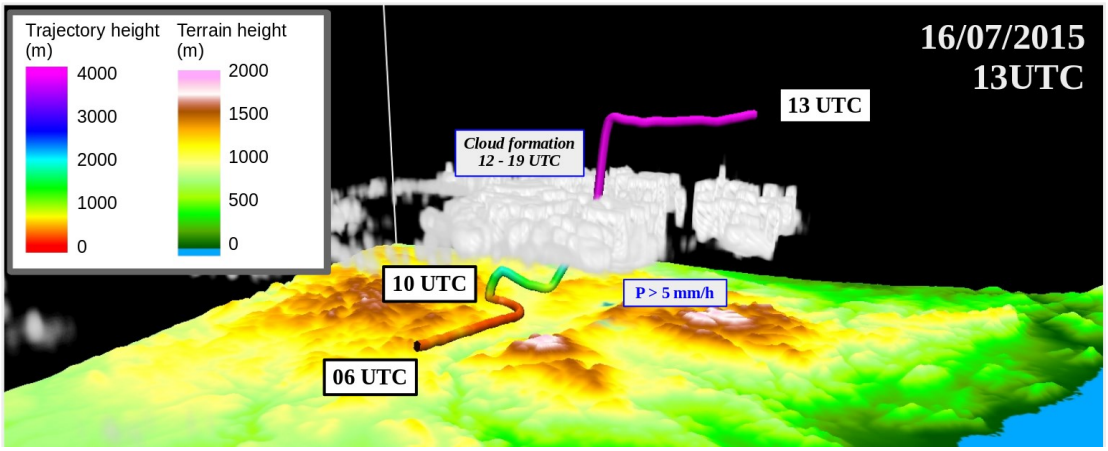

(a)

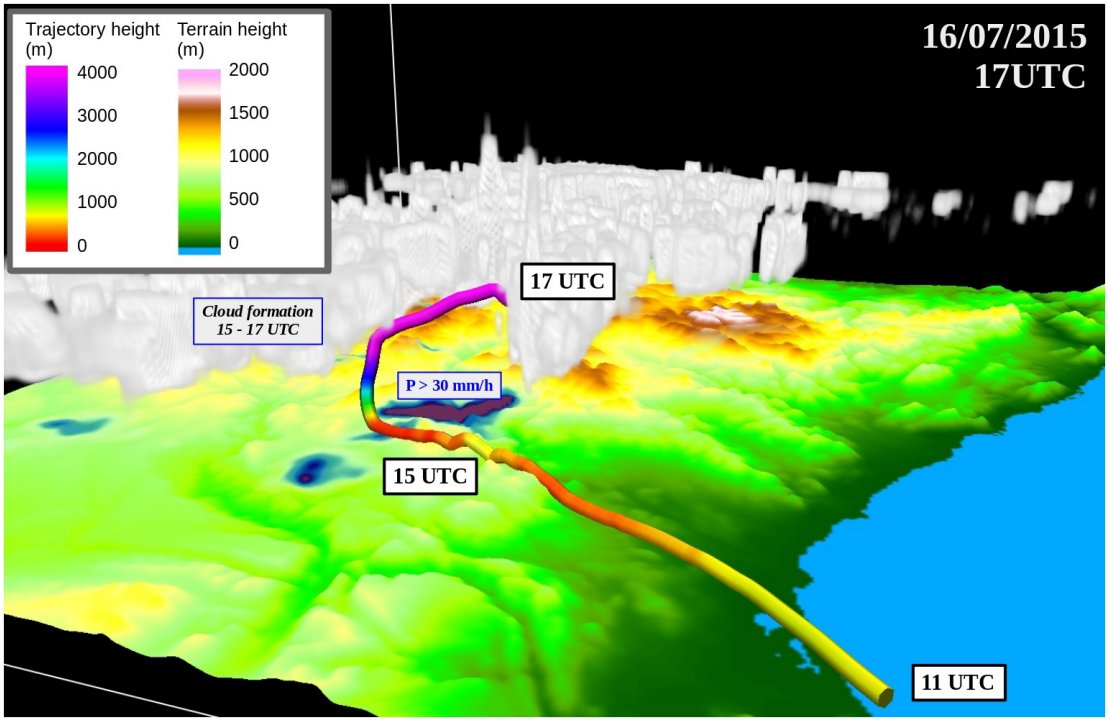

(b)

Figure 4.18 - 3D topographic maps with unsteady (time-varying) backward and forward trajectories calculated with the VAPOR tool (a) from convective clouds (represented in grey) generated over the TRB, and (b) from the ISBF for the 16th of July 2015. The coloring of trajectory lines denotes the height with respect to the ground at the given location. Annotations regarding time, convective cloud generation periods and precipitation intensity (P) are also shown, as well as precipitation is represented in blue to pink colors over topography.

In general, the initialization of convection at noon, as well as the intensification of precipitation in the afternoon, are subject to the properties of the air masses advected (i.e., the air parcels). In the morning, the properties of the air parcel (temperature and moisture content) delimit the cloud condensation level (CCL), in other words, the cloud formation and the further development of convective systems in the convergence zone. In the afternoon, convective precipitation enhancement depends on the water vapor content provided by the advected marine air (storm inflow) as storms displace toward littoral areas.

4.3.1. Variations of q and θ

The different characteristics of the two air parcels can be examined extracting vertical profiles of q and θ along the trajectory (see Section 6.2 in Chapter 2). To this end, q and θ variations in vertical along the trajectories shown in Figure 4.18 were extracted and analyzed in this section (Figures 4.19, 4.21, and 4.23). Besides, surface and entrainment influence over the air parcels were calculated using Equations 2.21-2.24, introduced in Chapter 2, and total contributions to q and θ within the PBL along the trajectory (cumulative summed contributions) are presented in Figures 4.20 and 4.22 for before (1) and after ISBF (2) trajectories, respectively. Additionally, these figures also show the evolutions of q (Figure 4.20) and θ (Figure 4.22). Total contributions provide information about the overall changes in the properties of the air parcel associated with the two estimated contributions: surface fluxes and entrainment.

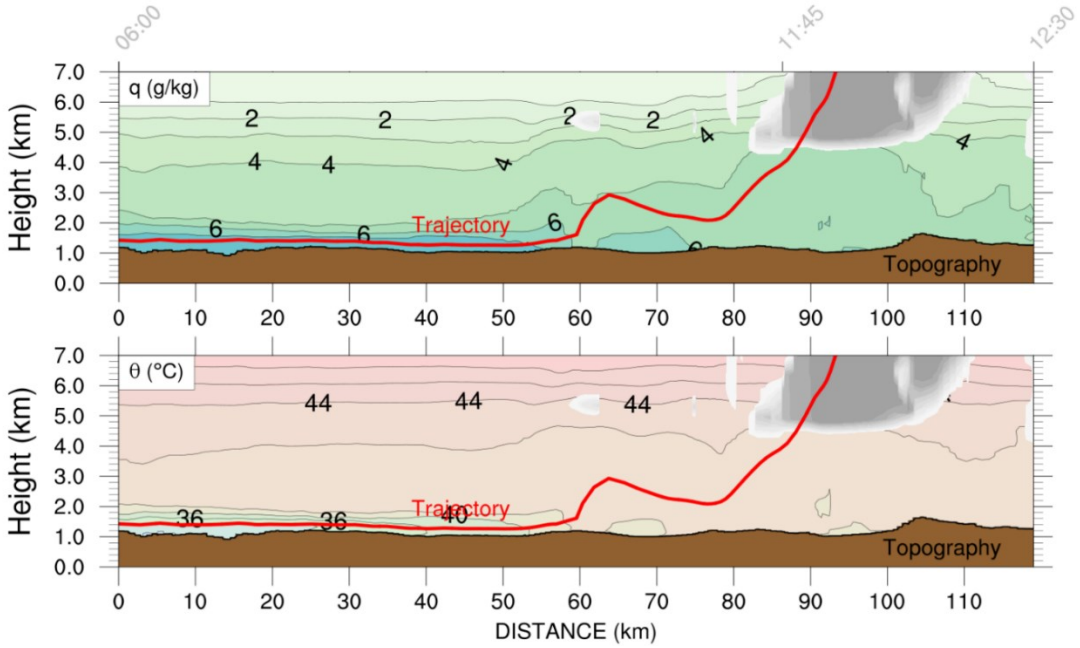

Figure 4.19 - Cross section contour plots corresponding to the trajectory in Figure 4.18a for (top) q and (bottom) θ together with trajectory height (red line), cloud fraction (in grey) and topography (in brown).

The two air parcels present strong differences regarding q and θ values along the considered trajectories linked to their origin and interactions. In the first case (1), the analysis of the air parcel associated with convective clouds generation at noon shows that

- Initially, the air parcel displaces about 55 km along the Turia valley between 06 and 10 UTC subject to a strong heating and slight humidity variations with $q >$ 6 g·kg^{-1} the first 1500 m asl in the vertical, approximately (Figure 4.19). In fact, the quantification of q and θ contributions to the air parcel (Equations 2.21-2.24 in Chapter 2) indicate that θ increase is mainly linked to H (about 4) and entrainment produces an additional increase of 3 ºC; contrarily, the entrainment generates a reduction in q of -1 g·kg^{-1} that exceeds the q increase of 0.5 g·kg^{-1} associated with LE (Figures 4.20a, b). The relatively low entrainment effect over the parcel is associated with the very limited PBL development (Figure 4.20c), indicating a very low interaction between the air parcel and the upper levels of the atmosphere during this period.
- After the initial 55 km approximately, at 10 UTC, the air parcel displaces uphill, reaches a convergence zone that forces it up achieving a height of 3 km asl

(about 2 km with respect to the ground) and then descends to about 2 km asl (Figure 4.19). It is important to highlight that the upslope winds force the air parcel to change direction toward a convergence zone (Figure 4.18) where shallow cumulus clouds begin to form (Figure 4.19). However, the air parcel escapes the upward flow and displaces over the Turia valley at a height of 2 km, where a surface layer of 1500 m (trajectory segment 65-75 km) seems to be detached from the general PBL evolution (Figure 4.19), that is, air is forced above this surface layer at this time. During this period (trajectory segment 55-80 km approximately), the entrainment effect produces a decrease in q of about -2 $g \cdot kg^{-1}$ due to the strong PBL growth of 2 km on average (Figures 4.20a,c), which also limits surface contribution to q (see Equation 2.21 in Chapter 2). The strong development of the PBL also implies θ increment to be dominated by the entrainment effect at the top of the PBL (Figure 4.20b). However, the surface layer is considered to be part of the air parcel in this approach (delimited between the ground and *PBLH*) so that entrainment produces a slight moistening (~0.2 $g \cdot kg^{-1}$) and cooling (-0.5 ºC) of the air parcel regarding the low variations of the *PBLH* at about 70 km (Figure 4.20). This situation is interpreted as a moistening and cooling due to entrainment at the front regarding the air parcel displacement, although it may lead to underestimating entrainment effects.

The last 5 km of the trajectory, the air parcel, with q and θ values of 5.5 $g \cdot kg^{-1}$ and 41 ºC, is forced upwards due to strong vertical winds (strong convergence zone) and condensation occurs at 4-5 km asl (Figure 4.19). Variations in q and θ due to surface fluxes and entrainment are very low during this brief period, as well as the PBLH is nearly constant (Figure 4.20), before the formation of convective clouds (Figure 4.19).

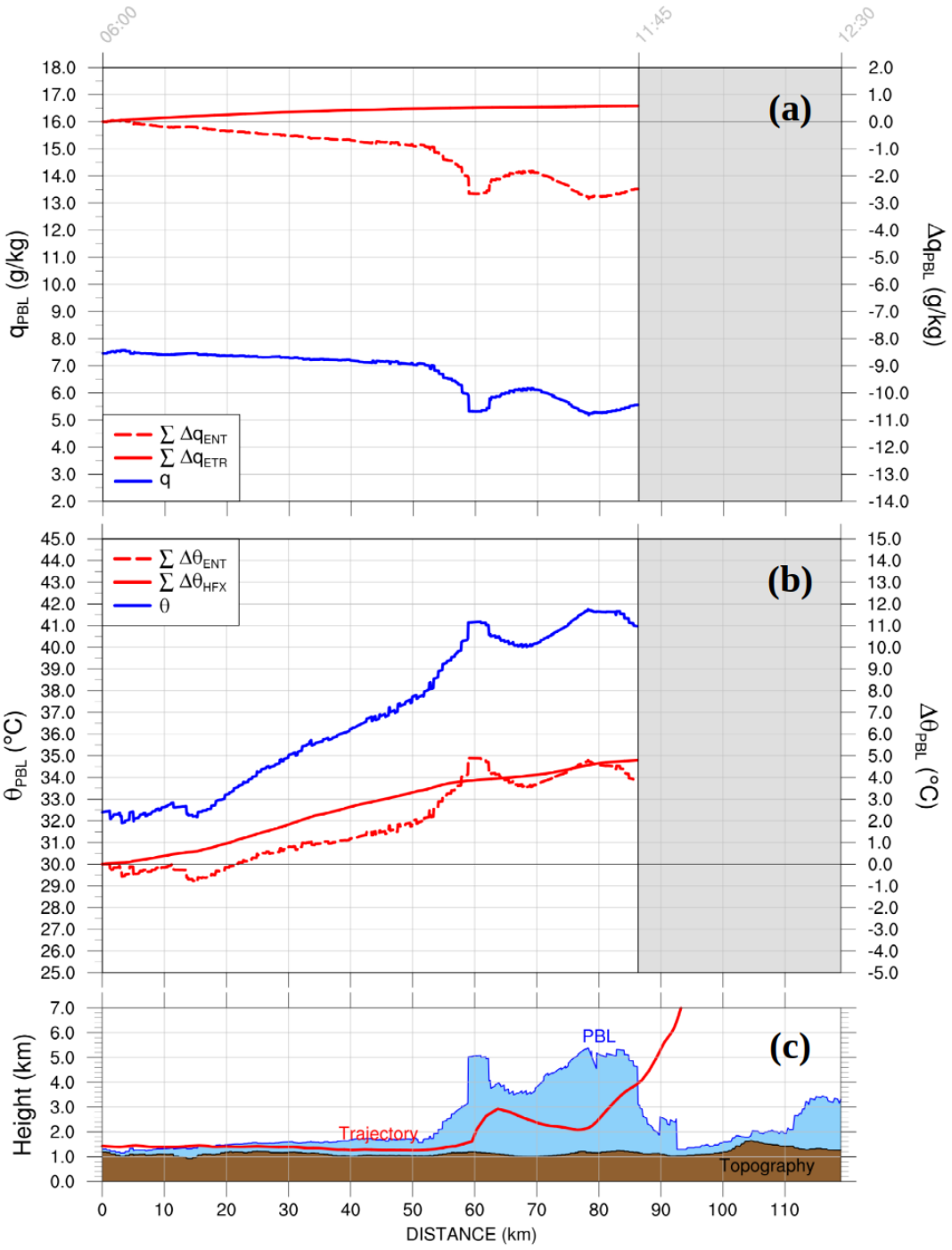

Figure 4.20 - Cross section corresponding to the trajectory in Figure 4.18a with the evolution of (a) q and (b) θ within the PBL (blue line) together with the corresponding cumulative summed contributions from the surface (red solid line) and the entrainment effect (red dashed line), and (c) trajectory height together with PBL (in blue) and topography (in brown).

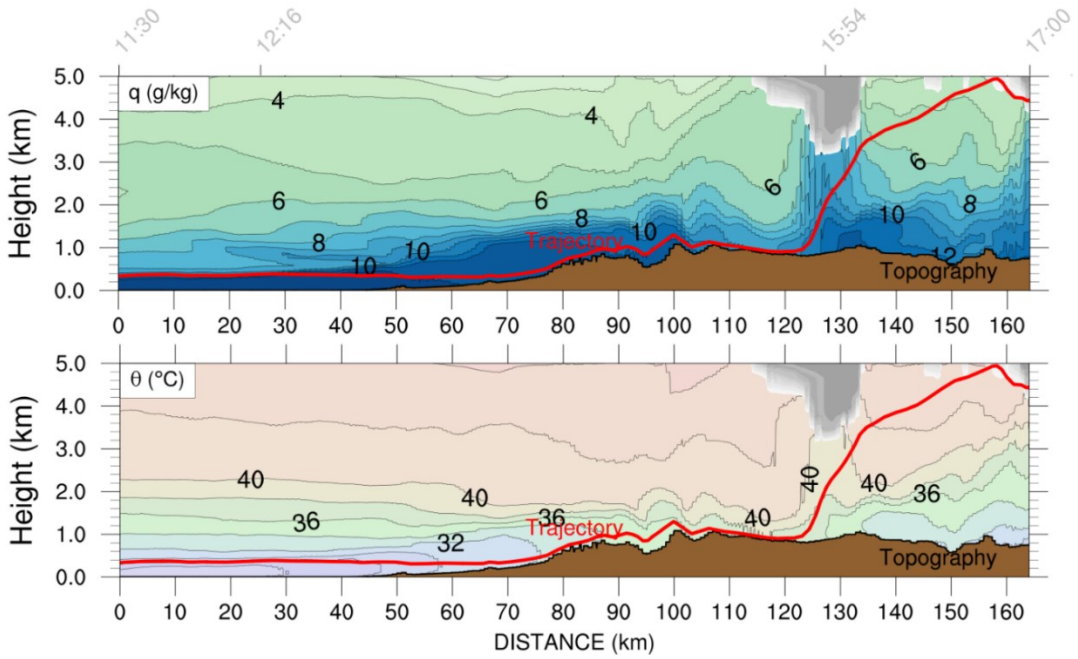

Figure 4.21 - Same as Figure 4.19 but for trajectory in Figure 4.18b.

In the second trajectory considered (2) for the 16th, describing the evolution of a marine air parcel, the analysis indicates that

- A moist (q > 14 g·kg^{-1}) and cool (θ < 28 ºC) marine air parcel moves inland along with the sea breeze (Figure 4.21). It presents an initial height of about 500 m (*PBLH*) which increments slightly as it moves inland due to H and entrainment effects (Figure 4.22c). Specifically, a low PBL development (up to 1 km above ground) occurs the first 100 km of the trajectory due to the combined effect of entrainment and surface heat fluxes (about 5 ºC and 4 ºC, respectively), together with a drying of the air parcel due to entrainment effect (-3 g·kg^{-1}) exceeding *LE* contribution to q of 1 g·kg^{-1} (Figure 4.22). Overall, a strong entrainment occurs during this segment of the trajectory (0-100 km) despite the low PBL growth (air parcel height), reducing initial q values of 16 g·kg^{-1} over the sea down to 13 g·kg^{-1}, indicating a strong upper-level dry air mixing into the air parcel considered. In other words, the air parcel displaces efficiently inland along a narrow channel coinciding with the sea breeze early mature stage defined in Miller et al. (2003) and connected to the beginning of insolation decline. Under this situation, it is expected a low entrainment as

surface sea breeze flows tend to detach from upper levels; however, the generation of convective systems may influence these conditions.

- The last 25 km of the trajectory, the convergence zone delimited by the gust front of the storm (see also Figure C.2 in Appendix C) forces the moist air parcel up providing additional water vapor and enhancing precipitation (Figure 4.21). The abrupt growth of the PBL produced by the storm gust front along with the convective cloud formation diminishes surface contributions to q and θ, as well as increases the air mixing at the PBL top, so that q further reduces (down to 12 $g \cdot kg^{-1}$) and θ increases from 35 ºC to 37 ºC (Figure 4.22). The gust front of the storm produces a substantial increment in q (about 4 $g \cdot kg^{-1}$) and decrease in θ (3 ºC) the last 15 km of the considered trajectory (Figure 4.22). However, a strong drying and heating of the air parcel occurs before the upward forcing of the parcel (Figure 4.22), which seems to be linked to the subsidence and mixing of upper-level air (Figure 4.21).

Overall, the PBL growth is the main limiting factor in the q increase due to LE at the surface, as well as in the further drying (and development) of the PBL due to entrainment. The 16th of July, the former effect reduces surface contributions to less than 1 $g \cdot kg^{-1}$ in the morning, prior to convection initialization, whereas the entrance of the ISBF enhancing precipitation is slightly less affected since the air parcel growth in the vertical is lower than in the morning. However, entrainment significantly reduces q in both trajectories; specifically, entrainment reduction of q is about four times the increase due to LE at the surface in the morning so that it is identified as the main factor influencing air parcel properties (Figure 4.22). Moreover, these results are obtained for the rest of analyzed trajectories with the summarized values for surface and entrainment effects over q and θ shown in Table 4.8.

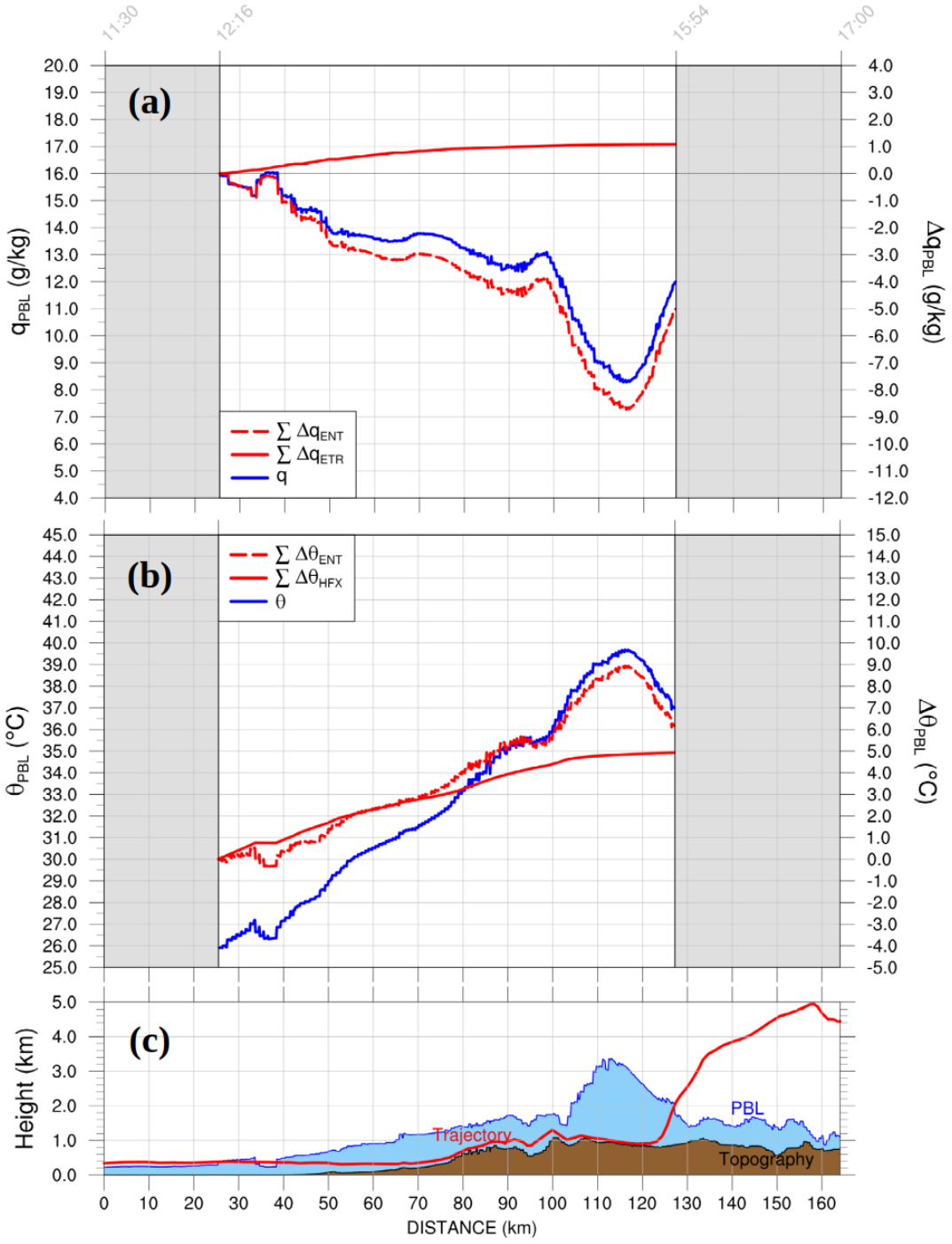

Figure 4.22 - Same as Figure 4.20 but for trajectory in Figure 4.18b.

Table 4.8 – Mean increment of q and θ regarding surface (*sfc*) and entrainment (*ent*) along the extracted unsteady trajectories (1) and (2), and each day (see subsection 6.2 in Chapter 2), together with the mean PBLH. Maximum and minimum q and θ contributions for the period are highlighted in red and blue, respectively, and the averaged increments (AVG) for trajectories (1) and (2) are shown at the bottom. The asterisk indicates a particular case regarding the extracted trajectory.

DATE	Traj.	Δq_{sfc} (g·kg^{-1})	Δq_{ent} (g·kg^{-1})	$\Delta\theta_{sfc}$ (ºC)	$\Delta\theta_{ent}$ (ºC)	PBLH (m)
15/07	**(1)**	**1.1**	-4.4	4.8	6.0	2160
	(2)	0.6	-7.4	5.7	**10.4**	1500
16/07	**(1)**	0.4	-2.2	4.8	3.8	2240
	(2)	1.0	-5.8	4.9	6.2	980
17/07	**(1)***	0.4	**-0.7**	4.0	5.8	1970
	(2)	0.5	-7.7	5.3	8.3	1840
18/07	**(1)**	0.5	-3.1	3.8	4.9	1560
	(2)	0.3	-7.5	3.7	7.3	1360
19/07	**(1)**	**0.2**	-1.5	**2.6**	4.6	2690
	(2)	0.5	-5.7	5.0	6.7	1290
20/07	**(1)***	0.5	-0.9	3.7	2.5	2520
	(2)	**1.1**	**-12.5**	**6.9**	9.1	1420
21/07	**(1)**	0.5	-3.7	4.7	7.3	**2900**
	(2)	0.3	-7.6	4.3	9.7	2110
22/07	**(1)***	0.3	-0.9	4.6	**2.2**	2660
	(2)	0.6	-11.4	6.6	7.1	1180
23/07	**(1)**	0.3	-2.0	4.5	3.4	1990
	(2)	0.6	-3.6	6.1	4.4	**440**
AVG	**(1)**	0.5	-2.2	4.2	4.5	2300
	(2)	0.6	-7.7	5.4	7.7	1350

Average values show that surface contributions to q are generally low (0.5 and 0.6 g·kg^{-1} for morning and marine trajectories, respectively) in contrast with the significant heating of air parcels linked to H at the surface, especially in the morning trajectories when it represents the main factor (Table 4.8). In general, entrainment and surface contributions to θ are similar, whereas q is mainly influenced by the entrainment effect with averaged contributions of -2.2 g·kg^{-1} in the morning and -7.7 g·kg^{-1} in the marine trajectories, despite the greater development of the PBL during the morning trajectories (PBLH of 2300 m), on average (Table 4.8). This result indicates that the dry air mixing occurring at the top of the PBL is generally greater than the values obtained for the 16th of July for moist marine air parcels displaced inland, with peak values of -12.5 g·kg^{-1} obtained the 20th of July in the afternoon (Table 4.8). However, low

entrainments (lower than -1 $g \cdot kg^{-1}$ and 3 ºC for q and θ, respectively) are obtained for the morning trajectories of the 20th and 22nd of July in comparison with the other days (Table 4.8). During the 20th, this occurs due to the fast but limited PBL growth (about 4 km) that reduces the drying and heating effect of entrainment at the PBL top and also facilitates shallow convection (Figure 4.23b). Instead, the low drying effect due to entrainment obtained the 17th and 22nd of July is produced by the displacement of the considered air parcel over moist air at the upper part of the TRB that generates a moistening and cooling effect associated with the entrainment (Figures 4.23a, c). Specifically, this mixing among the air parcel, the moist air at the front and the dry air at the top of the PBL produces a null change in q linked to entrainment the 17th for the last 10-15 km of the trajectory (Figure 4.23a). Besides, the initial moist conditions due to the generalized precipitation over inland areas during the previous day (Figure 4.7a) limit the development of the PBL (Figure 4.23a). The 22nd of July, entrainment generates a q increase of about 1 $g \cdot kg^{-1}$ near the convergence zone during the last segment of the trajectory between 75 and 85 km, approximately (Figure 4.23c).

Regarding the results summarized in Table 4.8, entrainment effects significantly overcome surface fluxes, and especially low water vapor surface contributions to the atmosphere under sea breeze dominating conditions.

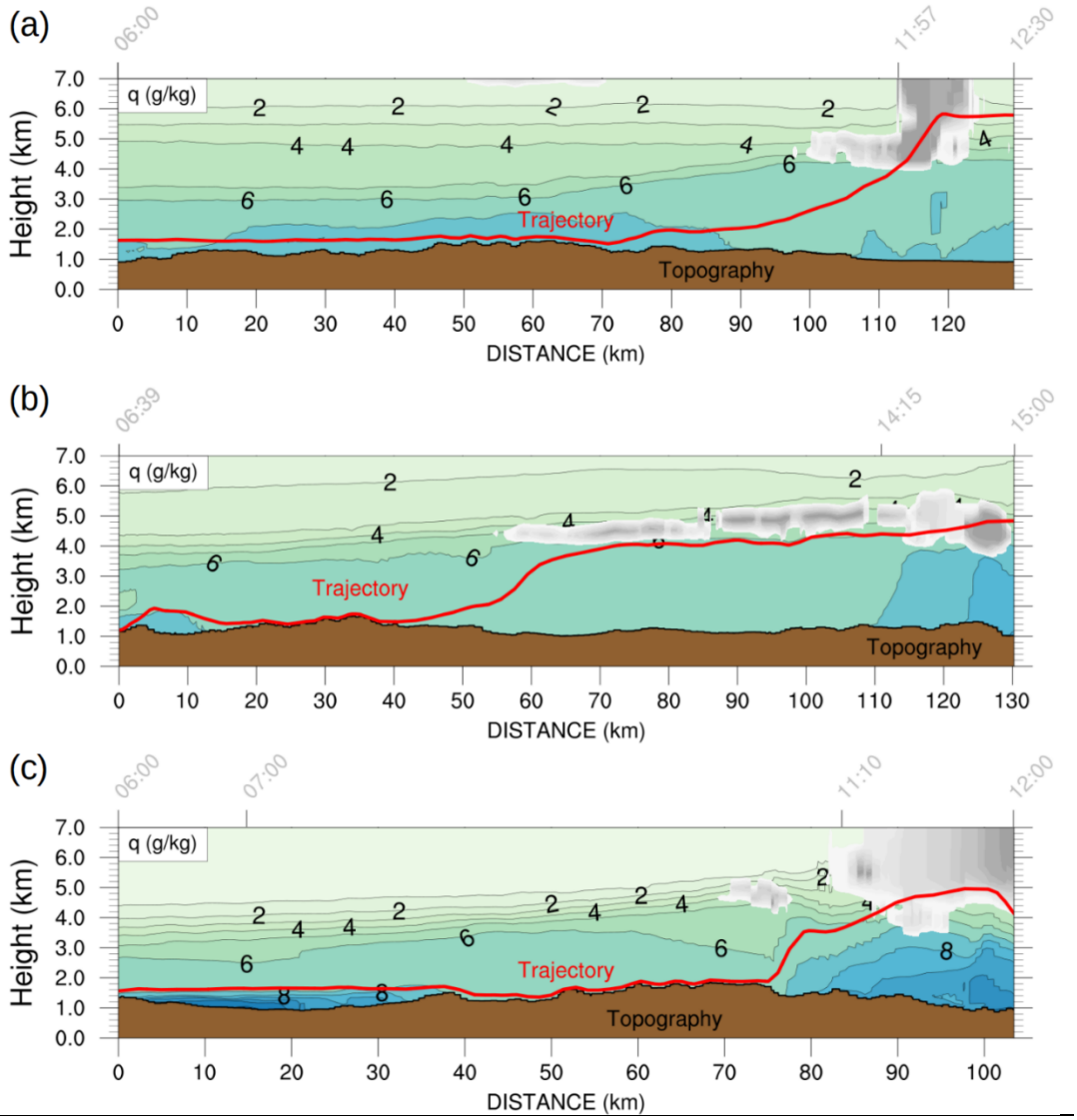

Figure 4.23 - Cross section contour plots corresponding to the trajectories together with trajectory height (red line), cloud fraction (in grey) and topography (in brown) for the (a) 17th, (b) 20th and (c) 22nd of July.

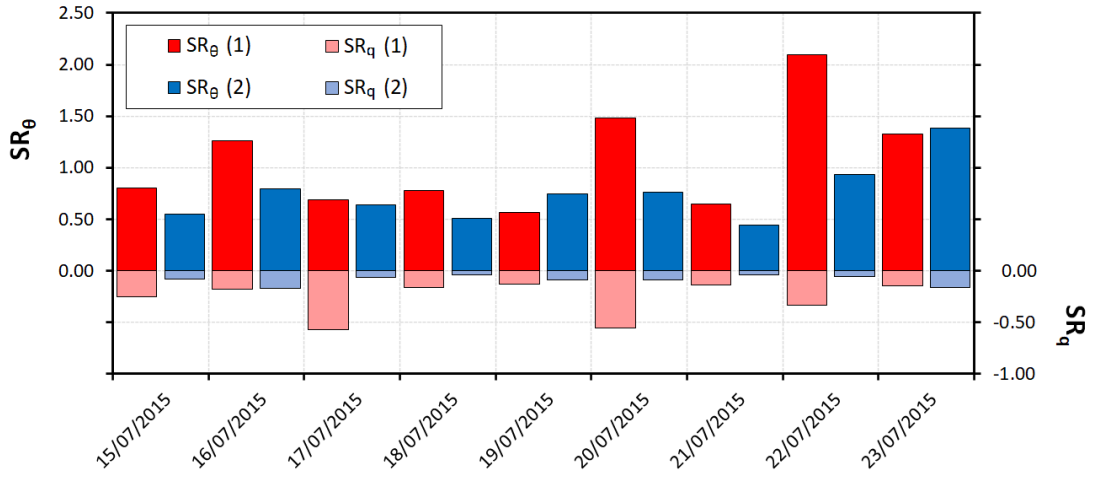

Figure 4.24 - Surface to entrainment ratios for θ and q (SR_θ and SR_q, respectively) for morning, in red, (1) and marine trajectories, in blue (2).

The significance of surface fluxes with respect to q decrease and θ increase linked to the entrainment can be quantified with the calculation of the surface to entrainment ratio (SR_q and SR_θ, Equations 2.17 and 2.18 respectively) regarding the values shown in Table 4.8. These ratios indicate that, according to Figure 4.24,

- In general, increments of θ due to H are similar to θ increase linked to entrainment with average SR_θ of 0.93 and 0.70 for morning and marine trajectories, respectively, so that surface heat fluxes play an important role in the air parcel heating.
- Almost half of the studied morning trajectories present higher surface contributions to θ than those produced by the entrainment effect. On the contrary, the entrainment effect dominates θ variations in the marine trajectories except for the 22nd ($SR_\theta \sim 1$) and the 23rd ($SR_\theta \sim 1.5$).
- Oppositely to air parcel heating, q variations are dominated by entrainment fluxes that tend to dry the air parcel, especially for moist marine air parcels, as indicated by SR_q average values of -0.23 and -0.08 for morning and marine trajectories, respectively.

Only three days (17th, 20th and 22nd) present considerable surface contributions to q showing SR_q values lower than -0.30 in the morning trajectories. However, morning air parcels during these days interact with moist air at the convergence zone that

produces an increment of q reducing the overall air parcel drying due to entrainment effect, as exposed previously (Figure 4.23).

4.3.2. Moisture variations due to surface fluxes

Air parcel moistening related to E is generally low in contrast to entrainment effects leading to a decreasing q tendency as the air parcel displaces over land areas and expands in the vertical (linked to increasing θ) as shown in Figure 4.25 for both morning and marine trajectories. However, the q decrease is more abrupt for marine trajectories with initial values ranging 16-18 $g \cdot kg^{-1}$ decreasing down to 7-12 $g \cdot kg^{-1}$ in contrast to morning trajectories with initial q values of 7-10 $g \cdot kg^{-1}$ decreasing to 5-7 $g \cdot kg^{-1}$ (Figure 4.25). Besides, in this figure, it is also highlighted the total surface contribution to q with respect to the q values at the end of the trajectory in order to visualize the relatively low water vapor provided by surface moist fluxes to the air parcels (Figure 4.25). On average, relative surface contributions to q represent about 7 % regarding final q values for both morning and marine trajectories. The amount of water vapor released to the atmosphere due to LE reduces the difference between initial and final moisture content of the air parcel (drying tendency) and its significance depends on the generally high drying effectivity of the entrainment (Figure 4.24), and the moisture content of the air parcel (Figure 4.25). Despite the low q increase in the air parcels linked to E, it is important to identify the contributions associated with each land use category.

The surface contribution to q normalized to the distance traveled over each land use category in the model is calculated using Equation 2.19 (section 6 in Chapter 2). The results obtained from this approach are presented in Figure 4.25 (right axis) for morning and marine trajectories. On one hand, morning trajectories show similar contributions for most land use categories, especially for forest categories, grassland and croplands, with peak values obtained over mixed forest (up to $1.5 \cdot 10^{-2}$ $g \cdot kg^{-1} \cdot km^{-1}$) and irrigated cropland and pasture categories (up to $1.2 \cdot 10^{-2}$ $g \cdot kg^{-1} \cdot km^{-1}$) on the 15th and 16th, respectively, as shown in Figure 4.25a. In contrast, marine trajectories in the afternoon show a very marked difference between the three cropland categories and the rest of categories with values exceeding $3.6 \cdot 10^{-2}$ $g \cdot kg^{-1} \cdot km^{-1}$ over irrigated cropland and pasture on the 17th of July (Figure 4.25b). These values are associated with the origin of marine trajectories (moving from the sea toward inland areas) and their displacement over

cropland fields situated near the coast providing the majority of water vapor to air parcels related to high vegetation fraction values and low *PBLH* (e.g., Figure 4.22c), in accordance with the results obtained in section 4.2. On average, cropland categories contribute between 0.8 $g \cdot kg^{-1}$ (DCR) and 1.5 $g \cdot kg^{-1}$ (ICR), considering trajectories of 100 km, in contrast with the low water vapor contributions of forest categories ranging from 0.2 $g \cdot kg^{-1}$ (DCR) to 0.4 $g \cdot kg^{-1}$ (FOR) according to values shown in Table 4.9.

Moisture variations are also strongly subject to the entrainment effect which generates a drying of the air parcel. This effect is connected to the growth of the PBL (increasing θ) partially determined by heat fluxes at the surface, especially along morning trajectories (Figure 4.24), so that H can determine the further drying of the air parcel as it moves over the different land use categories. Analogously to the q increase linked to E, the same calculation can be conducted for θ following Equation 2.19 (section 6 in Chapter 2) so that surface contributions to θ can be determined over each land use category (Figure 4.26). The previous analysis remarked the links among entrainment (air drying), PBL growth and surface heat fluxes so that it is important to identify the land use categories contributing the most to θ increase under sea breeze circulations.

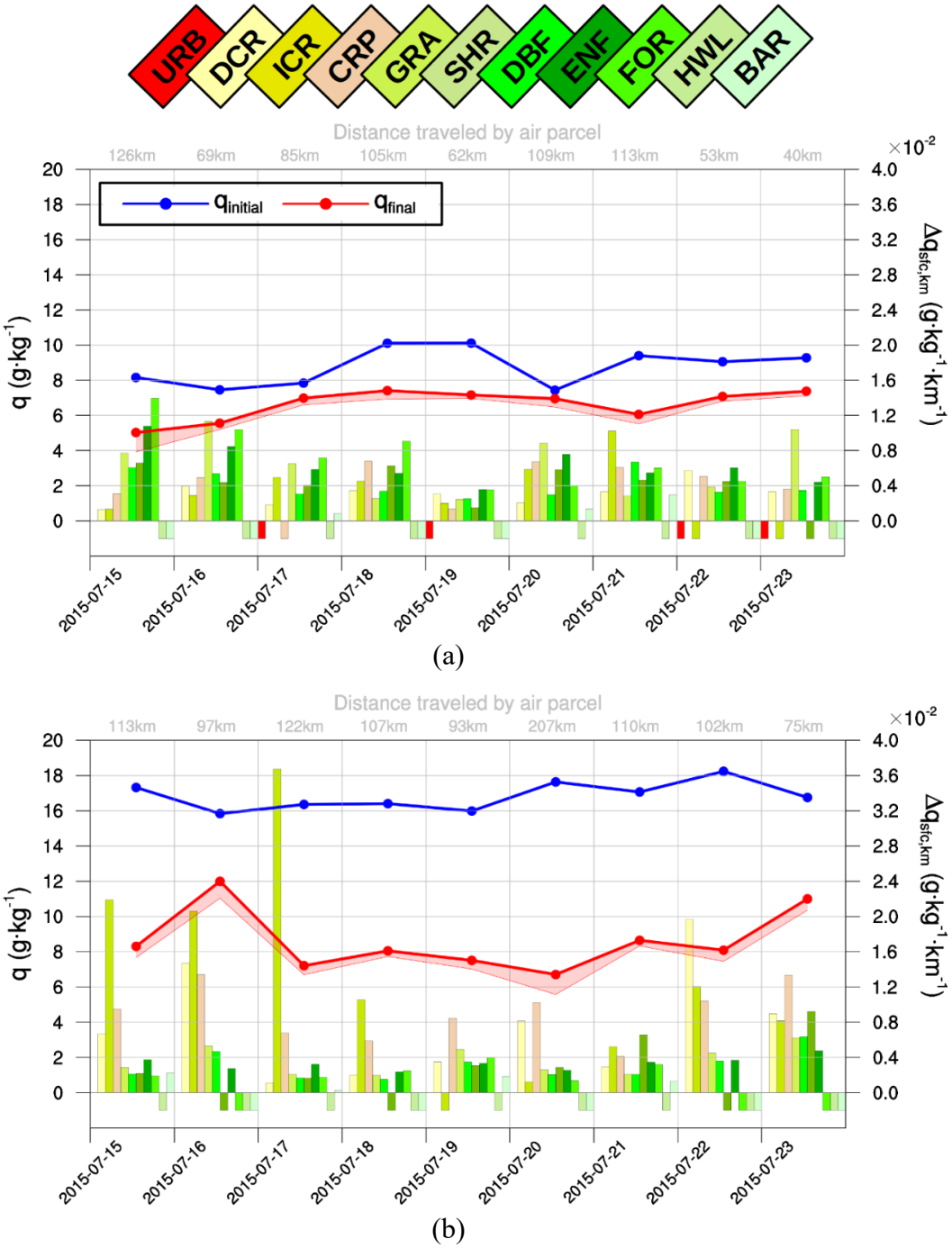

Figure 4.25 - Initial (blue line) and final (red line) *q* values for trajectories in the morning (top) and in the afternoon (bottom), along with the total surface contribution to *q* with respect to the final values (shadowed area under red line). The bars indicate the corresponding surface contributions to *q* per kilometer ($\Delta q_{sfc,km}$) for the corresponding land use category with negative values indicating that the land use category is not present along the extracted trajectory. The colors denoting each land use category are indicated at the top of the figure with URB (urban and built-up land), DCR (dryland/cropland and pasture), ICR (irrigated cropland and pasture), CRP (cropland/woodland mosaic), GRA (grassland), SHR (mixed shrubland/grassland), DBF (deciduous broadleaf forest), ENF (evergreen needleleaf forest), FOR (mixed forest), HWL (herbaceous wetland) and BAR (bare or sparsely vegetated).

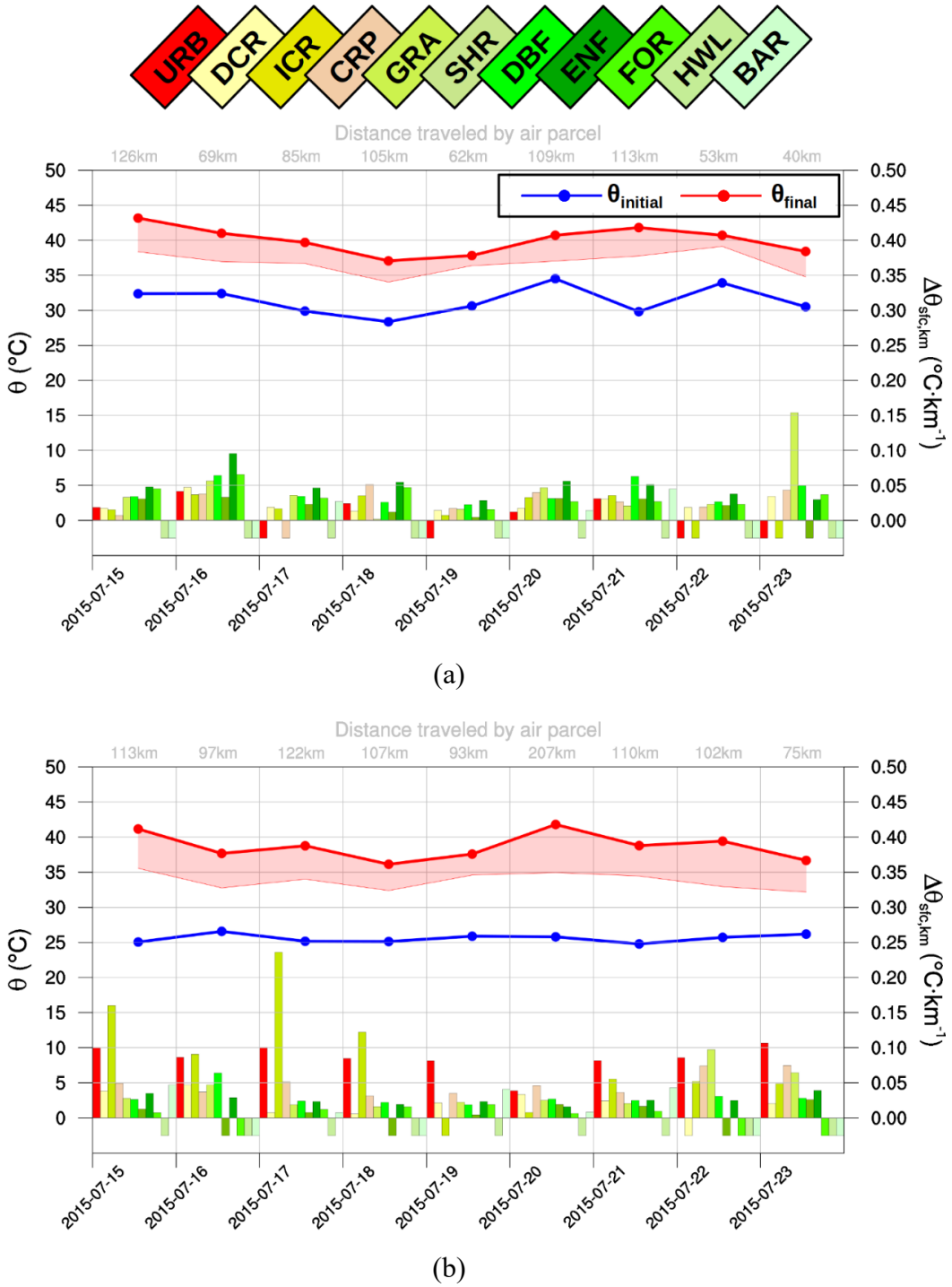

Figure 4.26 - Same as Figure 4.25 but for θ.

In the morning, the air situated within the TRB presents θ values from 28 ºC to 35 ºC reaching values up to 37-44 ºC as it is advected upwards due to the formation of thermally driven winds, as indicated by the different morning trajectories analyzed (Figure 4.26a). In the afternoon, the air parcels displaced inland during the early mature stages of the sea breeze present initial θ values ranging from 25 ºC to 26 ºC along the coast, increasing up to values between 36 ºC and 41 ºC when these reach inland areas (Figure 4.26b). On average, surface relative contributions to θ with respect to the difference between final and initial points of the studied trajectories represent 38 %, approximately, for both morning (with ranges of 20-60 %) and marine trajectories (with ranges of 25-48 %). According to these values, morning and marine air parcels are equally influenced by surface fluxes although morning trajectories show a wider variation range regarding relative surface contributions. Besides, marine air parcels show a greater absolute increment of θ associated with the low vertical development (about 1 km) and initial θ values (Figure 4.26b). The high temperature contrast between the surface and the air parcel along with its low height (lower air mass to heat) favor an effective heating. As commented in previous sections, the low PBL growth is linked to the early mature stage of the sea breeze in the afternoon, whereas the relatively low θ at the coast is caused by the slower heating of the sea surface than land which, in fact, leads to the formation of the sea breeze.

Analogously to surface moisture contributions, θ is normalized to the distance traveled over each land use category in the model using Equation 2.20 (section 6 in Chapter 2) and exposed in Figure 4.26 (right axis) for morning and marine trajectories. Normalized θ contributions in the morning are similar over all land use categories although two peak contributions are identified the 16th over evergreen needleleaf forest (ENF) and the 23rd over grassland (GRA) with contributions up to 0.10 and 0.15 ºC·km^{-1} respectively. In contrast, surface contributions to θ from urban and built-up land (URB) category are systematically important along the trajectories considered (about 0.10 ºC·km^{-1}), as well as over irrigated croplands and pastures (ICR) with a maximum contribution of about 0.25 ºC·km^{-1} obtained for the 17th of July. The average θ increments due to H indicate that main air parcel heating occurs over SHR, GRA and ENF (with $\Delta\theta$ of 3.9, 4.3 and 5.0 ºC, respectively, for a 100 km trajectory) in the morning trajectories, whilst the greatest θ increase of the marine air parcels occurs over URB and ICR (up to 8.5 ºC), as well as over CRP (Table 4.9). Contributions to θ are

subject to *PBLH* (air parcel height) which determines the amount of air mass to be heated. In the marine trajectories, the low heights of the PBL near the coast with dominating URB, ICR and CRP land use categories (see Figure 2.13 in Chapter 2) imply a more effective heating of the air parcel over littoral and pre-littoral areas.

Table 4.9 – Mean surface contributions to q and θ due to E and H, respectively, normalized for 100 km trajectories. Land use categories with no presence in the trajectories or null contribution are marked as '--', whereas italic values indicate low presence (less than 5 km on average) along the trajectory. The three land use categories with greatest contributions are highlighted in bold.

	Traj.	Land use category										
		URB	*DCR*	*ICR*	*CRP*	*GRA*	*SHR*	*DBF*	*ENF*	*FOR*	*HWL*	*BAR*
$\Delta q_{sfc,100km}$ **(g·kg^{-1})**	**(1)**	--	0.3	0.5	0.5	**0.6**	0.4	0.5	**0.6**	**0.7**	--	*0.2*
	(2)	--	**0.8**	**1.5**	**0.9**	0.4	0.3	0.4	0.3	0.2	--	*0.1*
$\Delta\theta_{sfc,100km}$ **(ºC)**	**(1)**	1.0	2.4	1.8	2.6	**4.3**	**3.9**	2.0	**5.0**	3.6	--	*0.3*
	(2)	**8.5**	2.1	**8.5**	**4.8**	3.8	3.0	0.6	2.6	0.5	--	*1.2*

CHAPTER 5

GENERAL DISCUSSION

This chapter introduces a general discussion of the main results exposed in Chapters 3 and 4 of this thesis. First, a discussion regarding the performance of the WRF model with the two parametrizations of surface processes (PX and Noah-MP LSMs) in reproducing hydrometeorological variables is conducted. Then, the discussion focuses on the representation of a specific summer storm episode (from 15th to 23rd of July 2015) with respect to the three parametrizations compared (PX-PX, PX-NoahMP and MM5-NoahMP) and the high-resolution simulation (STM). Finally, this chapter presents the discussion about land-atmosphere interactions regarding main features of the sea breeze characterization with in-situ measurements, and modeled moisture and heat contributions to the atmosphere for the specific summer storm episode.

5. Mesoscale modeling

5.1. The hydrological cycle

The WRF model is a globally used mesoscale model in atmospheric sciences and weather prediction continuously subject to improvements and updates by a large scientific community. This allows a wide range of options to account for the different processes occurring in the atmosphere, e.g., surface processes, which can be determinant in the outcome of a research. Hence, it is important to evaluate several options available in the WRF model to provide the most accurate representation of the processes to be studied. To this end, two parametrizations of the surface processes were evaluated against observations and reference products throughout direct comparison and statistical analyses, focusing on the hydrological cycle and favorable atmospheric conditions for the generation of summer storms.

In general, the WRF model reproduced temperature, humidity and wind variations accurately during the investigated period of May-October 2015. However, the calculation of mean biases and errors (MBE and RMSE, respectively) highlighted that PX and Noah-MP LSMs yielded greater wind intensities than observations along the coast during the days with the formation of summer storms, especially during daytime. This indicates that simulated sea breeze gravity flows near the surface tend to be slightly overestimated in the WRF model. This may also lead to overdraw updrafts at the convergence lines enhancing the injection of moist air to upper levels of the atmosphere along with the development of convective systems and precipitation. In fact, the WRF model with the two LSMs presents a slight wet bias in the total accumulated precipitation partly associated with summer storms although it shows a good performance in reproducing the areas affected by these convective systems. The amplified SBG in the model could be associated with the overestimation of surface heat fluxes yielding a greater land-sea temperature difference and the corresponding intensification of the SBC. Besides, an overestimation of surface fluxes (and 2-m temperature) suggests the formation of a more intense ITL over the Iberian Peninsula which further intensifies sea breeze along the Mediterranean coast. Contrarily, a strong ITL inhibits convection due to the generation of a compensatory subsidence over the mountain ranges near the coast as exposed in Millán et al., (2005b). In addition, the overall warm bias present in the model may have an important effect in convective precipitation such that overestimated 2-m temperature of the near-surface air injected

at the convergence lines increases the CCL and reduces or inhibits condensation. Furthermore, high air temperature may enhance entrainment effects at the upper boundary of the SBG due to a greater PBL growth, leading to a drying of the near-surface air mass (dry bias in WRF) and the corresponding further increase of the CCL. Despite these inhibiting effects over convective precipitation, the intensification of surface flows and their convergence at the mountain ranges prevail over the increase in CCL and enhanced entrainment effect so that WRF tends to overestimate precipitation.

The generalized overestimation of convective precipitation in the WRF model differs between the two parametrizations selected for the simulated period. In fact, ESS-PX overestimated precipitation more acute than ESS-NoahMP over the mountain ranges highlighting the importance of surface processes parametrization during summer storm episodes. However, both simulations present very similar MBE and RMSE for wind and relative humidity, whereas they present slightly different biases for temperature with ESS-PX temperature estimates 1 ºC lower than those in ESS-NoahMP, on average. As commented previously, higher near-surface air temperature tends to increase the entrainment effect and the CCL at the convergence lines so that ESS-PX would present weaker entrainment and lower CCL than ESS-NoahMP favoring the occurrence of convective precipitation.

The two parametrizations implemented present important differences as summarized in Table 2.1 (Chapter 2). A key aspect in the representation of precipitation is related to the greater complexity of the Noah-MP LSM compared to the PX LSM. For instance, the Noah-MP accounts for vegetation (trees) gaps to modify the incoming radiation from the radiation scheme and computes moisture and heat fluxes between the surface and the canopy, whereas these are not considered in the PX LSM. Besides, the Noah-MP calculates exchange coefficients over land and the SL scheme computes them over water bodies, whilst the SL scheme calculates these coefficients over land and water when the PX LSM is implemented. In contrast, the PX LSM presents a more realistic soil depth (1 m) compared to the Noah-MP LSM (2 m) and it considers weighted land use categories over each model grid point in contrast with the dominant land use category considered in the Noah-MP LSM. These characteristics can introduce significant differences between the two surface parametrizations in the atmosphere, e.g., the entrainment effect at the PBL top and the CCL over land areas, that affect the

generation of convective precipitation regarding SVA feedbacks (Heerwarden et al., 2009; Seneviratne et al., 2010).

On one hand, the PX LSM considers two soil layers of 0-1 and 1-100 cm so that changes in soil moisture are rapidly propagated to the atmosphere throughout evaporation, i.e., precipitation generates an increase in soil moisture that rapidly evaporates when atmospheric conditions change. This fact, along with the lower complexity of the PX LSM, may punctually lead to an overestimation of the water vapor contribution (q increase) to the atmosphere from the surface and reduce surface heat fluxes after a precipitation event. Under this situation, the PBL growth is less intense due to low surface sensible heat flux, crucial in the development of the PBL, whereas the CCL reduces considerably due to enhanced evaporation from the surface. Additionally, the ESS-PX presents an overall slight warm bias during the studied period and an overestimate of sea breeze intensity (wind speed) that enhanced updrafts at the converge lines. These factors may be determinant in the accumulated precipitation excess for the ESS-PX at the mountain ranges of the VR domain.

On the other hand, the Noah-MP is a more complex LSM that considers many parameters influencing surface processes as exposed previously. Despite this, it presents similar inconsistencies in comparison with the PX LSM regarding wind and relative humidity. However, this parametrization consists of a thicker soil than the PX LSM which slows down the propagation of soil moisture changes to the atmosphere throughout evaporation and generates strong surface heat fluxes. The lower evaporation and greater heat flux from the surface in the Noah-MP LSM compared to the PX LSM yielded lower CCL and deeper PBL. This leaded to a more accurate representation of accumulated precipitation associated with summer storms. Contrarily, the similar overestimation of surface flows in ESS-NoahMP and the corresponding enhanced convergence at the mountain ranges of the VR domain was likely to cause the excess in precipitation.

5.2. Representation of summer storms

5.2.1. Model initialization

The simulations covering the period May-October 2015 (ESS-PX and ESS-NoahMP) present some difficulties in representing precipitation accumulations and intensity during specific summer storm episodes despite the good performance in reproducing near-surface variables. This occurs since mesoscale models perform more accurately

when initialized slightly before the occurrence of the meteorological event to be studied. Besides, WRF model's representation of large-scale circulations in the WMB is also subject to the accuracy of the initialization, in this case, provided by the ERA5 product. This reanalysis product shows important improvements in the representation of atmospheric conditions with respect to its predecessors (e.g., ERA40 and ERA-Interim) due to finer horizontal (~25 km) and vertical resolutions (137 sigma levels), as well as a higher number of input observations from a wide variety of sources (Hersbach et al., 2020). The robustness of this product in reproducing the state of the atmosphere poses the feasibility to use this dataset to determine IC and BC in the WRF model episodic simulations. However, soil conditions such as soil moisture are likely to be more accurately represented in the WRF mesoscale model regarding its higher horizontal resolution and the surface and subsurface processes considered in the LSMs over each grid point. This fact states the reliability to use soil moisture from WRF estimates in the ESS simulations to initialize the episodic simulations, namely PX-PX, PX-NoahMP and MM5-NoahMP.

5.2.2. Comparative analysis

Apart from the initialization, the parametrization of atmospheric processes is key in the WRF model accuracy to reproduce summer storms. In fact, the methodologies implemented in LSMs to compute surface processes, along with the LSM complexity, produce important differences in estimating near-surface variables for the summer storm episode occurred between the 15th and 23rd of July 2015. In fact, all simulations present similar errors in representing temperature and relative humidity, although PX-PX shows slightly better scores than simulations implemented with the Noah-MP LSM despite the greater complexity of the latter. On one hand, this suggests that surface heat and moisture fluxes, the main drivers of 2-m temperature and humidity variations under these atmospheric conditions, are strongly subject to the more accurate representation of land use categories (weighted categories over each grid point) and/or the thinner (more realistic) soil depth considered in the PX LSM. On the other hand, these differences may also be associated with the approaches implemented to calculate exchange coefficients over land. The Noah-MP LSM conducts the calculation of exchange coefficients at the surface, i.e., it determines 2-m temperature, 2-m relative humidity and 10-m winds, whereas the PX SL is the scheme carrying out this calculation in the PX-PX configuration. In contrast, the estimate of atmospheric

dynamics near the surface is more accurately reproduced in the simulations using the Noah-MP parametrization, especially the MM5-NoahMP during daytime. This indicates two main aspects: the higher complexity of the Noah-MP LSM is crucial in the representation of near-surface flows, which is of great interest regarding the importance of sea breeze flows in this thesis, and the MM5 SL shows a slightly better performance in computing exchange coefficients over water bodies than the PX SL, at least when it is implemented with the Noah-MP SL.

The greater accuracy of the MM5-NoahMP configuration is further proven in the slightly better representation of total precipitable water than the other two parametrizations, key in the generation of precipitation (Kunkel et al., 2020). In fact, the MM5-NoahMP showed the most accurate representation of convective precipitation in the TRB at a daily basis, as well as accumulated values closer to the reference. These results indicate the importance of well-captured near-surface air flows to accurately reproduce the summer storms occurred along the Mediterranean coast of the Iberian Peninsula during the period from the 15th to the 23rd of July 2015. Besides, they remark that the occurrence and location of these summer storms were strictly connected to the characteristics of the convergence of surface flows at the mountain ranges in the TRB. An accurate representation of wind direction and speed at the surface yielded a more realistic injection of near-surface air to upper atmospheric levels at the convergence lines, key in the generation of summer storms (Millán, 2014).

5.2.3. High-resolution simulation

The representation of surface air flows near the coast are strictly linked to topography features since valleys produce a channeling effect over sea breeze and other thermally driven air flows. As commented previously, the convergence of these flows over the mountain ranges are a key factor in the formation of summer storms. Thus, a high-resolution simulation allowed a more detailed description of local characteristics such as topographic barriers and land use categories, the latter determining surface heat and moisture fluxes. In addition, the new implemented high-resolution land use categories from CLC2012 at 100 m and topography SRTM30 at 30 m significantly improved the physical description of the study domain (STM) leading to a more accurate representation of surface fluxes and atmospheric dynamics. The STM simulation at 680-m horizontal resolution provided the possibility to conduct a closer evaluation of the local processes influencing convective precipitation associated with summer storms

in the TRB. However, the inconsistencies associated with the modeling of these local processes must be quantified in order to evaluate model's performance.

In general, the high resolution with the MM5-NoahMP parametrization reproduced accurately the summer storm events occurred in the study period although the light dry and warm biases were still present. These were likely to be associated with a slight overestimation of entrainment effects and surface heat fluxes leading to a strong PBL drying and heating, respectively. Concretely, surface heat fluxes (increase in 2-m air temperature) yielded a strong development of the PBL with the following mixing of upper-level dry air into the PBL and the associated decrease in 2-m humidity. These effects induced warm and dry biases in the simulation more intense over coastal areas but light over the pre-littoral. These inconsistencies were not only linked to the MM5 SL scheme and the Noah-MP implemented in the simulation, but also to the ACM2 PBL scheme which determines the development of the PBL and the interactions between the different model levels.

6. Land-atmosphere interactions

6.1. Sea breeze and summer storms

The typical weak synoptic atmospheric conditions during summer over the Iberian Peninsula led to dominant local circulations that merge and organize in larger structures such as the characteristic ITL and the formation of sea breeze along coastal areas (Millán et al. 2000). The sea breeze circulation determines atmospheric dynamics at a local-to-regional scale along the Mediterranean coast and it is crucial in the generation of different meteorological phenomena such as summer storms. Thus, it is important to analyze how sea breeze influences atmospheric conditions at local scale within the study area.

An initial analysis of averaged atmospheric variables describing air properties (i.e., q and θ) during dominating sea breeze circulations depicted an inverted U shape in the mixing diagrams for all seasons. This q-θ variation was identified as a distinctive characteristic of sea breeze days in the Turia valley. The inverted U shape defined three periods related to the evolution of the sea breeze such that: (i) initially, surface heat fluxes dominate producing a temperature increase and the corresponding growth of the PBL and enhanced entrainment, limited by surface moisture fluxes and low advection, (ii) then, as sea breeze gravity flow intensifies, marine moist air advances effectively toward inland areas and produces a substantial increase in q at constant θ, approximately,

and, (iii) finally, a constant q remarks the homogeneity of the marine air mass advected and the decay in the incoming radiation (lower surface heat fluxes) generates a decrease in θ. This characteristic feature was observed over all the stations considered with a temporal delay from coast to inland associated with the occurrence of the effective moistening of the sea breeze. The characteristics of the inverted U shape were determined by the initial local air and soil conditions, the properties of the marine air mass, and the vertical extend of the residual layer, delimited by an inversion layer, absorbed by the PBL development.

Based on the characteristic evolution of q and θ under dominating sea breeze conditions, a comparison among several surface stations with different land use characteristics was conducted. This analysis indicates that vegetated areas showed greater q and lower θ than non-vegetated areas in the pre-littoral, whereas slight or no differences occurred over littoral stations. This denotes that coastal areas were under the influence of marine air since the early morning so that local processes generated low changes in the air properties although this could be propagated toward inland areas. Contrarily, pre-littoral and inland stations were subject to dominating local surface fluxes during a longer period, as well as to warm and dry air advection due to the moist marine air heating and drying effect of surface heat fluxes and entrainment, respectively, as it advanced along the valley. These conditions favored a strong change in q associated with the sea breeze air moistening, slightly greater over the vegetated location considered.

Most summer storms initiated during dominating sea breeze circulations over the TRB and prior to the marked moistening over inland areas, as well as they originated over mountain ranges outside the influence of sea breeze. This suggests that these convective systems were associated with local thermally driven circulations such as upslope winds which generate over inland areas. Under this situation, the near-surface air within the Turia valley in the early morning was advected upslope and injected to upper levels of the atmosphere at the mountain ranges such that its properties were key in the development of convective clouds and precipitation. The properties of this air mass were mainly determined by two factors: the local processes and the displacement toward inland areas of the sea breeze head the previous day during the late mature stage as pointed out in Clarke (1984).

Surface moisture and heat fluxes influenced the water vapor content and temperature of the near-surface air mass in the early morning. However, surface fluxes were low in

the early morning so that slight changes occurred due to these local processes. Instead, the displacement toward inland areas of the sea breeze front the previous day could be determinant in defining the characteristics of the near-surface air mass in the early morning. Regarding the different stages of the sea breeze described in the introduction (see section 2.1 in Chapter 1), the sea breeze front can travel further inland after the early mature stage reaching inland regions of the Iberian Peninsula. In the nighttime, light downslope winds develop returning the previously advected moist marine air during sea breeze circulations towards the sea. However, according to wind observations in the study area, these nighttime air flows are usually less intense than surface air flows associated with sea breeze so that moist air can remain within the valley the following morning when upslope winds originate. Thus, this remaining moist air in the early morning can be injected at the converge lines at noon and generate summer storms, even over areas outside the general influence of the sea breeze circulation. Besides, in some of the studied cases, the arrival of the ISBF intensified convective precipitation after the formation of summer storms.

6.2. Surface moisture and heat fluxes

6.2.1. Moisture contributions

The simulations conducted in this thesis allowed the quantification of water vapor contributions to the atmosphere during sea breeze circulation over different locations of the study area with various land use characteristics. This analysis remarked that the CRP (cropland/woodland mosaic) category was the main source of water vapor in the study area (up to 2.1 $g \cdot kg^{-1}$) with a considerable reduction of contributions from littoral to pre-littoral (about 0.6 $g \cdot kg^{-1}$) linked to vegetation fraction and PBLH differences. This is in accordance with the fact that the study period (and summer in general) was characterized for scarce precipitation over the littoral and pre-littoral, so that evapotranspiration from natural vegetation was low due to dry soils, except for the days with generalized convective precipitation. Instead, evapotranspiration from irrigated croplands was generally high due to the irrigation activities to maintain wet soil conditions. Thus, crop fields were described as the main contributors of water vapor to the atmosphere in the study area.

Interestingly, mixed shrubland/grassland (SHR) and evergreen needleleaf forest (ENF) inland areas showed very little differences in terms of water vapor contributions despite the differences in the soil layers considered as root zone (0-100 cm for SHR and 0-200

cm for ENF). This suggests that the deepest soil layer 100-200 cm provided low amounts of water to vegetation regarding the similar vegetation fraction values at the considered locations. Besides, the greater distance to the coastline of the SHR inland location led to lower moisture contributions from the surface to the atmosphere, as commented previously, and a stronger entrainment effect of about -5 $g \cdot kg^{-1}$. The coast-to-inland increasing entrainment was associated with the greater development of the PBL from littoral to inland areas due to the longer period under dominating surface heat fluxes. The heating of the PBL forced it to grow by incorporating dry air from upper levels of the atmosphere leading to a decrease in q as well.

In general, the amount of water vapor released to the atmosphere due to surface moisture fluxes counterposed the drying effect of entrainment and its significance was strictly dependent on the initial moisture of the air mass advected with the sea breeze. Besides, the thinner PBL over the littoral generated differences in surface contributions to q, i.e., the q increase due to surface moisture fluxes near the coast was greater than over inland areas regarding its dependence on *PBLH*. On average, total water vapor contributions from the surface represented about 7 % with respect to the q values near the convergence lines, i.e., q values at the end of the considered trajectories. However, entrainment drying effects significantly exceeded (by a factor between two and ten) surface water vapor contributions. In fact, moisture contributions from the surface were generally low under sea breeze dominating conditions during the summer storm episode. Thus, entrainment was the main factor driving q variations during thermally driven circulations, especially during sea breeze.

6.2.2. Heat contributions

In an analogous manner, heat contributions to the atmosphere from the surface could be estimated from simulated values. Contrarily to surface moisture flux, surface heat flux played an important role in the heating of the PBL (about 40 % of the total θ increase), which led to a strong PBL development throughout the enhanced entrainment effect (representing the 60 % of the total θ increase). In general, surface heat fluxes dominated before noon, prior to the effective moistening due to sea breeze circulations, such that it was substantially greater than moisture flux, except for croplands over littoral and pre-littoral areas. Interestingly, contributions to θ from the surface were similar for all the considered land use categories except for littoral locations after the effective sea breeze moistening, where croplands presented substantially lower average

contributions to θ in contrast with urban areas. This suggests an important role of land use categories near the coast in influencing air mass properties posteriorly displaced inland. According to this, urban areas tend to increase air temperature more effectively than cropland areas, with greater evapotranspiration rates, near the coastline. Besides, this local heating differences led to greater entrainment at the top of the PBL over urban areas compared to croplands such that PBL growth and dry air mixing were enhanced over urban areas, whereas these effects were less intense over croplands. These effects along the coast influence the CCL of the advected air mass which needs to be lower than the height of injection at the convergence line for summer storms to generate (Millán et al. 2005a; Millán, 2014).

Generally, the PBL over the littoral is thinner than over pre-littoral and inland areas during daytime so that the air mass to be heated is lower. Under these conditions, a more effective heating occurs near the coast regarding the dependence of surface contributions to θ on *PBLH*. This implies that marine moist air advected from the sea is subject to a strong heating along the coast, which also depends on the dominating land use categories as exposed previously. Similarly, the PBL presents a low vertical development in the early morning over inland areas, and it rapidly grows with the increasing surface heat fluxes. However, the low surface heat fluxes in the early morning provide low contributions to θ despite the thin PBL. Hence, contributions to θ from the surface increase as incoming solar radiation intensifies over inland areas, further enhanced by entrainment, with a low dependence on the dominating land use category (pine forest, shrublands or grasslands).

6.2.3. Influence in summer storms

Summer storms are associated with the convergence of surface flows due to combined breeze circulations (upslope winds and sea breeze) along the Mediterranean coast. Under these dominating atmospheric conditions, land-atmosphere interactions play an important role in determining the characteristics of the air mass advected toward mountain ranges. Moisture and heat fluxes from the surface modify the initial air properties that can be determinant in the formation of this type of convective systems.

On one hand, moisture fluxes provide additional water vapor to the lower atmosphere slightly counterposing the substantial drying due to entrainment pointed out in this thesis. Despite the low amount of water vapor released to the atmosphere during the studied period, a slight increase in q together with a decrease in θ could reduce the CCL

sufficiently to favor the initiation of summer storms. In fact, it has been shown that the greatest contributions to temperature and water vapor content within the PBL from the surface are substantially dependent on the land use category near the coast. Hence, the heating and moistening of a marine air mass near the coast is a factor to be considered in the formation of summer storms at the mountain ranges of the TRB. However, the further heating and moistening of the marine air mass as it displaces along the Turia valley also depends on the characteristics of the land use so that q and θ additional variations due to surface fluxes can further favor or inhibit the formation of summer storms.

On the other hand, surface heat fluxes are key in the development of the PBL and the corresponding entrainment at the top of it. Specifically, the PBL grows rapidly due to surface heat fluxes by absorbing upper-level dry air which decreases q and increases θ. It has been pointed out that the entrainment effect is the main driver in the PBL drying and much stronger than the moistening due to evapotranspiration in the study area. Besides, it is strictly connected to surface heat fluxes that produce an air temperature increase and, hence, to the corresponding characteristics of the land use. However, low variations in q and θ associated with surface contributions and entrainment were detected for the different land use categories over pre-littoral and inland areas, in contrast with the differences highlighted near the coast. This points out that local humidity and temperature variations in the littoral were substantially exceeded by the surface heating and entrainment effect over pre-littoral and inland areas reducing their impact on the generation of summer storms at the mountain ranges of the TRB. Besides, it has been shown that the air situated within the uppermost part of the Turia valley in the early morning was subject to heating and drying (entrainment) before being injected to upper atmospheric levels throughout upslope circulations. Thus, this suggests that the initial thermodynamic properties of this continental air mass advected prior to the marine air mass (i.e., temperature and humidity) are likely to be crucial for the generation of summer storms.

CHAPTER 6
CONCLUSIONS

The main conclusions obtained in this thesis are summarized in the following points:

1. PX and Noah-MP LSMs available in the WRF model with different degree of complexity and characteristics were compared for an extended summer season. Overall, both parametrizations show similar behavior in reproducing typical meteorological variables, although marked differences arose in representing convective precipitation associated with summer storms. The Noah-MP showed the best performance in comparison with observations from different sources. Besides, the performance of the Noah-MP LSM in reproducing a particular summer storm episode was slightly improved when implemented with the MM5 SL and increasing spatial resolution.

2. An analysis of average q-θ variations observed at different stations within the study area showed a characteristic inverted U shape in the energy space per unit mass (mixing diagrams) during sea breeze circulations. This was determined by dominating local land-atmosphere interactions and advection associated with the sea breeze such that three periods could be identified:

    a. Strong increase in θ at constant q linked to dominating surface heat fluxes and entrainment, together with low surface moisture fluxes and advection.

    b. Marked increase in q at constant θ associated with the entrance of a marine moist air mass, effective moistening effect of the sea breeze, despite the generally strong surface heat fluxes and entrainment.

    c. Decrease in θ at constant q linked to the incoming solar radiation decay and the homogeneity of the moist marine air mass advected along the sea breeze circulation, respectively.

3. Observations of q and θ variations were studied over different locations (littoral, pre-littoral and inland) and land use categories (urban, non-vegetated land and croplands) so that a dependence on distance to the sea and land use characteristics could be identified. On one hand, vegetated areas presented

slightly lower θ and greater q than non-vegetated areas over the pre-littoral, whereas no significant differences were detected over the littoral. On the other hand, the delay in the effective moistening over pre-littoral and inland stations with respect to littoral ones remarks the relevance of local surface fluxes and entrainment at these locations despite the considerable advection. Besides, it indicates that summer storms can originate prior to the effective moistening occurrence.

4. Modeled atmospheric dynamics and q-θ variations indicate that most summer storms initiate before the arrival of a moist marine air mass indicated in the mixing diagrams as a marked q increase. This remarks the importance of local interactions and entrainment during sea breeze circulations.

5. The atmospheric recharge in water vapor and temperature variations were estimated from modeled values during a summer storm episode consisting of several events. These estimates indicate that q contributions due to evapotranspiration represents about 7 % of the air-mass q before the formation of summer storms, on average. Main contributions to q from the surface (up to 2 $g \cdot kg^{-1}$) occurred over croplands and near the coast associated with low *PBLH.*

6. Air temperature variations linked to surface heat fluxes represented about 40 % of the total increase in θ during dominating sea breeze conditions. This remarks the relevance of surface heating in the θ increasing, leading to CCL increase at the convergence lines. As for q, greatest increase in θ occurs near the coast over urban areas regarding its dependence on the *PBLH*.

7. Entrainment is the main factor influencing q and θ variations at the top of the PBL. This effect produces a substantial drying of the air mass by dilution between two and ten times stronger than the water vapor recharged from the surface, whilst θ increase at the same level as that produced by surface heat fluxes. Contrarily to surface contributions to q and θ, entrainment presents a coast-to-inland gradient corresponding to the development of the PBL.

APPENDIX

1. WRF model parametrizations

The WRF model integrates the compressible, non-hydrostatic Euler equations which are formulated using a terrain-following mass vertical coordinate proposed by Laprise (1992). Temporal discretization is performed differently depending on the frequency modes to be integrated using the so-called time-split integration scheme. On one hand, low-frequency (slow) modes integration is carried out using a 2nd or 3rd-order Runge-Kutta (RK3) time integration scheme; on the other hand, a forward-backward integration scheme and a vertically implicit scheme are used to integrate horizontally propagating acoustic modes and gravity waves (high-frequency modes), respectively. The former modes are integrated over smaller time steps than slow modes in order to maintain numerical stability. Spatial discretization in WRF uses an Arakawa C-grid staggering in both horizontal and vertical grids (Figure A.1), with 2nd to 6th-order advection options for horizontal and vertical momentum although 5th and 3rd orders are recommended respectively, also including full Coriolis terms. Turbulent mixing and model filters are also available in the WRF model. Turbulent mixing filters determine unresolved sub-grid scale turbulent processes in both coordinate and physical space (spatial diffusion), whereas other model filters are implemented for numerical reasons such as the divergence damping in the time-split RK3 scheme to remove acoustic modes from the solution, the gravity wave absorbing layers to prevent unphysical wave reflections and the vertical-velocity damping used to stabilize vertical motion. In mesoscale models, vertical turbulent fluxes are often represented by the planetary boundary layer (PBL) parametrization; thus, in the case a PBL scheme is used, all other vertical mixing options are disabled.

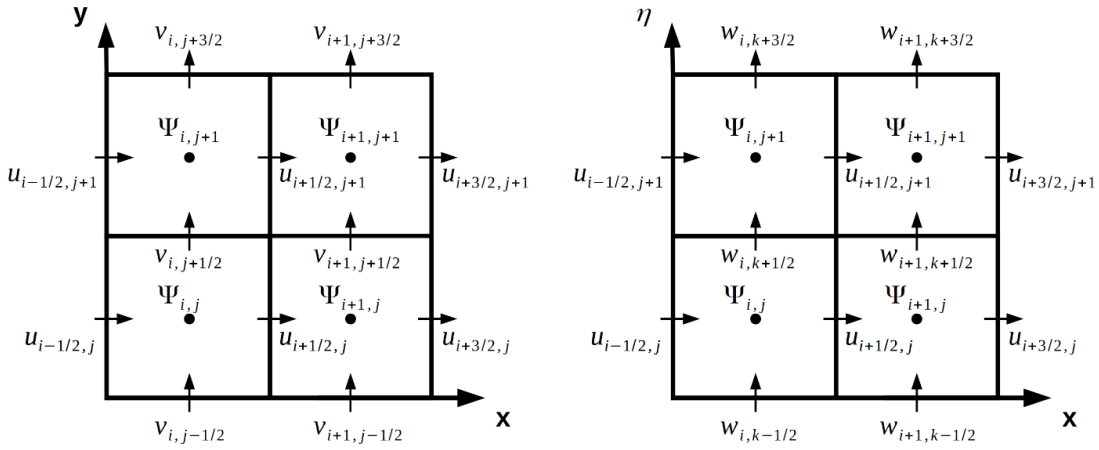

Figure A.1 - Horizontal (left) and vertical (right) Arakawa C-grids of the WRF model.

Initial conditions can be defined by the user for idealized cases or interpolated from external analysis or forecast for real cases. In order to interpolate meteorological data and prepare input files for the real case, the so-called WRF Preprocessing System (WPS) is used. This system consists of three components: the GEOGRID, which defines the model domains and extracts static data, the UNGRIB, used to convert GRIB meteorological data into WPS format, and the METGRID, that interpolates horizontal meteorological fields over the model domains. Finally, the REAL program performs an interpolation of vertical meteorological fields to the defined vertical model levels and generates WRF input and boundary files. Lateral boundary conditions can be set to periodic (for global simulations), open, symmetric, polar or specified (always used for nested grids). Besides, the model allows two interaction options between the coarse grid and the fine grid: one-way or two-way grid nesting. In the one-way option the exchange of information between domains occurs from the coarse grid to the fine grid only (fine grid boundary conditions), whilst in the two-way option the coarse grid solution is also replaced by the fine grid solution over the coarse grid points located inside the fine grid, hence, information exchange between grids is in both directions.

The WRF model includes physics parametrizations for shortwave and longwave radiation, cumulus, microphysics, PBL, SL and LSM, allowing several parametrization options within each category, as well as various data assimilation methods and initializations. In order to start a simulation, initial conditions are set prior to the first-time step from WRF input files, physics tables or look-up tables of functions. Then, tendencies are calculated for radiation, surface (SL and LSM), PBL and cumulus physics. Finally, microphysics scheme is called at the end of the time step in order to

guarantee proper saturation conditions. In the following paragraphs the two WRF PBL schemes selected to conduct this study are described.

1.1. Planetary Boundary Layer schemes

The so-called *K*-theory or gradient transport theory (local closure) states that turbulent shear stress can be described in analogy with molecular viscosity so that for a given adiabatically conserved variable Ψ (e.g., heat, moisture or momentum), it can be written that:

$$\overline{\Psi' w'} = -K_\Psi \frac{\partial \Psi}{\partial z} \tag{A.1}$$

where w' is the vertical velocity fluctuation, Ψ' is the Ψ fluctuation and K_Ψ is the corresponding turbulent eddy coefficient (eddy diffusivity) that relates turbulent fluxes to the gradient of mean Ψ at adjacent levels only, with the overbar denoting averaged values. Equation (A.1) represents a simple (first order) approach which describes small-size eddies in the flow although it does not apply when large-size eddies are present, e.g., in the convective boundary layer. In order to consider the effect due to large-scale eddies in the boundary layer higher-order turbulent closures must be used.

In non-local schemes Ψ can be modeled using a *K* profile with a non-local correction γ_Ψ that aggregates the contribution of large-scale eddies to the total flux, thus:

$$\overline{\Psi' w'} = -K_\Psi \left(\frac{\partial \overline{\Psi}}{\partial z} - \gamma_\Psi \right) \tag{A.2}$$

where the adjustment term γ_Ψ is interpreted as the large-scale eddies (or convective eddies) filling the boundary layer that distribute surface flux of Ψ upwards independently of Ψ local gradients, and it is usually set to zero in stable boundary layer. This formulation has been typically used in many PBL parametrizations to account for non-local effects (Troen and Mahrt, 1986; Holstag and Boville, 1993; Noh et al., 2003); however, more recent PBL schemes have improved the boundary layer representation by including other terms related to entrainment at the top of the PBL, e.g., YSU PBL.

Another method also used to consider explicitly non-local fluxes is the transilient turbulence theory, in which for a given pair of grid points in the vertical column, adjacent or not, mass flux is defined using a so-called transilient matrix. The equation used to describe this method for a given atmospheric column with *n* grid points is

$$\bar{\Psi}_i(t+\Delta t) = \sum_{j=1}^{n} c_{ij}\,(t,\Delta t)\bar{\Psi}_j(t) \tag{A.3}$$

where Ψ_j is the initial value of Ψ at time t at source grid point j, Ψ_i is the final value at time $t + \Delta t$ at destination grid point i and c_{ij} represents the transilient matrix which indicates the amount of air that came from grid point j and ended in destination grid point i. The final value is the sum over all the n grid points in the column of air. The formulation in Equation (A.3) have been implemented in some non-local PBL schemes such as Blackadar (1978) and Pleim and Chang (1992); and also implemented in more recent PBL schemes, e.g. ACM2.

a) YSU PBL

The YSU PBL scheme, described in Hong et al., (2006), is similar to the non-local Holtslag-Boville (HB) scheme (Holtslag and Boville, 1993), which is based on Equation A.2. Additionally, the YSU scheme introduces a term proportional to the surface buoyancy flux in order to represent explicitly the effects of entrainment at the top of the PBL; hence:

$$\overline{\Psi' w'} = -K_\Psi \left(\frac{\partial \bar{\Psi}}{\partial z} - \gamma_\Psi \right) + \left(\overline{\Psi' w'}\right)_h \left(\frac{z}{h}\right)^3 \tag{A.4}$$

where h is the PBL height, z is the model height and $(w'\Psi')_h$ represents the flux at the inversion layer. Equation (A.4) applies for $z \leq h$, whereas free atmospheric diffusion is considered using a local diffusion approach for $z > h$. In the YSU scheme eddy diffusivity for momentum is parametrized as a function of mixed layer velocity scale, z and h; whilst eddy diffusivity for moisture and heat are computed using the Prandtl number (see Appendix A.2). The main difference between this scheme and its predecessors is the use of Ri_{cr} of zero to determine h suggesting that small Ri_{cr} diminishes the entrainment effect. Hence, the PBL top depends effectively on the buoyancy profile and is defined at the layer where maximum entrainment occurs. For stable conditions, $Ri_{cr} = 0.25$ and Ri_b is calculated as:

$$Ri_b(z) = \frac{g[\theta_v(z) - \theta_v(z_1)]z}{\theta_v[u(z)^2 - v(z)^2]} \tag{A.5}$$

where θ_v is the virtual potential temperature, z_1 represents the height of the lowest model level, g is the gravitational acceleration, and u and v are the horizontal wind

components in x and y directions, respectively. For unstable conditions, $Ri_{cr} = 0$ and the term $\theta_v(z_1)$ is replaced by θ_s, given as:

$$\theta_s = \theta_v(z_1) + b\frac{\left(\overline{w'\theta_v'}\right)_0}{w_m} \tag{A.6}$$

where $b = 7.8$ (as in Hong and Pan., 1996), w_m the convective velocity scale and $\left(\overline{w'\theta_v'}\right)_0$ the sensible heat flux at the surface.

b) ACM2 PBL

The description of this scheme has been conducted according to Pleim (2007). The ACM2 PBL scheme is a combination of the ACM1, based on the Blackadar convective model (Blackadar, 1978) which used a simple transilient method, and an eddy diffusion model. Thus, it is considered a hybrid scheme as it combines local and non-local closure. The non-local part is based on the transilient turbulence theory (Equation A.3) as in the ACM1, whereas the local part implements Equation A.1. This combination allows the model to account for both rapid upward transport and turbulent diffusion induced at local scale. Considering a staggered vertical grid where subscript l denotes the grid center and $l + 1/2$ the layer interface, the equation that describes the ACM2 scheme can be written as:

$$\begin{aligned}\overline{\Psi'w'}_{l+\frac{1}{2}} = &-f_{conv}Mu\left(h - z_{l+\frac{1}{2}}\right)(\Psi_1 - \Psi_l) \\ &- (1 - f_{conv})\left[K_{\Psi\left(l+\frac{1}{2}\right)}\frac{\overline{\Psi}_{l+1} - \overline{\Psi}_l}{\Delta z_{l+\frac{1}{2}}}\right. \\ &\left. + K_{\Psi\left(l-\frac{1}{2}\right)}\frac{\overline{\Psi}_l - \overline{\Psi}_{l-1}}{\Delta z_{l-\frac{1}{2}}}\right]\end{aligned} \tag{A.7}$$

where Ψ_1 the values of Ψ at the first model layer,z_l and Δz_l the height and thickness of a layer l, respectively, f_{conv} the partitioning factor calculated as:

$$f_{conv} = \left[1 + \frac{k^{\frac{-2}{3}}}{0.1a}\left(\frac{-h}{L}\right)^{\frac{-1}{3}}\right]^{-1} \tag{A.8}$$

where $k = 0.4$ is the von Kármán constant, L the Monin-Obukhov length scale and $a = 7.2$ following Holtslag and Boville, (1993). Mu is the upward convective mixing rate given by:

$$Mu = \frac{K_{\Psi} z_{1+\frac{1}{2}}}{\Delta z_{1+\frac{1}{2}} \left(h - z_{1+\frac{1}{2}}\right)} \tag{A.9}$$

The f_{conv} (Equation A.8) controls the partitioning between local and non-local mixing so that it contributes to smooth transitions from local transport for stable conditions to both local and non-local transport for unstable conditions. For stable or neutral conditions $f_{conv} = 0$ so that the total mixing depends only on the local transport (last term on the right-hand side of Equation A.7), whereas the non-local transport (first term on the right-hand side of Equation A.7) is dominant under unstable conditions with $f_{conv} > 0$. In the ACM2 scheme eddy diffusivity is obtained similarly to Holtslag and Boville, (1993); that is, it is a function of friction velocity, z and h.

The top of the PBL is computed using the Ri_{cr} although different approaches are implemented depending on the atmospheric conditions as in YSU. For stable conditions, Ri_b is diagnosed similarly to Equation A.5, such that:

$$Ri_b(z) = \frac{g[\theta_v(h) - \theta_v(z_1)]z}{\acute{\theta_v}[u(z)^2 + v(z)^2]} \tag{A.10}$$

where $\acute{\theta_v}$ is the averaged virtual potential temperature between model layers at z_1 and h. For unstable conditions, the Richardson method is applied to the entrainment zone so that h is defined as the height where Ri_b equals Ri_{cr} within the entrainment layer only. Thus, Ri_b is given as:

$$Ri_b(z) = \frac{g[\theta_v(z) - \theta_s](h - z_{mix})}{\overline{\theta_v}\{[u(h) - u(z_{mix})]^2 + [v(h) - v(z_{mix})]^2\}} \tag{A.11}$$

where z_{mix} represents the top of the unstable layer, calculated by setting $\theta_v(z_{mix}) = \theta_s$, and θ_s is given by Equation A.6, although in this case $b = 8.5$ as suggested in Holtslag et al., (1990).

1.2. Calculation of H

In Pleim-Xiu LSM, the sensible heat flux H is determined by the expression:

$$H = \rho C_p \left(\frac{\theta_g - \theta_1}{r_{ah}}\right) \tag{A.12}$$

where θ_1, θ_g and r_{ah} are the potential temperature at the first half layer (povided by the SL scheme), the potential temperature at the ground and the aerodynamic resistance for heat. Similarly to Equations 2.5 - 2.7, in the Noah-MP LSM, the total H over a grid cell

is the sum of the following components (namely for bare ground, vegetated ground and vegetation canopy):

$$H_{g,b} = \rho C_p \frac{T_{g,b} - T}{r_{ah}} \quad \text{(A.13)}$$

$$H_{g,v} = \rho C_p \frac{T_{g,v} - T_c}{r_{ah,g}} \quad \text{(A.14)}$$

$$H_v = 2(LAI_e + SAI_e)\rho C_p \frac{T_v - T_c}{r_b} \quad \text{(A.15)}$$

where $r_{ah,g}$ the aerodynamic resistance for heat below the canopy, T_c the temperature of air below the canopy, r_b the leaf boundary layer resistance per unit LAI, and LAI_e and SAI_e the effective LAI and SAI, respectively. Further information can be consulted in Niu et al., (2011).

1.3. Noah-MP input vegetation tables

Table A.1 – Main vegetation parameters for Noah-MP from VEGPARM.TBL and MPTABLE.TBL: SHDFAC (vegetation fraction), NROOT (rooting depth [m]), HVT (canopy top [m]), HVB (canopy bottom [m]) and DEN (vegetation density [number·m^{-2}]).

Landuse	Description	VEGPARM		MPTABLE		
		SHDFAC	**NROOT**	**HVT**	**HVB**	**DEN**
URB	Urban and built-up land	0.10	1	15.00	1.00	0.01
DCR	Dryland/Cropland and pasture	0.80	3	2.00	0.10	25.00
ICR	Irrigated cropland and pasture	0.80	3	2.00	0.10	25.00
CRP	Cropland/Woodland mosaic	0.80	3	8.00	0.15	25.00
GRA	Grassland	0.80	3	8.00	0.15	25.00
SHR	Mixed shrubland/grassland	0.70	3	1.10	0.10	10.00
DBF	Deciduous broadleaf forest	0.80	4	16.00	11.5	0.10
ENF	Evergreen needleleaf forest	0.70	4	20.00	8.50	0.28
FOR	Mixed forest	0.80	4	16.00	10.00	0.10
HWL	Herbaceous wetland	0.60	2	0.50	0.05	10.00
BAR	Barren or sparely vegetated	0.01	1	0.00	0.00	0.01

1.4. Data flow using *ndown.exe*

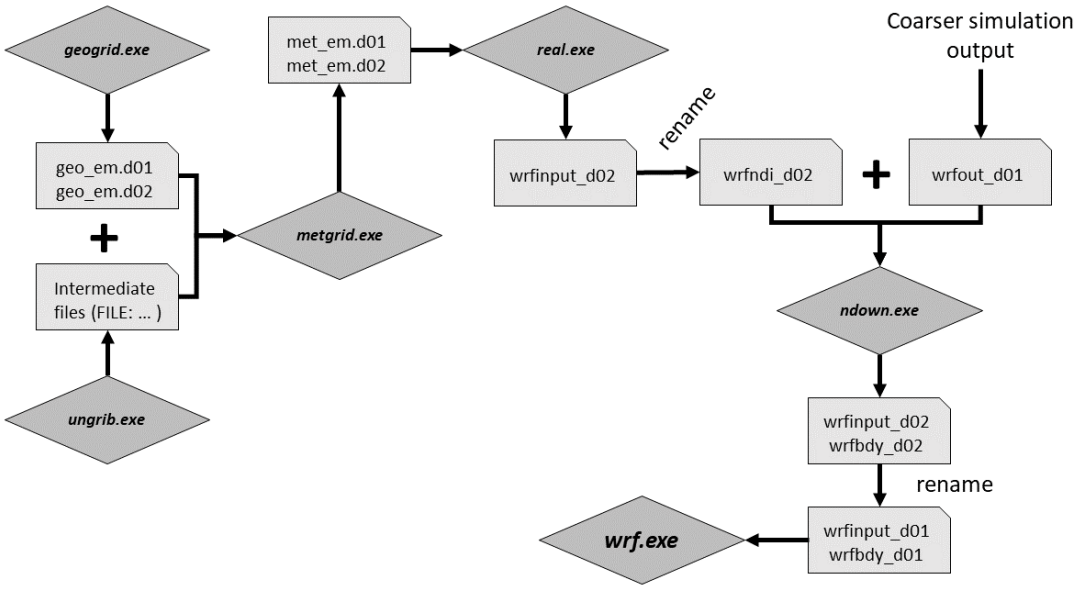

Figure A.2 - Schematic representation of the data flow when using *ndown.exe* program to generate boundary conditions for a one-way high-resolution simulation. Adapted from Skamarock et al. (2008).

2. Mixing diagrams from observations

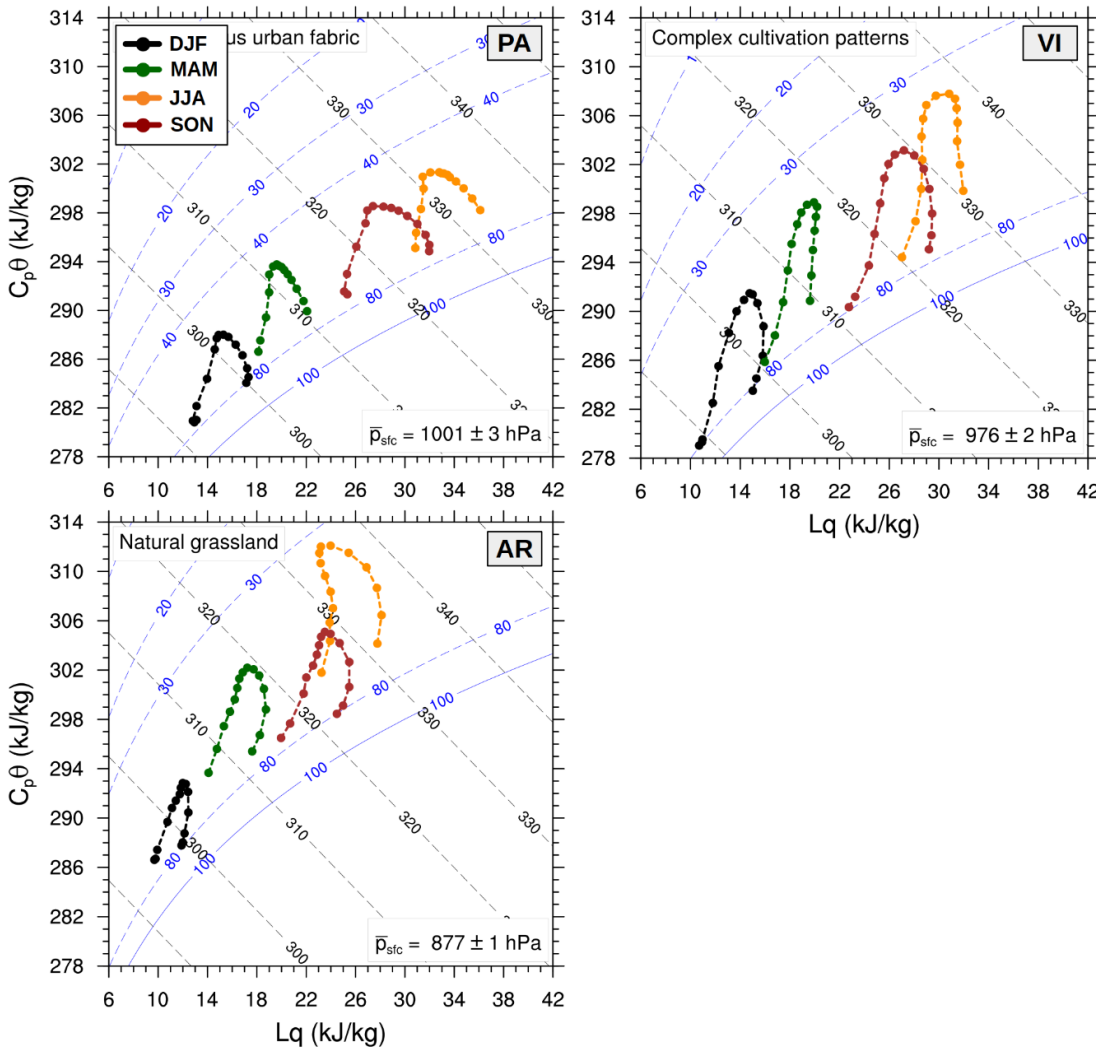

Figure B.1 - Mixing diagrams from 06 to 20 UTC at PA, VI and AR using 10-year hourly averaged values (2005-2015) during DJF (black), MAM (green), JJA (orange) and SON (brown) for days with sea breeze circulation.

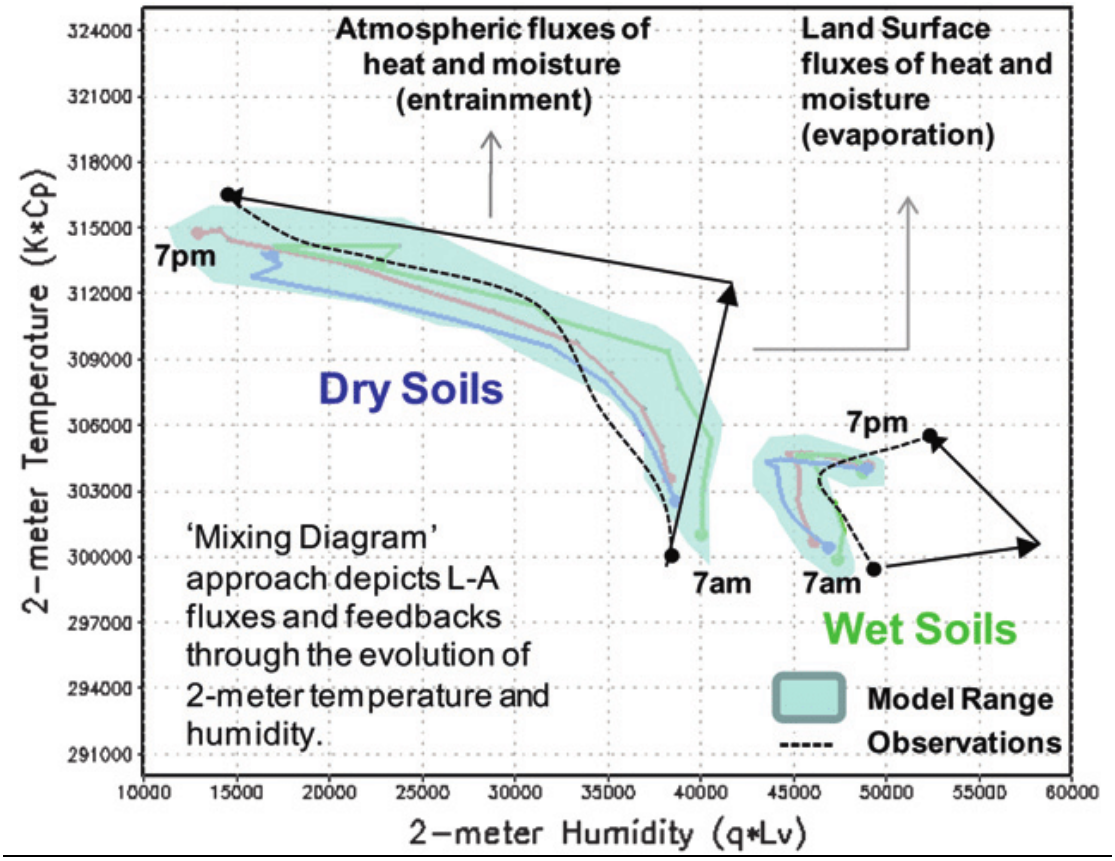

Figure B.2 - Mixing diagrams for dry and wet soil. Extracted from Santanello et al. (2011).

3. Intermediate Sea Breeze Front

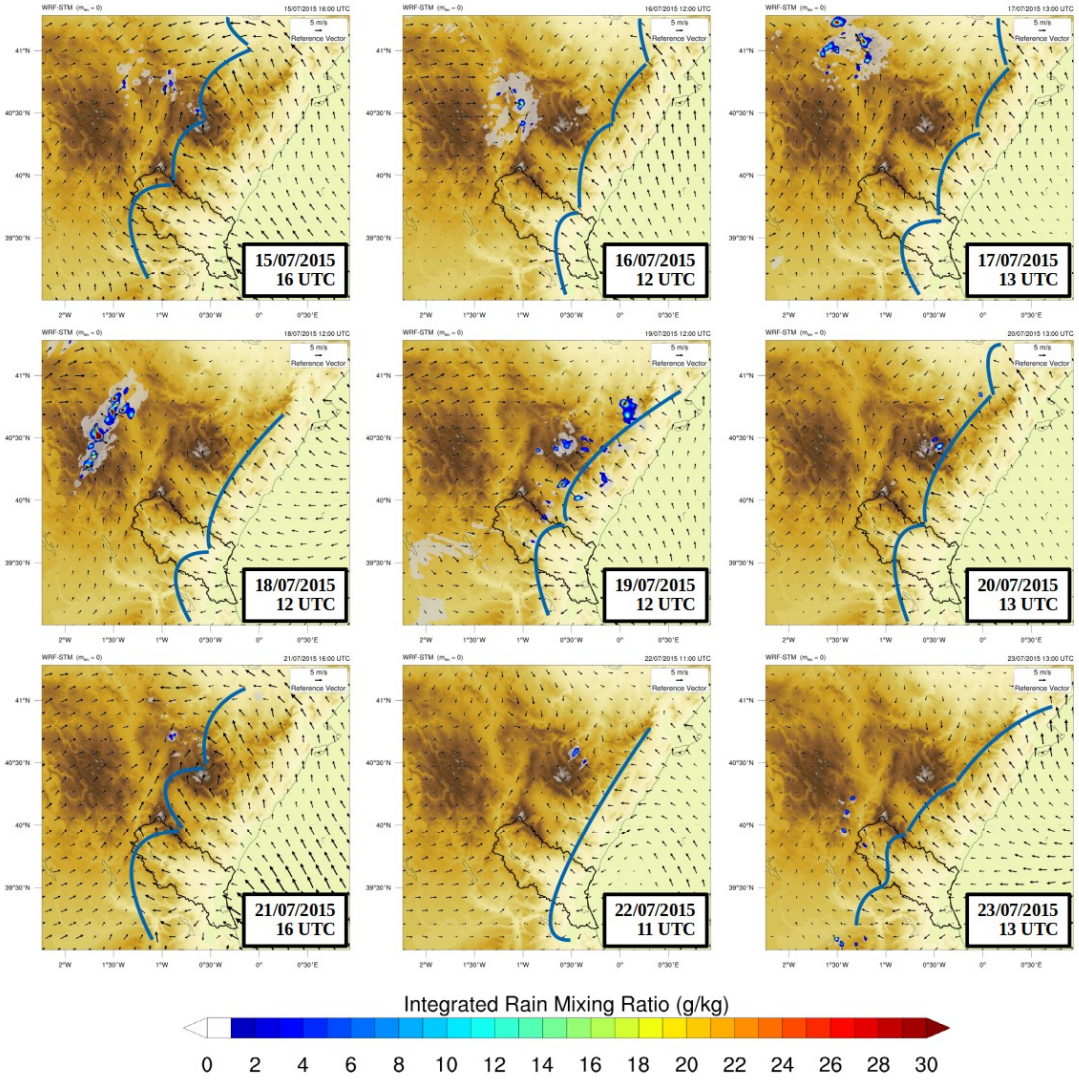

Figure C.1 - Topographic maps with horizontal wind vectors, cloud cover and integrated rain (q_{rain}) from STM for the period 15th - 23rd of July 2015 at summer storm formation time. The ISBF is denoted by the blue line.

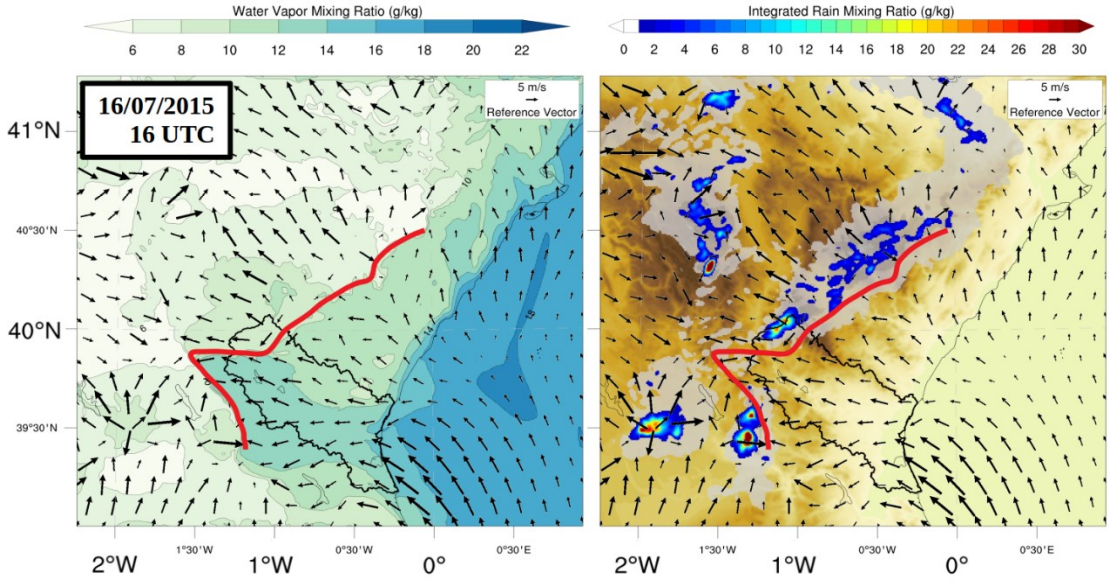

Figure C.2 - Horizontal wind vectors (black arrows) with (a) 2-m mixing ratio, (b) topography, cloud cover (in gray) and integrated rain (q_{rain}) from STM for the 16th of July 2015 at 16 UTC. The ISBF is denoted by the solid red line.

4. Mixing diagrams from STM simulation

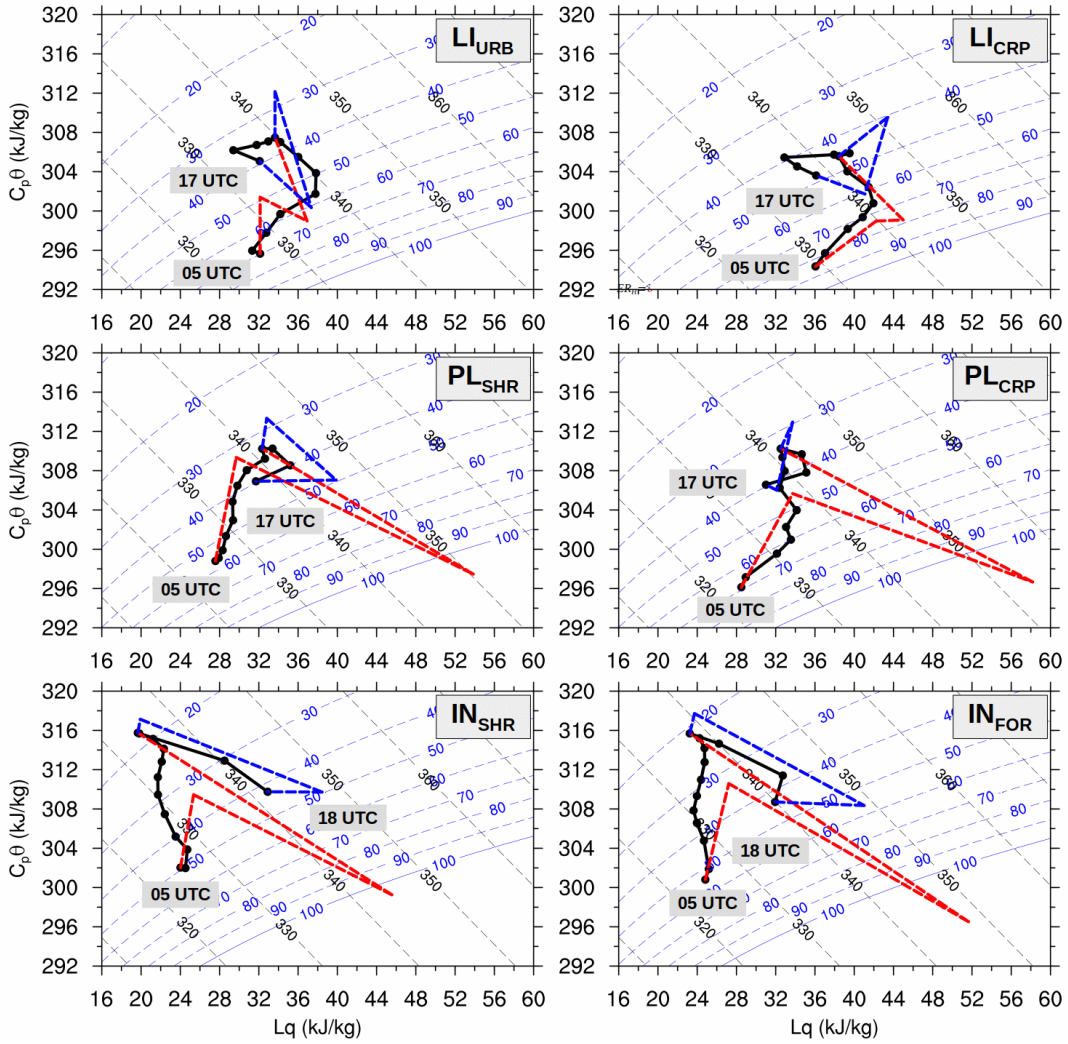

Figure D.1 - Mixing diagrams with calculated vectors for the 15th of July 2015 over littoral (LI), prelittoral (PL) and inland (IN) locations and the different land use categories (URB, CRP, SHR and FOR) using the STM output, together with surface-advection ratios for *H* and *LE* (see subsection 6.1 in Chapter 2).

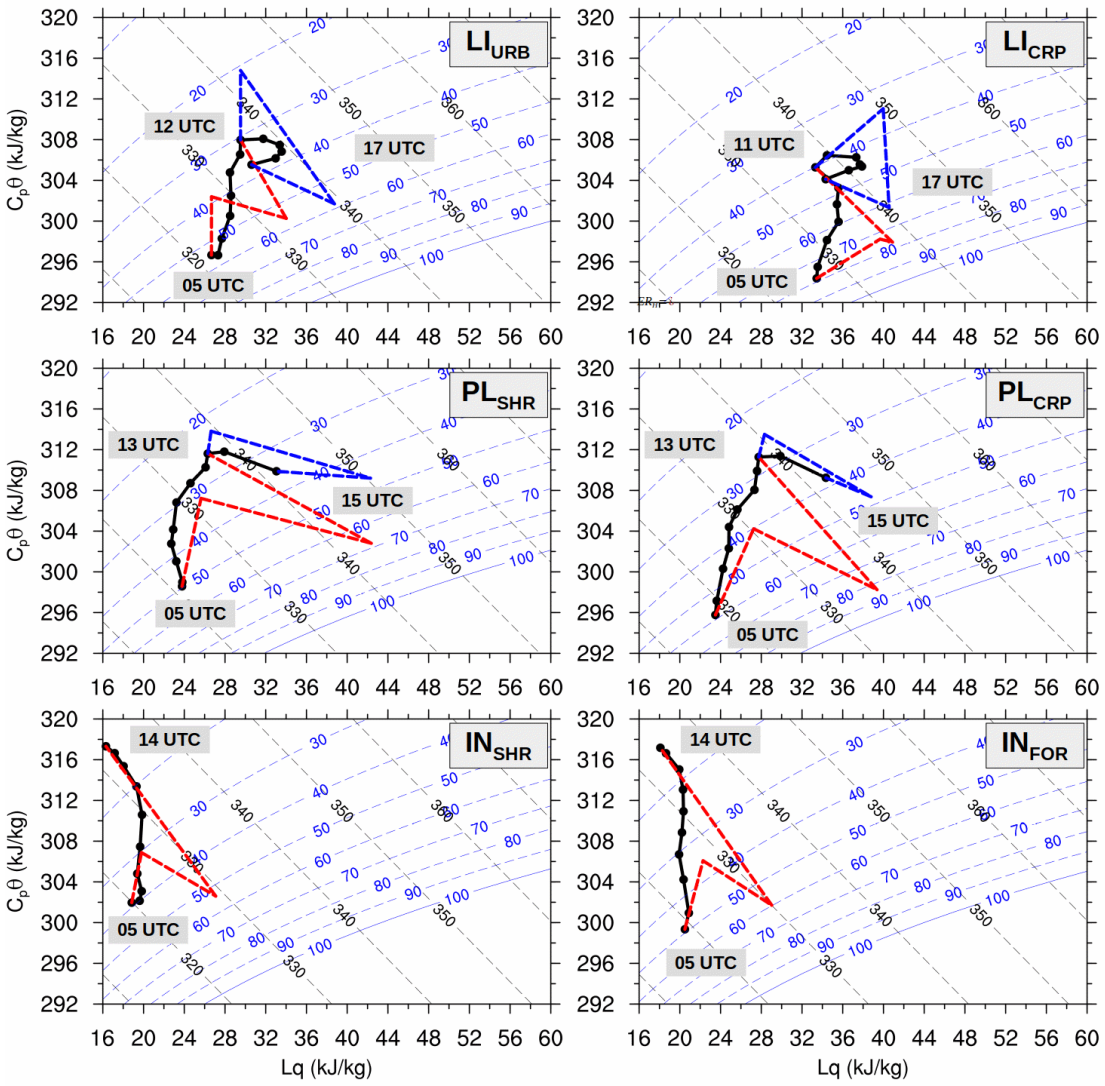

Figure D.2 - Same as Figure C.1 but for the 16th of July 2015.

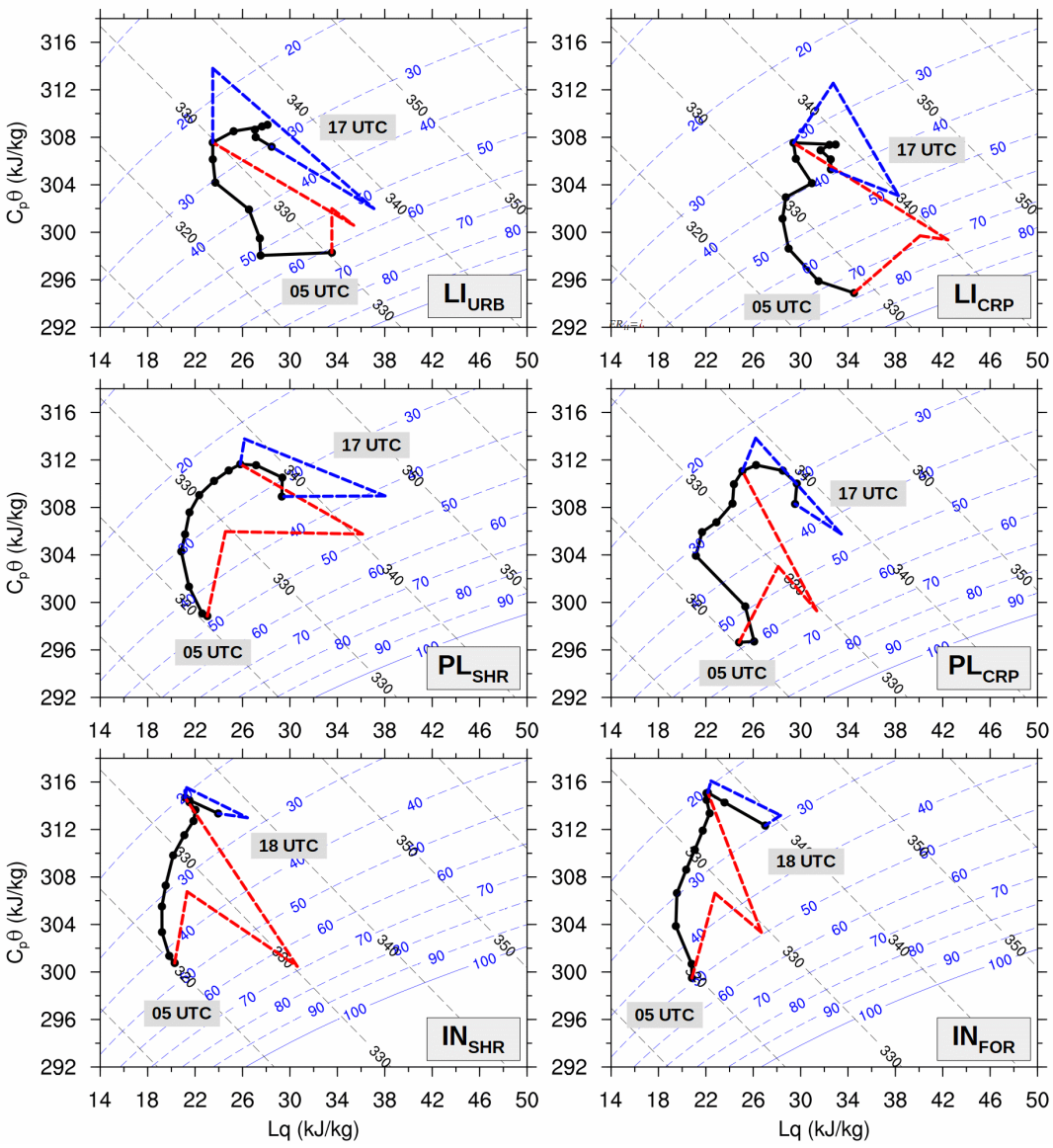

Figure D.3 - Same as Figure C.1 but for the 17th of July 2015.

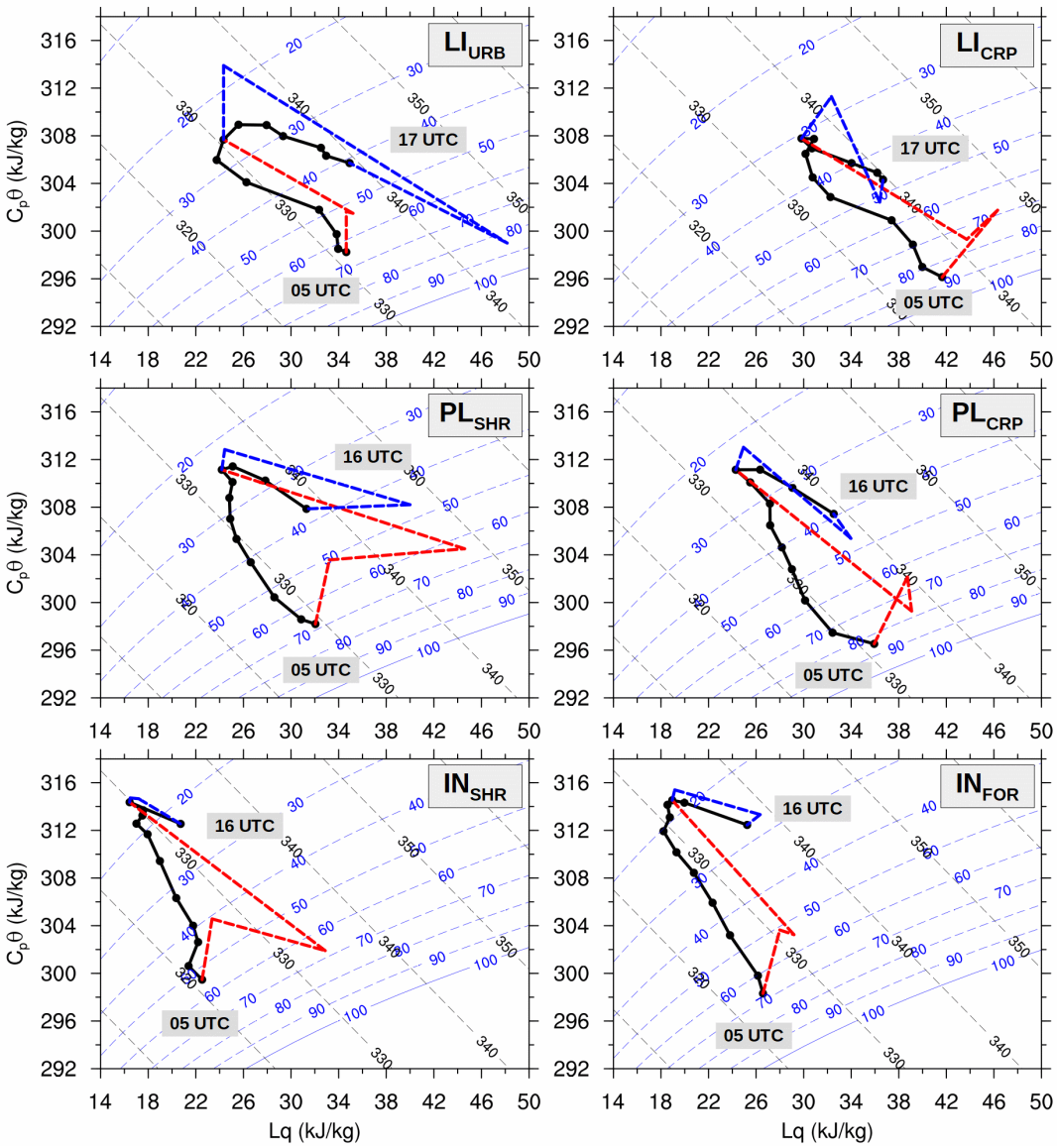

Figure D.4 - Same as Figure C.1 but for the 18th of July 2015.

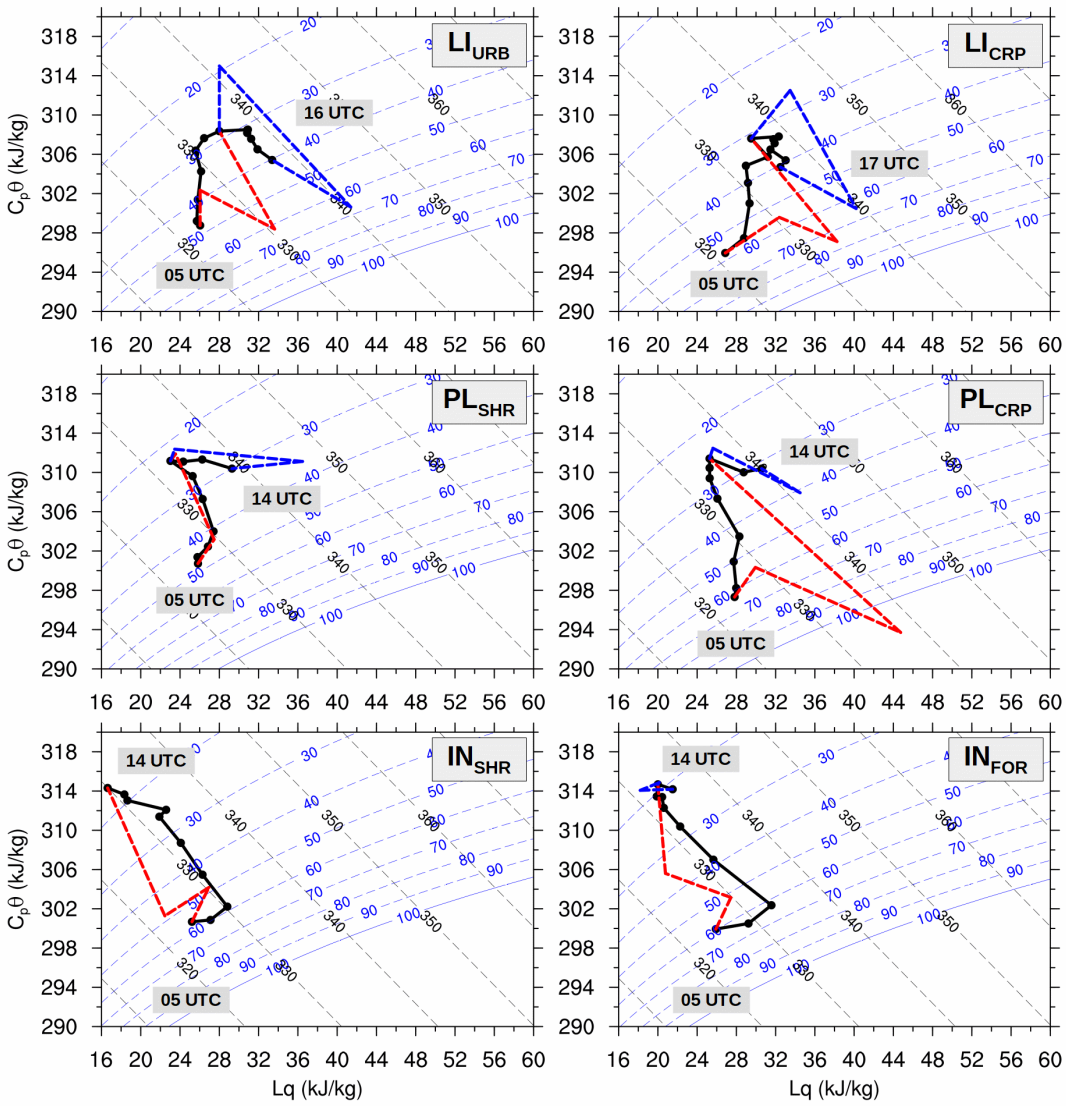

Figure D.5 - Same as Figure C.1 but for the 19th of July 2015.

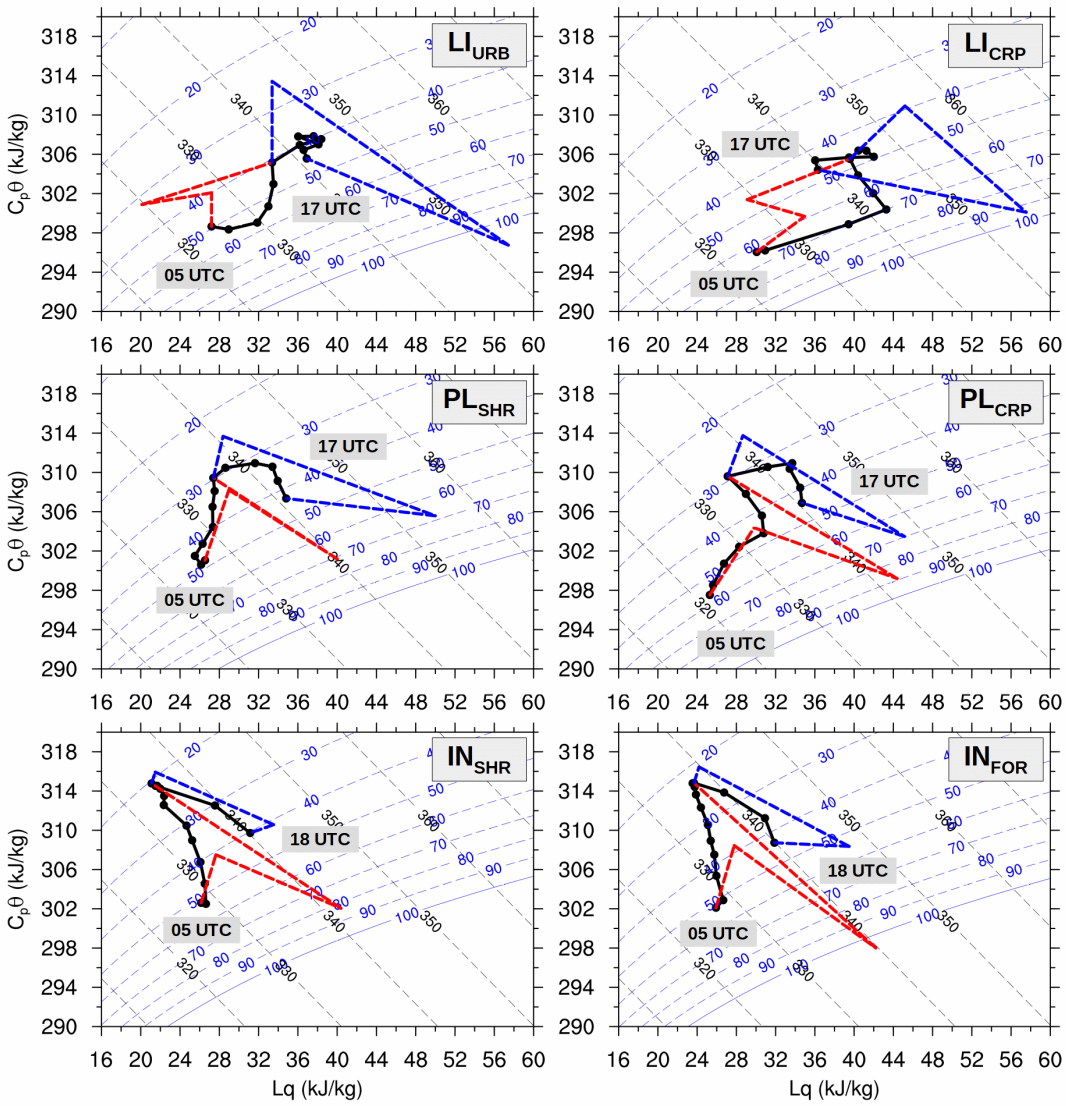

Figure D.6 - Same as Figure C.1 but for the 20th of July 2015.

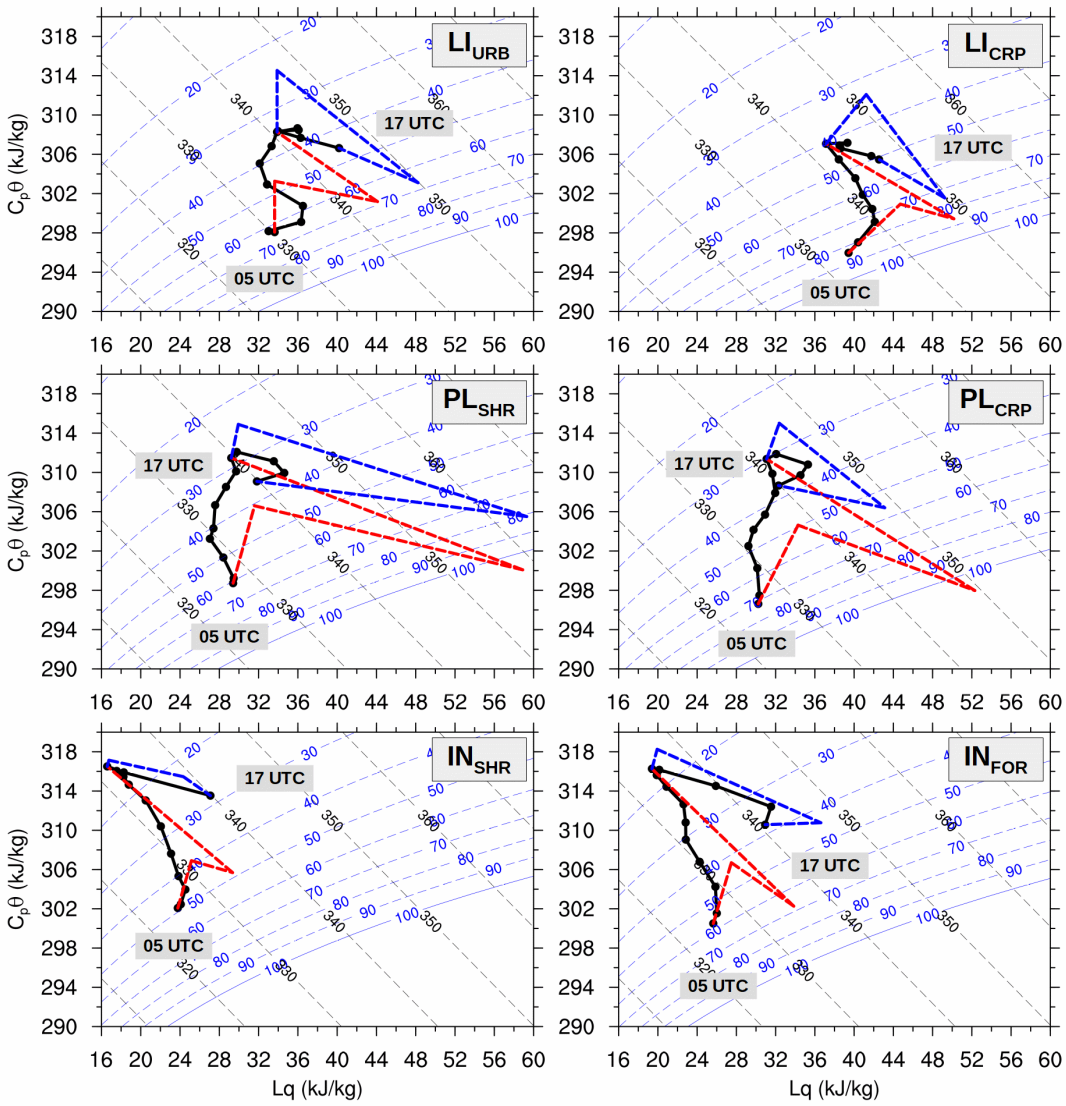

Figure D.7 - Same as Figure C.1 but for the 21st of July 2015.

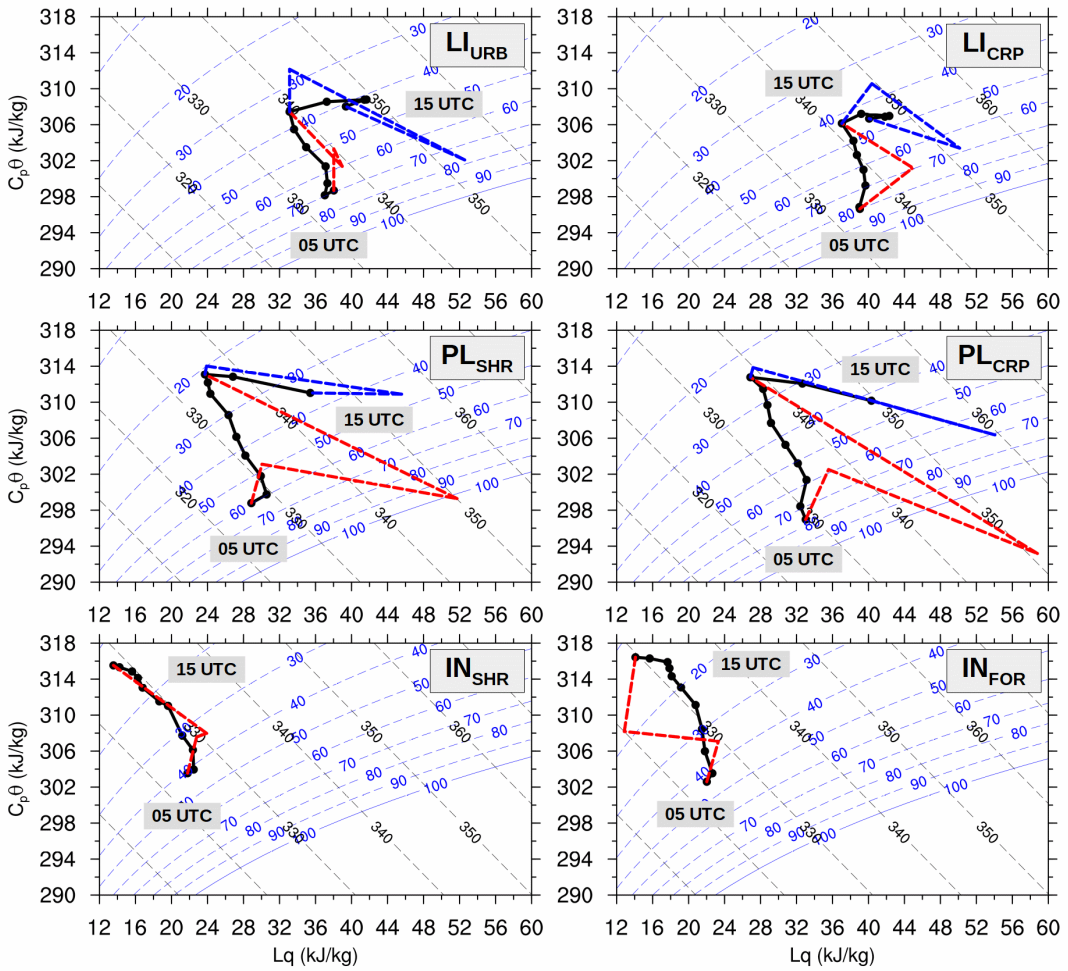

Figure D.8 - Same as Figure C.1 but for the 22nd of July 2015.

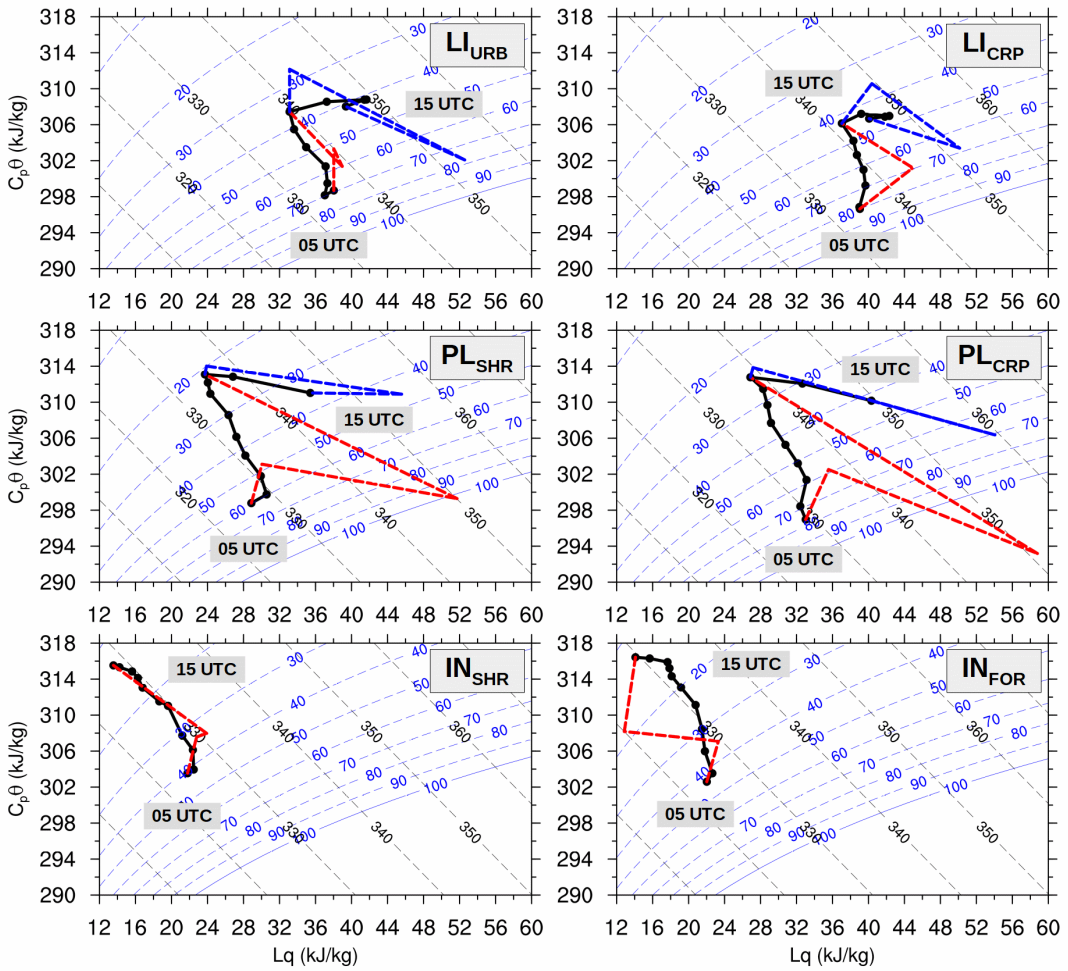

Figure D.9 - Same as Figure C.1 but for the 23rd of July 2015.

5. Trajectories

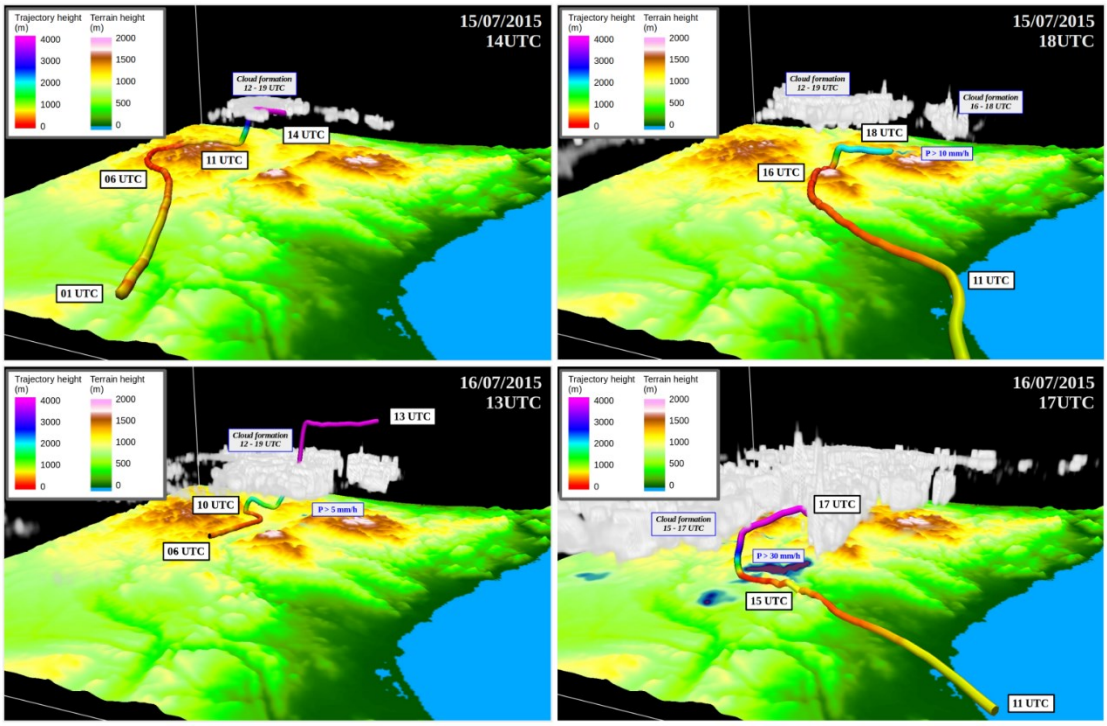

(a) (b)

Figure E.1 - 3D topographic maps with unsteady (time-varying) backward and forward trajectories calculated with the VAPOR tool (a) from convective clouds (represented in grey) generated over the TRB, and (b) from the SBF for the period 15th - 16th of July 2015. The coloring of trajectory lines denotes the height with respect to the ground at the given location. Annotations regarding time, convective cloud generation periods and precipitation intensity (P) are also shown, as well as precipitation is represented in blue to pink colors over topography.

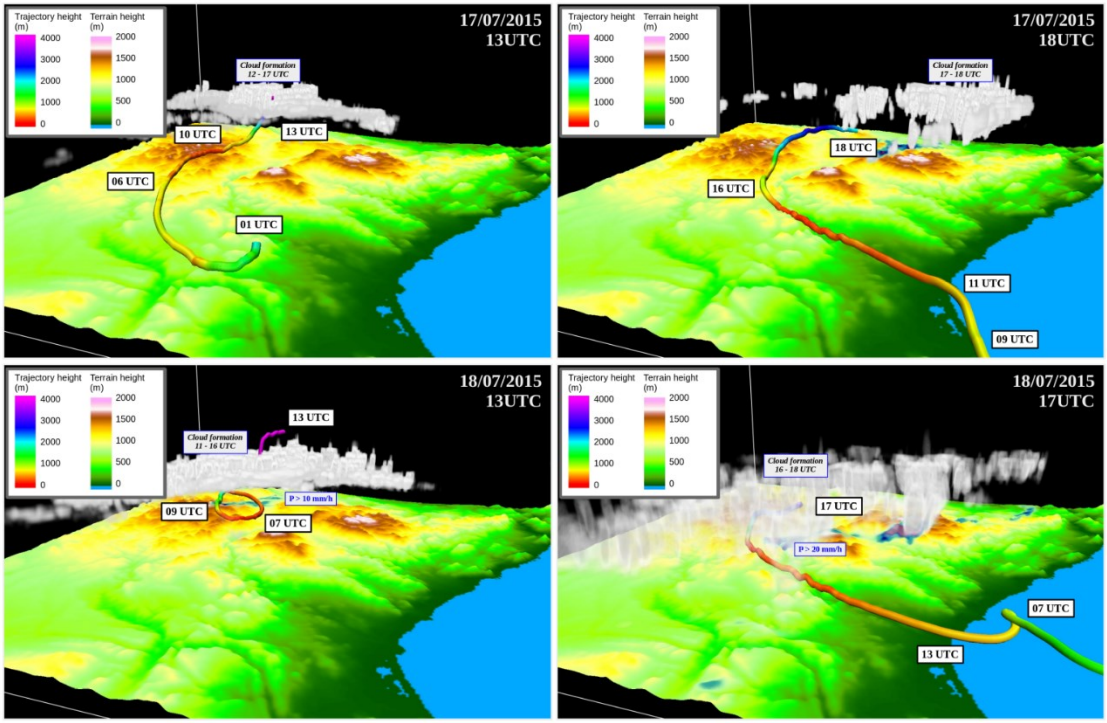

(a) (b)

Figure E.2 - Same as Figure D.1 but for the period 17th - 18th of July 2015.

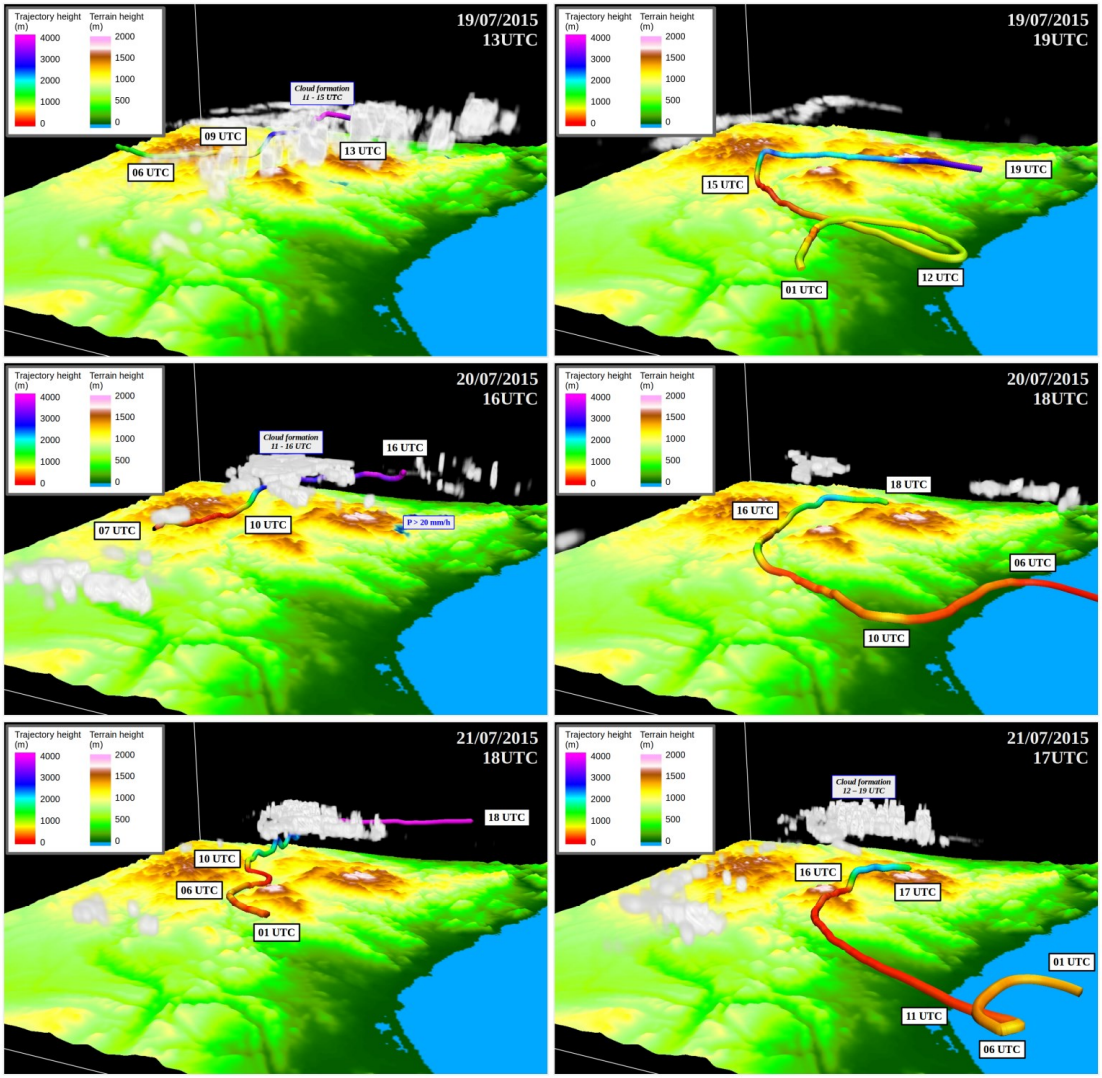

(a) (b)

Figure E.3 - Same as Figure D.1 but for the period 19th - 21st of July 2015.

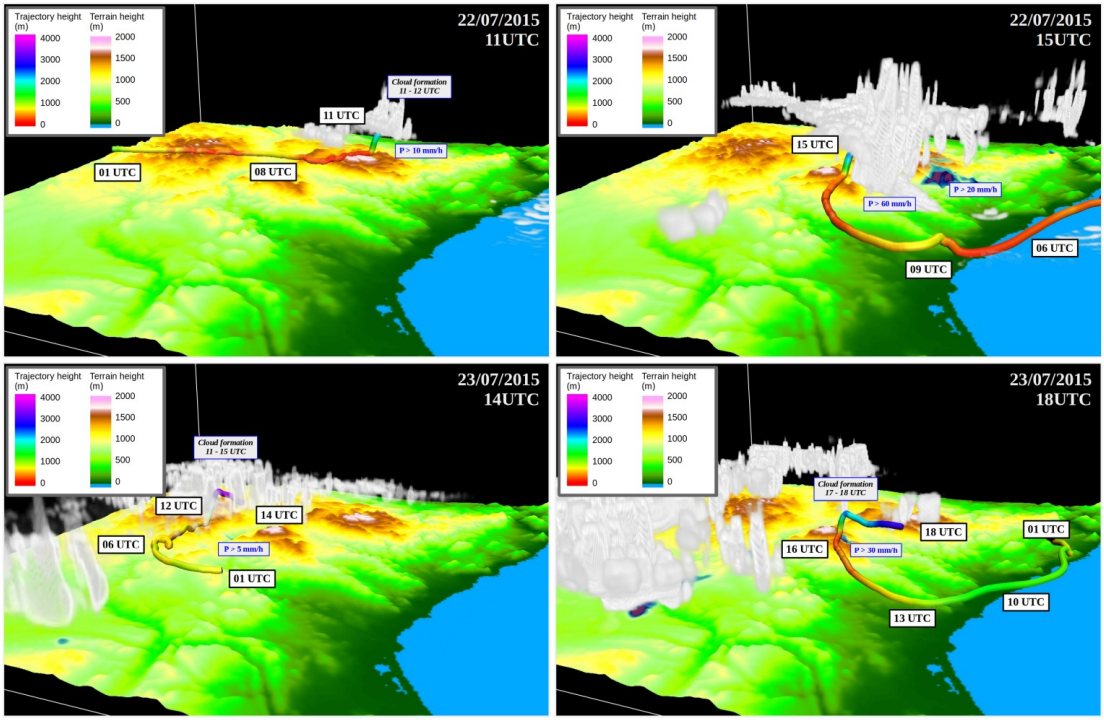

(a) (b)

Figure E.4 - Same as Figure D.1 but for the period 22nd - 23rd of July 2015.

BIBLIOGRAPHY

Adams, E. (1997). Four ways to win the sea breeze game. *Sailing World, 3*, 412.

Ado, H. Y. (1992). Numerical Study of the Daytime Urban Effect and Its Interaction with the Sea Breeze. *Journal of Applied Meteorology and Climatology, 31*, 1146-1164. https://doi.org/10.1175/1520-0450(1992)031<1146:NSOTDU>2.0.CO;2

AEMET. (2010). *Informe Climatológico Mensual: Agosto 2010.* Tech. rep.

AEMET. (2010). *Informe Climatológico Mensual: Julio 2010.* Tech. rep.

AEMET. (2010). *Informe Climatológico Mensual: Junio 2010.* Tech. rep.

AEMET. (2013). *Informe Climatológico Mensual: Agosto 2013.* Tech. rep.

AEMET. (2013). *Informe Climatológico Mensual: Julio 2013.* Tech. rep.

AEMET. (2013). *Informe Climatológico Mensual: Junio 2013.* Tech. rep.

AEMET. (2015). *Informe Climatológico Mensual: Agosto 2015.* Tech. rep.

AEMET. (2015). *Informe Climatológico Mensual: Julio 2015.* Tech. rep.

AEMET. (2015). *Informe Climatológico Mensual: Junio 2015.* Tech. rep.

Allende-Arandía, M. E., Zavala-Hidalgo, J., Torres-Freyermuth, A., Appendini, C. M., Cerezo-Mota, R., & Taylor-Espinosa, N. (2020). Sea-land breeze diurnal component and its interaction with a cold front on the coast of Sisal, Yucatan: A case study. *Atmospheric Research, 244*, 105051. https://doi.org/10.1016/j.atmosres.2020.105051

Alonso, L., Gangoiti, G., Navazo, M., Millán, M. M., & Mantilla, E. (2000). Transport of Tropospheric Ozone over the Bay of Biscay and the Eastern Cantabrian Coast of Spain. *Journal of Applied Meteorology, 39*, 475-486. https://doi.org/10.1175/1520-0450(2000)039<0475:TOTOOT>2.0.CO;2

Alpert, P., & Rabinovich-Hadar, M. (2003). Pre- and Post-Sea-Breeze Frontal Lines—A Meso-γ-Scale Analysis over South Israel. *Journal of the Atmospheric Sciences, 60*, 2994-3008. https://doi.org/10.1175/1520-0469(2003)060<2994:PAPFLM>2.0.CO;2

Anthes, R. A., & Warner, T. T. (1978). Development of Hydrodynamic Models Suitable for Air Pollution and Other Mesometerological Studies. *Monthly Weather Review, 106*, 1045-1078. https://doi.org/10.1175/1520-0493(1978)106<1045:DOHMSF>2.0.CO;2

Astraldi, M., & Gasparini, G. P. (1992). The seasonal characteristics of the circulation in the north Mediterranean basin and their relationship with the atmospheric-climatic conditions. *Journal of Geophysical Research: Oceans, 97*, 9531-9540. https://doi.org/10.1029/92JC00114

Azorin-Molina, C., Chen, D., Tijm, S., & Baldi, M. (2011). A multi-year study of sea breezes in a Mediterranean coastal site: Alicante (Spain). *International Journal of Climatology, 31*, 468-486. https://doi.org/10.1002/joc.2064

Azorin-Molina, C., Connell, B. H., & Baena-Calatrava, R. (2009). Sea-Breeze Convergence Zones from AVHRR over the Iberian Mediterranean Area and the Isle of Mallorca, Spain. *Journal of Applied Meteorology and Climatology, 48*, 2069-2085. https://doi.org/10.1175/2009JAMC2141.1

Azorin-Molina, C., Tijm, S., Ebert, E. E., Vicente-Serrano, S. M., & Estrela, M. J. (2014). Sea breeze thunderstorms in the eastern Iberian Peninsula. Neighborhood verification of HIRLAM and HARMONIE precipitation forecasts. *Atmospheric Research, 139*, 101-115. https://doi.org/10.1016/j.atmosres.2014.01.010

Balmaseda, M., and Anderson, D. (2009), Impact of initialization strategies and observations on seasonal forecast skill, *Geophys. Res. Lett.*, 36, L01701, https://doi.org/10.1029/2008GL035561.

Banks, R. F., Tiana-Alsina, J., Baldasano, J. M., Rocadenbosch, F., Papayannis, A., Solomos, S., & Tzanis, C. G. (2016). Sensitivity of boundary-layer variables to PBL schemes in the WRF model based on surface meteorological observations, lidar, and radiosondes during the HygrA-CD campaign. *Atmospheric Research, 176*, 185-201. https://doi.org/10.1016/j.atmosres.2016.02.024

Bauer, P., Thorpe, A., & Brunet, G. (2015). The quiet revolution of numerical weather prediction. *Nature, 525*, 47–55. https://doi.org/10.1038/nature14956

Bellot, J., & Chirino Miranda, E. (2013-09-24). Hydrobal: An eco-hydrological modelling approach for assessing water balances in different vegetation types in semi-arid areas. *Hydrobal: An eco-hydrological modelling approach for assessing water balances in different vegetation types in semi-arid areas*.

Bellot, J., & Chirino, E. (2013). Hydrobal: An eco-hydrological modelling approach for assessing water balances in different vegetation types in semi-arid areas. *Ecological Modelling, 266*, 30-41. https://doi.org/10.1016/j.ecolmodel.2013.07.002

Berg, L. K., Jr., W. I., Kassianov, E. I., & Deng, L. (2013, January). Evaluation of a Modified Scheme for Shallow Convection: Implementation of CuP and Case Studies. *Monthly Weather Review, 141*, 134–147. https://doi.org/10.1175/MWR-D-12-00136.1

Bergthorsson, P., DÖÖs, B. R., Fryklund, S., Haug, O., & Lindquist, R. (1955). Routine Forecasting with the Barotropic Model. *Tellus, 7*, 272-274. https://doi.org/10.3402/tellusa.v7i2.8775

Berrisford, P., Dee, D. P., Poli, P., Brugge, R., Fielding, K., Fuentes, M., . . . Simmons, A. (2011, November). *The ERA-Interim archive Version 2.0.* Shinfield, Park, Reading: ECMWF.

Betts, A. K. (1992). FIFE atmospheric boundary layer budget methods. *Journal of Geophysical Research: Atmospheres, 97*, 18523-18531. https://doi.org/10.1029/91JD03172

Betts, A. K., & Ball, J. H. (1995). The FIFE surface diurnal cycle climate. *Journal of Geophysical Research: Atmospheres, 100*, 25679-25693. https://doi.org/10.1029/94JD03121

Betts, A. K., Ball, J. H., Beljaars, A. C., Miller, M. J., & Viterbo, P. A. (1996). The land surface-atmosphere interaction: A review based on observational and global

modeling perspectives. *Journal of Geophysical Research: Atmospheres, 101*, 7209-7225. https://doi.org/10.1029/95JD02135

Bevis, M., Businger, S., Chiswell, S., Herring, T. A., Anthes, R. A., Rocken, C., & Ware, R. H. (1994). GPS Meteorology: Mapping Zenith Wet Delays onto Precipitable Water. *Journal of Applied Meteorology and Climatology, 33*, 379-386. https://doi.org/10.1175/1520-0450(1994)033<0379:GMMZWD>2.0.CO;2

Bevis, M., Businger, S., Herring, T. A., Rocken, C., Anthes, R. A., & Ware, R. H. (1992). GPS meteorology: Remote sensing of atmospheric water vapor using the global positioning system. *Journal of Geophysical Research: Atmospheres, 97*, 15787-15801. https://doi.org/10.1029/92JD01517

Blackadar, A. K. (1978). Modeling pollutant transfer during daytime convection. *Preprints Fourth Symposium on Atmospheric Turbulence, Diffusion and Air Quality. Reno. Amer. Met. Soc., 1978*, (pp. 443–447).

Brief, A., Gcms, H., & Edwards, P. (2001, July). A Brief History of Atmospheric General Circulation Modeling.

Brief, A., Gcms, H., & Edwards, P. (2001, July). A Brief History of Atmospheric General Circulation Modeling.

BRÜMMER, B., HENNEMUTH, B., RHODIN, A., & THIEMANN, S. (1995). Interaction of a cold front with a sea breeze front Observations. *Tellus A, 47*, 383-402. https://doi.org/10.1034/j.1600-0870.1995.t01-2-00001.x

Buckley, R. L., & Kurzeja, R. J. (1997). An Observational and Numerical Study of the Nocturnal Sea Breeze. Part I: Structure and Circulation. *Journal of Applied Meteorology (1988-2005), 36*, 1577–1598. https://www.jstor.org/stable/26182348

Caicedo, V., Rappenglueck, B., Cuchiara, G., Flynn, J., Ferrare, R., Scarino, A. J., . . . Lefer, B. (2019). Bay Breeze and Sea Breeze Circulation Impacts on the Planetary Boundary Layer and Air Quality From an Observed and Modeled DISCOVER-AQ Texas Case Study. *Journal of Geophysical Research: Atmospheres, 124*, 7359-7378. https://doi.org/10.1029/2019JD030523

Campo, L., Castelli, F., Entekhabi, D., & Caparrini, F. (2009). Land-atmosphere interactions in an high resolution atmospheric simulation coupled with a surface data assimilation scheme. *Natural Hazards and Earths System Sciences, 9*, 1613–1624. https://doi.org/10.5194/nhess-9-1613-2009

Chen, L., Ma, Z.-g., & Fan, X.-g. (2012, December). A Comparative Study of Two Land Surface Schemes in WRF Model over Eastern China. *Journal of Tropical Meteorology, 18*, 445–456.

Clarke, R. H. (1984). Colliding sea breezes and the creation of internal atmospheric bore waves: two-dimensional numerical studies. *Aust. Met. Mag., 32*, 207–226.

(2019). *Climate Change and Land: an IPCC special report on climate change, desertification, land degradation, sustainable land management, food security, and greenhouse gas fluxes in terrestrial ecosystems.* Tech. rep., IPCC.

Cohen, A. E., Cavallo, S. M., Coniglio, M. C., & Brooks, H. E. (2015, June). A Review of Planetary Boundary Layer Parameterization Schemes and Their Sensitivity in Simulating Southeastern U.S. Cold Season Severe Weather Environments.

Weather and Forecasting, 30, 591–612. https://doi.org/10.1175/WAF-D-14-00105.1

Cook, B. I., Anchukaitis, K. J., Touchan, R., Meko, D. M., & Cook, E. R. (2016). Spatiotemporal drought variability in the Mediterranean over the last 900 years. *Journal of Geophysical Research: Atmospheres, 121*, 2060-2074. https://doi.org/10.1002/2015JD023929

Coppola, E., Nogherotto, R., Ciarlo', J. M., Giorgi, F., van Meijgaard, E., Kadygrov, N., . . . Wulfmeyer, V. (2021). Assessment of the European Climate Projections as Simulated by the Large EURO-CORDEX Regional and Global Climate Model Ensemble. *Journal of Geophysical Research: Atmospheres, 126*, e2019JD032356. https://doi.org/10.1029/2019JD032356

Cossu, F., & Hocke, K. (2014). Influence of microphysical schemes on atmospheric water in the Weather Research and Forecasting model. *Geoscientific Model Development, 7*, 147–160. https://doi.org/10.5194/gmd-7-147-2014

Côté, J., Gravel, S., Méthot, A., Patoine, A., Roch, M., & Staniforth, A. (1998). The Operational CMC–MRB Global Environmental Multiscale (GEM) Model. Part I: Design Considerations and Formulation. *Monthly Weather Review, 126*, 1373-1395. https://doi.org/10.1175/1520-0493(1998)126<1373:TOCMGE>2.0.CO;2

De Haan, S. (2006). Measuring Atmospheric Stability with GPS. *Journal of Applied Meteorology and Climatology, 45*, 467–475. Retrieved from http://www.jstor.org/stable/26171696

de Luis, M., Brunetti, M., Gonzalez-Hidalgo, J. C., Longares, L. A., & Martin-Vide, J. (2010). Changes in seasonal precipitation in the Iberian Peninsula during 1946–2005. *Global and Planetary Change, 74*, 27-33. https://doi.org/10.1016/j.gloplacha.2010.06.006

De Ridder, K. (1997). Land surface processes and the potential for convective precipitation. *Journal of Geophysical Research: Atmospheres, 102*, 30085-30090. https://doi.org/10.1029/97JD02624

Delrieu, G., Nicol, J., Yates, E., Kirstetter, P.-E., Creutin, J.-D., Anquetin, S., . . . Wobrock, W. (2005). The Catastrophic Flash-Flood Event of 8–9 September 2002 in the Gard Region, France: A First Case Study for the Cévennes–Vivarais Mediterranean Hydrometeorological Observatory. *Journal of Hydrometeorology, 6*, 34-52. https://doi.org/10.1175/JHM-400.1

Dirmeyer, P. A., Zeng, F. J., Ducharne, A., Morrill, J. C., & Koster, R. D. (2000). The Sensitivity of Surface Fluxes to Soil Water Content in Three Land Surface Schemes. *Journal of Hydrometeorology, 1*, 121-134. https://doi.org/10.1175/1525-7541(2000)001<0121:TSOSFT>2.0.CO;2

Drobinski, P., Bastin, S., Arsouze, T., Béranger, K., Flaounas, E., & Stéfanon, M. (2018). North-western Mediterranean sea-breeze circulation in a regional climate system model. *Climate Dynamics, 51*, 1077–1093. https://doi.org/10.1007/s00382-017-3595-z

Dudhia, J. (2014). A history of mesoscale model development. *Asia-Pacific Journal of Atmospheric Sciences, 50*, 121–131. https://doi.org/10.1007/s13143-014-0031-8

Duzenli, E., Yucel, I., Pilatin, H., & Yilmaz, M. T. (2021). Evaluating the performance of a WRF initial and physics ensemble over Eastern Black Sea and Mediterranean regions in Turkey. *Atmospheric Research, 248*, 105184. https://doi.org/10.1016/j.atmosres.2020.105184

Edwards, P. (2001, January). Representing the Global Atmosphere: Computer Models, Data, and Knowledge about Climate Change.

Erlingis, J. M., & Barros, A. P. (2014). A Study of the Role of Daytime Land–Atmosphere Interactions on Nocturnal Convective Activity in the Southern Great Plains during CLASIC. *Journal of Hydrometeorology, 15*, 1932-1953. https://doi.org/10.1175/JHM-D-14-0016.1

Farr, T. G., Rosen, P. A., Caro, E., Crippen, R., Duren, R., Hensley, S., . . . Alsdorf, D. (2007). The Shuttle Radar Topography Mission. *Reviews of Geophysics, 45*. https://doi.org/10.1029/2005RG000183

Fernández-Montes, S., & Rodrigo, F. S. (2015). Trends in surface air temperatures, precipitation and combined indices in the southeastern Iberian Peninsula (1970-2007). *Clim Res, 63*, 43–60. http://www.int-res.com/abstracts/cr/v63/n1/p43-60/

Ferraro, R. R. (1997). Special sensor microwave imager derived global rainfall estimates for climatological applications. *Journal of Geophysical Research: Atmospheres, 102*, 16715-16735. https://doi.org/10.1029/97JD01210

Ferraro, R. R., Weng, F., Grody, N. C., & Zhao, L. (2000). Precipitation characteristics over land from the NOAA-15 AMSU sensor. *Geophysical Research Letters, 27*, 2669-2672. https://doi.org/10.1029/2000GL011665

Flesch, T. K., & Reuter, G. W. (2012). WRF Model Simulation of Two Alberta Flooding Events and the Impact of Topography. *Journal of Hydrometeorology, 13*, 695-708. https://doi.org/10.1175/JHM-D-11-035.1

Fovell, R. G. (2005). Convective Initiation ahead of the Sea-Breeze Front. *Monthly Weather Review, 133*, 264-278. https://doi.org/10.1175/MWR-2852.1

Fovell, R. G., & Dailey, P. S. (2001). Numerical Simulation of the Interaction between the Sea-Breeze Front and Horizontal Convective Rolls. Part II: Alongshore Ambient Flow. *Monthly Weather Review, 129*, 2057-2072. https://doi.org/10.1175/1520-0493(2001)129<2057:NSOTIB>2.0.CO;2

Freitas, E. D., Rozoff, C. M., Cotton, W. R., & Dias, P. L. (2007). Interactions of an urban heat island and sea-breeze circulations during winter over the metropolitan area of São Paulo, Brazil. *Boundary-Layer Meteorology, 122*, 43–65. https://doi.org/10.1007/s10546-006-9091-3

García-Díez, M., Fernández, J., Fita, L., & Yagüe, C. (2013, March). Seasonal dependence of WRF model biases and sensitivity to PBL schemes over Europe. *Quarterly Journal of the Royal Meteorological Society, 139*, 501–514. https://doi.org/10.1002/qj.1976

Geisler, J. E., & Bretherton, F. P. (1969). The Sea-Breeze Forerunner. *Journal of Atmospheric Sciences, 26*, 82-95. https://doi.org/10.1175/1520-0469(1969)026<0082:TSBF>2.0.CO;2

Gentine, P., Entekhabi, D., Chehbouni, A., Boulet, G., & Duchemin, B. (2007). Analysis of evaporative fraction diurnal behaviour. *Agricultural and Forest Meteorology, 143*, 13-29. https://doi.org/10.1016/j.agrformet.2006.11.002

Gevorgyan, A. (2018). Convection-Permitting Simulation of a Heavy Rainfall Event in Armenia Using the WRF Model. *Journal of Geophysical Research: Atmospheres, 123*, 11,008-11,029. https://doi.org/10.1029/2017JD028247

Gilliam, R. C., & Pleim, J. E. (2010, April). Performance Assessment of New Land Surface and Planetary Boundary Layer Physics in the WRF-ARW. *Journal of Applied Meteorology and Climatology, 49*, 760–774. https://doi.org/10.1175/2009JAMC2126.1

Giorgi, F. (2006). Climate change hot-spots. *Geophysical Research Letters, 33*. https://doi.org/10.1029/2006GL025734

Giorgi, F., & Lionello, P. (2008). Climate change projections for the Mediterranean region. *Global and Planetary Change, 63*, 90-104. https://doi.org/10.1016/j.gloplacha.2007.09.005

Goler, R. A. (2009). Eastward-Propagating Undular Bores over Cape York Peninsula. *Monthly Weather Review, 137*, 2632-2645. https://doi.org/10.1175/2009MWR2833.1

Hai, S., Miao, Y., Sheng, L., Wei, L., & Chen, Q. (2018). Numerical Study on the Effect of Urbanization and Coastal Change on Sea Breeze over Qingdao, China. *Atmosphere, 9*. https://doi.org/10.3390/atmos9090345

Han, J., & Pan, H.-L. (2011, August). Revision of Convection and Vertical Diffusion Schemes in the NCEP Global Forecast System. *Weather and Forecasting, 26*, 520–533. https://doi.org/10.1175/WAF-D-10-05038.1

Harper, K., Uccellini, L. W., Kalnay, E., Carey, K., & Morone, L. (2007). 50th Anniversary of Operational Numerical Weather Prediction. *Bulletin of the American Meteorological Society, 88*, 639-650. https://doi.org/10.1175/BAMS-88-5-639

He, B.-J., Ding, L., & Prasad, D. (2020). Relationships among local-scale urban morphology, urban ventilation, urban heat island and outdoor thermal comfort under sea breeze influence. *Sustainable Cities and Society, 60*, 102289. https://doi.org/10.1016/j.scs.2020.102289

Hersbach, H., Bell, B., Berrisford, P., Hirahara, S., Horányi, A., Muñoz-Sabater, J., . . . Thépaut, J.-N. (2020). The ERA5 global reanalysis. *Quarterly Journal of the Royal Meteorological Society, 146*, 1999-2049. https://doi.org/10.1002/qj.3803

Hertig, E., & Tramblay, Y. (2017). Regional downscaling of Mediterranean droughts under past and future climatic conditions. *Global and Planetary Change, 151*, 36-48. https://doi.org/10.1016/j.gloplacha.2016.10.015

Hoerling, M., Eischeid, J., Perlwitz, J., Quan, X., Zhang, T., & Pegion, P. (2012). On the Increased Frequency of Mediterranean Drought. *Journal of Climate, 25*, 2146-2161. https://doi.org/10.1175/JCLI-D-11-00296.1

Hogan, R. J., & Bozzo, A. (2016). *ECRAD: A new radiation scheme for the IFS.* ECMWF.

Holtslag, A. A., & Boville, B. A. (1993). Local Versus Nonlocal Boundary-Layer Diffusion in a Global Climate Model. *Journal of Climate, 6*, 1825-1842. https://doi.org/10.1175/1520-0442(1993)006<1825:LVNBLD>2.0.CO;2

Hong, S.-Y., Noh, Y., & Dudhia, J. (2006). A New Vertical Diffusion Package with an Explicit Treatment of Entrainment Processes. *Monthly Weather Review, 134*, 2318-2341. https://doi.org/10.1175/MWR3199.1

Hu, X.-M., & Xue, M. (2016). Influence of Synoptic Sea-Breeze Fronts on the Urban Heat Island Intensity in Dallas–Fort Worth, Texas. *Monthly Weather Review, 144*, 1487-1507. https://doi.org/10.1175/MWR-D-15-0201.1

Hu, X.-M., Nielsen-Gammon, J. W., & Zhang, F. (2010, September). Evaluation of Three Planetary Boundary Layer Schemes in the WRF Model. *Journal of Applied Meteorology and Climatology, 49*, 1831-1844. https://doi.org/10.1175/2010JAMC2432.1

Iacono, M. J., Delamere, J. S., Mlawer, E. J., Shephard, M. W., Clough, S. A., & Collins, W. D. (2008). Radiative forcing by long-lived greenhouse gases: Calculations with the AER radiative transfer models. *Journal of Geophysical Research: Atmospheres, 113*, n/a–n/a. https://doi.org/10.1029/2008JD009944

IPCC, 2019: Climate Change and Land: an IPCC special report on climate change, desertification, land degradation, sustainable land management, food security, and greenhouse gas fluxes in terrestrial ecosystems [P.R. Shukla, J. Skea, E. Calvo Buendia, V. Masson-Delmotte, H.-O. Pörtner, D. C. Roberts, P. Zhai, R. Slade, S. Connors, R. van Diemen, M. Ferrat, E. Haughey, S. Luz, S. Neogi, M. Pathak, J. Petzold, J. Portugal Pereira, P. Vyas, E. Huntley, K. Kissick, M. Belkacemi, J. Malley, (eds.)]. In press.

Janjić, Z. I. (1994). The Step-Mountain Eta Coordinate Model: Further Developments of the Convection, Viscous Sublayer, and Turbulence Closure Schemes. *Monthly Weather Review, 122*, 927-945. https://doi.org/10.1175/1520-0493(1994)122<0927:TSMECM>2.0.CO;2

Jiang, Q. (2021). Impact of Elevated Kelvin–Helmholtz Billows on the Atmospheric Boundary Layer. *Journal of the Atmospheric Sciences, 78*, 3983-3999. https://doi.org/10.1175/JAS-D-21-0062.1

Jiménez, P. A., Dudhia, J., González-Rouco, J. F., Navarro, J., Montávez, J. P., & García-Bustamante, E. (2012). A Revised Scheme for the WRF Surface Layer Formulation. *Monthly Weather Review, 140*, 898-918. https://doi.org/10.1175/MWR-D-11-00056.1

Joyce, R. J., Janowiak, J. E., Arkin, P. A., & Xie, P. (2004). CMORPH: A Method that Produces Global Precipitation Estimates from Passive Microwave and Infrared Data at High Spatial and Temporal Resolution. *Journal of Hydrometeorology, 5*, 487-503. https://doi.org/10.1175/1525-7541(2004)005<0487:CAMTPG>2.0.CO;2

Kallos, G., Kotroni, V., Lagouvardos, K., Papadopoulos, A., Varinou, M., Kakaliagou, O., . . . Uliasz, M. (1998). Temporal and Spatial Scales for Transport and Transformation Processes in the Eastern Mediterranean. In S.-E. Gryning, & N. Chaumerliac (Eds.), *Air Pollution Modeling and Its Application XII* (pp. 15–24). Boston, MA: Springer US. https://doi.org/10.1007/978-1-4757-9128-0_2

Khvorostyanov, D. V., Menut, L., Dupont, J.-C., Morille, Y., & Haeffelin, M. (2010, June). The Role of WRF Land Surface Schemes on Weather Simulations in Paris Area.

Kunkel, K. E., Stevens, S. E., Stevens, L. E., & Karl, T. R. (2020). Observed Climatological Relationships of Extreme Daily Precipitation Events With Precipitable Water and Vertical Velocity in the Contiguous United States. *Geophysical Research Letters, 47*, e2019GL086721. https://doi.org/10.1029/2019GL086721

Laprise, R. (1992, January). The Euler Equations of Motion with Hydrostatic Pressure as an Independent Variable. *Monthly Weather Review, 120*, 197-207. https://doi.org/10.1175/1520-0493(1992)120<0197:TEEOMW>2.0.CO;2

Larsen, E. K. (2021). Transpiration patterns of Pinus halepensis Mill in response to environmental stresses in a Mediterranean climate. *PhD thesis*, http://hdl.handle.net/10045/116474

Lebeaupin, C., Ducrocq, V., & Giordani, H. (2006). Sensitivity of torrential rain events to the sea surface temperature based on high-resolution numerical forecasts. *Journal of Geophysical Research: Atmospheres, 111*. https://doi.org/10.1029/2005JD006541

Li, S., Jaroszynski, S., Pearse, S., Orf, L., & Clyne, J. (2019). VAPOR: A Visualization Package Tailored to Analyze Simulation Data in Earth System Science. *Atmosphere, 10*. https://doi.org/10.3390/atmos10090488

Lim, H.-J., & Lee, Y.-H. (2021). High-Resolution Modeling of Mesoscale Circulation in the Atmospheric Boundary Layer over a Complex Coastal Area. *Atmosphere, 12*. https://doi.org/10.3390/atmos12121649

Lionello, P., & Scarascia, L. (2018, June). The relation between climate change in the Mediterranean region and global warming. *Regional Environmental Change, 18*, 1481–1493. https://doi.org/10.1007/s10113-018-1290-1

López-Moreno, J. I., Vicente-Serrano, S. M., Gimeno, L., & Nieto, R. (2009). Stability of the seasonal distribution of precipitation in the Mediterranean region: Observations since 1950 and projections for the 21st century. *Geophysical Research Letters, 36*. https://doi.org/10.1029/2009GL037956

Lorenzo-Lacruz, J., Amengual, A., Garcia, C., Morán-Tejeda, E., Homar, V., Maimó-Far, A., . . . Romero, R. (2019). Hydro-meteorological reconstruction and geomorphological impact assessment of the October 2018 catastrophic flash flood at Sant Llorenç, Mallorca (Spain). *Natural Hazards and Earth System Sciences, 19*, 2597–2617. https://doi.org/10.5194/nhess-19-2597-2019

Lutgens, F. K., Tarbuck, E. J., & Tusa, D. (1995). *The atmosphere* (Vol. 462). Prentice-Hall Englewood Cliffs, NJ, USA.

Lynch, P. (2008). The origins of computer weather prediction and climate modeling. *Journal of Computational Physics, 227*, 3431-3444. https://doi.org/10.1016/j.jcp.2007.02.034

Mahrer, Y., & Pielke, R. A. (1977). The Effects of Topography on Sea and Land Breezes in a Two-Dimensional Numerical Model. *Monthly Weather Review, 105*, 1151-1162. https://doi.org/10.1175/1520-0493(1977)105<1151:TEOTOS>2.0.CO;2

Manrique-Alba, À., Ruiz-Yanetti, S., Moutahir, H., Novak, K., Luis, M. d., & Bellot, J. (2017-01-01). Soil moisture and its role in growth-climate relationships across an aridity gradient in semiarid Pinus halepensis forests. *Soil moisture and its role in growth-climate relationships across an aridity gradient in semiarid Pinus halepensis forests*.

Mariani, L., & Parisi, S. G. (2014). Extreme Rainfalls in the Mediterranean Area. In N. Diodato, & G. Bellocchi (Eds.), *Storminess and Environmental Change: Climate Forcing and Responses in the Mediterranean Region* (pp. 17–37). Dordrecht: Springer Netherlands. https://doi.org/10.1007/978-94-007-7948-8_2

MedECC. (2020). Climate and Environmental Change in the Mediterranean Basin – Current Situation and Risks for the Future. First Mediterranean Assessment Report. https://doi.org/10.5281/zenodo.4768833

Miao, J.-F., Kroon, L. J., Vilà-Guerau de Arellano, J., & Holtslag, A. A. (2003). Impacts of topography and land degradation on the sea breeze over eastern Spain. *Meteorology and Atmospheric Physics, 84*, 157–170. https://doi.org/10.1007/s00703-002-0579-1

Milano, M., Ruelland, D., Fernandez, S., Dezetter, A., Fabre, J., Servat, E., . . . Thivet, G. (2013). Current state of Mediterranean water resources and future trends under climatic and anthropogenic changes. *Hydrological Sciences Journal, 58*, 498-518. https://doi.org/10.1080/02626667.2013.774458

Millán, M. M. (2014). Extreme hydrometeorological events and climate change predictions in Europe. *Journal of Hydrology, 518*, 206-224. https://doi.org/10.1016/j.jhydrol.2013.12.041

Millán, M. M., Estrela, M. J., & Badenas, C. (1998). Meteorological Processes Relevant to Forest Fire Dynamics on the Spanish Mediterranean Coast. *Journal of Applied Meteorology, 37*, 83-100. https://doi.org/10.1175/1520-0450(1998)037<0083:MPRTFF>2.0.CO;2

Millán, M. M., Estrela, M. J., & Miró, J. (2005, July). Rainfall Components: Variability and Spatial Distribution in a Mediteranean Area (Valencia Region). *Journal of Climate, 18*, 2682–2705.

Millán, M. M., Estrela, M. J., Sanz, M. J., Mantilla, E., Martín, M., Pastor, F., . . . Versino, B. (2005). Climatic Feedbacks and Desertification: The Mediterranean Model. *Journal of Climate, 18*, 684-701. https://doi.org/10.1175/JCLI-3283.1

Millán, M. M., Mantilla, E., Salvador, R., Carratalá, A., Sanz, M. J., Alonso, L., . . . Navazo, M. (2000). Ozone Cycles in the Western Mediterranean Basin: Interpretation of Monitoring Data in Complex Coastal Terrain. *Journal of Applied Meteorology, 39*, 487-508. https://doi.org/10.1175/1520-0450(2000)039<0487:OCITWM>2.0.CO;2

Millán, M. M., Salvador, R., Mantilla, E., & Kallos, G. (1997). Photooxidant dynamics in the Mediterranean basin in summer: Results from European research projects. *Journal of Geophysical Research: Atmospheres, 102*, 8811-8823. https://doi.org/10.1029/96JD03610

Millán, M. M., Sanz, M. J., Salvador, R., & Mantilla, E. (2002). Atmospheric dynamics and ozone cycles related to nitrogen deposition in the western Mediterranean.

Environmental Pollution, 118, 167-186. https://doi.org/10.1016/S0269-7491(01)00311-6

Miller, S. T., Keim, B. D., Talbot, R. W., & Mao, H. (2003). Sea breeze: Structure, forecasting, and impacts. *Reviews of Geophysics, 41*. https://doi.org/10.1029/2003RG000124

Milovac, J., Warrach-Sagi, K., Behrendt, A., Späth, F., Ingwersen, J., & Wulfmeyer, V. (2016). Investigation of PBL schemes combining the WRF model simulations with scanning water vapor differential absorption lidar measurements. *Journal of Geophysical Research: Atmospheres, 121*, 624–649. https://doi.org/10.1002/2015JD023927

Miró, J. J., Estrela, M. J., Caselles, V., & Gómez, I. (2018). Spatial and temporal rainfall changes in the Júcar and Segura basins (1955–2016): Fine-scale trends. *International Journal of Climatology, 38*, 4699-4722. https://doi.org/10.1002/joc.5689

Miró, J. J., Estrela, M. J., Olcina-Cantos, J., & Martin-Vide, J. (2021). Future Projection of Precipitation Changes in the Júcar and Segura River Basins (Iberian Peninsula) by CMIP5 GCMs Local Downscaling. *Atmosphere, 12*. https://doi.org/10.3390/atmos12070879

Mlawer, E. J., Taubman, S. J., Brown, P. D., Iacono, M. J., & Clough, S. A. (1997). Radiative transfer for inhomogeneous atmospheres: RRTM, a validated correlated-k model for the longwave. *Journal of Geophysical Research: Atmospheres, 102*, 16663–16682. https://doi.org/10.1029/97JD00237

Molina, M. O., Gutiérrez, C., & Sánchez, E. (2021). Comparison of ERA5 surface wind speed climatologies over Europe with observations from the HadISD dataset. *International Journal of Climatology, 41*, 4864-4878. https://doi.org/10.1002/joc.7103

Montornès, A., Codina, B., & Zack, J. W. (2015, December). A discussion about the role of shortwave schemes on real WRF-ARW simulations. Two case studies: cloudless and cloudy sky. *Tethys*, 13–31. https://doi.org/10.3369/tethys.2015.12.02

Montornès, A., Codina, B., & Zack, J. W. (2015, March). Analysis of the ozone profile specifications in WRF-ARW model and their impact on the simulation of the direct solar radiation. *Atmospheric Chemistry and Physics, 15*, 2693–2707. https://doi.org/10.5194/acp-15-2693-2015

Moutahir, H. (2016). Likely effects of climate change on water resources and vegetation growth period in the province of Alicante, southeastern Spain. *Likely effects of climate change on water resources and vegetation growth period in the province of Alicante, southeastern Spain*.

Moutahir, H., Fernández Mejuto, M., Andreu Rodes, J. M., Touhami, I., Ayanz López-Cuervo, J., & Bellot, J. (2019-12). Observed and projected changes on aquifer recharge in a Mediterranean semi-arid area, SE Spain. *Observed and projected changes on aquifer recharge in a Mediterranean semi-arid area, SE Spain*.

Mu, Q., Zhao, M., & Running, S. W. (2013). MODIS global terrestrial evapotranspiration (ET) product (NASA MOD16A2/A3). *Algorithm Theoretical Basis Document, Collection, 5*, 600.

Navascués, B., Rodriguez-Camino, E., Ayuso, J. J., & Järvenoja, S. (2003, January). Analysis of surface variables and parameterization of surface processes in HIRLAM. Part II: Seasonal assimilation experiment. *Analysis of surface variables and parameterization of surface processes in HIRLAM. Part II: Seasonal assimilation experiment*.

Niu, G.-Y., Yang, Z.-L., Dickinson, R. E., Gulden, L. E., & Su, H. (2007). Development of a simple groundwater model for use in climate models and evaluation with Gravity Recovery and Climate Experiment data. *Journal of Geophysical Research: Atmospheres, 112*. https://doi.org/10.1029/2006JD007522

Niu, G.-Y., Yang, Z.-L., Mitchell, K. E., Chen, F., Ek, M. B., Barlage, M., . . . Xia, Y. (2011). The community Noah land surface model with multiparameterization options (Noah_{M}{P}{)}: 1. Model description and evaluation with local-scale measurements. *Journal of Geophysical Research, 116*, 1–19. https://doi.org/10.1029/2010JD015139

Noh, Y., Cheon, W. G., Hong, S. Y., & Raasch, S. (2003). Improvement of the K-profile Model for the Planetary Boundary Layer based on Large Eddy Simulation Data. *Boundary-Layer Meteorology, 107*, 401–427. https://doi.org/10.1023/A:1022146015946

Noilhan, J., & Planton, S. (1989, March). A Simple Parameterization of Land Surface Processes for Meteorological Models. *Monthly Weather Review, 117*, 536–549. http://www2.mmm.ucar.edu/wrf/users/phys_refs/LAND_SURFACE/pleim_xu_part1.pdf

Ohashi, Y., & Kida, H. (2002). Local Circulations Developed in the Vicinity of Both Coastal and Inland Urban Areas: A Numerical Study with a Mesoscale Atmospheric Model. *Journal of Applied Meteorology (1988-2005), 41*, 30–45. http://www.jstor.org/stable/26184930

Palau, J. L., Pérez-Landa, G., Diéguez, J. J., Monter, C., & Millán, M. M. (2005). The importance of meteorological scales to forecast air pollution scenarios on coastal complex terrain. *Atmospheric Chemistry and Physics, 5*, 2771–2785. https://doi.org/10.5194/acp-5-2771-2005

Pastor, F., Estrela, M. J., Peñarrocha, D., & Millán, M. M. (2001). Torrential Rains on the Spanish Mediterranean Coast: Modeling the Effects of the Sea Surface Temperature. *Journal of Applied Meteorology, 40*, 1180-1195. https://doi.org/10.1175/1520-0450(2001)040<1180:TROTSM>2.0.CO;2

Pastor, F., Valiente, J. A., & Palau, J. L. (2018). Sea Surface Temperature in the Mediterranean: Trends and Spatial Patterns (1982-2016). *Pure and Applied Geophysics, 175*, 4017–4029. https://doi.org/10.1007/s00024-017-1739-z

Pastor, F., Valiente, J. A., & Palau, J. L. (2019). Sea Surface Temperature in the Mediterranean: Trends and Spatial Patterns (1982–2016). In I. Vilibić, K. Horvath, & J. L. Palau (Eds.), *Meteorology and Climatology of the Mediterranean and Black Seas* (pp. 297–309). Cham: Springer International Publishing. https://doi.org/10.1007/978-3-030-11958-4_18

Peral, C., Navascués, B., & Ramos, P. (2017). Serie de precipitación diaria en rejilla con fines climáticos. *Serie de precipitación diaria en rejilla con fines climáticos*.

Pérez, J. J., Navarro, M. J., & Cantos, J. O. (2015). Statistical downscaling and attribution of air temperature change patterns in the Valencia region (1948–2011). *Atmospheric Research, 156*, 189-212. https://doi.org/10.1016/j.atmosres.2015.01.003

Pérez-Landa, G., Ciais, P., Sanz, M. J., Gioli, B., Miglietta, F., Palau, J. L., . . . Millán, M. M. (2007). Mesoscale circulations over complex terrain in the Valencia coastal region, Spain – Part 1: Simulation of diurnal circulation regimes. *Atmospheric Chemistry and Physics, 7*, 1835–1849. https://doi.org/10.5194/acp-7-1835-2007

Pineda, N., Jorba, O., Jorge, J., & Baldasano, J. M. (2004). Using NOAA AVHRR and SPOT VGT data to estimate surface parameters: application to a mesoscale meteorological model. *International Journal of Remote Sensing, 25*, 129-143. https://doi.org/10.1080/0143116031000115201

Plant, R. S., & Keith, G. J. (2007). Occurrence of Kelvin-Helmholtz Billows in Sea-breeze Circulations. *Boundary-Layer Meteorology, 122*, 1–15. https://doi.org/10.1007/s10546-006-9089-x

Pleim, J. E. (2006). A Simple, Efficient Solution of Flux–Profile Relationships in the Atmospheric Surface Layer. *Journal of Applied Meteorology and Climatology, 45*, 341-347. https://doi.org/10.1175/JAM2339.1

Pleim, J. E. (2007). A Combined Local and Nonlocal Closure Model for the Atmospheric Boundary Layer. Part I: Model Description and Testing. *Journal of Applied Meteorology and Climatology, 46*, 1383-1395. https://doi.org/10.1175/JAM2539.1

Pleim, J. E., & Chang, J. S. (1992). A non-local closure model for vertical mixing in the convective boundary layer. *Atmospheric Environment. Part A. General Topics, 26*, 965-981. https://doi.org/10.1016/0960-1686(92)90028-J

Pleim, J. E., & Gilliam, R. C. (2009, July). An Indirect Data Assimilation Scheme for Deep Soil Temperature in the Pleim-Xiu Land Surface Model. *Journal of Applied Meteorology and Climatology, 48*, 1362–1376. http://www2.mmm.ucar.edu/wrf/users/phys_refs/LAND_SURFACE/pleim_xu_part5.pdf

Pleim, J. E., & Xiu, A. (1995). Development and Testing of a Surface Flux and Planetary Boundary Layer Model for Application in Mesoscale Models. *Journal of Applied Meteorology and Climatology, 34*, 16-32. https://doi.org/10.1175/1520-0450-34.1.16

Pleim, J. E., & Xiu, A. (2003, December). Development of a Land Surface Model. Part II: Data Assimilation. *Journal of Applied Meteorology, 42*, 1811–1822. http://www2.mmm.ucar.edu/wrf/users/phys_refs/LAND_SURFACE/pleim_xu_part4.pdf

Poulos, S. E. (2020). The Mediterranean and Black Sea Marine System: An overview of its physico-geographic and oceanographic characteristics. *Earth-Science Reviews, 200*, 103004. https://doi.org/10.1016/j.earscirev.2019.103004

Quintana Seguí, P., Peral, C., Turco, M., Llasat, M., & Martin, E. (2016, June). Meteorological analysis systems in north-east Spain: validation of SAFRAN

and SPAN. *Journal of Environmental Informatics, 27*. https://doi.org/10.3808/jei.201600335

Quintana-Seguí, P., Turco, M., Herrera, S., & Miguez-Macho, G. (2017). Validation of a new SAFRAN-based gridded precipitation product for Spain and comparisons to Spain02 and ERA-Interim. *Hydrology and Earth System Sciences, 21*, 2187–2201. https://doi.org/10.5194/hess-21-2187-2017

Rebora, N., Molini, L., Casella, E., Comellas, A., Fiori, E., Pignone, F., . . . Parodi, A. (2013). Extreme Rainfall in the Mediterranean: What Can We Learn from Observations? *Journal of Hydrometeorology, 14*, 906-922. https://doi.org/10.1175/JHM-D-12-083.1

Rhodin, A. (1995). Interaction of a cold front with a sea breeze front Numerical simulations. *Tellus A, 47*, 403-420. https://doi.org/10.1034/j.1600-0870.1995.t01-3-00002.x

Rodriguez-Camino, E., Navascués, B., Ayuso, J. J., & Järvenoja, S. (2003, January). Analysis of surface variables and parameterization of surface processes in HIRLAM. Part I: Approach and verification by parallel runs. *Analysis of surface variables and parameterization of surface processes in HIRLAM. Part I: Approach and verification by parallel runs, 58*.

Rosselló-Geli, J., & Grimalt-Gelabert, M. (2021). Mapping of the Flood Distribution in an Urban Environment: The Case of Palma (Mallorca, Spain) in the First Two Decades of the 21st Century. *Earth, 2*, 960–971. https://doi.org/10.3390/earth2040056

Santanello, J. A., Dirmeyer, P. A., Ferguson, C. R., Findell, K. L., Tawfik, A. B., Berg, A., . . . Wulfmeyer, V. (2018). Land–Atmosphere Interactions: The LoCo Perspective. *Bulletin of the American Meteorological Society, 99*, 1253-1272. https://doi.org/10.1175/BAMS-D-17-0001.1

Santanello, J. A., Friedl, M. A., & Kustas, W. P. (2005). An Empirical Investigation of Convective Planetary Boundary Layer Evolution and Its Relationship with the Land Surface. *Journal of Applied Meteorology, 44*, 917-932. https://doi.org/10.1175/JAM2240.1

Santanello, J. A., Peters-Lidard, C. D., & Kumar, S. V. (2011). Diagnosing the Sensitivity of Local Land–Atmosphere Coupling via the Soil Moisture–Boundary Layer Interaction. *Journal of Hydrometeorology, 12*, 766-786. https://doi.org/10.1175/JHM-D-10-05014.1

Santanello, J. A., Peters-Lidard, C. D., Kennedy, A., & Kumar, S. V. (2013). Diagnosing the Nature of Land–Atmosphere Coupling: A Case Study of Dry/Wet Extremes in the U.S. Southern Great Plains. *Journal of Hydrometeorology, 14*, 3-24. https://doi.org/10.1175/JHM-D-12-023.1

Santanello, J. A., Peters-Lidard, C. D., Kumar, S. V., Alonge, C., & Tao, W.-K. (2009). A Modeling and Observational Framework for Diagnosing Local Land–Atmosphere Coupling on Diurnal Time Scales. *Journal of Hydrometeorology, 10*, 577-599. https://doi.org/10.1175/2009JHM1066.1

Santanello, J. A., Roundy, J., & Dirmeyer, P. A. (2015). Quantifying the Land–Atmosphere Coupling Behavior in Modern Reanalysis Products over the U.S.

Southern Great Plains. *Journal of Climate, 28*, 5813-5829. https://doi.org/10.1175/JCLI-D-14-00680.1

Schmetz, J., Pili, P., Tjemkes, S., Just, D., Kerkmann, J., Rota, S., & Ratier, A. (2002). An Introduction to Meteosat Second Generation (MSG). *Bulletin of the American Meteorological Society, 83*, 977-992. https://doi.org/10.1175/1520-0477(2002)083<0977:AITMSG>2.3.CO;2

Seneviratne, S. I., Corti, T., Davin, E. L., Hirschi, M., Jaeger, E. B., Lehner, I., . . . Teuling, A. J. (2010). Investigating soil moisture–climate interactions in a changing climate: A review. *Earth-Science Reviews, 99*, 125-161. https://doi.org/10.1016/j.earscirev.2010.02.004

Sha, W., Kawamura, T., & Ueda, H. (1991). A Numerical Study on Sea/Land Breezes as a Gravity Current: Kelvin–Helmholtz Billows and Inland Penetration of the Sea-Breeze Front. *Journal of Atmospheric Sciences, 48*, 1649-1665. https://doi.org/10.1175/1520-0469(1991)048<1649:ANSOSB>2.0.CO;2

Shaltout, M., & Omstedt, A. (2014). Recent sea surface temperature trends and future scenarios for the Mediterranean Sea. *Oceanologia, 56*, 411-443. https://doi.org/10.5697/oc.56-3.411

Shuman, F. G. (1989). History of Numerical Weather Prediction at the National Meteorological Center. *Weather and Forecasting, 4*, 286-296. https://doi.org/10.1175/1520-0434(1989)004<0286:HONWPA>2.0.CO;2

Silva Dias, M. A., & Jaschke Machado, A. N. (1997). The role of local circulations in summertime convective development and nocturnal fog in São Paulo, brazil. *Boundary-Layer Meteorology, 82*, 135–157. https://doi.org/10.1023/A:1000241602661

Simpson, J. E. (1994). *Sea breeze and local winds.* cambridge university press.

Simpson, M., Warrior, H., Raman, S., Aswathanarayana, P. A., Mohanty, U. C., & Suresh, R. (2007). Sea-breeze-initiated rainfall over the east coast of India during the Indian southwest monsoon. *Natural Hazards, 42*, 401–413. https://doi.org/10.1007/s11069-006-9081-2

Singh, K. S., Albert, J., Bhaskaran, P. K., & Alam, P. (2021). Numerical simulation of an extremely severe cyclonic storm over the Bay of Bengal using WRF modelling system: influence of model initial condition. *Modeling Earth Systems and Environment, 7*, 2741–2752. https://doi.org/10.1007/s40808-020-01069-1

Skamarock, W. C., Klemp, J. B., Dudhia, J., Gili, D. O., Barker, D. M., Duda, M. B., . . . Powers, J. G. (2008, June). *A Description of the Advanced Research WRF Versuion 3.* Tech. rep., NCAR, Boulder, Colorado 80308-2195.

Soler, M. R., Arasa, R., Merino, M., Olid, M., & Ortega, S. (2011). Modelling Local Sea-Breeze Flow and Associated Dispersion Patterns Over a Coastal Area in North-East Spain: A Case Study. *Boundary-Layer Meteorology, 140*, 37–56. https://doi.org/10.1007/s10546-011-9599-z

Steele, C. J., Dorling, S. R., von Glasow, R., & Bacon, J. (2015). Modelling sea breeze climatologies and interactions on coasts in the southern North Sea: implications for offshore wind energy. *Quarterly Journal of the Royal Meteorological Society, 141*, 1821-1835. https://doi.org/10.1002/qj.2484

Stull, R. B. (1988). *An introduction to boundary layer meteorology* (Vol. 13). Springer Science & Business Media.

Sun, G., Hu, Z., Ma, Y., Xie, Z., Wang, J., & Yang, S. (2020). Simulation analysis of local land atmosphere coupling in rainy season over a typical underlying surface in the Tibetan Plateau. *Hydrology and Earth System Sciences, 24*, 5937–5951. https://doi.org/10.5194/hess-24-5937-2020

Sun, G., Hu, Z., Ma, Y., Xie, Z., Yang, S., & Wang, J. (2020). Analysis of local land-atmosphere coupling in rainy season over a typical underlying surface in Tibetan Plateau based on field measurements and ERA5. *Atmospheric Research, 243*, 105025. https://doi.org/10.1016/j.atmosres.2020.105025

Touhami, I., Andreu, J. M., Chirino, E., Sánchez, J. R., Moutahir, H., Pulido-Bosch, A., . . . Bellot, J. (2013). Recharge estimation of a small karstic aquifer in a semiarid Mediterranean region (southeastern Spain) using a hydrological model. *Hydrological Processes, 27*, 165-174. https://doi.org/10.1002/hyp.9200

Touhami, I., Andreu, J. M., Chirino, E., Sánchez, J. R., Pulido-Bosch, A., Martínez-Santos, P., . . . Bellot, J. (2014). Comparative performance of soil water balance models in computing semi-arid aquifer recharge. *Hydrological Sciences Journal, 59*, 193-203. https://doi.org/10.1080/02626667.2013.802094

Touhami, I., Chirino, E., Andreu, J. M., Sánchez, J. R., Moutahir, H., & Bellot, J. (2015). Assessment of climate change impacts on soil water balance and aquifer recharge in a semiarid region in south east Spain. *Journal of Hydrology, 527*, 619-629. https://doi.org/10.1016/j.jhydrol.2015.05.012

Tramblay, Y., & Somot, S. (2018, November). Future evolution of extreme precipitation in the Mediterranean. *Climatic Change, 151*, 289–302. https://doi.org/10.1007/s10584-018-2300-5

Troen, I. B., & Mahrt, L. (1986). A simple model of the atmospheric boundary layer; sensitivity to surface evaporation. *Boundary-Layer Meteorology, 37*, 129–148. https://doi.org/10.1007/BF00122760

Tuel, A., & Eltahir, E. A. (2020). Why Is the Mediterranean a Climate Change Hot Spot? *Journal of Climate, 33*, 5829-5843. https://doi.org/10.1175/JCLI-D-19-0910.1

Valdes-Abellan, J., Pardo, M. A., & Tenza-Abril, A. J. (2017). Observed precipitation trend changes in the western Mediterranean region. *International Journal of Climatology, 37*, 1285-1296. https://doi.org/10.1002/joc.4984

van Heerwaarden, C. C., Vilà-Guerau de Arellano, J., Moene, A. F., & Holtslag, A. A. (2009). Interactions between dry-air entrainment, surface evaporation and convective boundary-layer development. *Quarterly Journal of the Royal Meteorological Society, 135*, 1277-1291. https://doi.org/10.1002/qj.431

Walko, R. L., & Tremback, C. J. (2005). *ATMET Technical Note 1, Modifications for the Transition from LEAF-2 to LEAF-3.* Tech. rep., ATMET, LLC. http://www.atmet.com/html/docs/rams/

Wallace, J. M., & Hobbs, P. V. (2006). *Atmospheric science: an introductory survey* (Vol. 92). Elsevier.

Weverberg, K. V., Goudenhoofdt, E., Blahak, U., Brisson, E., Demuzere, M., Marbaix, P., & van Ypersele, J.-P. (2014). Comparison of one-moment and two-moment

bulk microphysics for high-resolution climate simulations of intense precipitation. *Atmospheric Research, 147*, 145-161. https://doi.org/10.1016/j.atmosres.2014.05.012

Wheatley, D. M., Yussouf, N., & Stensrud, D. J. (2014). Ensemble Kalman Filter Analyses and Forecasts of a Severe Mesoscale Convective System Using Different Choices of Microphysics Schemes. *Monthly Weather Review, 142*, 3243-3263. https://doi.org/10.1175/MWR-D-13-00260.1

Williamson, D. L. (2007). The Evolution of Dynamical Cores for Global Atmospheric Models. *Journal of the Meteorological Society of Japan. Ser. II, 85B*, 241-269. https://doi.org/10.2151/jmsj.85B.241

Willmott, C. J., Ackleson, S. G., Davis, R. E., Feddema, J. J., Klink, K. M., Legates, D. R., . . . Rowe, C. M. (1985, September). Statistics for the evaluation and comparison of models. *J. Geophys. Res., 90*, 8995–9005. https://doi.org/10.1029/JC090iC05p08995

Xie, B., Fung, J. C., Chan, A., & Lau, A. (2012). Evaluation of nonlocal and local planetary boundary layer schemes in the WRF model. *Journal of Geophysical Research, 117*, 1–26. https://doi.org/10.1029/2011JD017080

Xie, P., Joyce, R., Wu, S., Yoo, S.-H., Yarosh, Y., Sun, F., & Lin, R. (2017). Reprocessed, Bias-Corrected CMORPH Global High-Resolution Precipitation Estimates from 1998. *Journal of Hydrometeorology, 18*, 1617-1641. https://doi.org/10.1175/JHM-D-16-0168.1

Xiu, A., & Pleim, J. E. (2001). Development of a Land Surface Model. Part I: Application in a Mesoscale Meteorological Model. *Journal of Applied Meteorology, 40*, 192–209. http://www2.mmm.ucar.edu/wrf/users/phys_refs/LAND_SURFACE/pleim_xu_part3.pdf

Yang, Z.-L., Niu, G.-Y., Mitchell, K. E., Chen, F., Ek, M. B., Barlage, M., . . . Xia, Y. (2011). The community Noah land surface model with multiparameterization options (Noah_MP): 2. Evaluation over global river basins. *Journal of Geophysical Research, 116*, 1–16. https://doi.org/10.1029/2010JD015140

Zeng, X.-M., Wang, N., Wang, Y., Zheng, Y., Zhou, Z., Wang, G., . . . Liu, H. (2015, September). WRF-simulated sensitivity to land surface schemes in short and medium ranges for a high-temperature event in East China: A comparative study. *Journal of Advances in Modeling Earth Systems, 7*, 1305–1325. https://doi.org/10.1002/2015MS000440

Zheng, Y., Alapaty, K., Herwehe, J. A., & Niyogi, D. (2016, March). Improving High-Resolution Weather Forecast Using the Weather Research and Forecast (WRF) Model with an Updated Kain-Fritsch Scheme. *Monthly Weather Review, 144*, 833–860. https://doi.org/10.1175/MWR-D-15-0005.1

Zollo, A. L., Rillo, V., Bucchignani, E., Montesarchio, M., & Mercogliano, P. (2016). Extreme temperature and precipitation events over Italy: assessment of high-resolution simulations with COSMO-CLM and future scenarios. *International Journal of Climatology, 36*, 987-1004. https://doi.org/10.1002/joc.4401